Vibration-based monitoring of structures: Algorithms for fault detection and uncertainty quantification of modal indicators

Szymon Gres

Vibration-based monitoring of structures

Algorithms for fault detection and uncertainty quantification of modal indicators

Szymon Gres

Department of Civil Engineering

Aalborg University

Ph.D. Dissertation

Dissertation submitted June, 2019

Thesis submitted:	June, 2019
Ph.D. Supervisor:	Prof. Lars Damkilde, Aalborg University
Company Supervisor:	M.Sc. Søren Andreas Nielsen, Universal Foundation A/S
Ph.D. Committee:	Prof. Jean-Claude Golinval, University of Liége
	Prof. Christof Devriendt, Vrije University
	Dr Mohsen N. Soltani, Aalborg University
Ph.D. Series:	Faculty of Engineering and Science, Aalborg University

ISSN: 2446-1636
ISBN: 978-87-7210-469-0

Published by:
Aalborg University Press
Skjernvej 4A, 2nd floor
DK - 9220 Aalborg East
Phone: +45 99407140
aauf@forlag.aau.dk
forlag.aau.dk

Printed in Denmark by Rosendahls, 2019

To Wojtek and Krzysiek, my brothers.

Acknowledgments

This thesis would not have been possible without the funding from Innovationsfonden Denmark and Universal Foundation A/S (a private company) for which I am utterly grateful. Therefore, first, I would like to thank Søren Andreas Nielsen, my company supervisor, for his support, open-mind and the freedom he granted me during the course of my study. The time I've spent in Universal Foundation A/S was truly an engineering experience thanks to the great team therein: Morten Fejerskov, Dr Mohammad Javad Vahdatirad, Laura Garcia Castillo, Dr Emanuel Stroescu, Andreas Langbak, Jeppe Pryds, Kristian Ravn and Jette Anna Nielsen- I would like to thank you all for the good time in the office.

Next, I would like to express my gratitude to my main supervisor Prof. Lars Damkilde. His many initiatives, like the Structural Health Monitoring (SHM) group, were an inspiration for methods developed in this thesis and an opportunity to meet with other researchers in Danish SHM field, which was very rewarding. In particular Dr Martin Dalgaard Ulriksen and Rasmus Johan Johansen, with whom I collaborated on several conference papers, have my big thanks. Special thanks are also to Prof. Lars Bo Ibsen for supervising my M.Sc. thesis and inspiring me to pursue the research, which ended up with a doctoral study.

I am very thankful to Dr Palle Andersen, whose company- Structural Vibration Solutions (SVS) A/S, co-hosted and partly financed my study for almost two years. His constant support, strive for innovation and insight on the practical aspects of structural monitoring has pushed this study forward and opened doors to many collaboration possibilities, one of which, with Niels Jørgen Jacobsen (B&K Nærum) and Dr Christopher Hoen (Kongsberg Digital) resulted in the development of the harmonic removal method. Through Palle I was encouraged to participate in many conferences and research projects, which were a great experience. In particular, I am grateful for taking part in the Innobooster project for the mode shape uncertainty quantification, which lead to a collaboration with the I4S team at the *French Institute for Research in Computer Science and Automatic Control* (Inria) in Rennes, which I've visited for a research stay.

The research stay in I4S team at Inria was a pivotal point of my study and I would like to express my deepest gratitude to Dr Laurent Mevel and Dr Michael Döhler for the support and the confidence they gave me during, and after, that period. Their enthusiasm, brilliant ideas, realism, eyes for details and the countless hours spent with me in front of the whiteboard and revising my writing has shaped this Ph.D. thesis, and me. They were always available for a technical conversation and for a cup of coffee, and for both I am immensely grateful. Big thanks goes as well to other members of I4S team, Prof. Frédéric Gillot and Dr Qinghua Zhang, with whom

I shared many good discussions. The combined five months I've spent in Rennes, and its beautiful surroundings, were a remarkable period, and for this opportunity I would like to thank all the people who enabled it- the leader of the I4S team Dr Laurent Mevel, Dr Michael Döhler who supervised me there, both of my supervisors Søren Andreas Nielsen and Prof. Lars Damkilde, and Dr Palle Andersen.

Finally, I would like to thank all who kept up my good spirit during those three years. My rowing team at Aalborg Roklub, my friends, my family and Estela. Your endless moral support, your love and an occasional sauna after a rowing session has helped me more then I can quantify.

Szymon Gres
Aalborg, March, 2019

Introduction and outline of the thesis

Context of the thesis

Vibration-based structural monitoring is an interdisciplinary field within the Structural Health Monitoring (SHM) domain. It refers to the implementation of a strategy that allows to monitor structural integrity based on vibration measurements collected from a structure during its operation. Its real-life deployment consists of several interconnected tasks such as the design of the monitoring system, which comprises different sensors arranged in a specific layout, and the choice or design of appropriate signal processing methods to analyze the measurements. Such monitoring systems are applied on various engineering structures, e.g. wind turbines, offshore structures (see Figure 1), bridges, high rise buildings, gearboxes, rotors and engines.

Figure 1: Offshore meteorological mast (left). Cracks in a offshore platform (right). Both pictures available by the courtesy of Universal Foundation A/S.

The recent growth in this field is dictated by an industrial demand and technological developments in both hardware and software for storing and analyzing the data. The industrial resolve emerges not only from reducing the costs of operation and maintenance of monitored structures by e.g. data-driven inspection planning, but also from reducing the risk of catastrophic failures by an early fault detection, and enhancing the design routines by merging virtual design models with measurements. All those factors lead to minimize the *human* factor, ranging from e.g. engineers analyzing the data to groups of divers or climbers conducting visual inspections on offshore structures, which requires considerable costs.

Methods that analyze vibration measurements and give the actual information about the structural condition are at the heart of the SHM problem. In practice the integrity of structures is monitored during their operation, hence under unknown, unmeasured, ambient excitation conditions. These particular conditions pose some challenges for the underlying methods, which may lead to false alarms appearing during damage detection or inaccurate estimates of modal parameters, if not treated correctly. In this thesis three problems revolving around these conditions are considered. First, the effect of periodic excitation on the estimation of vibration characteristics is explored and treated. Second, the uncertainties related to noisy data are quantified for modal indicators. Third, the changes in the natural excitation conditions are accounted for in the design of a robust damage detection method. The context of these problems is detailed in the following.

A standard assumption in many methods is the stationarity of the unknown ambient excitation. However, this assumption is sometimes violated, e.g. in the presence of periodic excitation originating from rotating components of the structure during its operation. Those external disturbances influence recorded output measurements, such as accelerations, displacements, velocities or strains, which are the structural responses to the unknown excitation. As such, those measurements are used to identify the modal parameters, namely natural frequencies, damping ratios and mode shapes, which are key characteristics of a structure. These quantities are estimated in Operational Modal Analysis (OMA) by system identification techniques, where the eigenstructure of a linear system is identified from the measurements. The periodic excitation might render OMA difficult in practice, since this eigenstructure then contains a mix of periodic and structural modes, which are sometimes hard to separate. Moreover, when structural and periodic modes are close, the correct identification of the structural mode may become impossible with classical methods.

Estimates of the modal parameters are impaired with statistical uncertainties, since they are computed from ambient vibration data of finite length, which are usually afflicted by noise. Hence, they are never equal to the true physical parameters of the structure. Those uncertainties should be quantified or accounted for, which is often crucial in practice when interpreting the outcome from system identification methods. Moreover, such interpretation can be enhanced by so-called modal indicators, which are quantities reflecting some physical aspects of the estimated mode shapes. Those indicators, Modal Assurance Criterion (MAC) and Modal Phase Collinearity (MPC), inherit the statistical uncertainties from the underlying mode shape estimates. While the statistical framework for modal parameters is well-known and developed in the context of subspace-based system identification methods, uncertainty quantification of modal indicators has not been carried out yet. A particular challenge for this analysis is the boundedness of these modal indicators between the values 0 and 1, for which, at the endpoints of this interval, the classical Gaussian uncertainty quantification frameworks that are used in OMA are inadequate.

Monitoring of the structural integrity based on measurements refers to detecting changes with some damage-sensitive features derived from the data. These features, as any estimated parameters, are inherently affected by uncertainty, which, when not accounted for, can mask small changes inflicted on the system. Often, modal parameters are used as such features, since they are affected by changes in stiffness due to damage. However, the performance of modal parameter-based methods depends on several factors e.g. the quality of parameters estimated from the data and the ability to track the selected estimates after identifying them from the healthy state of the

system. Hence it is desirable to compute those features directly on the data without the need of modal parameter estimation. Together with a statistical evaluation of such features, it can yield automated damage detection. In addition to the statistical variability, those data-based damage features are inherently dependent on the natural changes in the ambient excitation conditions. That poses a major challenge in the evaluation of such indicators, since excitation conditions are in principle unknown and unmeasured, hence any change due to that may be falsely classified as damage. A solution to that problem lies in the design of a damage detection residual, whose mean value is independent of changes in excitation conditions. Such robustness towards the changes in the excitation properties is prerequisite for the use of any residual in practical applications to damage detection.

Contributions of the thesis

The methods developed in this thesis aim to account for challenges connected to vibration-based structural monitoring during ambient excitation conditions. First, a time domain method to remove periodic frequencies originating from rotating components on the structure is presented. Second, a statistical framework to quantify the uncertainty in the estimates of MAC and MPC is developed. Lastly, a data driven damage detection method robust to changes in the excitation properties under the healthy state of the structure is designed.

The theoretical developments of this thesis revolve around stochastic subspace-based (SSI) algorithms, which are considered as practical tools for the identification of the eigenstructure of linear vibrating systems. In particular, their capacity of solving large models, appealing statistical properties like non-stationary consistency and known distribution characteristics are important features for OMA and SHM applications.

The contributions of the thesis are detailed as follows:

1. **Harmonic removal for subspace-based system identification**.

   In the context of structural systems excited with random loads combined with periodic signals, subspace-based methods identify the harmonics as very lightly damped modes that one could filter in the mode selection process. However, when the harmonic excitation coincides with structural modes or is of high energy that masks the system response to the random part of the input, it is desirable to discard their influence over the output signal prior to system identification and without additional knowledge of e.g. tachometer measurements. The proposed scheme is based on three steps: **1**) formulation of a Kalman filter to predict the structural response due to harmonic modes, **2**) orthogonal projection of the raw time series onto the computed harmonic realizations, and **3**) use of the projected harmonic-free measurements for system identification. This allows time domain removal of the modes that are corresponding to the periodic inputs originating from the rotating components on the structure. Compared to classical approaches e.g. discarding the modes corresponding the periodic frequencies, the developed method offers better estimates of the underlying structural modes, which is reflected in more accurate estimates of their damping ratios and reduced statistical uncertainties.

2. **Uncertainty quantification of modal indicators: Modal Phase Collinearity and Modal Assurance Criterion**.

Modal indicators reflect some physical aspects of the estimated mode shapes. In particular, the Modal Phase Collinearity (MPC) quantifies the complexity of the underlying mode shape estimate, and the Modal Assurance Criterion (MAC) is a measure of similarity between two mode shapes. Both indicators are afflicted with statistical uncertainties since the mode shapes used in their computation are stochastic variables. In many cases, estimates computed from the data are asymptotically Gaussian distributed, such as modal parameters in subspace system identification. Then, a classical approach to approximate their distribution is to use a Gaussian approximation, by means of the first order Delta method [1], which allows to approximate the law of a function of an asymptotic Gaussian variable. However, when the function is bounded, the Gaussian framework is inadequate on its limits, which applies to the following cases of modal indicators:

(a.) for Modal Modal Phase Collinearity when its estimates are computed from asymptotically real-valued mode shapes,

(b.) for Modal Assurance Criterion when its estimates are computed between an exact mode shape from a model and its counterpart estimated from measurements,

(c.) for Modal Assurance Criterion when its estimates are computed between different mode shape estimates belonging to one mode e.g. mode shapes in the stabilization diagram corresponding to one modal alignment.

This thesis depicts the derivation of a statistical framework to analyze the uncertainties of the modal indicators at the limits of their range. The novelty of the proposed approach lies in employing the second order Delta Method, to illustrate that the asymptotic distribution of the modal indicators is not Gaussian but a quadratic form of their underlying mode shapes. The law of the quadratic form is non-trivial but can be approximated by a χ^2 distribution. Consequently, the distributions of the modal indicators are characterized in the aforementioned cases and their confidence intervals are established.

3. **Hankel matrix normalization for damage detection robust to excitation changes**.

   It is well-known that the Hankel matrices of the output covariance sequences contain information of the system matrices, which define the dynamic behavior of a structural system. However, their stochastic part depends on the excitation conditions, which often can rapidly change based on the environment. A damage detection scheme based on Hankel matrices should hence be designed to monitor the changes only in the structural system, which requires appreciation of this environmental variation. In that context, a new residual using the difference of the Hankel matrices in the reference state and the excitation normalized Hankel matrix in the tested, potentially damaged, state is proposed. As such, the corresponding residual is evaluated in the framework of the local asymptotic approach for Gaussian residuals [2]. To decide about the health of the system, the resulting test statistic is compared to a threshold. The robustness of the new approach is achieved via a normalization scheme that is adapted from the multipatch subspace-based system identification [3, 4]. The influence of the excitation properties on the residual is thoroughly studied from a theoretical point

of view. Consequently, the mean value of the proposed residual under healthy and faulty conditions of the system is proved both theoretically and empirically not to depend on the variances of the excitation. Practical aspects of the proposed damage detection test such as robustness to complex excitation conditions and different data size are validated and its numerically stable computation is derived.

The proposed methods are first validated for their theoretical properties in numerical simulations as a proof of concept. Then, they are tested on experimental data from laboratory tests, and if applicable, on real life examples like an offshore meteorological mast at the North Sea, an operating ferry or several examples of full-scale bridges. The resultant publications comprise [5, 6, 7, 8, 9, 10, 11, 12, 13, 14, 15, 16].

Outline of the thesis

This thesis contains two parts that are comprised of two and five chapters, respectively, and an Appendix. Part I describes the preliminaries and Part II contains the contributions. The Appendix contains the proofs and the theoretical derivations that are crucial for the technical correctness of the developed methods, but which are too lengthy for the main body of the thesis.

Part I contains Chapters 1 and 2. In Chapter 1, the state of the art on system identification, harmonic removal, uncertainty quantification of modal parameters, quadratic form approximations and damage detection is presented. In Chapter 2, some background theory on subspace-based system identification, corresponding uncertainty quantification and modal validation, with its real-life application example are given.

Part II is devoted to the contributions of this work and contains Chapters 3-7. In Chapter 3, the method for harmonic removal is described. In Chapter 4, the uncertainty quantification of Modal Phase Collinearity is addressed. In Chapter 5, the uncertainty quantification of the Modal Assurance Criterion is given. In Chapter 6, the uncertainty quantification of the Modal Assurance Criterion from a stabilization diagram is described. In Chapter 7, a new damage detection scheme robust to ambient vibration changes is proposed.

The Appendix consists of Chapters A-E. Each is labeled after the respective chapter of this thesis and contains the corresponding technical developments within.

Notation

Symbols

A^T	Transposed matrix of A
A^{-1}	Inverse of A
$A^\dagger$	Pseudoinverse of A
$\mathrm{d}[A]$	Total derivative of A
$\triangleq$	Definition
i	Imaginary unit, $\mathrm{i}^2 = -1$
$\Re(a)$, $\Im(a)$	Real and imaginary part of variable a
$\overline{A}$, $\overline{a}$	Complex conjugate
$\mathrm{vec}(A)$	Column-wise vectorization of matrix A
$A \otimes B$	Kronecker product of matrices or vectors A and B
$\hat{X}$	Estimate of variable X
X_*	True value of variable X
$\mathrm{E}(X)$	Expected value of variable X
$\mathcal{N}(M, V)$	Normal distribution with mean M and (co-)variance V
χ^2_l	Chi-squared distribution with l degrees of freedom
$\hat{a} \xrightarrow{a.s.} a_*$	estimate of a convergences almost surely to a_*
$\hat{a} \xrightarrow{\mathcal{L}} a_*$	estimate of a convergences in law to a_*
$O(\cdot)$, $o(\cdot)$	Bachmann-Landau notation
$\mathbb{N}$, $\mathbb{R}$, $\mathbb{C}$	Set of natural, real, complex numbers
I_m	Identity matrix of size $m \times m$

Variables

n	System order
r	Number of sensors
$r^{(\mathrm{pc})}$, r_0	Projection channel, number of projection channels
A	State transition matrix
C	Observation matrix
$\mathcal{H}^{dat}$	Data Hankel matrix
$\mathcal{H}$	Hankel matrix of output covariance sequences
$\mathcal{J}$	Jacobian matrix
H	Hessian matrix
Σ	Covariance matrix
N	Number of samples

Abbreviations

DOF	Degree of freedom
FE	Finite Element
MAC	Modal Assurance Criterion
MPC	Modal Phase Collinearity
MCF	Modal Complexity Factor
EMA	Experimental Modal Analysis
OMA	Operational Modal Analysis
OMAX	Operational Modal Analysis with Exogenous inputs
SHM	Structural Health Monitoring
SSI	Stochastic Subspace Identification
SVD	Singular Value Decomposition
UPC	Unweighted Principal Component algorithm (for data-driven SSI)
PSD	Power Spectral Density
CPSD	Cross Power Spectral Density

Contents

Part I

Preliminaries

CHAPTER 1

State of the art

1.1 Modal analysis and system identification

Modal parameters of a linear time invariant (LTI) mechanical system, namely natural frequencies, damping ratios and mode shapes, can be estimated from vibration measurements. For that, three different areas of the modal analysis field can be distinguished, namely *Operational Modal Analysis* (OMA), *Experimental Modal Analysis* (EMA) and combined Experimental and Operational Modal analysis [17], or in other words *Operational Modal Analysis with eXogenous inputs* (OMAX) [18]. OMA, EMA and OMAX differ in the interpretation of the nature of an input/output (load/response) signals. A flowchart of different modal analysis areas is illustrated on Figure 1.1.

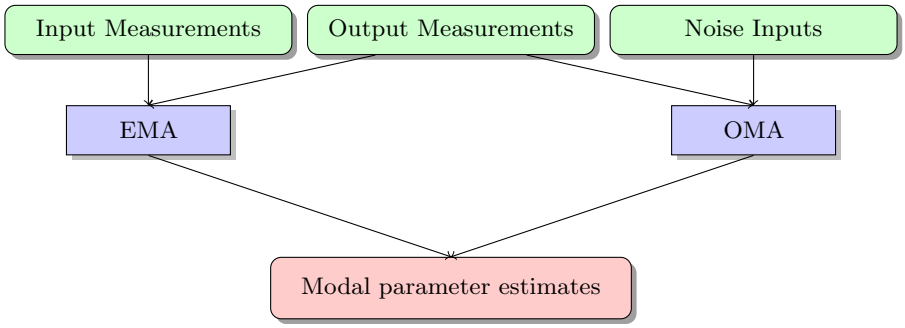

Figure 1.1: Areas in modal analysis that estimate modal parameters from data.

In EMA tested structures are excited with artificial measures, for example impact hammers or shakers, hence inputs and consequent outputs are considered as known, measured signals. No ambient vibration sources can be present during EMA, making its application limited to controlled environments, like a laboratory.

In OMA the output data, such as accelerations, velocities, displacements or strains

are recorded on the structure during some ambient, uncontrolled excitation conditions, thus input signals are considered unknown and often modeled as Gaussian white noise processes. For those reasons OMA is often called output-only modal analysis and is used for monitoring of structures under natural environmental conditions, like wind, waves or traffic. For example, its application involves ambient vibration tests of high-rise buildings [19, 20, 21], bridges [22, 23, 24], offshore platforms [25], wind turbines [26, 27], flutter tests of aircraft [28, 29, 30] and vibration-based monitoring of historic structures [31, 32].

OMAX is a hybrid of EMA and OMA which exploits that some of the excitation forces are known e.g. induced with a shaker. Thus, the measured outputs are partly due to inputs that are known and inputs that are unknown. The former can be considered as realizations of a stochastic process, as explained in [33] and the latter are modeled as a Gaussian white noise. OMAX is often applied to cases when some controlled signals are available to boost the ambient excitation, like in flutter tests [18] or modal tests of bridges [34].

The core of modal analysis are the methods to estimate the modal parameters from the aforementioned combinations of the input/output measurements.

One of the most popular methods, due to its simplicity, is the *Complex Mode Indicator Function* CMIF [35]. Its based on peak-picking the frequency response functions (FRFs) which are decomposed at each discrete frequency by Singular Value Decomposition (SVD). Selected peaks (singular values) and corresponding singular vectors are the estimates of natural frequencies and mode shapes of the underlying mechanical system. The OMA counterparts of CMIF are the *Frequency Domain Decomposition* (FDD) [36] and its enhanced version (EFDD) [37]. Both methods use SVD to decompose the cross power spectral density (CPSD) matrix of output measurements into a combination of single-degree-of-freedom systems. The estimates of modal parameters are represented by a hand-picked or automatically chosen [38] singular values and corresponding singular vectors of the CPSD matrix at selected frequency lines.

Another group of methods, initially designated for EMA, is based on fitting a common denominator model to FRFs with the Least-Squares Complex Frequency (LSCF) domain method [39] and transforming it to pole-residue form to estimate the mode shapes. The LSCF method was extended to polyreference LSCF, also called *PolyMAX*, in [40]. PolyMAX can also be used for OMA applications [41]. The time domain equivalent of LSCF fits a common denominator model to Impulse Response Functions (IRF) and is called Least-Squares Complex Exponential (LSCE) method [42], where its polyreference counterpart was presented in [43].

Many methods for modal analysis originate from the system identification field in automatic control. System identification involves the estimation of parameters of a mathematical model from measurements. Amongst methods therein, one can distinguish e.g. *prediction error methods* (PEM) and *subspace-based system identification*. A historical review of those methods can be found in [44]. Reference books on system identification are [45] and [46].

PEM estimate parameters of the LTI system by minimizing a parametric prediction error between the measurements and the response of the system predicted by a parametric model called a predictor. For an overview of PEM see [46]. Under assumptions that the disturbances in the model are modeled as a Gaussian process, PEM are equivalent to maximum likelihood (ML) estimates of the system parameters [47, 45]. In that context, some methods use an expectation maximization approach

connected to state-space models to estimate the modal parameters in OMA like e.g. the *expectation maximization-stochastic subspace identification* EM-SSI [48, 49] or the *structural identification using expectation maximization* STRIDE [50] algorithms.

Subspace-based methods employ some geometric transformation on the vector spaces of the collected measurements. The subspace of the resulting matrix is used to approximate the model matrices which yield the eigenstructure (collection of eigenvalues and eigenvectors) of the considered system. Those methods are of particular interest in applications to engineering problems, notably for their capacity of solving large models and for the consistency in parameter estimates under non-stationary noise excitation [51].

The important contributions in the subspace system identification field relate to the *minimal state realization* [52, 53]. A major milestone was the work presented in [54] who proposed the solution to a *deterministic realization* based on the factorization property of the Hankel matrix of Markov parameters. The *stochastic realization* given in [55] introduced innovation states which, based on the projection of vector spaces of present and future outputs onto spaces of present and past outputs, enabled to predict future outputs from its past counterparts [56]. Another important contribution is the *Balanced Realization* (BR) algorithm given in [57] that used the SVD to factor the observability and the controlability matrices from the Hankel matrix of the system. It featured some good statistical properties like non-stationary consistency, proven in [58]. A popular implementation of the BR algorithm is the *Eigensystem Realization Algorithm* (ERA) introduced in [59] and, in the context of OMA, the *Natural Excitation Technique* (NExT ERA) [60] and the *observer Kalman filter identification of output-only systems* (ERA-OKID-OO) [61].

The above-mentioned developments were unified to one general geometric framework in [17]. That work yielded a data-driven *N4SID* algorithm [62], which used SVD and LQ decompositions for an efficient numerical implementation of the desired projections of the input/output signals. Further reduction in computational efforts was achieved by introducing a subset of a reference sensors, so-called the *projection channels*, when building the Hankel matrix (both from the data or the covariance sequences). That resulted in two algorithms namely, the *reference-based stochastic subspace identification* (SSI/ref) [63] and the *reference-based combined deterministic-stochastic subspace identification* (CSI/ref) [64]. The former is often applied to OMA e.g. [65] and the latter to OMAX e.g. [34]. Subsequently, the SSI algorithms from [17] were mathematically reformulated in terms of a multi-order computation efficiency in [66]. That reduced time of estimating the *stabilization diagram* by a factor of 200, comparing to the classical algorithms. The problem of system identification with using moving and non-simultaneous measurement records under varying excitation conditions was considered in [3, 4], which introduced a *modular subspace-based system identification* method.

A complete review on modal analysis methods can be found in [67].

Asymptotic properties of subspace methods and uncertainty quantification in modal parameter estimates

The asymptotic properties of subspace-based system identification methods are an extensively researched topic. In that context, the consistency in their estimates was shown under stationary excitation conditions in [68] and [69], and for the non-stationary case in [70]. The theoretical expressions for their asymptotic variances were derived

in [71] and [72]. A detailed survey on the asymptotic properties of subspace-based estimators can be found in [73].

Estimates of modal parameters obtained from the subspace-based identification methods are consistent, however, since they are computed from data of finite lengths and afflicted by noise, they are impaired with statistical uncertainties. Those uncertainties can be quantified and the underlying distribution of the modal parameter estimates can often be inferred.

The explicit expressions for the asymptotic variance of the modal parameter estimates can be developed for any subspace-based method that has a functional relation with the output covariance sequences, whose covariance can easily be computed as a covariance of the sample mean. In that context, *first order perturbation theory* is used to compute the variance of modal parameter estimates from the covariance-driven output-only stochastic subspace identification in [74], which is based on the developments of [75]. An efficient multi-order implementation of the latter scheme was derived in [76, 77], which achieved a significant, two order of magnitude, improvement in the computational complexity compared to the original version of the algorithm. That enabled the application of the uncertainty quantification of the modal parameters in practical applications e.g. for computing the variance of natural frequencies, damping ratios and mode shapes estimated from bridge measurements [78, 79, 80]. The framework in [76] was extended to multi-setup subspace identification in [81]. Subsequently, the scheme for the uncertainty quantification of modal parameters was generalized to the family of input-output and output-only data-driven stochastic subspace identification methods in [33].

A classical approach to approximate the distribution of a stochastic variable is to use a Gaussian approximation by means of the aforementioned first order perturbation theory and *first order Delta method* [1]. The Delta method is based on the *Central Limit Theorem* and allows to approximate the law of a function of an asymptotic Gaussian variable by the law of another Gaussian variable assuming that the derivative of that function with respect to the considered parameter is continuous, non-zero, also knowing the asymptotic variance of the original variable, and most important with the limit inside the parameter domain. For example, since the estimates of output covariance sequences are Gaussian due to the CLT, a classical approach is to characterize the asymptotic distribution of the modal parameters estimates with a Gaussian variable, as shown in [33]. This is the theoretical justification of the aforementioned covariance computation based on the perturbation theory. In the context where the derivative is not fully defined or non-zero, extensive works have been performed to extend the CLT for non trivial cases, like in e.g. [82]. In particular, the *second order Delta method* [1] allows to express the Central Limit framework in terms of second order derivatives, and thus in terms of quadratic forms of the considered Gaussian variables. Establishing distribution of such quadratic forms is also a subject of an extensive research, like e.g. in [83, 84].

Stabilization diagrams

The stabilization diagram is an engineering tool used to handle bias errors in the estimates of modal parameters, considering the order of the system is unknown. The system order determines the size of the eigenstructure of the system. In the context of subspace-based system identification methods, it relates the number of poles in the state matrix to the number of identified modal parameters. Different system orders

result in different estimates of the modal parameters that may vary depending on the selected order. Among those parameters there exist some that correspond to non-physical, noise and mathematical poles. Conversely to the physical poles, which are stable in the stabilization diagram, the spurious estimates have high dispersion, based on which they can be discarded from a further analysis of the stabilization diagram.

The estimates of modal parameters can be clustered into so-called *modal alignments* by some practical criteria, like the relative difference between the consecutive parameters and the modal indicators. Thus one modal alignment is a group of modal parameters that correspond to one mode and are estimated for a range of system orders. They are aligning themselves (hence the name) with respect to some criteria. A group of modal alignments of some selected parameters, like natural frequencies, forms the stabilization diagram.

The multi-order computation of stabilization diagrams requires a lot of time and memory of the computer, and many, already mentioned, work has been devoted to remove this constraint e.g. [66, 76]. Another development, related both to the stabilization diagrams and the uncertainty quantification field, is a strategy to compute so-called *global estimates* of modal parameters [79]. There, the global estimates correspond to the means of the respective natural frequencies and the damping ratios from different modal orders, weighted with their statistical uncertainties. Like estimates of the modal parameters computed for a single model order, the global estimates are stochastic variables thus their covariance and consequently their confidence bounds can be quantified, which was also done in [79].

Modal indicators

The interpretation of modal parameters estimated from the data can be facilitated by so-called modal indicators, variables depicting some physical aspects of the estimated mode shapes. One of the modal indicators is the *Modal Phase Collinearity* (MPC) [85], which is a quantity that measures the complexity of a mode shape vector. Another modal indicator reflecting the complexity of the estimated mode shape is the *Modal Complexity Factor* (MCF) developed in [86], which is an equivalent of the MPC. Estimates of the MPC are bounded between 0 and 1, depending on the complexity of the underlying mode shape estimate.

The *Modal Assurance Criterion* (MAC) [87] is a popular modal indicator used in application to e.g. model updating [88], mode shape matching in modal alignments, comparison of the mode shape estimates between different system identification routines and many more applications that involve investigating the linearity between estimated mode shape vectors. The MAC represents a squared cosine of an angle between two mode shapes [89] and similar to MPC it is bounded between 0 and 1 respectively for orthogonal and collinear vectors.

Operational Modal Analysis in presence of periodic excitation

Despite the apparent convenience of OMA in vibration testing, the unknown and uncontrolled nature of the excitation conditions can render estimation of modal parameters difficult in practice. In that context, the influence of periodic excitation on the results obtained from system identification is a subject of extensive research both in signal processing and control communities. It is well-known that the eigenstructure of a linear system identified from data with oscillatory components contains a mix of

periodic and structural modes. In that case there are two possible paths for modal parameter estimation, namely first is to separate the periodic poles from the structural ones, which is sometimes difficult in practical applications, and second, is to use the system identification techniques robust towards the influence of such periodic components. In the former case different methods have been developed to remove the periodic signals from the output measurements. For example, *time-synchronous-averaging* (TSA) is a method originated from signal processing field that extracts periodic waveforms from signals by averaging synchronized blocks of the signal in the angular domain. That averaged signal is subtracted from the raw measurements, what results in removal of the frequencies selected to synchronize the blocks, which coincide with the harmonics, like exhibited in [90]. Angle matching is often achieved with tachometers measuring the periodic signals, which is not practical in real-life applications and was attempted to overcome in the context of TSA in [91]. A family of methods that does not require tachometer measurements are based on *cepstrum* (an inverse Fourier transform of logarithm of spectrum). A number of applications of the cepstral lifters to harmonic removal can be found in [92], where a detailed review on cepstral methods can be found in [93]. Moreover, cepstral techniques can be also used for OMA by computing the pole and zero part of system transfer function by curve-fitting the liftered response measurements as shown in [94, 95]. Another group of methods that involves removing the periodic frequencies from the responses is based on subtracting parametric estimates of the former from the raw measurements. Such parametric estimates of the harmonic signal can be achieved with e.g. numerical Gauss-Newton algorithm, like in [96], or parametric frequency modulation, like in [97].

Some research has also been conducted in the context of system identification methods robust towards the influence of harmonics in the output measurements. For example, in [98] and [99] the authors explore the use of a combination of *transmissibility functions* under different loading conditions (location or amplitude) to estimate the eigenstructure of the system. The transmissibility function itself is invariant towards the nature of excitation conditions, what makes it suitable for the problem of OMA with the influences of periodic excitation and was further investigated in [100, 101].

In this context, the subspace system identification techniques are also used. In [102] authors show that the subspace-based methods are consistent in the parameter estimates for a system with the oscillatory input components. That fact can be used to discard the periodic poles of the system from the estimate of its eigenstructure. That was illustrated on some theoretical example in [103]. The selection of harmonic modes can be done via simple indicators like *kurtosis* [104, 105], *entropy* [106] or damping ratios [107].

1.2 Vibration-based damage detection

Algorithms and methods for damage detection are a classical task in the development of modern Structural Health Monitoring (SHM) systems [108]. SHM refers to the monitoring of the structural integrity by reacting to some significant changes herein, based on measurements and sometimes a model. The different levels of diagnosis of such changes can be classified with a popular scheme of an increasing level of complexity: namely, damage detection, localization, quantification and lifetime prediction [109] (for illustration see Figure 1.2).

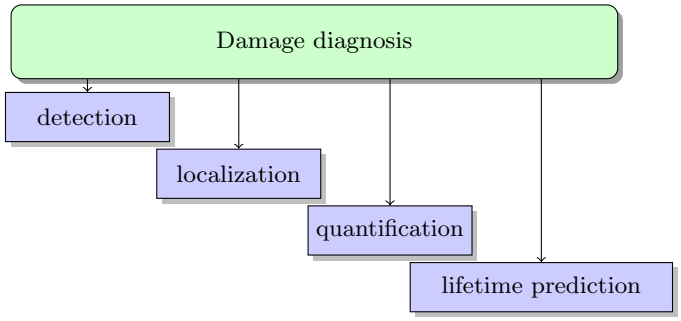

Figure 1.2: Flowchart of damage diagnosis, after [109].

These tasks can be addressed by defining a residual or a characteristic feature of the system, modeled after some properties of the system in the reference (healthy) state, which are evaluated to test for damages and their locations during the operating states of the structure. Those residuals are designed to be sensitive towards damages and preferably not sensitive to noise and changing environmental conditions, like variable temperature or excitation. A general perception is that damage detection can be carried out using only output measurements whereas damage localization, quantification and lifetime prediction require a model and its mapping towards the damage-sensitive features derived from the data [110]. That, in principal, makes the damage detection aspect of SHM less difficult, since accurate structural models are often complicated to establish and require some calibration with its real counterpart, which can be difficult in practice and is an research area of its own [111]. The resulting damage detection framework can be summarized to *residual generation* and *residual evaluation*, which are classical aspects of *Fault Detection and Isolation* (FDI) [112, 110].

In the context of FDI, the residuals are typically zero mean in the reference state and significantly different from zero in the damaged state of the system [110]. The statistical evaluation of residuals revolves around the premise that their probability distribution is known and can be parameterized such that a decision about the fault can be reached via hypothesis testing. Such a test usually follows a distribution which is known a priori, which enables the design and selection of a threshold to discriminate between the reference and the faulty states.

Damage detection methods

Detecting damages based on vibration data collected from structures has reached a certain level of maturity over the recent years, reflected in the number of approaches developed and their real-life applications. Some reviews of the early developments therein can be found in [113, 114, 115]. In that context, many works have been devoted to creating residuals based on the modal parameter estimates e.g. mode shapes components [116] and natural frequencies [117], which can be evaluated for damages using some control charts [118]. The evaluation of data-based residuals in context of SHM often relies on an outlier analysis [119, 120, 121], cointegration [122, 123], whiteness test of the Kalman filter innovations [124] and many other techniques from the statistical signal processing field. The performance of these methods is conditioned on several factors, e.g. the quality of parameters estimated from the data, the ability to track the selected parameter estimates after identifying

them from the healthy state of the structure and the ability to account for changing environmental conditions like the temperature. The quality of the modal parameter estimates is often related to the statistical uncertainties perturbing the measurements, which when not accounted for, can mask small faults in the system. The estimates of modal parameters are also affected by temperature changes, which in the context of damage detection is a well-known problem. It can be accounted for e.g. by using nonlinear models for system identification while generating the residual [125], merging different data setups [126] or with a robust regression to discriminate the environmental changes from the structural damages during the residual evaluation [127].

In addition to the statistical variability, data-based damage features are inherently dependent on the natural changes in the ambient excitation conditions. That poses a major challenge for their evaluation, since excitation is in principle unknown and unmeasured, hence any changes therein may be falsely classified as damages. A solution to that problem lies in the design of a damage detection residual, whose mean value is independent of the excitation conditions.

In this context, *subspace-based damage detection* [128, 129, 130] is a well-known group of methods that are often applied to vibration-based SHM of engineering structures e.g. [131, 132]. In its *classical* form the subspace-based residual identifies changes in the subspace spanned by the Hankel matrix build from the output covariance sequences of the tested data by confronting it with the left nullspace of the Hankel matrix of the output covariances in the reference, undamaged, state. The resulting residual is asymptotically Gaussian and can be parametrized with any parameter that has a functional relation with the eigenstructure of the vibrating system [128]. Such parametrization is optional and allows to focus the damage identification on a subset of predefined damage-sensitive variables e.g. estimates of modal parameters or structural stiffnesses [133]. Small deviations from the reference are detected using the asymptotic local approach for change detection [2], a statistical framework designed to detect changes by monitoring the mean of parametric Gaussian residuals [110]. There, the decision about the health of the system is achieved via hypothesis testing, where the resultant test statistics are known and are compared to a predefined threshold.

In context of invariance towards changes in the excitation, the classic subspace residual depends on the excitation properties. The so-called *robust* subspace residual [129, 134] and *null* subspace-based residual [130] was illustrated to be invariant towards changes in the excitation conditions based on some real-life application. The former residual based on a frame structure which was gradually damaged while subjected to a significantly changing load [135] and the latter based on a small-scale airplane model subjected to a similar conditions. The theoretical proof of their invariance, however, is incomplete. In addition, most works on the subspace residuals assume that the reference model is perfect, whereas in most applications, it has to be estimated. That drawback was recently overcome by accounting for the uncertainty of the reference left kernel in [136].

CHAPTER 2

Background theory and some illustrative examples

In this chapter, some background theory for the techniques used in this thesis is recalled, and presented in the context of a real-life application example. The chapter is organized as follows. First the state-space model and the underlying mechanical system are recalled and the expressions for modal parameter estimation are given. Next, definitions of two popular modal indicators- Modal Assurance Criterion (MAC) and Modal Phase Collinearity (MPC) are presented. Subsequently, a theoretical framework for the uncertainty quantification of modal parameters with the Delta method and the first order perturbation approach is recalled. The chapter is concluded with a practical application of the recalled schemes, which also sets the context for the methods developed in this thesis.

2.1 Vibration modeling

Let model (2.1) represent the motion behavior of a viscously damped, linear time-invariant (LTI) structural system with d degrees of freedom, observed at r measurement points, i.e. sensors,

$$\begin{cases} M\ddot{q}(t) + D\dot{q}(t) + Kq(t) = u(t) \ , \\ y(t) = C_a\ddot{q}(t) + C_v\dot{q}(t) + C_d q(t) + v(t) \ , \end{cases} \tag{2.1}$$

where $y(t) \in \mathbb{R}^r$ is the output vector and $(\dot{})$ expresses a derivative with respect to time t. Matrices K, M, $D \in \mathbb{R}^{d\times d}$ denote stiffness, mass and damping matrices respectively. Matrices C_a, C_v, $C_d \in \mathbb{R}^{r\times d}$ are selection matrices for accelerations, velocities and displacements. Vectors $q(t) \in \mathbb{R}^d$ and $u(t) \in \mathbb{R}^d$ denote the continuous-time displacements and external forces respectively. Vector $v(t) \in \mathbb{R}^r$ denotes the sensor noises. Considering a sampling rate of $1/\tau$, System (2.1) can be represented by

a discrete-time stochastic state-space model

$$\begin{cases} x_{k+1} = A_n x_k + B_n u_k + w_k \ , \\ y_k = C_n x_k + D_r u_k + v_k \ , \end{cases} \tag{2.2}$$

where $x_k \in \mathbb{R}^n$ are the states; $A_n \in \mathbb{R}^{n\times n}$, $C_n \in \mathbb{R}^{r\times n}$ are the state transition and observation matrices estimated for a model order n and $B_n \in \mathbb{R}^{n\times d}$ with $D_r \in \mathbb{R}^{r\times d}$ are the input and feedthrough matrices respectively. Vectors w_k with v_k denote the process and output noises. Matrices A_n and C_n are here of particular interest since they are used to identify modal parameters of the structure. In practical applications like OMA, matrices B_n and D_r are null since there are no inputs measured.

The eigenfrequencies f_i, damping ratios ζ_i and mode shapes φ_i of the underlying mechanical system (2.1) are identified for $i = 1 \dots n$ from the i-th eigenvalue λ_i and eigenvector Φ_i of A_n such that

$$A_n \Phi_i = \lambda_i \Phi_i, \tag{2.3}$$

$$f_i = \frac{|\lambda_{ci}|}{2\pi}, \ \zeta_i = \frac{-\Re(\lambda_{ci})}{|\lambda_{ci}|}, \ \varphi_i = C_n \Phi_i \ , \tag{2.4}$$

where the eigenvalue of the continuous system λ_{ci} is computed as $\mathrm{e}^{\lambda_{ci}\tau} = \lambda_i$. The $|(\cdot)|$ denotes modulus operator and $\Re(\cdot)$ and $\Im(\cdot)$ express real and imaginary parts of a complex variable. Modal parameters can be estimated from data, as well as their variances. An example of a output-only data-driven identification algorithm, namely Stochastic Subspace Identification with Unweighted Principal Component, SSI-UPC, is given in the next section.

Remark 2.1 (Regarding parameter estimates) *Any parameter computed from measurements is an estimate of the true parameter of the underlying system. Such estimates are never equal to the exact parameters, since they are computed from finite data that is perturbed by noise, hence are subjected to statistical errors. Any estimate is hereafter labeled with* $(\hat{\cdot})$ *symbol.*

Remark 2.2 (Regarding mode shape normalization) *Any mode shape estimate* $\hat{\varphi}$ *computed from* (2.4) *is called the unnormalized mode shape since its scaling is arbitrary and its components can be written as* $\hat{\varphi} = \begin{bmatrix} \hat{\varphi}_1 & \hat{\varphi}_2 & \dots & \hat{\varphi}_r \end{bmatrix}^T$. *To make it comparable between different model orders, a normalization scheme is needed. Two well-known normalization schemes are recalled in the Remark A.1 in Appendix A.1.1.*

Remark 2.3 (Regarding the stabilization diagram) *Each estimate of a modal parameter at a given model order in one modal alignment is a valid representative of the estimated parameter. In engineering, however, a mode of a structure is characterized by a single estimate of natural frequency, damping ratio and mode shape. These can be extracted based on the alignments established in the stabilization diagram for each model order n. A strategy to compute so-called global estimates of modal parameters, with their underlying uncertainties, was proposed in [79] and is recalled in Appendix A.1.2.*

2.1.1 SSI-UPC identification algorithm

The UPC algorithm is based on a projection of the 'future' data horizon $\mathcal{Y}^+$ onto the 'past' data horizon $\mathcal{Y}^-$, which associates the column space of the resulting projection matrix $\hat{\mathcal{H}}^{\text{dat}}$ with the column space of the estimate of extended observability matrix Γ, whereas its rows space corresponds to the row space of the estimate of a forward Kalman filter state sequence Z. The projection can be written as

$$\hat{\mathcal{H}}^{\text{dat}} = \mathcal{Y}^+/\mathcal{Y}^- = \mathcal{Y}^+(\mathcal{Y}^-)^T(\mathcal{Y}^-(\mathcal{Y}^-)^T)^{-1}\mathcal{Y}^- \ , \tag{2.5}$$

where $\hat{\mathcal{H}}^{\text{dat}} \in \mathbb{R}^{(p+1)r\times N}$ with $N+p+q$ denoting the total number of samples such that parameters p, q are usually $p = q+1$. Matrices $\mathcal{Y}^+ \in \mathbb{R}^{(p+1)r\times N}$ and $\mathcal{Y}^- \in \mathbb{R}^{qr_0\times N}$ are defined such that

$$\mathcal{Y}^+ = \frac{1}{\sqrt{N}}\begin{bmatrix} y_{q+1} & y_{q+2} & \vdots & y_{N+q} \\ y_{q+2} & y_{q+3} & \vdots & y_{N+q+1} \\ \vdots & \vdots & \vdots & \vdots \\ y_{p+q+1} & y_{p+q+2} & \vdots & y_{p+q+N} \end{bmatrix}, \ \mathcal{Y}^- = \frac{1}{\sqrt{N}}\begin{bmatrix} y_q^{\text{pc}} & y_{q+1}^{\text{pc}} & \vdots & y_{N+q-1}^{\text{pc}} \\ y_{q-1}^{\text{pc}} & y_q^{\text{pc}} & \vdots & y_{N+q-2}^{\text{pc}} \\ \vdots & \vdots & \vdots & \vdots \\ y_1^{\text{pc}} & y_2^{\text{pc}} & \vdots & y_N^{\text{pc}} \end{bmatrix} \tag{2.6}$$

with pc labeling r_0 projection channels. An efficient and numerically stable scheme to compute the data Hankel matrix $\hat{\mathcal{H}}^{\text{dat}}$ has been proposed in [17] and [66]. Instead of the direct computation of the projection as in (2.5), it involves selecting an appropriate partition of the stacked and LQ decomposed $\mathcal{Y}^-$ and $\mathcal{Y}^+$ matrices. Matrix $\mathcal{H}^{\text{dat}}$ enjoys the factorization property into $\mathcal{H}^{\text{dat}} = \Gamma Z$ where $\Gamma \in \mathbb{R}^{(p+1)r\times n}$ and $Z \in \mathbb{R}^{n\times N}$ are defined as

$$\Gamma = \begin{bmatrix} C_n \\ C_nA_n \\ \vdots \\ C_nA_n^p \end{bmatrix}, \quad Z = \begin{bmatrix} G & A_nG & \dots & A_n^{q-1}G \end{bmatrix}\Sigma_{\mathcal{Y}^-}^{-1}\mathcal{Y}^- \ , \tag{2.7}$$

where $\Sigma_{\mathcal{Y}^-} = \text{E}(\mathcal{Y}^-(\mathcal{Y}^-)^T)$ is the covariance of the past outputs and $G = \text{E}(x_{k+1}y_k^T)$ expresses the cross covariance computed between the states at model order n and the outputs. In practice, the observability matrix Γ and the forward Kalman states Z are estimated from the data. A well-known scheme to compute estimates of Γ and Z is to balance the singular values of the Hankel matrix, $\hat{\mathcal{H}}^{\text{dat}}$, whose SVD writes

$$\hat{\mathcal{H}}^{\text{dat}} = \begin{bmatrix} U_s & U_{ker} \end{bmatrix}\begin{bmatrix} D_s & 0 \\ 0 & D_0 \end{bmatrix}\begin{bmatrix} V_s^T \\ V_{ker}^T \end{bmatrix} \ , \tag{2.8}$$

where an estimate of Γ is taken as $\hat{\Gamma} = U_sD_s^{1/2}$ and $\hat{Z} = D_s^{1/2}V_s^T$. Matrices U_s and V_s are the left and right singular vectors corresponding to first n non-zero singular values D_s and U_{ker} with V_{ker} are the left and right kernel of $\hat{\mathcal{H}}^{\text{dat}}$ where $D_0 \to 0$. The estimates $\hat{A}_n$ and $\hat{C}_n$ of the state transition matrix and the Kalman states can be computed in a least-square sense from the shift invariance property of $\hat{\Gamma}$.

2.1.2 MAC computation

Let $\hat{\varphi}$ and $\hat{\psi}$ be two mode shapes estimates on N samples. As N goes to infinity both mode shapes converge almost surely to their respective true values φ_* and ψ_*. The MAC formulation between two complex valued mode shapes vectors φ and ψ follows [87] and writes

$$g_{mac}(\varphi, \psi) = \frac{|\varphi^H \psi|^2}{\varphi^H \varphi \psi^H \psi} = \frac{\varphi^H \psi \psi^H \varphi}{\varphi^H \varphi \psi^H \psi}. \tag{2.9}$$

A consistent estimate of the MAC can be obtained by using some consistent estimates of mode shape vectors φ and ψ. The relevant choice of those for the MAC computation depends on the application of interest. For example, a classic formulation of MAC between different estimates of mode shapes at a single model order n can be obtained by using $\hat{\varphi}$ and $\hat{\psi}$. The standard computation of MAC can be extended to the global MAC, computed using a global mode shapes estimates from the stabilization diagram. Another application for the MAC metric is to correlate a mode shape estimated from the data and a true mode shape computed from a numerical model.

An important feature in the design of the MAC indicator is that when assuming $\hat{\varphi} = \hat{\psi}$ it yields

$$g_{mac}(\hat{\varphi}, \hat{\psi}) = \frac{|\hat{\psi}^H \hat{\psi}|^2}{\hat{\psi}^H \hat{\psi} \hat{\psi}^H \hat{\psi}} = \frac{\hat{\psi}^H \hat{\psi} \hat{\psi}^H \hat{\psi}}{\hat{\psi}^H \hat{\psi} \hat{\psi}^H \hat{\psi}} = 1 \ , \tag{2.10}$$

which is a constant value with no statistical uncertainty. On the other hand when two modes shapes of interest are orthogonal $\hat{\varphi}^H \hat{\psi} = 0$ the MAC yields

$$g_{mac}(\hat{\varphi}, \hat{\psi}) = \frac{|\hat{\psi}^H \hat{\psi}|^2}{\hat{\psi}^H \hat{\psi} \hat{\psi}^H \hat{\psi}} = \frac{\hat{\psi}^H \hat{\psi} \hat{\psi}^H \hat{\psi}}{\hat{\psi}^H \hat{\psi} \hat{\psi}^H \hat{\psi}} = 0 \ , \tag{2.11}$$

which is also a constant with no statistical uncertainty. Based on that MAC indicator is bounded between 0 and 1, which makes its uncertainty assessment difficult, especially when estimates of MAC approach their theoretical bounds. That subject is investigated in this thesis.

2.1.3 MPC computation

In classical mechanical engineering problems system matrices from (2.1) are assumed symmetric and yield real-valued eigensolution of (2.1), because M, K and D are diagonalizeable by the mode shape vectors. In practice, however, the system in (2.1) can yield complex valued eigenvectors due to e.g. non classical formulation of the damping matrix D.

In addition, estimates of system matrices identified from measured responses are not symmetric, even for simulations of a theoretical system, due to a finite lengths of data sequences and noise. Both of these factors can result in the estimate of the mode shape $\hat{\varphi}$ from (2.4) being a complex vector. In the former case by design, in the latter due to estimation errors. A geometric depiction of a complex mode shape is illustrated on Figure 2.1.

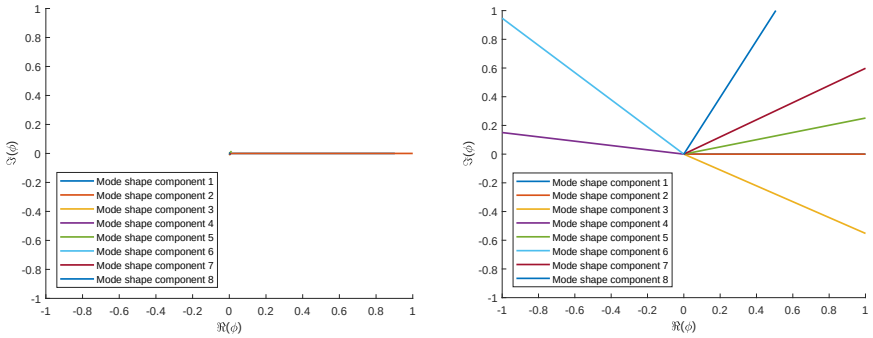

Figure 2.1: Mode shape vector with low complexity (left). Mode shape vector with high complexity (right).

One can see that the mode shape components plotted in the complex plain align around one axis and exhibit small imaginary parts for the mode shape with the low degree of complexity and show significant dispersion in the complex plain for the mode shape with the high complexity. The complexity of the vector can be quantified by the Modal Phase Collinearity (MPC) and the Modal Complexity Factor (MCF), where the former indicator is more recognized in the literature. This section links computation of the MPC and the MAC. The following links were established in [89] and are recalled here for the sake of completeness. Recall the definition of MPC(φ) [59, 85] and MAC(φ, ψ) [87]

$$g_{mac}(\varphi, \psi) \triangleq \frac{|\varphi^H \psi|^2}{\varphi^H \varphi \psi^H \psi} = \frac{\varphi^H \psi \psi^H \varphi}{\varphi^H \varphi \psi^H \psi} \ , \tag{2.12}$$

$$\mathrm{MPC}(\varphi) \triangleq \frac{(\lambda_1 - \lambda_2)^2}{(\lambda_1 + \lambda_2)^2} \ , \tag{2.13}$$

where λ_1 and λ_2 are the eigenvalues of $\begin{bmatrix} S_{xx} & S_{xy} \\ S_{yx} & S_{yy} \end{bmatrix} \in \mathbb{R}^{2\times 2}$ matrix. The scalar products $S_{xx} = \Re(\varphi)^T \Re(\varphi)$, $S_{yy} = \Im(\varphi)^T \Im(\varphi)$ and $S_{xy} = S_{yx} = \Re(\varphi)^T \Im(\varphi)$.

Lemma 2.4 *Following expressions are equivalent*

$$\mathrm{MPC}(\varphi) = \mathrm{MAC}(\varphi, \overline{\varphi}) = \frac{(S_{xx} - S_{yy})^2 + 4(S_{xy})^2}{(S_{xx} + S_{yy})^2}. \tag{2.14}$$

Proof: See Appendix B.1. □

Consequently, similar to the MAC, the MPC indicator computed from the data has some stochastic properties, that are a function of the stochastic properties of the mode shapes. Also, as well as the MAC, it is bounded by 0 and 1. Quantification of statistical uncertainties in the estimates of MPC is one of the topics investigated in this thesis.

2.2 Variance of modal parameters

The estimates of the system matrices in (2.2) and modal parameters from (2.4) are subjected to two types of statistical errors, namely variance and bias. The variance

errors are related to a statistical dispersion of the modal parameters due to finite length of the data sets used for the system identification and the noise present in the measurements. The bias errors are connected to the choice of the system order and are related to the presence of spurious modes, which can be to some extent removed with stabilization diagrams.

A statistical framework that provides a explicit expressions to compute the variance in the estimates of the modal parameters is recalled in the next section. Variance of a parameter estimate can be quantified by the confidence intervals, when the approximation of its distribution is known. An illustrative example of of the 95% confidence interval computed for an estimate of a Gaussian variable is depicted on Figure 2.2.

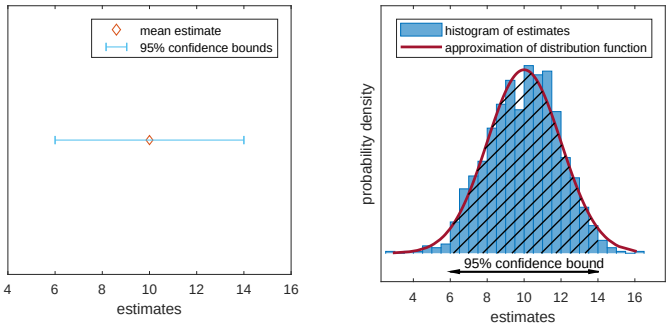

Figure 2.2: Confidence intervals and approximate distribution of the estimated parameter.

2.2.1 The Delta method and first order perturbation theory

The strategy to propagate the statistical uncertainties from the measurements on the estimates of modal parameters is based on the Delta method and first order perturbation theory. The core of the aforementioned strategy is presented on Figure 2.3.

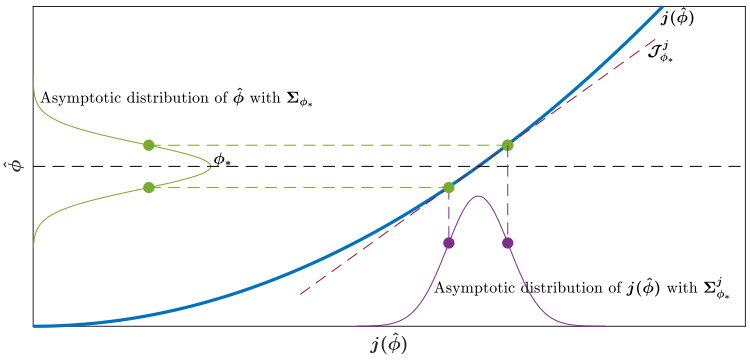

Figure 2.3: Illustrative example of the variance propagation. Explanation of the symbols in the paragraph below.

Let ϕ be a matrix and $\hat{\phi}$ its estimate computed on N samples. Matrix $\hat{\phi}$ is a random and, as N goes to infinity, it converges to ϕ_* and the CLT holds $\sqrt{N}\text{vec}(\hat{\phi} - \phi_*) \xrightarrow{\mathcal{L}} \mathcal{N}(0, \Sigma_{\phi_*})$, where Σ_{ϕ_*} is the asymptotic covariance of $\text{vec}(\hat{\phi})$. An equivalent CLT can be formulated for the output covariance sequences, which, in practice, allows to propagate their covariance to the estimates of modal parameters from e.g. subspace-based system identification.

To give an example of such propagation, define a function $j(\phi)$ such that $\text{vec}(j(\phi))$ is twice differentiable in ϕ_* with a non-zero sensitivity matrix $\mathcal{J}^j_{\phi_*} = \partial\text{vec}(j)/\partial\text{vec}(\phi)\ (\phi_*)$. The first order perturbation of $\text{vec}(j(\hat{\phi}))$ writes as

$$\text{vec}\left(\Delta j(\hat{\phi})\right) = \text{vec}\left(j(\hat{\phi}) - j(\phi_*)\right) = \mathcal{J}^j_{\hat{\phi}}\text{vec}\left(\Delta\hat{\phi}\right) \approx \mathcal{J}^j_{\phi_*}\text{vec}\left(\Delta\hat{\phi}\right) \ , \tag{2.15}$$

where $\Delta\hat{\phi} = \hat{\phi} - \phi_*$ and $\mathcal{J}^j_{\hat{\phi}} \xrightarrow{a.s.} \mathcal{J}^j_{\phi_*}$. Consequently, the covariance of $\text{vec}(j(\hat{\phi}))$ can be expressed with the statistical Delta method such that $\sqrt{N}\text{vec}\left(j(\hat{\phi}) - j(\phi_*)\right) \xrightarrow{\mathcal{L}} \mathcal{N}(0, \Sigma^j_{\phi_*})$, where $\Sigma^j_{\phi_*} = \mathcal{J}^j_{\phi_*}\Sigma_{\phi_*}(\mathcal{J}^j_{\phi_*})^T$. Thus, the Delta method allows to approximate a function j of a Gaussian parameter ϕ by another Gaussian assuming that the derivative of function j with respect to the parameter ϕ namely, $\mathcal{J}^j_{\phi_*}$, is continuous and the asymptotic variance of the parameter ϕ namely, Σ_{ϕ_*}, is known. This framework is heavily used in the next chapters of this thesis.

An example of variance quantification of the modal parameters with the presented framework, outlined for subspace-based system identification, is recalled in Appendix A.1.1.

2.3 Illustrative example

This section presents a practical application of the background theory described in this chapter and addresses problems that can be encountered during its use for the structural monitoring. The tested structure is a full scale meteorological mast, located in West of a Dogger Bank site at the North Sea, supported by a novel, at that time, concept of offshore foundation- a Mono Bucket foundation. The geometry of the Mono Bucket and the on-site photo of one of the foundations on the deck of the installation vessel is depicted on Figure 2.4.

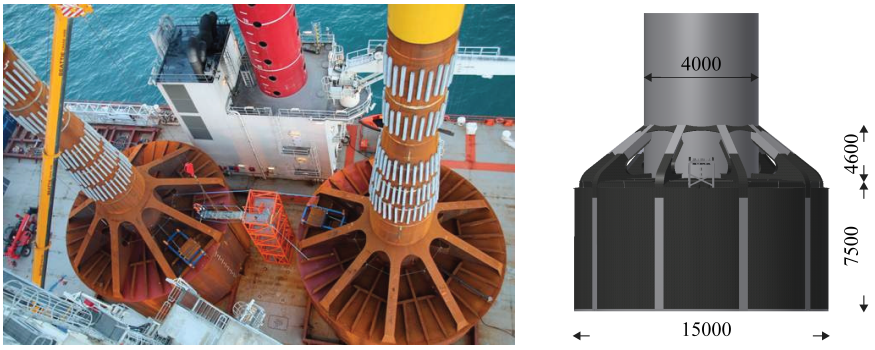

Figure 2.4: Mono Bucket foundations on the board of a installation vessel (left). The geometry of the foundation in millimeters (right). Both pictures available by the courtesy of Universal Foundation A/S.

The Mono Bucket is a steel foundation, divided into a shaft, webs, lid, and skirt modules. The webs and the shaft form a main frame of the foundation. The lid and the skirt create a horizontal and vertical base respectively. Foundation itself is installed in the seabed by a combination of the self-weight and externally applied suction. The foundation on Dogger Bank West site is designed with 9 radial webs, diameter of 15m, 7.5m skirt length and 42.5m shaft length.

In addition, the meteorological mast consist of a platform and the mast itself. The platform is connected to the shaft of the Mono Bucket by 4 radial girders. The lattice mast of 91.5m is bolted to the platform. The structure is equipped with a comprehensive monitoring system that consists of accelerometers, inclinometers, strain gauges, pressure transducers and a wave radar. More detailed description of the structure and the measurements can be found in [137]. The responses of the structure to ambient vibrations (wind, waves and current) are continuously recorded in the total of 56 channels, over a period of 181 days with a sampling frequency of 20Hz. This section focuses on the analysis of the responses recorded by 8 acceleration channels, which are placed along the Mono Bucket structure. One 12 hour long data set is considered. The following example illustrates how the stabilization diagram of natural frequencies can look in practice and provides a practical motivation behind the uncertainty quantification of modal parameters.

Considered data set is decimated up to frequency of 10Hz and the data-driven SSI-UPC algorithm to estimate the modal parameters is set with 40 time lags to compute the data Hankel matrix, which is subsequently divided into 200 blocks for its covariance computation. System orders from 10 to 80 are considered. Figure 2.5 illustrates the stabilization diagram of the natural frequencies with their corresponding confidence intervals resulting from this analysis, plotted on top of three largest singular values of each instance of the CPSD matrix from the acceleration measurements.

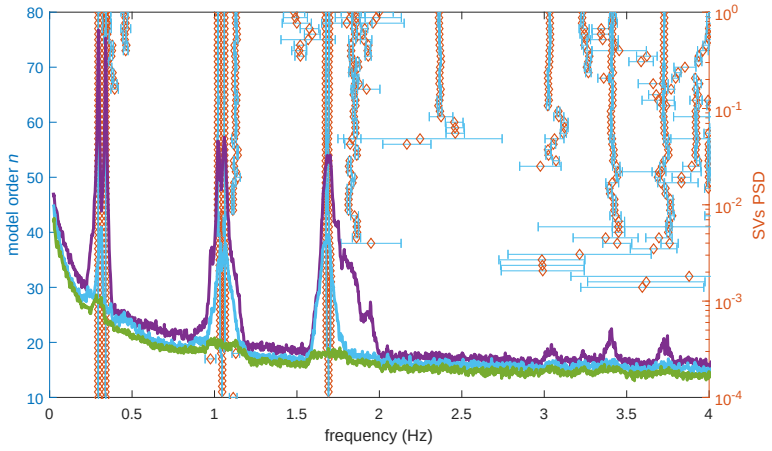

Figure 2.5: Stabilization diagram of the natural frequencies of the meteorological mast.

From the analysis of Figure 2.5 it can be observed that 6 closely spaced modes are well excited and estimated at each model order by the SSI-UPC algorithm. In addition, some estimates with large confidence intervals are visible. Those can be discarded from the analysis by setting up a threshold on the computed uncertainties. Figure

2.6 illustrates the stabilization diagram of the natural frequencies with a threshold of 2.5% on their maximum standard deviations.

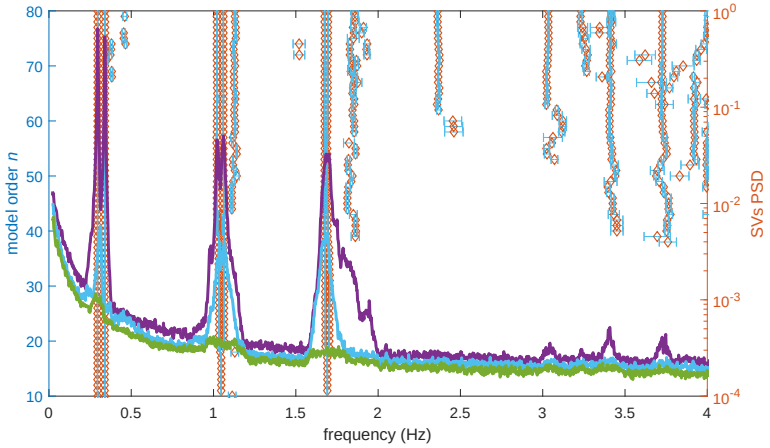

Figure 2.6: Stabilization diagram of the natural frequencies of the meteorological mast with a threshold on a maximum deviations of the natural frequency estimates.

It can be observed that most of the uncertain estimates are removed from the stabilization chart on Figure 2.5. Still, some estimates that correspond to the modes in the noise floor are present and will be selected as so-called stable modes, when no other modal indicator is used. That might be avoided by selecting a threshold on the uncertainty related to the estimated mode shapes. That however, might be difficult to interpret from a practical reasons since every measured DOF has its own confidence interval. The dimensionality of the problem can be reduced when considering confidence intervals of the estimates of the modal indicators, MAC and MPC, which even though scalar valued are functions of the variance of the mode shapes. This idea is developed further in Chapter 4.

This section is concluded with a practical depiction of the global modal parameter computation scheme. The global estimates are computed for each of the modal alignments, which are established based on the criteria like

- difference in two consecutive natural frequencies $\leq 5\%$,
- difference in two consecutive damping ratios $\leq 50\%$,
- MAC level between two consecutive mode shapes $\geq 90\%$.

The previous thresholds allow large deviations of the parameters within one alignment and are selected to illustrate the variation in the estimates of natural frequency and damping ratio within the chosen range of model orders. The natural frequencies and damping ratios for the first modal alignment with their corresponding confidence intervals and the global estimates are illustrated on Figure 2.7.

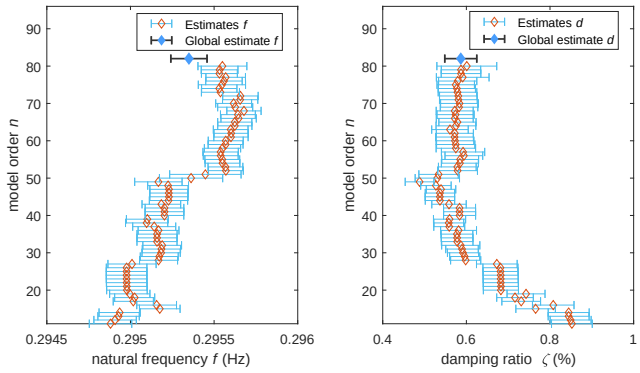

Figure 2.7: Estimates of the natural frequencies and damping ratios for the first modal alignment.

As expected, both estimates of the natural frequencies and damping ratios vary within one alignment. The global estimates are defined as an average of the parameters from selected alignment weighted with their covariance matrix and, by design, represent the average position of the most certain estimates, which is reflected on Figure 2.7. That is very practical, since it can be clearly seen that selecting one estimate at a single model order is difficult and it does not encompass the behavior of the whole modal alignment. Therefore, development of the uncertainty quantification of the global estimates, like global mode shapes or global modal indicators, is important when interpreting the modal results. This idea is pursued for global estimates of MAC and MPC in Chapter 6.

Part II

Contributions

CHAPTER 3

Operational modal analysis in presence of periodic excitation

Structural monitoring is problematic when applied to structures equipped with rotating machinery, like for instance wind turbines, ships or trains due to the presence of periodic inputs generated by rotating components. Those periodic signals often exhibit time-varying properties and their fundamental frequency, as well as its multiple harmonic orders, can be positioned in vicinity of the natural frequency of the structure, which apart from resulting in severe vibrations, masks the true response of the system, caused by the random part of the input. During the system identification with e.g. SSI methods, the eigenstructure of the system contains a mix of periodic and structural modes, often not straightforward to distinguish. In addition, when fault detection is considered, the periodic inputs can cause false positive scores in damage detection tests due to their non-stationary nature. A desirable countermeasure for this problem is to remove the periodic part of the signal prior to its blind analysis.

In this chapter, a harmonic removal method in a SSI framework is developed. Such method can be used to preprocess structural responses afflicted by the harmonics, prior to OMA or SHM purposes. In short, this chapter comprises

- example illustrating why the harmonic modes, when in vicinity to a natural frequency of the structure, should be removed from measurements analyzed with the classic SSI methods,
- development of a new method to remove harmonic modes from the structural responses, based on the orthogonal projection of raw measurements onto their predicted harmonic counterparts,
- empirical illustration of the consistency of the proposed approach, based on numerical Monte Carlo simulations,
- application of the proposed approach to a real-life examples of experimental plate, ferry in operation and offshore meteorological mast.

3.1 Illustrative example

This section illustrates the influence of a periodic input on the responses collected from structures and addresses the challenges in the estimation of modal parameters for such excitation cases. That problem is illustrated on a theoretical 6 DOF chain-like system that, for any consistent set of units, is modeled with a spring stiffness $k_1 = k_3 = k_5 = 100$ and $k_2 = k_4 = k_6 = 200$, mass $m_{1-6} = 1/20$ and a proportional damping matrix. The system is subjected to white noise signal in all DOFs and sampled with a frequency of 50 Hz for 2000 seconds. Additional sinusoidal excitation with a frequency of 8.74 Hz, 0.5% from a third natural frequency of the system, is added to all DOF. That excitation is devised to mimic a periodic input from e.g. an engine rotating at a constant speed. The responses are measured at 1, 2 and 5 DOF. Gaussian white noise with 5% of the standard deviation of the output is added to the response at each channel. Figure 3.1 illustrates two largest singular values of the Power Spectral Density (PSD) matrix constructed from the structural responses with and without the harmonic influence.

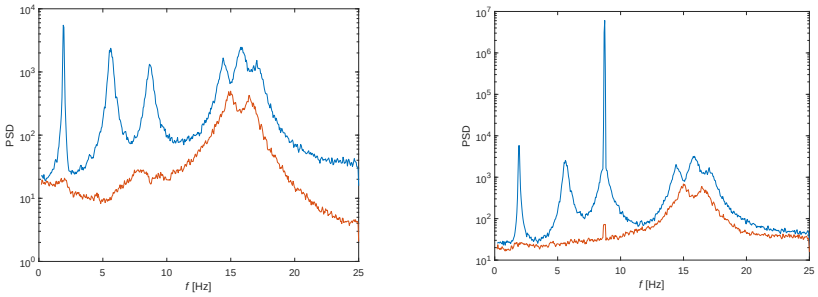

Figure 3.1: Two largest singular values of the output PSD matrix without harmonic (left) and with harmonic (right) excitation.

It can be observed that the fundamental frequency of the periodic signal added to the random input manifests as a sharp spike in the power spectra, indicating undamped vibrations at that frequency.

The next example will illustrate how periodic signals in the outputs of the aforementioned simple system influence the estimates of its natural frequencies and damping ratios. The computations are performed in a Monte Carlo setup with $m = 1000$ simulations. The output-only data driven subspace-based system identification with the unweighted principal component (SSI-UPC) and the variance computation in the corresponding framework are set up with system orders of 12 and 14, time lags of 15 and 200 blocks for the covariance computation of the data Hankel matrix. Two sets of modes, respectively for model order 12 and 14, with respective modal parameters, are tracked in each simulation. Figures 3.2 and 3.3 illustrate histograms of the natural frequency and the damping ratio corresponding to the third mode and identified for system orders of 12 and 14.

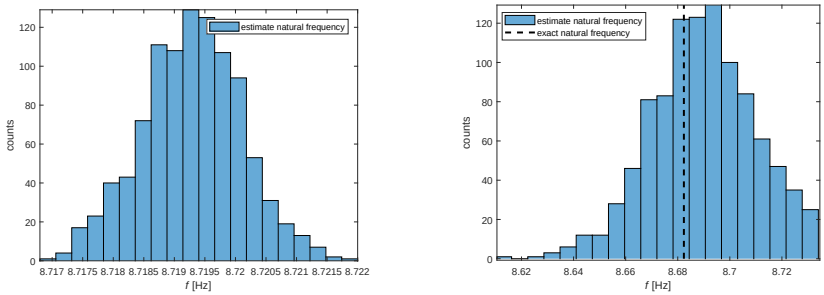

Figure 3.2: Histograms of the natural frequency of the third mode identified with model order 12 (left) and 14 (right).

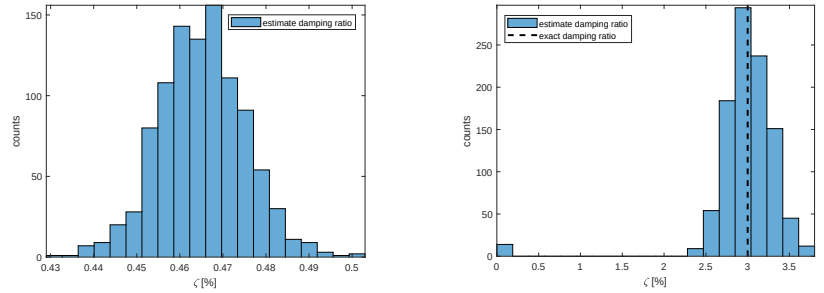

Figure 3.3: Histograms of the damping ratio of the third mode identified with model order 12 (left) and 14 (right).

It can be observed that the pair natural frequency damping ratio estimated for the model order 12, depicted on the left parts of Figure 3.2 and Figure 3.3, corresponds to a mix of the structural mode at 8.68 Hz and the harmonic mode at 8.74 Hz.

The mean values of the histogram of the natural frequency and the damping ratio from the right parts of Figure 3.2 and Figure 3.3 are in the vicinity of the exact values from the model. However, one can observe that some of the identified damping ratios are approaching 0 and the histogram of the natural frequency estimates is skewed towards the periodic frequency. That suggests that some of the estimated parameters still correspond to the forced periodic excitation. Thus, over-modeling the system is not optimal for the estimation of modal parameters from the measurements containing harmonics. That is also reflected in the standard deviations of the natural frequency and the damping ratio computed with the perturbation theory for each realization of the Monte Carlo simulations. Their histograms are illustrated on Figure 3.4.

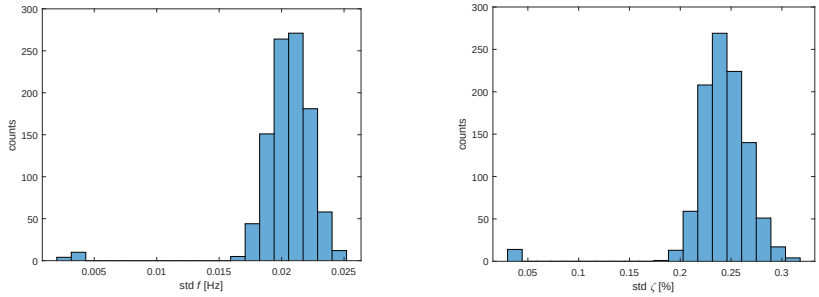

Figure 3.4: Histograms of the standard deviation of the natural frequency (left) and the damping ratio (right) of the third mode identified with model order 14.

It can be observed that both histograms depicted on Figure 3.4 are not adequate to be approximated by a Gaussian distribution, due to some standard deviations close to zero. Those standard deviations correspond to estimates of the natural frequency and the damping ratio related to the harmonic excitation that were mentioned earlier.

3.2 Orthogonal projection-based harmonic removal

This section describes the strategy for removing the harmonic modes from response measurements. The proposed scheme is based on the fact that the harmonic modes are well identified during the system identification, hence the response of the system due to these modes can be predicted. In the following, it is assumed that the frequency of the periodic input is known a priori, which is not always the case in practice. Therefore first, the strategy for the harmonic detection is recalled, based on [104] and [105].

3.2.1 Harmonic detection

Since the distribution of response of a structural system subjected to a random input is asymptotically Gaussian, the periodic components therein can be detected by examining its statistical moments. The fourth moment, namely kurtosis γ (3.1), is a measure of the heaviness of the tail of the distribution and yields $\gamma = 3$ for signals following standard normal distribution and $\gamma \approx 1.5$ for a sinusoidal signals x with zero mean μ and a unit variance σ. The computation of the kurtosis writes

$$\gamma(x|\mu,\sigma) = \frac{\mathrm{E}[(x-\mu^4)]}{\sigma^4} \ , \tag{3.1}$$

where $\mathrm{E}(\cdot)$ is the expectation operator. The following can be illustrated based on responses of the chain system described in the previous section. An illustration of the probability density function (PDF) of measurements from the second sensor is depicted on Figure 3.5.

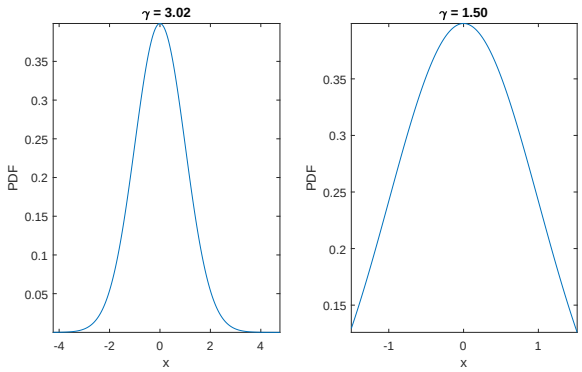

Figure 3.5: The PDF of the response due to random (left) and periodic (right) inputs.

The response of the system due to periodic inputs has a much lighter tail of the distribution, see right part of the Figure 3.5, thus smaller kurtosis. This fact can be used to detect the harmonics in the structural responses, like presented in [104] and [105]. Therefore, it is assumed here that the frequency of the harmonic inputs is either known or can be detected automatically by the scheme above.

3.2.2 Harmonic removal

The procedure that follows consists of three steps: first a similarity transform of the innovation state space to a modal state space, second, a prediction of modes that correspond to the harmonic frequencies and last an orthogonal projection of raw time series onto the harmonic realization of the output. Recall a discrete time state-space representation of the linear time-invariant (LTI) and viscously damped structural system, observed at r measurement points, i.e. sensors, which writes

$$\begin{aligned} x_{k+1} &= A_n x_k + v_k \ , \\ y_k &= C_n x_k + w_k \ , \end{aligned} \tag{3.2}$$

where $x_k \in \mathbb{R}^n$ are the states; $A_n \in \mathbb{R}^{n\times n}$, $C_n \in \mathbb{R}^{r\times n}$ are the state transition and observation matrices estimated for a model order n and vectors w_k, v_k denote the process and output noises respectively. The eigenfrequency f_i, damping ratio ζ_i and mode shape φ_i of the underlying mechanical system are identified for $i = 1 \dots n$ from the i-th eigenvalue λ_i and eigenvector Φ_i of A_n such that

$$f_i = \frac{|\lambda_{ci}|}{2\pi}, \ \zeta_i = \frac{-\Re(\lambda_{ci})}{|\lambda_{ci}|}, \ \varphi_i = C_n \Phi_i \ , \tag{3.3}$$

where the eigenvalue of the continuous system λ_{ci} is computed with $\mathrm{e}^{\lambda_{ci}\tau} = \lambda_i$. Optimal, in the least-square sense, solution to compute the states, is developed with applying a Kalman filter to (3.2), which transforms (3.2) into a innovation state-space model

$$z_{k+1} = A_n z_k + K_n e_k \ , \tag{3.4}$$

$$y_k = C_n z_k + e_k \ , \tag{3.5}$$

where $z_k \in \mathbb{R}^n$ are the Kalman states; $e_k \in \mathbb{R}^r$ are called the innovations and $K_n \in \mathbb{R}^{n\times r}$ denotes the Kalman gain. The states are not unique since there exists a linear transformation such that

$$z_k^V = V z_k \ , \tag{3.6}$$

where V denotes a transformation matrix. Let V yield the right eigenvectors of A_n, such that $A_n V = V\lambda, \quad \lambda \in \mathbb{C}^{n\times n}, \quad V \in \mathbb{C}^{r\times n}$. Now the innovation state-space model in the modal space writes as

$$z_{k+1}^V = V^{-1} A_n V z_k^V + V^{-1} K_n e_k \ , \tag{3.7}$$

$$y_k = C_n V z_k^V + e_k \ , \tag{3.8}$$

where the transformed state matrices can be written as $A_n^V = V^{-1} A_n V \in \mathbb{C}^{n\times n}$, $C_n^V = C_n V \in \mathbb{C}^{r\times n}$, $K_n^V = V^{-1} K_n \in \mathbb{C}^{n\times r}$. Notice that $A_n^V = \lambda$ and $C_n^V = \Phi$. Inserting (3.8) to (3.7) yields the one step ahead predictor of the modal states z_k^V

$$z_{k+1}^V = (A_n^V - K_n^V C_n^V) z_k^V + K_n^V y_k \ , \tag{3.9}$$

$$y_k = C_n^V S_n z_n^V + e_k \ , \tag{3.10}$$

where S_n is a diagonal matrix that selects the modes for which the response of the model is predicted. For example, $S_n = I_n$ computes the realization of the model due to all identified modes. To select only the modes that are corresponding to the periodic input define a matrix $I_n^{k_{\text{har}}}$ such that

$$I_n^{k_{\text{har}}} = \begin{bmatrix} 0 & & & & & \\ & \ddots & & & & \\ & & k_{\text{har}}^1 & & & \\ & & & k_{\text{har}}^2 & & \\ & & & & \ddots & \\ & & & & & 0 \end{bmatrix} \ , \tag{3.11}$$

where k_{har}^1 and k_{har}^2 are the positions of the complex-conjugate pair of the modes that correspond to harmonics. Thus, the realization of the modes that correspond to the periodic input writes as

$$y_k^{\text{har}} = C_n^V I_n^{k_{\text{har}}} z_k^V \ . \tag{3.12}$$

Subsequently, one can decouple the system response from the response affected by the periodic input by projecting the latter orthogonally onto its harmonic realization. For that denote p as a number of block rows and $q = p + 1$ with $pq = p + q$. Next, define the past $\mathcal{Y}_{\text{har}}^- \in \mathbb{R}^{(p+1)r\times N-pq}$ and future $\mathcal{Y}_{\text{har}}^+ \in \mathbb{R}^{(p+1)r\times N-pq}$ data matrices built from the predicted harmonic realizations y^{har} and denote $\mathcal{Y}_{\text{raw}}^- \in \mathbb{R}^{(p+1)r\times N-pq}$ and $\mathcal{Y}_{\text{raw}}^+ \in \mathbb{R}^{(p+1)r\times N-pq}$ as respectively the past and the future matrices built from the raw data y^{raw}, as in (2.6). The orthogonal projection is illustrated, in 2-dimensional space, on Figure 3.6.

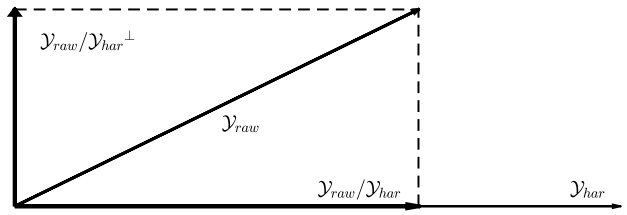

Figure 3.6: Illustration of orthogonal projection of $\mathcal{Y}_{\text{raw}}$ and $\mathcal{Y}_{\text{sys}}$ in 2-dimensional space, after [17].

The response of the system due to the structural modes can be represented by data matrices $\mathcal{Y}^{-}_{\text{sys}} \in \mathbb{R}^{(p+1)r\times N-pq}$ and $\mathcal{Y}^{+}_{\text{sys}} \in \mathbb{R}^{(p+1)r\times N-pq}$ where the periodic inputs are decorrelated respectively from the past and the future of the raw time series such that

$$\begin{aligned}\mathcal{Y}^{-}_{\text{sys}} &= \mathcal{Y}^{-}_{\text{raw}}/\mathcal{Y}^{-}_{\text{har}}{}^{\perp} = \mathcal{Y}^{-}_{\text{raw}} - \mathcal{Y}^{-}_{\text{raw}}/\mathcal{Y}^{-}_{\text{har}} \\ &= \mathcal{Y}^{-}_{\text{raw}} - \mathcal{Y}^{-}_{\text{raw}}(\mathcal{Y}^{-}_{\text{har}}{}^{T})(\mathcal{Y}^{-}_{\text{har}}\mathcal{Y}^{-}_{\text{har}}{}^{T})^{-1}\mathcal{Y}^{-}_{\text{har}}\ , \\ \mathcal{Y}^{+}_{\text{sys}} &= \mathcal{Y}^{+}_{\text{raw}}/\mathcal{Y}^{+}_{\text{har}}{}^{\perp} = \mathcal{Y}^{+}_{\text{raw}} - \mathcal{Y}^{+}_{\text{raw}}/\mathcal{Y}^{+}_{\text{har}} \\ &= \mathcal{Y}^{+}_{\text{raw}} - \mathcal{Y}^{+}_{\text{raw}}(\mathcal{Y}^{+}_{\text{har}})^{T}(\mathcal{Y}^{+}_{\text{har}}\mathcal{Y}^{+}_{\text{har}}{}^{T})^{-1}\mathcal{Y}^{+}_{\text{har}}\ .\end{aligned} \tag{3.13}$$

The proposed scheme is summarized in the pseudo-algorithm below.

Algorithm 1: Pseudo-algorithm for the harmonic removal.

Input : y^{raw} raw measurements containing harmonics, system order n.
Output : y^{sys} processed measurements without harmonics.

1 compute A_n, C_n, K_n for the selected system order n ;
2 compute similarity transform A_n^V, C_n^V, K_n^V ;
3 map harmonic poles of A_n^V and build $I_n^{k_{\text{har}}}$;
4 compute predictor z_{k+1}^V from (3.9) for each step k ;
5 compute harmonic realization y_k^{har} from (3.12) for each step k ;
6 build future and past of $\mathcal{Y}_{\text{raw}}$ and $\mathcal{Y}_{\text{har}}$ matrices ;
7 compute orthogonal projections from (3.13) ;
8 **return** y^{sys} retrieved from respective parts of $\mathcal{Y}^{-}_{\text{sys}}$ and $\mathcal{Y}^{+}_{\text{sys}}$;

Now system identification can be done with y^{sys}, where the harmonic modes are excluded.

3.2.3 Numerical validation

In this section the proposed harmonic removal scheme is deployed to remove the harmonic mode at 8.74 HZ from the numerical simulations of a chain system described in the Section 3.1. First, the results from one realization of the Monte Carlo are presented. Figure 3.7 illustrates the two highest singular values of PSD matrix computed on the raw time series (left) and time series after the harmonic removal (right).

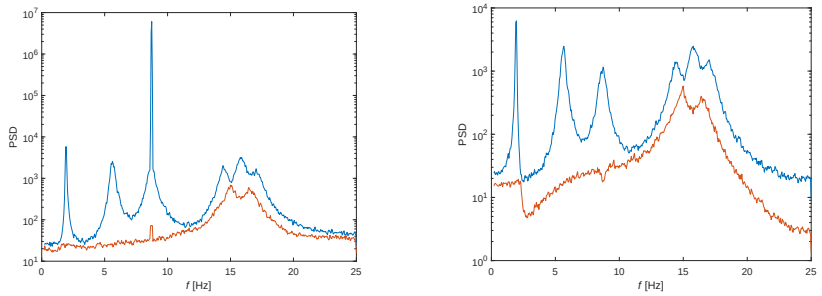

Figure 3.7: Two largest singular values of output PSD matrix with periodic (left) and after orthogonal projection of predicted periodic (right) excitations.

From the right part of Figure 3.7 it can be observed that the periodic mode at 8.74 Hz is removed from the response measurements,which resembles the plot on the left of Figure 3.1, depicting the case when no periodic inputs are present. To further validate the proposed scheme the Monte Carlo histograms of the natural frequency and damping ratio estimated from measurements after the harmonic removal are presented. Those histograms, computed for modal parameters of the third mode are presented on Figure 3.8.

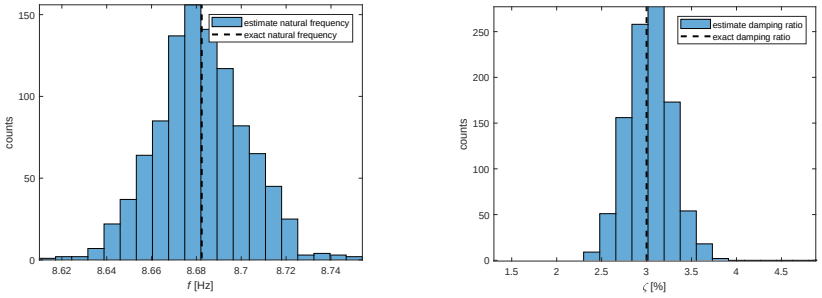

Figure 3.8: Histograms of the natural frequency (left) and damping ratio (right) of the third mode identified with model order 12 after harmonic removal.

It can be observed that both histograms are centered around the exact values from the model and both are symmetric. That suggests that the harmonic mode is removed from all the simulated data sets and no visible bias on the estimated modal parameters is introduced. To conclude the numerical validation the influence of removing the harmonic mode on the uncertainty of the estimated modal parameters is investigated. Figure 3.9 illustrates the histograms of the standard deviations of natural frequencies and damping ratios computed with the first order perturbation theory.

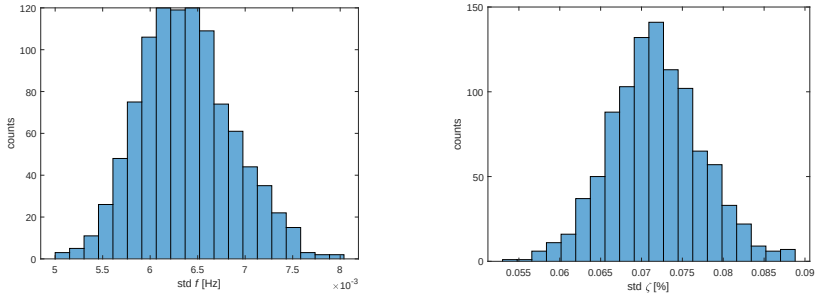

Figure 3.9: Histograms of the standard deviation of the natural frequency (left) and the damping ratio (right) of the third mode identified with model order 12 after harmonic removal.

Both histograms are symmetric and the standard deviations of both parameters are a order of magnitude lower then ones depicted on Figure 3.4. That concludes the numerical validation of the proposed method.

3.3 Application

Three experimental cases depicted in this section illustrate the application of the proposed method to real-life vibration problems. The first example is a plate subjected to a mix of random and periodic excitations induced in laboratory conditions. The second example is a full-scale test of a ferry excited by a random environmental load (wind and waves) with a harmonic interference from rotating machinery on-board. The third example is the meteorological mast which was described in the previous chapter. In this example it is shown how the proposed algorithm can be used to remove any mode of the structure, not necessarily a harmonic one.

3.3.1 Plate with harmonics

The geometry of the plate and the experimental setup are illustrated on Figure 3.10.

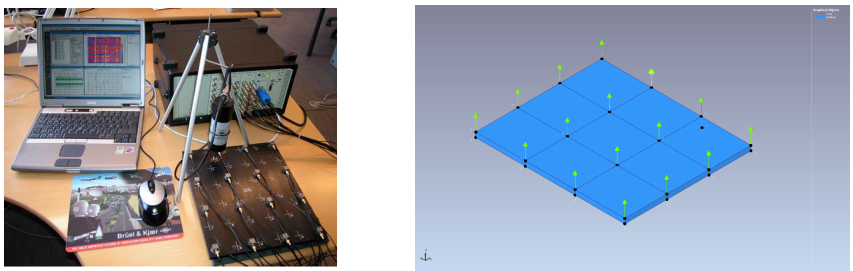

Figure 3.10: The experimental setup: plate with 16 acceleration channels, shaker, acquisition system (right). The plate model with 16 acceleration channels attached (left).

The measurements were sampled with 4096 Hz over 120 seconds interval. To challenge the harmonic removal a periodic signal of three different frequencies and amplitudes is introduced by the shaker, namely at 374 Hz, 748 Hz and 1496 Hz. The

algorithm is initiated with 45 block-rows for the data Hankel matrix and maximum system order of 80. Three pairs of complex-conjugate poles are selected to predict the harmonic modes and consequently used in the orthogonal projection. Figure 3.11 illustrates the two largest singular values of PSD from measurements before and after harmonic removal.

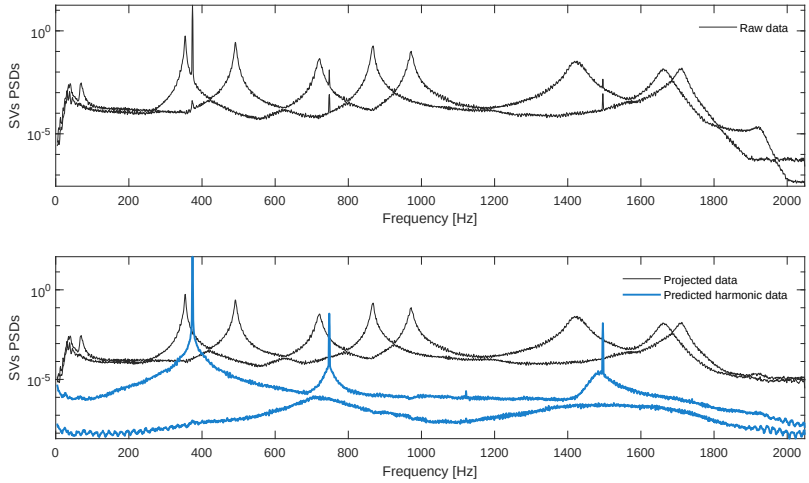

Figure 3.11: Two largest singular values of PSD of output measurements from a plate with harmonics. Raw data (top). Predicted harmonic modes and filtered data (bottom).

The singular values of the PSD from the predicted harmonic modes (blue line) match well with the harmonic peaks in the raw measurements, as depicted on Figure 3.11. The singular values of the measurements after the projection do not contain any harmonic peaks and the underlying structural modes are not visually distorted by the orthogonal projection.

3.3.2 Operating ferry

The dynamic test is undergone under fully operational conditions; 16 output accelerations channels are sampled with 128 Hz for 5400 seconds. The geometry of the ship with the measured degrees of freedom is illustrated on Figure 3.12. Prior to harmonic removal measurements are decimated to 16 Hz.

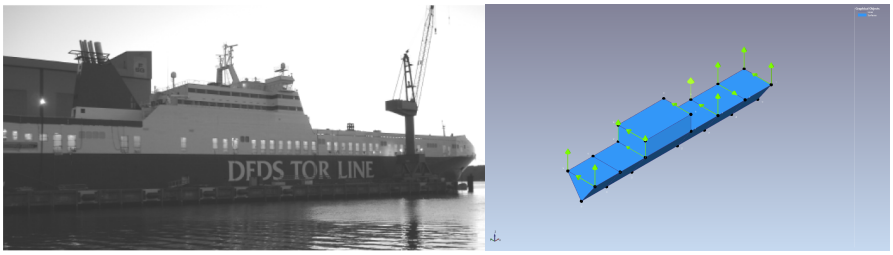

Figure 3.12: The ferry at the Flensburg shipyard (left). The geometry of the ferry with 16 acceleration channels attached (right).

During the test the fundamental rotational frequency of the engine is 2.05 Hz, hence a family of three harmonic frequencies: 4.1 Hz, 6.15 Hz and 7.8 Hz is present in the decimated response signals, see Figure 3.13.

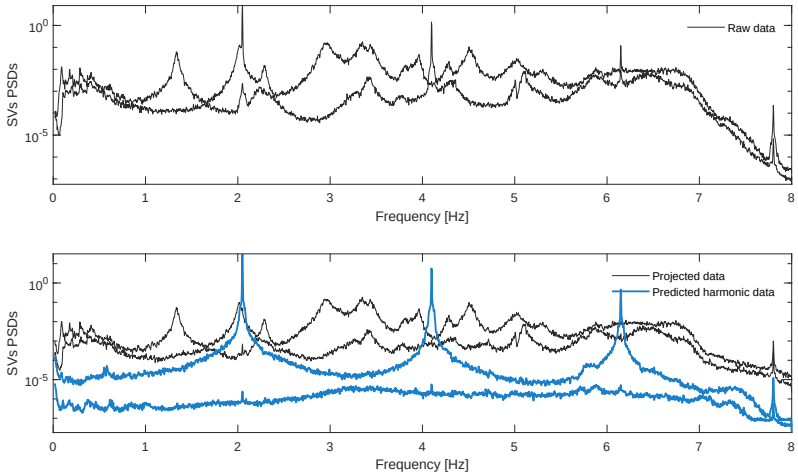

Figure 3.13: Two largest singular values of PSD of output measurements from the ferry. Raw data (top). Predicted harmonic modes and filtered data (bottom).

Three of these frequencies, namely 2.05 Hz, 4.1 Hz, 6.15 Hz, are selected to map the harmonic poles. The harmonic reduction is prepared with 50 block-rows of data Hankel matrix and maximum system order of 100. Figure 3.13 illustrates a plot of the two largest singular values of PSD from measurements before and after harmonic removal.

It can be observed that all three selected harmonic modes are successfully removed. The sharp peak at 7.8 Hz represents harmonics from the propeller, as mentioned above, however was not selected to be removed since it is in the noise floor of the decimated signal.

3.3.3 Offshore meteorological mast

In this example the proposed method for harmonic removal is generalized to removal of any mode of the structure. In this particular case the mode removal doesn't benefit any further analysis and it is conducted here as a proof of concept.

The data set used in this section is equivalent to the one analyzed in Section 2.3. The measurements are decimated to a frequency of 5 Hz and the harmonic removal is set up with 40 block-rows in data Hankel matrix and maximum system order of 100. The mode at 0.339 Hz is mapped to be removed. Figure 3.14 illustrates a plot of two largest singular values of PSD from measurements before and after deploying the algorithm.

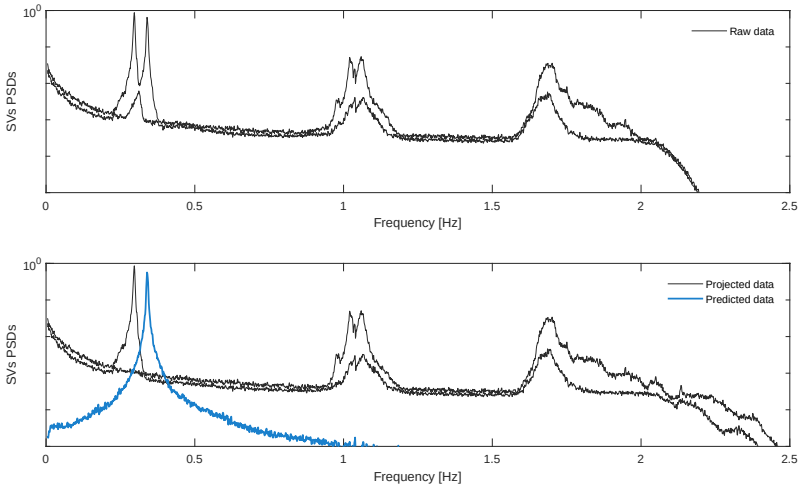

Figure 3.14: Two largest singular values of PSD of output measurements from the offshore meteorological mast at Dogger Bank West. Raw data (top). Predicted modes and filtered data (bottom).

It can be observed that the mapped mode is successfully removed from the measurements and the remaining data are not visually affected by the procedure.

3.4 Conclusions

This chapter outlined the development and application of the harmonic removal algorithm. The new method operates under the premise that the modes corresponding to the periodic frequencies originating from rotating components on the structures can be identified by the SSI algorithm and subsequently removed from the time series using the orthogonal projection of the raw time series onto predicted harmonic responses. The proposed method was validated on simulations of a chain system and its consistency was illustrated based on numerical Monte Carlo simulations. Its practical application addressed removing the harmonic frequencies induced by a shaker to an aluminum plate and removing the harmonic frequencies induced by propellers and a diesel engine of a full-scale ferry, tested during its operation. The last real-life application example, the full-scale meteorological mast, generalized the proposed

method to removing an priori selected and identified mode of the structure from the recorded responses.

3.5 Dissemination

Parts of this chapter have been published in [5, 6, 7]:

[5] S. Gres, P. Andersen, C. Hoen, L. Damkilde, Orthogonal projection-based harmonic signal removal for operational modal analysis, in: IMAC - XXXVI International Modal Analysis Conference, Orlando, USA, 2018.

[6] S. Gres, P. Andersen, L. Damkilde, Operational modal analysis of rotating machinery, in: IMAC - XXXVI International Modal Analysis Conference, Orlando, USA, 2018.

[7] S. Greś, M. Döhler, P. Andersen, L. Mevel, Kalman filter-based subspace identification for operational modal analysis under unmeasured periodic excitation, Mechanical Systems and Signal Processing 146 (2021) 106996 .

In addition, the algorithm for harmonic removal was implemented, by the author, in ARTeMIS Modal Pro 6.0 [138].

External acknowledgments

The experimental tests on the plate were carried out by Niels-Jørgen Jacobsen from B&K Nærum in Denmark. The measurements on the ferry were carried out by Dr Sven-Erik Rosenow, Santiago Uhlenbrock and Prof. Günter Schlottmann from University of Rostock in Germany and made available to analysis by Structural Vibration Solutions A/S.

CHAPTER 4

Uncertainty quantification of Modal Phase Collinearity

In this chapter, a framework to quantify the uncertainty of Modal Phase Collinearity (MPC) is developed. That can be used in a structural design validation to classify whether the true mode shapes are real or complex valued vectors and to filter uncertain estimates of the MPC from the stabilization diagrams, which improves the estimation of stable modes.

First, different statistical characteristics of estimates of the MPC indicator are observed, which subsequently leads to two different frameworks to quantify its uncertainty. A classical Gaussian framework is used to asses the variance and infer the distribution of MPC when its estimates are in the interior of $[0, 1]$ interval. A quadratic framework is proposed when the estimates of MPC are converging to its theoretical distribution boarders, namely 0 or 1. That occurs when the estimated mode shapes are e.g. asymptotically real-valued. Subsequently, a strategy for a numerical validation of both the Gaussian and the quadratic frameworks is developed. The chapter is concluded with a real-life application example.

In short, this chapter comprises

- illustrative example depicting different empirical distributions of the MPC indicator,
- development of a classic Gaussian approximation of the MPC for the complex-valued mode shapes,
- development of a novel approach to approximate a distribution of the MPC when its estimates are close to their theoretical boarder, meaning that the underlying mode shape is asymptotically a real-valued vector,
- development of a framework to classify whether the true mode shapes are real or complex valued vectors, based on the confidence intervals of the MPC indicator,

- application of the proposed approach on a real-life example of offshore meteorological mast.

4.1 Illustrative example

As discussed in Section 2.1.3, the MPC is the function defined for an arbitrary mode shape φ as follows

$$\mathrm{MPC}(\varphi) = \frac{(S_{xx} - S_{yy})^2 + 4(S_{xy})^2}{(S_{xx} + S_{yy})^2} \ . \tag{4.1}$$

When the mode shapes are estimated from data, the MPC has some statistical properties, which are a function of underlying mode shape estimates. As such, computing it independently for a multiple times will yield to a histogram approaching the statistical distribution of the MPC. To illustrate different distributions of MPC that may appear in practice, consider a theoretical 6 DOF chain-like system that, for any consistent set of units, is modeled with a spring stiffness $k_1 = k_3 = k_5 = 100$ and $k_2 = k_4 = k_6 = 200$, mass $m_{1-6} = 1/20$ and non-diagonal modal damping matrix selected to yield both complex and close to real mode shapes. The system is excited by some white noise signal in all DOFs and sampled with a frequency of 50Hz for 2000 seconds. The responses are measured at DOF numbered 1, 2 and 5. Gaussian white noise with 5% of the standard deviation of the output is added to the response at each channel. The computations are performed in a Monte Carlo setup with $m = 1000$ simulations. Both the output-only data driven subspace-based system identification with the unweighted principal component (SSI-UPC) and the variance computation in the corresponding framework are set up with a single system order of 12, time lags of 15 and 200 blocks for the covariance computation of the data Hankel matrix. Six modes, with respective modal parameters, are tracked in each simulation. Figure 4.1 shows three histograms of MPC_5, MPC_3, MPC_1 computed using the corresponding mode shape vector.

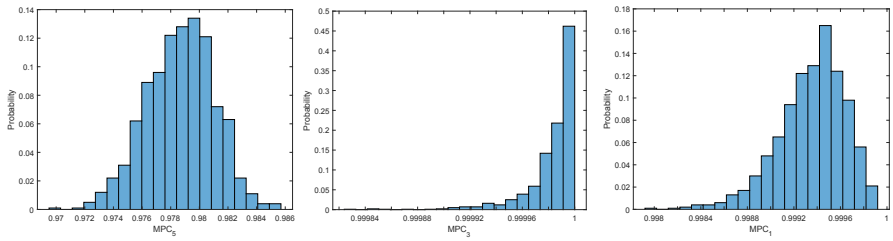

Figure 4.1: Histograms of MPC from simulations of non-proportionally damped chain-like system with $N = 100000$ samples. MPC_5 left, MPC_3 middle, MPC_1 right.

Since the histograms depicted on Figure 4.1 illustrate three distinctively different cases of the MPC distributions they are hereby denoted as base-case examples and will be referred to as such throughout the course of this chapter. Different distribution of the base-case MPC originate from the different degrees of the complexity of the estimated mode shapes. That fact is investigated later in this chapter.

4.2 Gaussian case

In this section a Gaussian approximation is developed to approximate the distribution of the MPC based one a single data set, when the MPC indicator is in the interior of the interval $[0, 1]$, like the MPC_5 on the left part of Figure 4.1.

4.2.1 Asymptotic properties of the MPC indicator

Define $g_{mpc}(\varphi)$ to be a function computing the MPC indicator evaluated for a given estimate of the mode shape vector $\hat{\varphi}$. The analytical function $g_{mpc}(\varphi)$ is smooth and twice differentiable at its unknown limit point φ_*, where $\hat{\varphi} \xrightarrow{a.s.} \varphi_*$. Define the relation between $\Delta g_{mpc}(\hat{\varphi})$ and the real and imaginary parts of $\Delta\hat{\varphi}$ as the first order perturbation that can be written as

$$\Delta g_{mpc}(\hat{\varphi}) = g_{mpc}(\hat{\varphi}) - g_{mpc}(\varphi_*) \triangleq \hat{\mathcal{J}}_{\hat{\varphi}}^{g_{mpc}} \Delta \begin{bmatrix} \Re(\hat{\varphi}) \\ \Im(\hat{\varphi}) \end{bmatrix} \approx \mathcal{J}_{\varphi_*}^{g_{mpc}} \left(\begin{bmatrix} \Re(\hat{\varphi}) \\ \Im(\hat{\varphi}) \end{bmatrix} - \begin{bmatrix} \Re(\varphi_*) \\ \Im(\varphi_*) \end{bmatrix} \right) . \tag{4.2}$$

The covariance estimate of $g_{mpc}(\hat{\varphi})$ is expressed as

$$\Sigma_{g_{mpc}(\hat{\varphi})} = \hat{\mathcal{J}}_{\hat{\varphi}}^{g_{mpc}} \Sigma_{\hat{\varphi}} (\hat{\mathcal{J}}_{\hat{\varphi}}^{g_{mpc}})^T ,$$

where $\hat{\mathcal{J}}_{\hat{\varphi}}^{g_{mpc}} \approx \mathcal{J}_{\varphi_*}^{g_{mpc}}$ and $\Sigma_{\hat{\varphi}} \approx \Sigma_{\varphi_*}$. Notice that here $\hat{\mathcal{J}}_{\hat{\varphi}}^{g_{mpc}} = \mathcal{J}_{\hat{\varphi}}^{g_{mpc}}$. Remark that $\hat{\mathcal{J}}_{\hat{\varphi}}^{g_{mpc}}$ can always be obtained by perturbation of the matrix $g_{mpc}(\hat{\varphi})$, even if the matrix $\mathcal{J}_{\varphi_*}^{g_{mpc}}$ is unknown.

4.2.2 Gaussian approximation

Let $k = 1 \dots r$ be the components of the mode shape $\varphi = \begin{bmatrix} \varphi_1 & \varphi_2 & \dots & \varphi_r \end{bmatrix}^T$. A consistent estimate of the Jacobian $\mathcal{J}_{\varphi_*}^{g_{mpc}}$ writes

$$\mathcal{J}_{\hat{\varphi}}^{g_{mpc}} \triangleq \left[\frac{\partial g_{mpc}}{\partial \Re(\varphi_1)} \ \cdots \ \frac{\partial g_{mpc}}{\partial \Re(\varphi_r)} \ \frac{\partial g_{mpc}}{\partial \Im(\varphi_1)} \ \cdots \ \frac{\partial g_{mpc}}{\partial \Im(\varphi_r)} \right] ,$$

where the estimate $\hat{\varphi} \xrightarrow{a.s.} \varphi_*$. Based on (2.14), the partial derivatives defined as $\frac{\partial g_{mpc}}{\partial \Re(\varphi)} = [\frac{\partial g_{mpc}}{\partial \Re(\varphi_1)} \ \cdots \ \frac{\partial g_{mpc}}{\partial \Re(\varphi_r)}]$ and $\frac{\partial g_{mpc}}{\partial \Im(\varphi)} = [\frac{\partial g_{mpc}}{\partial \Im(\varphi_1)} \ \cdots \ \frac{\partial g_{mpc}}{\partial \Im(\varphi_r)}]$ write

$$\begin{aligned} \frac{\partial g_{mpc}}{\partial \Re(\varphi)} &= \frac{\frac{\partial \left((S_{xx} - S_{yy})^2 + 4S_{xy}^2 \right)}{\partial \Re(\varphi)} c^2 - \left((S_{xx} - S_{yy})^2 + 4S_{xy}^2 \right) \frac{\partial c^2}{\partial \Re(\varphi)}}{c^4} \\ &= \frac{4(S_{xx} - S_{yy}) \Re(\varphi)^T + 8 S_{xy} \Im(\varphi)^T}{c^2} - \frac{4 g_{mpc}(\varphi) \Re(\varphi)^T}{c} , \end{aligned} \tag{4.3}$$

$$\begin{aligned} \frac{\partial g_{mpc}}{\partial \Im(\varphi)} &= \frac{\frac{\partial \left((S_{xx} - S_{yy})^2 + 4S_{xy}^2 \right)}{\partial \Im(\varphi)} c^2 - \left((S_{xx} - S_{yy}) + 4S_{xy}^2 \right) \frac{\partial c^2}{\partial \Im(\varphi)}}{c^4} \\ &= \frac{4(S_{yy} - S_{xx}) \Im(\varphi)^T + 8 S_{xy} \Re(\varphi)^T}{c^2} - \frac{4 g_{mpc}(\varphi) \Im(\varphi)^T}{c} , \end{aligned} \tag{4.4}$$

where scalar $c = S_{xx} + S_{yy}$. To approximate the MPC estimate with a Gaussian with the Delta method, the $\mathcal{J}_{\varphi_*}^{g_{mpc}}$ from (4.2) must be a non-zero matrix [1].

Lemma 4.1 *The necessary and sufficient condition for* $\mathcal{J}_{\varphi_*}^{g_{mpc}} \neq 0$ *is*

$$\forall \varphi_* \in \mathbb{C}^r \, \mathcal{J}_{\varphi_*}^{g_{mpc}} \neq 0 \Leftrightarrow g_{mpc}(\varphi_*) \neq \{0, 1\} \ .$$

Proof: See Appendix B.2. □

Subsequently, the Gaussian approximation of the MPC is summarized in the following Lemma.

Theorem 4.2 *Suppose that* $\mathcal{J}_{\varphi_*}^{g_{mpc}} \neq 0$ *and* $\sqrt{N}\left(\begin{bmatrix}\Re(\hat{\varphi})\\ \Im(\hat{\varphi})\end{bmatrix} - \begin{bmatrix}\Re(\varphi_*)\\ \Im(\varphi_*)\end{bmatrix}\right) \xrightarrow{\mathcal{L}} \mathcal{N}(0, \Sigma_{\varphi_*})$*, then* $g_{mpc}(\hat{\varphi})$ *is asymptotically Gaussian distributed with*

$$\sqrt{N}\left(g_{mpc}(\hat{\varphi}) - g_{mpc}(\varphi_*)\right) \xrightarrow{\mathcal{L}} \mathcal{N}\left(0, \mathcal{J}_{\varphi_*}^{g_{mpc}} \Sigma_{\varphi_*} \mathcal{J}_{\varphi_*}^{g_{mpc}\,T}\right) \ . \tag{4.5}$$

The estimate of covariance of $g_{mpc}(\hat{\varphi})$ *writes as* $\Sigma_{g_{mpc}(\hat{\varphi})} = \hat{\mathcal{J}}_{\hat{\varphi}}^{g_{mpc}} \Sigma_{\hat{\varphi}} (\hat{\mathcal{J}}_{\hat{\varphi}}^{g_{mpc}})^T$*, where* $\hat{\mathcal{J}}_{\hat{\varphi}}^{g_{mpc}} \approx \mathcal{J}_{\varphi_*}^{g_{mpc}}$ *and* $\Sigma_{g_{mpc}(\hat{\varphi})} \approx \Sigma_{g_{mpc}(\varphi_*)}$.

4.2.3 Gaussian approximation validation

In this section a strategy to validate the Gaussian approximation from Theorem 4.2 is devised and applied to two base-case examples depicted on Figure 4.1 namely, MPC_5 and MPC_1. For those cases the MPC estimates are far from the boarder of their domain and the Gaussian approximation should adequate to infer their statistical distributions.

For each Monte Carlo simulation consider the estimated MPC value and denote $\text{MPC}_{MC} \in \mathbb{R}^{m\times 1}$ the vector of all the MPC estimates from all m Monte Carlo simulations. From the histogram, it is straightforward to infer and compute μ_{MC} as its mean and $\sigma_{MC} = \sqrt{\text{var}(\text{MPC}_{MC})}$ as its standard deviation, where var is variance operator. Both terms are computed as sample means, also called the first two cumulants of the distribution. Considering the Gaussian assumption, both quantities are the only information needed to characterize the stochastic distribution of the considered MPC. Next let $\overline{\text{MPC}}_{MC}$ be the normalized MPC_{MC}, such that

$$\overline{\text{MPC}}_{MC} = \left(\text{MPC}_{MC} - \mu_{MC}\right)/\sigma_{MC} \ . \tag{4.6}$$

Based on the Monte Carlo independence assumption and its expected Gaussian properties, the vector $\overline{\text{MPC}}_{MC}$ should yield a histogram of the standard Gaussian distribution $\mathcal{N}(0, 1)$. Now, consider the variance computation using the aforementioned perturbation theory. Denote $\sigma_{PT} \in \mathbb{R}^{m\times 1}$ the vector of all standard deviations computed as in Theorem 4.2, where each component of σ_{PT} is the proposed standard deviation estimate $\sigma_{PT,j}$ based solely on the j-th data set. Then, for $j = 1 \ldots m$, define

$$\overline{\text{MPC}}_{PT,j} = \left(\text{MPC}_{MC,j} - \mu_{MC}\right)/\sigma_{PT,j} \tag{4.7}$$

as MPC estimate normalized by parameters computed with the perturbation theory. Based on the Gaussian assumption, $\overline{\text{MPC}}_{PT,j}$ should be a realization of a standard normal distribution $\mathcal{N}(0, 1)$. Since all MPCs are computed on independent data sets, the collection of all $\overline{\text{MPC}}_{PT,j}$, namely $\overline{\text{MPC}}_{PT} \in \mathbb{R}^{m\times 1}$, should yield a histogram of the Gaussian distribution. Such histogram computed for respective MPC_1 and MPC_5, along with the CDF of $\overline{\text{MPC}}_{MC}$ and $\mathcal{N}(0, 1)$, are presented on Figure 4.2 and on

Figure 4.3. As expected, the plots illustrate that entries of $\overline{\text{MPC}}_{PT}$ and $\overline{\text{MPC}}_{MC}$ follow $\mathcal{N}(0,1)$ closer for MPC_5 than for MPC_1, however the Gaussian approximation of MPC_1 is still visually acceptable.

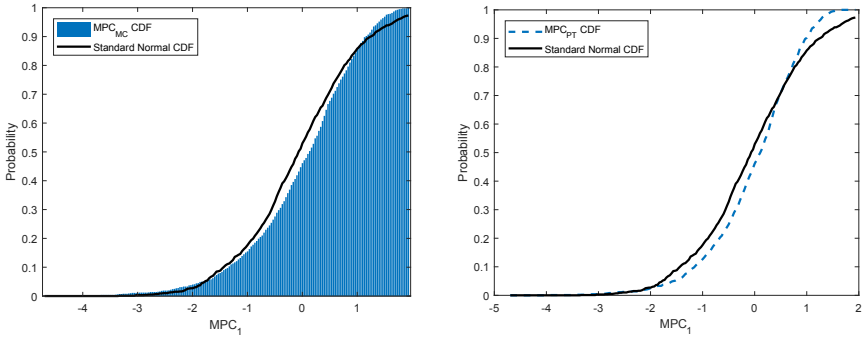

Figure 4.2: CDF of MPC_{MC} (left) and MPC_{PT} (right) computed for MPC_1.

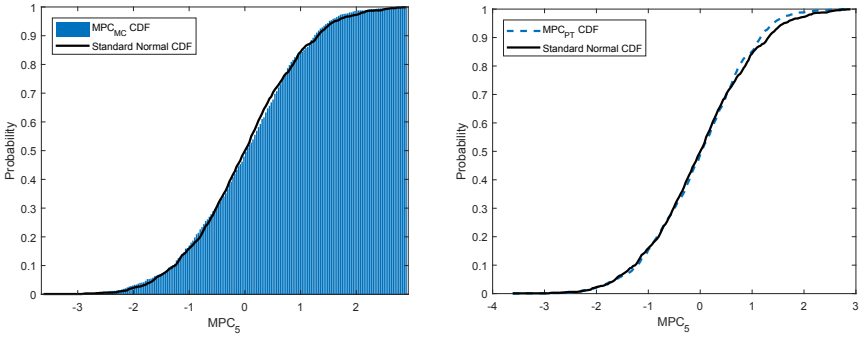

Figure 4.3: CDF of MPC_{MC} (left) and MPC_{PT} (right) computed for MPC_5.

The statistical uncertainties are quantified by confidence intervals thus a scheme to compare the approximated and theoretical confidence intervals is devised. For that define the theoretical two-sided normal cumulative confidence interval (CCI) function as $f_{t,cci} = 2(f_{t,cdf} - 0.5)$, where $f_{t,cdf}(t)$ is the function for the standard normal cumulative distribution i.e the integral of the density from minus infinity to t, and $f_{PT,cci}$ is the similarly defined cumulative function for computing two-sided confidence interval corresponding to $\overline{\text{MPC}}_{PT}$. Function $f_{t,cci}$ is purely theoretical, whereas $f_{PT,cci}$ is derived empirically from the histogram of $\overline{\text{MPC}}_{PT}$. A comparison of both $f_{t,cci}$ and $f_{PT,cci}$ for the base-case MPC_1 and MPC_5 is illustrated on Figure 4.4. As expected, both functions coincide much more for MPC_5 than for MPC_1.

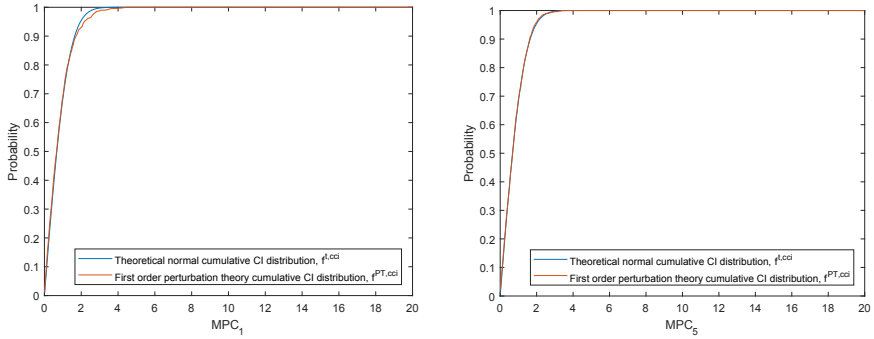

Figure 4.4: $f_{t,cci}$ and $f_{PT,cci}$ computed for MPC_1 (left) and MPC_5 (right).

In practice, the proposed framework is applied to assess uncertainty about one MPC estimate, computed solely on a single data set. Until now, this section showed a comparison between the MC histogram and the perturbation-based histogram. Both are mixing all information from all the available simulations. By a proper normalization, it was possible to compare them to the standard normal distribution, which reveals whether or not entries of $\overline{\mathrm{MPC}}_{PT}$ and $\overline{\mathrm{MPC}}_{MC}$ are Gaussian and illustrates the dispersion in all the estimated parameters.

A procedure that quantifies the errors in the Gaussian approximation when using just a single data set is now proposed. For each simulation j, assume that the computed standard deviation $\sigma_{PT,j}$ is a correct estimate of the desired σ_{MC}. Then, define a properly normalized vector $\overline{\mathrm{MPC}}^{j}_{PT}$ as the collection of normalized $\mathrm{MPC}_{MC,k}$ such that $\overline{\mathrm{MPC}}^{j}_{PT,k} = \left(\mathrm{MPC}_{MC,k} - \mu_{MC}\right)/\sigma_{PT,j}$. Under the Gaussian approximation, assuming independence and correct variance estimation, the histogram derived from $\overline{\mathrm{MPC}}^{j}_{PT}$ should be close to the histogram of the standard Gaussian distribution. Such closeness can be calculated by a classical Pearson Goodness of Fit test, a χ^2 statistics computed between the theoretical $\mathcal{N}(0,1)$ and the distribution corresponding to each simulation. The test itself is defined as

$$P_{\chi^2} = \sum_{i=1}^{b_n} \frac{(O_i - E_i)^2}{E_i} \ , \tag{4.8}$$

where O_i are observations of $\overline{\mathrm{MPC}}^{j}_{PT}$ within each i-th interval, E_i are counts corresponding to a theoretical $\mathcal{N}(0,1)$ distribution and b_n denotes a number of intervals used. As such, a median, best and worst quantiles of the Pearson statistics can be derived from the approximate histogram of its distribution. Best and worst cases are defined as the 2.5% and 97.5% quantiles of the P_{χ^2} distribution.

The CDFs of the best, median and worst quantiles among all $\overline{\mathrm{MPC}}^{k}_{PT}$ are plotted in the left parts of Figure 4.5 and Figure 4.6. Distributions of P_{χ^2} for both MPC_5 and MPC_1 are displayed in the right parts of Figure 4.5 and Figure 4.6. Notice that the first quantile measures the best possible outcome; there are 2.5% among all the realizations, which are equal or better than the plotted *best quantile plot*. The last quantile similarly measures the worst possible outcome; there are 2.5% among all the realizations, which are equal or worse than the plotted *worst quantile plot*. The median measures the most central outcome.

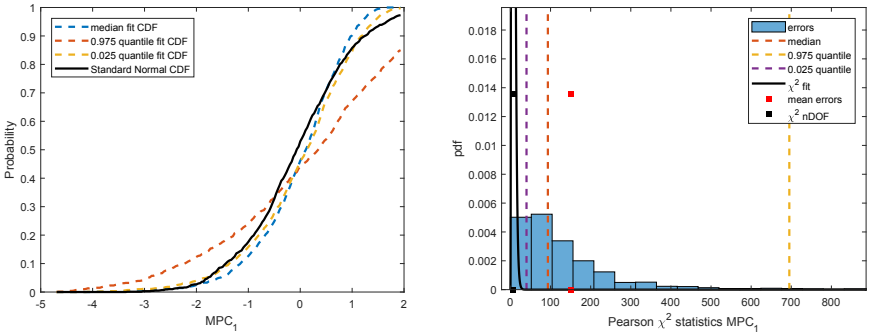

Figure 4.5: Best, median and worst Gaussian fits for MPC_1 (left). Histogram of Pearson χ^2 statistics with corresponding cases of Gaussian fits to MPC_1 (right).

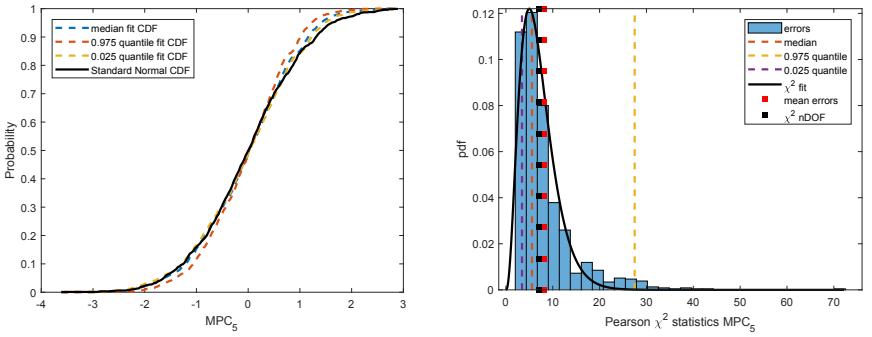

Figure 4.6: Best, median and worst Gaussian fits for MPC_5 (left). Histogram of Pearson χ^2 statistics with corresponding cases of Gaussian fits to MPC_5 (right).

Figure 4.5 and Figure 4.6 show the performance of the Gaussian approximation to fit to a standard Gaussian law for MPC_1 and MPC_5.

For MPC_1 the results are dispersive; inaccurate when looking at the worst quantile but satisfying for the median and the best quantiles. It means that the Gaussian approximation for MPC_1 should be adequate, on average, for a small set of experiments. The same plots for MPC_5 show a total equivalence to the Gaussian approximation even for the worst quantile, truly showing the Gaussianity of this mode.

To conclude this section median, best and worst Gaussian fits to the base-case MPCs are illustrated on Figure 4.7.

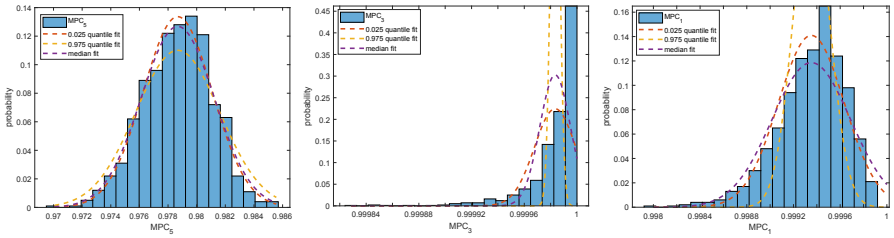

Figure 4.7: Gaussian fits to empirical probability distribution of base case MPCs based on median, 0.95 and 0.025 quantiles of Pearson χ^2 statistics.

It appears that the Gaussian approximation is good for MPC_5 (left) and adequate for MPC_1 (right), whereas being inexact for MPC_3 (center), which is expected from the inspection of the histograms. This is also expected not to be able to approximate a parameter at the border of its domain by a Gaussian law. Notice that the variance of different fits for MPC_1 is still a good indicator of the dispersion of its Monte Carlo estimates.

The distributions of MPC_5 and MPC_1 can be approximated with a Gaussian reasonably well, however a better approximation scheme, with deeper theoretical insight than the usual classical Gaussian approximation is needed to accurately characterize MPCs very close to 1, such as MPC_3. Before focusing on a proper approximation for MPC_3, the behavior of MPC_1 as the number of samples increases is investigated.

4.2.4 Influence of sample length on distribution of MPC: a Gaussian case

The density approximation for MPC_1 based on the Gaussian approximation is tested with respect to the number of samples, see Figure 4.8 and Figure 4.9.

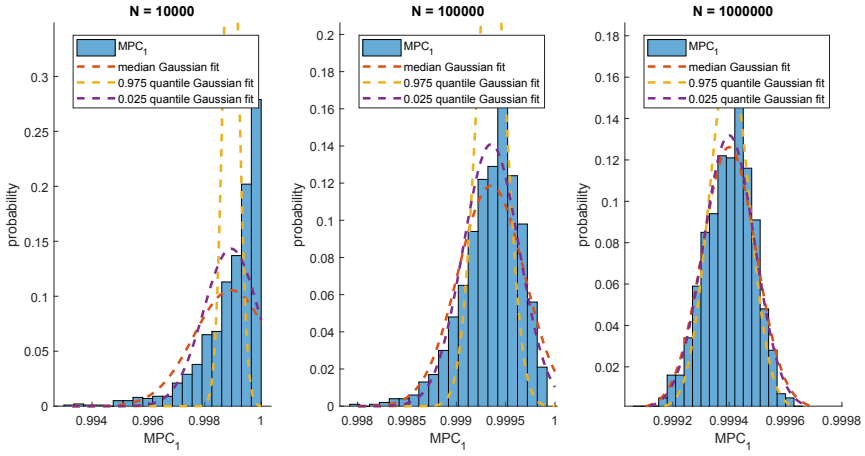

Figure 4.8: Histograms of MPC_1 computed on data sets with different sample lengths.

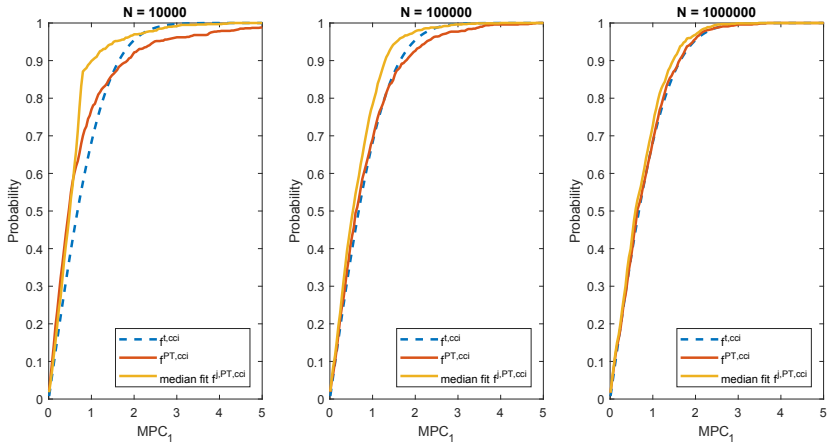

Figure 4.9: $f_{t,cci}$ and $f_{PT,cci}$ computed for MPC_1.

As it can be seen from Figure 4.8 and Figure 4.9, the more samples the better the approximation. It can be conjectured that the more real the mode shape is, the more samples are needed to satisfy the Gaussian approximation. At some point, for almost real modes, the Gaussian approximation will require many samples to be realistically applied. The next section addresses the problem of approximating distribution of the MPC estimate being in the vicinity of its boundary.

4.3 Quadratic case

There are two cases where the Gaussian approximation is not sufficient: when the MPC is equal to 1 and when the MPC is equal to 0. For these cases, since at the limit the mode shapes converge to their true values, $\hat{\varphi} \xrightarrow{a.s.} \varphi_*$, so are their respective real and imaginary parts. Based on that a relation between the $\Im(\varphi_*)$ and $\Re(\varphi_*)$ can be defined such that for any non-zero scalar a it holds

$$a \cdot \Re(\varphi_*) = \Im(\varphi_*) \ . \tag{4.9}$$

Moreover, when the MPC $= 1$ it is computed for a real mode shape, which also indicates that the histogram of its estimates is very close to the right boundary of the [0 1] interval. That is illustrated on Figure 4.1 (center). It can also happen that too few samples are available to characterize the mode shape. In that case histogram of its MPC estimates aggregates close the 1 as illustrated on Figure 4.9 (left). For both cases, the Gaussian approximation is no more valid.

This section considers the quadratic approximation, which is a step beyond the linear Gaussian approximation that is suitable for the classical problems as in e.g. [76]. In this case, consider $g_{mpc}(\hat{\varphi})$ at the border of its support, namely $g_{mpc}(\hat{\varphi}) \approx 1$. When the mode shape estimate $\hat{\varphi}$ converges to φ_* for $N \to \infty$, then $g_{mpc}(\varphi_*) = 1$ and thus $\mathcal{J}_{\varphi_*}^{g_{mpc}} = 0$ as shown in Lemma 4.1. Let $g_{mpc}(\varphi)$ be twice differentiable in φ_*, then the second order Taylor expansion of $g_{mpc}(\hat{\varphi})$ writes as

$$g_{mpc}(\hat{\varphi}) = 1 + \frac{1}{2}\hat{X}^T \, \mathrm{H}_{\varphi_*}^{g_{mpc}} \, \hat{X} + o(||\hat{\varphi} - \varphi_*||^2) \ , \tag{4.10}$$

where $\hat{X} = \begin{bmatrix} \Re(\hat{\varphi} - \varphi_*)^T & \Im(\hat{\varphi} - \varphi_*)^T \end{bmatrix}^T$ and $\mathrm{H}_{\varphi_*}^{g_{mpc}} \in \mathbb{R}^{2r \times 2r}$ is the Hessian of $g_{mpc}(\hat{\varphi})$ evaluated in φ_*. The asymptotic properties of $g_{mpc}(\hat{\varphi})$ follow from (4.10)

$$N(1 - g_{mpc}(\hat{\varphi})) \approx -\frac{1}{2} \hat{X}_{\mathcal{N}}^T \mathrm{H}_{\varphi_*}^{g_{mpc}} \hat{X}_{\mathcal{N}} = \hat{X}_{\mathcal{N}}^T \overline{\mathrm{H}}_{\varphi_*}^{g_{mpc}} \hat{X}_{\mathcal{N}} \ , \tag{4.11}$$

where $\hat{X}_{\mathcal{N}} = \sqrt{N}\hat{X}$ and $\overline{\mathrm{H}}_{\varphi_*}^{g_{mpc}} = -\frac{1}{2}\mathrm{H}_{\varphi_*}^{g_{mpc}}$. Vector $\hat{X}_{\mathcal{N}}$ converges to a Gaussian random variable $X_{\mathcal{N}}$ whose distribution is $\mathcal{N}(0, \Sigma_{\varphi_*})$ for $N \to \infty$. Expression (4.11) suggests that $N(1 - g_{mpc}(\hat{\varphi}))$ is asymptotically approximated by a quadratic form, defined as

$$Q(\hat{X}_{\mathcal{N}}) = \hat{X}_{\mathcal{N}}^T \overline{\mathrm{H}}_{\hat{\varphi}}^{g_{mpc}} \hat{X}_{\mathcal{N}} \approx X_{\mathcal{N}}^T \overline{\mathrm{H}}_{\varphi_*}^{g_{mpc}} X_{\mathcal{N}} \tag{4.12}$$

and related to the MPC by

$$Q(\hat{X}_{\mathcal{N}}) \approx N\left(1 - g_{mpc}(\hat{\varphi})\right) \ . \tag{4.13}$$

Since the exact distribution of a quadratic form is difficult to obtain, an approximate distribution in a form of a scaled χ^2 distribution from [84] is chosen, which can be applied when the Hessian matrix $\overline{\mathrm{H}}_{\varphi_*}^{g_{mpc}}$ is positive semi-definite. With this approximation, the variance of the quadratic form can be related to the mode shape variance, and subsequently the uncertainty of the MPC estimate can be quantified through relation (4.13).

Remark 4.3 (Regarding mode shape normalization and rank of Σ_{φ_*})
Since the mode shape estimate is defined up to a constant, it can be decided whether or not to normalize it. If it is not normalized, the asymptotic mode shape covariance is full rank, $\mathrm{rank}(\Sigma_{\varphi_*}) = 2r$*, assuming no dependencies between the estimates of the mode shape components. If it is normalized, assume that the considered mode shape is either normalized by one component k, i.e.* $\hat{\varphi} = \tilde{\varphi}/\tilde{\varphi}_k$ *[74], where* $\tilde{\varphi}_k \neq 0$ *at the limit, or additionally normalized to norm 1, i.e.* $\hat{\varphi} = \breve{\varphi}/||\breve{\varphi}||$ *with* $\breve{\varphi} = \tilde{\varphi}/\tilde{\varphi}_k$ *[81], where* $\tilde{\varphi}$ *is the unnormalized mode shape estimate. In these cases,* $\mathrm{rank}(\Sigma_{\varphi_*}) = 2r - 2$.

4.3.1 Approximation of the quadratic form

As stated above, the quadratic form is characterized by its inner matrix called Hessian, due to its expression as the second derivative in the Delta method. An estimate of the Hessian from (4.11) writes as

$$\mathrm{H}_{\hat{\varphi}}^{g_{mpc}} = \begin{bmatrix} \frac{\partial^2 g_{mpc}}{\partial \Re(\varphi) \partial \Re(\varphi)} & \frac{\partial^2 g_{mpc}}{\partial \Im(\varphi) \partial \Re(\varphi)} \\ \frac{\partial^2 g_{mpc}}{\partial \Re(\varphi) \partial \Im(\varphi)} & \frac{\partial^2 g_{mpc}}{\partial \Im(\varphi) \partial \Im(\varphi)} \end{bmatrix} \ . \tag{4.14}$$

For its derivation some simplified notation is introduced. First, since $\hat{\varphi} \xrightarrow{a.s.} \varphi_*$, so is $\mathrm{H}_{\hat{\varphi}}^{g_{mpc}} \xrightarrow{a.s.} \mathrm{H}_{\varphi_*}^{g_{mpc}}$. Then, its imaginary part $\Im(\varphi_*)$ can be related to $\Re(\varphi_*)$ such as in (4.9). Second, recall after Lemma 4.1 that since $g_{mpc}(\varphi_*) = 1$ thus $\mathcal{J}_{\varphi_*}^{g_{mpc}} = 0$. Third, introduce the following variables

$$\begin{aligned} M_{xx}^* &= \Re(\varphi_*)\Re(\varphi_*)^T, \quad M_{yy}^* = \Im(\varphi_*)\Im(\varphi_*)^T \ , \\ M_{xy}^* &= \Re(\varphi_*)\Im(\varphi_*)^T, \quad M_{yx}^* = \Im(\varphi_*)\Re(\varphi_*)^T \ . \end{aligned} \tag{4.15}$$

which will be plugged in after deriving each of the components of (4.14) evaluated in the limit φ_*.

The expression for $\mathrm{H}_{\varphi_*}^{g_{mpc}}$ writes

$$\mathrm{H}_{\varphi_*}^{g_{mpc}} = \underbrace{\frac{8}{(1+a^2)^2 S_{xx}^{*2}}}_{=n_{xx}} \begin{bmatrix} a^2(M_{xx}^* - I_r S_{xx}^*) & -a(M_{xx}^* - I_r S_{xx}^*) \\ -a(M_{xx}^* - I_r S_{xx}^*) & (M_{xx}^* - I_r S_{xx}^*) \end{bmatrix} \tag{4.16}$$

$$= n_{xx} \underbrace{\begin{bmatrix} a^2 & -a \\ -a & 1 \end{bmatrix}}_{=M_a} \otimes \underbrace{(M_{xx}^* - I_r S_{xx}^*)}_{=K_x} .$$

For its complete derivation see Appendix B.3.

Lemma 4.4 *The Hessian $\mathrm{H}_{\varphi_*}^{g_{mpc}}$ has non-positive eigenvalues thus is a negative semi-definite matrix. Its rank is* $\operatorname{rank}\left(\mathrm{H}_{\varphi_*}^{g_{mpc}}\right) = r - 1$.

Proof: See Appendix B.4. □

Since the Hessian matrix $\overline{\mathrm{H}}_{\varphi_*}^{g_{mpc}} = -\frac{1}{2}\mathrm{H}_{\varphi_*}^{g_{mpc}}$ is positive semidefinite, the probability distribution of the quadratic form corresponding to (4.11) can be approximated based on [84]. That is summarized by the following theorem.

Theorem 4.5 (After [84]) *The distribution of the quadratic form $Q(\hat{X}_{\mathcal{N}})$ defined in* (4.12) *can be approximated with a scaled $\chi^2_{l_{PT}}$ distribution of density*

$$f_Q(y) = \frac{1}{\alpha} f_{\chi^2_{l_{PT}}}\left(\frac{y-\beta}{\alpha}\right), \quad y \in [\beta, +\infty] , \tag{4.17}$$

where $f_Q(y) = 0$ for $y < \beta$, $l_{PT} = c_2^3/c_3^2$ is the number of degrees of freedom and

$$c_k = \operatorname{tr}\left((\overline{\mathrm{H}}_{\varphi_*}^{g_{mpc}} \Sigma_{\varphi_*})^k\right) \tag{4.18}$$

is the k-th asymptotic cumulant of $Q(\hat{X}_{\mathcal{N}})$. The respective scaling and shift parameters of the approximating distribution, α and β, are defined such that $\alpha = \sigma_Q/\sigma_{\chi^2}$ and $\beta = \mu_Q - (\mu_{\chi^2}\sigma_Q)/\sigma_{\chi^2}$. The mean μ_Q and standard deviation σ_Q of the quadratic form are computed using its first asymptotic cumulants, c_1 and c_2, namely $\mu_Q = c_1$ and $\sigma_Q = \sqrt{2c_2}$. The mean μ_{χ^2} and standard deviation σ_{χ^2} of the $\chi^2_{l_{PT}}$ distribution are computed from its number of degrees of freedom l_{PT}, namely $\mu_{\chi^2} = l_{PT}$ and $\sigma_{\chi^2} = \sqrt{2l_{PT}}$.

Proof: See Appendix B.5. □

Remark 4.6 (Regarding the notation of χ^2_l distribution) *χ^2_l is formally a Gamma distribution $\Gamma(l/2)$, where the term χ^2_l is related to distribution with a number of degrees of freedom l where $l \in \mathbb{N}$, which is used as such in the remainder of this thesis.*

Lemma 4.7 *The degrees of freedom l_{PT} of the $\chi^2_{l_{PT}}$ distribution used in the approximation of the distribution of $Q(\hat{X}_{\mathcal{N}})$ in Theorem 4.5 are bounded between $1 \leq l_{PT} \leq r - 1$.*

Proof: See Appendix B.6. □

The validity of the proposed framework, both for the $\chi^2_{l_{PT}}$ approximation but also for the $\chi^2_{l_{MC}}$ approximation of the empirical histogram of MPC indicators, can be directly assessed by Monte Carlo simulations, which are conducted in the next section. Before, however, it is important to clarify some facts about above mentioned $\chi^2_{l_{MC}}$ approximation. When approximating the distribution of the Monte Carlo histogram, a similar strategy to $\chi^2_{l_{PT}}$ approximation applies, albeit its cumulants are not derived from the Hessian but from the empirical histogram of the Monte Carlo distribution. As such, the bound on l_{MC} is deduced from the rank of $\Sigma_{\hat{\varphi}}$, which is bounded by $2r-2$.

Corollary 4.8 *The $\chi^2_{l_{MC}}$ distribution used to approximate the distribution of the Monte Carlo histogram $(1-g_{mpc}(\hat{\varphi}))$ is assumed to have l_{MC} degrees of freedom bounded between $1 \leq l_{MC} \leq 2r-2$.*

The next section is devoted to the numerical validation of the proposed approximation for the quadratic form stated above.

4.3.2 Quadratic approximation validation

Two strategies established in this section validate the χ^2_l approximation from Lemma 4.5. These strategies are possible because of the Monte Carlo simulations of the simple chain system from Section 4.1. They are derived along the same principles as in Section 4.2.3, adapted to the specific case of the quadratic framework. The developed schemes are tested on mode shape 3, whose exact MPC is equal to 1. Recall that the estimates of MPC computed from each realization of m Monte Carlo simulations are collected in $\mathrm{MPC}_{MC} \in \mathbb{R}^{m\times 1}$, where each estimate approaches the theoretical boundary of the MPC domain, here 1. Consequently, the corresponding vector is derived

$$Q_{\mathrm{MPC}_{MC}} = N\left(1-\mathrm{MPC}_{MC}\right) \ , \tag{4.19}$$

under the form shown in (4.13), which, based on Theorem 4.5, is a quadratic form, which can be approximated with a χ^2_l distribution. The number of degrees of freedom l_{MC} of the MPC Monte Carlo distribution can be derived from the empirical cumulants of the Monte Carlo histogram, similar as described in Theorem 4.5. The density of the χ^2 approximation can be analytically expressed as in (4.17); let $\overline{Q}_{\mathrm{MPC}_{MC}}$ be a scaled and shifted $Q_{\mathrm{MPC}_{MC}}$ such that

$$\overline{Q}_{\mathrm{MPC}_{MC}} = (Q_{\mathrm{MPC}_{MC}} - \bar{\beta})/\bar{\alpha} \ , \tag{4.20}$$

where $\bar{\alpha} = \bar{\sigma}_Q/\bar{\sigma}_{\chi^2}$ and $\bar{\beta} = \bar{\mu}_Q - (\bar{\mu}_{\chi^2}\bar{\sigma}_Q)/\bar{\sigma}_{\chi^2}$. The scalars $\bar{\sigma}_Q$, $\bar{\mu}_Q$, $\bar{\sigma}_{\chi^2}$ and $\bar{\mu}_{\chi^2}$ are computed from the cumulants of $Q_{\mathrm{MPC}_{MC}}$ as in Theorem 4.5. As such, knowing the Monte Carlo histograms, the characterization of their χ^2 approximation is easily performed. That can be achieved by defining a vector $v_1 \in \mathbb{R}^{m\times 1}$ whose j-th entry is drawn from a $\chi^2_{l_{MC}}$ distribution such that $v_j \sim \chi^2_{l_{MC}}$. As such, each entry of v_1 is drawn from a corresponding realization of $\chi^2_{l_{MC}}$ and the resulting aggregated histogram of all components of v_1 should correspond to the theoretical histogram of $\chi^2_{l_{MC}}$. A comparison of the cumulative distribution functions of both $\overline{Q}_{\mathrm{MPC}_{MC}}$ and v_1 is shown in the left part of Figure 4.10.

Having established the validity of the approximate distribution for the empirical Monte Carlo histogram, comparison is made with a collection of the approximations

from the perturbation theory, each computed on a single data set. For that, first define a vector $\overline{Q}_{\mathrm{MPC}_{PT}} \in \mathbb{R}^{m\times 1}$ such that for $j = 1 \dots m$ its j-th entry writes

$$\overline{Q}_{\mathrm{MPC}_{PT,j}} = (Q_{\mathrm{MPC}_{MC,j}} - \beta_j)/\alpha_j \ , \tag{4.21}$$

where β_j and α_j are the j-th β and α estimated after Theorem 4.5 for the corresponding realization of the Monte Carlo simulation. Here, each $\overline{Q}_{\mathrm{MPC}_{PT,j}}$ is drawn from some distribution that can be characterized by a different l_j, thus a common baseline is needed. For that purpose a new validation strategy, to compare them all, is introduced. This consists of modifying the approximated distributions to fit a theoretical χ^2_p distribution, where p is a constant for all realizations and not equal to l_j but $2r-1$ as explained below. Contrary to (4.20), each $Q_{\mathrm{MPC}_{MC,j}}$ is normalized with its own α and β coming from the perturbation theory and not from averaging over the Monte Carlo histogram. In that sense, $Q_{\mathrm{MPC}_{MC,j}}$ is properly following a $\chi^2_{l_{PT,j}}$ distribution, where $l_{PT,j}$ is computed from β_j and α_j. Still, each realization follows its own distinct distribution, which is not optimal for a comparison. The comparison is also more difficult, considering that the Monte Carlo histogram is fitted with its own χ^2 distribution, characterized with l_{MC}. To establish some common baseline for the comparison, the additive property of independent χ^2 distributions is used. Recall that the sum of two independent χ^2 with two different numbers of degrees of freedom results in a χ^2 distribution with a number of degrees of freedom equal to the sum of both previous numbers. Also, recall from Lemma 4.7 that $1 \leq l_{PT,j} \leq r-1$ for any j. The bounds for l_{MC}, as stated in Corollary 4.8, are $1 \leq l_{MC} \leq 2r-2$. As such, it exists some complement for all these numbers that is equal to $2r-1$ such that both $2r-1-l_{PT,j} > 0$ for all j and $2r-1-l_{MC} > 0$. Now, define random vectors $v_2, v_3 \in \mathbb{R}^{m\times 1}$ such that $v_2 \sim \chi^2_{2r-1-l_{MC}}$, and for $j = 1 \dots m$ each entry of $v_{3,j} \sim \chi^2_{2r-1-l_{PT,j}}$. Consequently, using the additive property of independent χ^2 distributions, define

$$Z_{MC} = \overline{Q}_{\mathrm{MPC}_{MC}} + v_2, \quad Z_{MC} \sim \chi^2_{2r-1} \ , \tag{4.22}$$

$$Z_{PT} = \overline{Q}_{\mathrm{MPC}_{PT}} + v_3, \quad Z_{PT} \sim \chi^2_{2r-1} \ . \tag{4.23}$$

A comparison between CDFs of Z_{MC}, Z_{PT} evaluated for MPC_3 and a theoretical χ^2_{2r-1} CDF is illustrated in the right part of Figure 4.10.

Now, when the theoretical reference distribution is known, a statistical measure can be used to quantify the dispersion between the above mentioned distributions. That dispersion can be computed with the Pearson χ^2 statistics between the expected χ^2_{2r-1} distributed variable and the observed $Z^j_{PT} \in \mathbb{R}^{m\times 1}$ vector computed such that

$$Z^j_{PT} = (Q_{\mathrm{MPC}_{MC}} - \beta_j)/\alpha_j + v_{4,j} \ , \tag{4.24}$$

where $v_{4,j} \sim \chi^2_{2r-1-l_{PT,j}}$. This leads to a collection of histograms that mirror the quality of each α_j, β_j, similarly as in the Gaussian case. The histogram of the Pearson χ^2 statistic for MPC_3 is depicted on Figure 4.11. As a consequence, a comparison of using the best, median and the worst approximations of MPC_3 to the χ^2_{2r-1} distribution, corresponding to respective quantiles of the Pearson χ^2 statistics, is depicted in the right part of Figure 4.10.

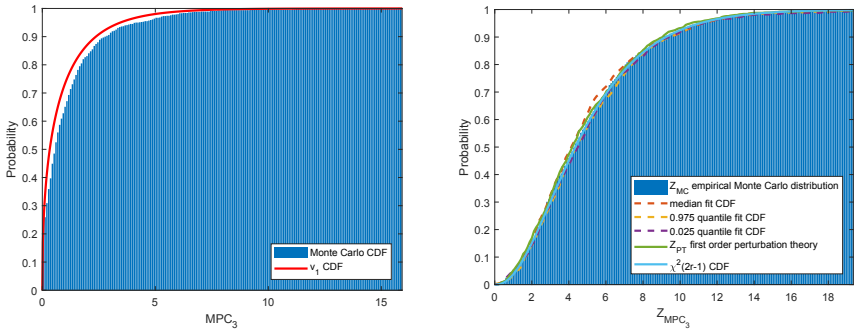

Figure 4.10: $\chi^2_{l_{MC}}$ CDF and CDF of MPC_3 from Monte Carlo simulations (left). Theoretical χ^2_{2r-1} CDF compared to CDF of Z_{MC} (4.22) and Z_{PT} (4.23) computed with parameters estimated for MPC_3 (right).

The left part of Figure 4.10 shows that the fit of the empirical Monte Carlo CDF to $\chi^2_{l_{MC}}$ is adequate, meaning that the distribution for the Monte Carlo histogram is well characterized by a quadratic distribution. The right part of Figure 4.10 shows that the corrected Z_{MC} for Monte Carlo and the full histogram Z_{PT} have similar CDF. This pleads for the validity of the perturbation theory approach to compute the variances needed to characterize the quadratic distribution and yield to similar distribution parameters as the full Monte Carlo histogram. Also, the plots corresponding to best, median and worst quantiles are all quite similar. They match the Monte Carlo and perturbation-based Z plots. This means that almost any of the realizations among the Monte Carlo experiments can be used to give such variance information.

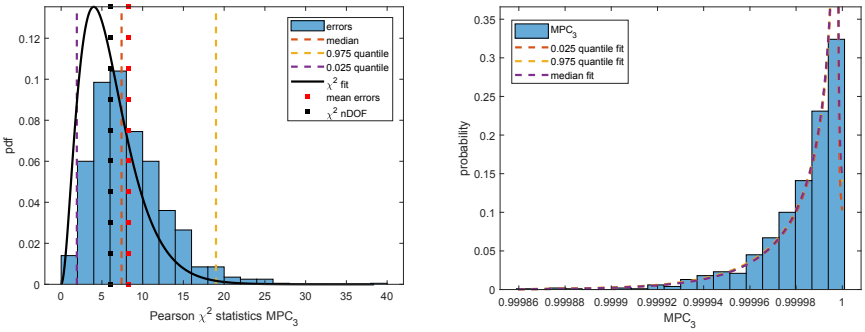

Figure 4.11: Histogram of errors in $\chi^2_{l_{PT}}$ approximation with best, median and worst fits for MPC_3 (left). Scaled and shifted χ^2 fits to empirical probability distribution of MPC_3 based on median, 0.95 and 0.025 quantiles of Pearson χ^2 statistics (right).

Figure 4.11 shows the dispersion of the distance between all the empirical histograms based on the perturbation theory. It can be seen that the empirical mean of the Pearson histogram matches well its theoretical mean as well. Based on the selection of best, median and worst quantiles, the right part of Figure 4.11 shows the fitting of MPC Monte Carlo histogram by the perturbation-based densities. It can be seen that

the quadratic assumption here is a much more reasonable assumption for MPC_3 than the Gaussian approximation on Figure 4.7.

4.3.3 Influence of sample length on distribution of MPC: a χ^2 case

Section 4.2.4 presented how sample length influence the underlying distribution of MPC. That was illustrated based on a Gaussian approximation of the base-case example of MPC_1, which is computed from a mode shape with a small degree of complexity. Whereas the Gaussian approximation was viable for the large sample sizes, for the small ones it was inadequate. This section studies the density approximation for MPC_1 based on the χ^2 approximation with respect to the number of samples. Such study is depicted on Figure 4.12.

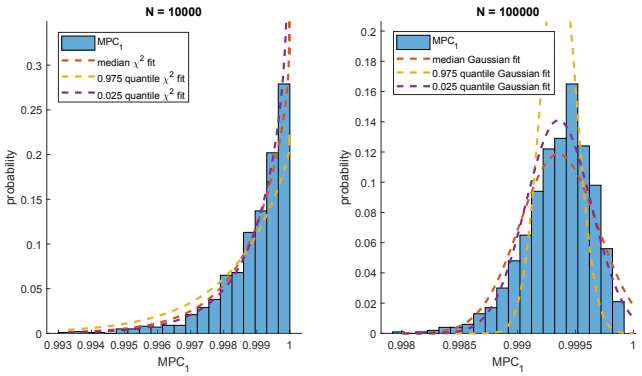

Figure 4.12: Histograms of MPC_1 computed on data sets with different sample lengths.

It can be seen that when the number of samples is sufficiently small the distribution of MPC_1 estimates can be well approximated with a χ^2 approximation. Otherwise, since MPC_1 estimates converge to a Gaussian relatively fast, its distribution is better approximated with a Gaussian distribution, as seen on Figure 4.8.

4.4 Influence of mode shape complexity on distribution of MPC

Sections 4.2 and 4.3 established a theoretical basis to approximate the distribution of MPC computed on mode shapes estimated on the chain-like system introduced in Section 2.1.3. Complexity of such system can be modified at-will which, as concluded from the both sections above, influences the distribution of MPC estimates. A study of the distribution of MPC estimates as a function of mode shape complexity is a subject of this section. For that the Kullback-Leibler divergence is computed for a decreasing order of the complexity of mode shape 1. The divergence is computed with respect to a Gaussian law and to a quadratic form, and both lead to two plots illustrated on Figure 4.13. Several points reflecting different fits of the respective distributions are highlighted. For example, two points that correspond to a minimum divergence reflecting the best Gaussian and quadratic fits, the point where both divergence meet and the point corresponding to the previously investigated cases. The distribution

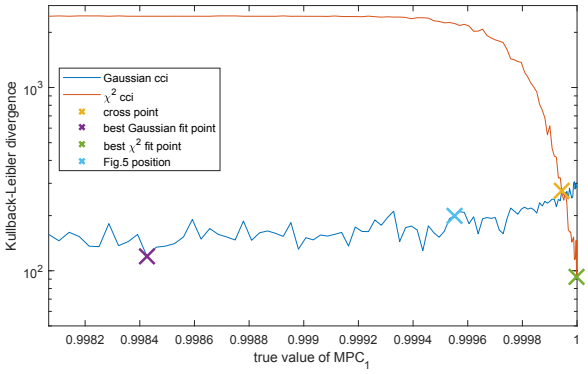

Figure 4.13: Kullback-Leibler divergence computed respectively between the $f_{t,cci}$ and $f_{PT,cci}$ estimated for MPC_1. Kullback-Leibler divergence computed respectively between the theoretical χ^2_{2r-1} CDF and CDF of Z_{PT} (4.23) computed with parameters estimated for MPC_1.

of the MPC indicator corresponding to the selected point is validated according to appropriate scheme, depicted for the Gaussian approximation in Section 4.2.3 and for the quadratic approximation in Section 4.3.2. Plots illustrating different distribution fits to the cross point are illustrated on Figure 4.14.

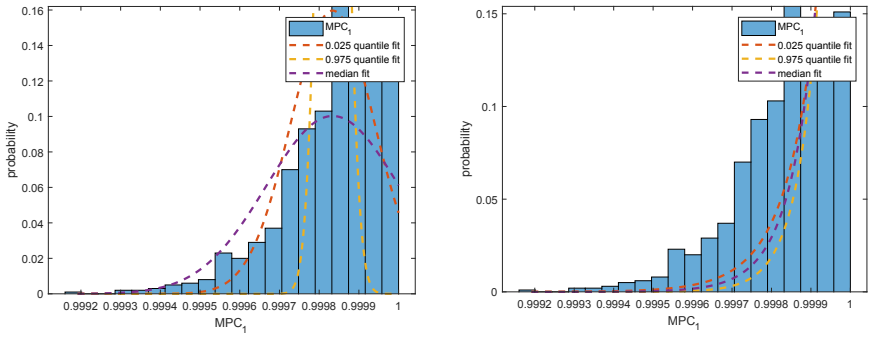

Figure 4.14: Gaussian (left) and χ^2 probability distribution fits computed with parameters estimated for cross point MPC_1.

It can be observed that both approximations exhibit rather poor fit to the empirical histograms. Thus, the proposed framework for the uncertainty quantification is not suitable to approximate the distribution which is between a Gaussian and a quadratic. Plots illustrating different distribution fits to the points of minimum divergence are illustrated on Figure 4.15. The best Gaussian and the best quadratic fits illustrate that for these points of complexity the expected distribution is a correct match for the Monte Carlo histogram.

To conclude, this section showed that the Gaussian approximation is well suited to complex modes, whereas the quadratic form is the most adequate for real or close to real modes. It can also be seen that the shift from Gaussian to quadratic is quite

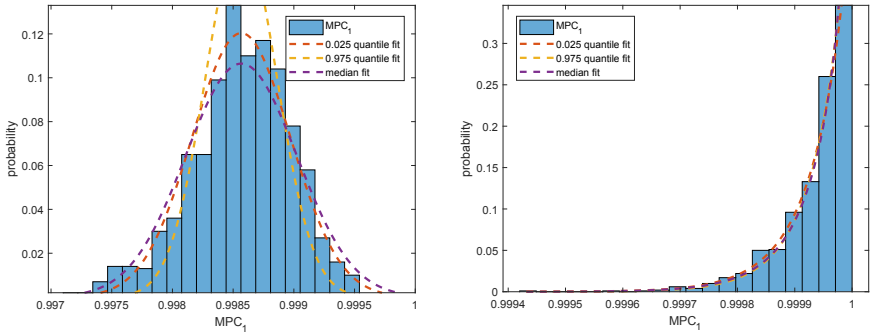

Figure 4.15: Gaussian (left) and χ^2 probability distribution fits computed with parameters estimated for corresponding to best fits to MPC_1.

abrupt and that for the most part, the Gaussian approximation is well suited.

4.5 Data-based choice of the approximation framework

So far, two frameworks for the uncertainty quantification of the MPC indicator have been derived and validated in the previous sections, showing that the respective confidence interval can be computed either based on a Gaussian or a χ^2 approximation. In this section, a scheme facilitating the choice between both approximations is proposed.

The confidence interval computed with a Gaussian approximation is symmetric and centered around the computed estimate. It covers a range of values that will include with some given confidence level, e.g. 95%, the true value of the MPC indicator. As such, the confidence interval length itself can be an indication that the Gaussian or the χ^2 assumption is possibly correct. For example, if the computed confidence interval is well situated in the $[0, 1]$ interval for a given 95% confidence level, then it can be assumed that the Gaussian approximation is plausible, i.e. there is a 95% certainty that the MPC estimate follows a Gaussian distribution. The probability that the approximating distribution is Gaussian can then be defined as $p_G = L/t + 0.5$, where L is the length of the sub-segment of the confidence interval measuring the distance from the estimate to the boundary 1, and t is the length of the whole confidence interval. Note that L is defined here such that $L \in [0, 0.5t]$, meaning that if the MPC estimate is equal to 1, then the probability that this MPC estimate follows a Gaussian distribution is still $p_G = 0.5$. Now, consider that a higher confidence level is needed, e.g. 99%. Subsequently, the confidence interval will be larger, and there is a possibility that it now overlaps the domain boundary of the MPC at 1. Note that if the confidence level increases, e.g. from 95% to 99%, then the probability of Gaussian acceptation will likely decrease. As a consequence, obtaining the same decision at 99% as at 95% would require an increase in the number of data samples. In a concluding remark for the Gaussian case, notice that $p_G \in [0.5, 1]$ because of the symmetry of the Gaussian distribution, and there is always at least a 50% chance that the unknown true value is inside the $[0, 1]$ interval. The previous discussion is summarized in parts 'a' and 'b' in Figure 4.16.

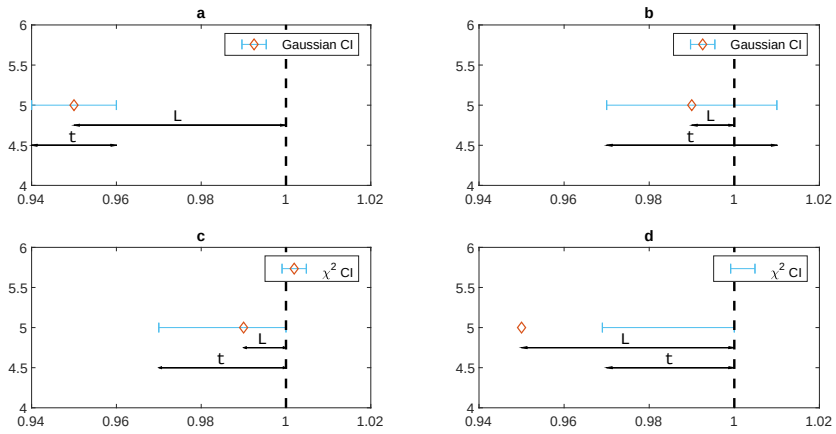

Figure 4.16: Example of 95% confidence intervals of MPC computed with both approximation frameworks for a given data set.

The confidence intervals computed based on the χ^2 approximation are not symmetric. They always cover an interval ending at 1, since the limit value of the MPC estimate is known to be at 1 in this case, unlike as in the Gaussian case. Now, the probability of the approximating distribution to be χ^2 is computed as $p_Q = (t - L)/t$, where L and t are defined similarly as in the paragraph above. Note that here $L \in [0, t]$ and $p_Q \in [0, 1]$. As such, $p_Q = 0$ when $t = L$, which corresponds to a MPC estimate situated the furthest from its potential true value 1, whereas $p_Q = 1$ indicates that the estimate of the MPC is equal to 1. Any position of the MPC estimate further to the left of the confidence interval yields a rejection of the quadratic assumption. The previous discussion is summarized in parts 'c' and 'd' in Figure 4.16.

Besides case 'a' where the Gaussian acceptation is triqqvial, and case 'd' where quadratic rejection is trivial, one can distinguish the following cases:

- the MPC follows a Gaussian distribution with probability $p_G = L/t + 0.5$, after part 'b' in Figure 4.16,
- the MPC follows a χ^2 distribution with probability $p_Q = (t - L)/t$, after part 'c' in Figure 4.16.

4.6 Application

This section illustrates the application of the proposed framework to the meteorological mast example described in Section 2.3. One of the motivations behind the uncertainty quantification of MPC is to use the estimated variance as a practical modal indicator during the formation of the stabilization diagrams. That is presented below. First, recall the stabilization diagram of the natural frequencies where the threshold on the maximum deviation of each estimate is set to 2.5%.

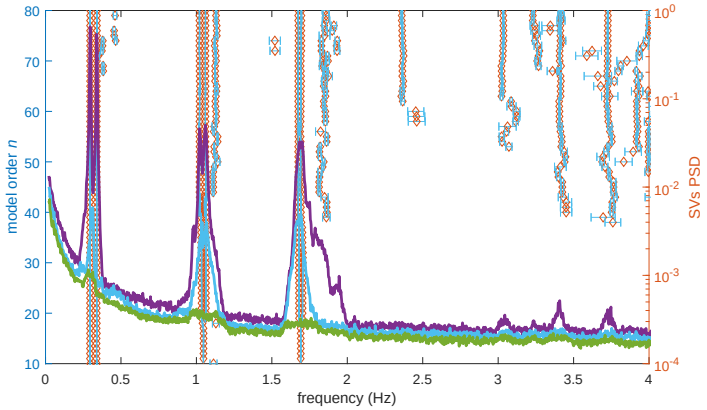

Figure 4.17: Stabilization diagram of natural frequencies of the meteorological mast with a threshold on a maximum deviations of natural frequency estimates.

Next, suppose that the distribution of the MPC can be approximated with a Gaussian, such as described in Section 4.2. Subsequently, the estimates of MPC and their variances are computed from the mode shapes corresponding to modes whose frequencies are depicted on Figure 4.17. Figure 4.18 illustrates the stabilization diagram rejecting the estimates that surpass the threshold of 2.5% defined on the standard deviations of the MPC.

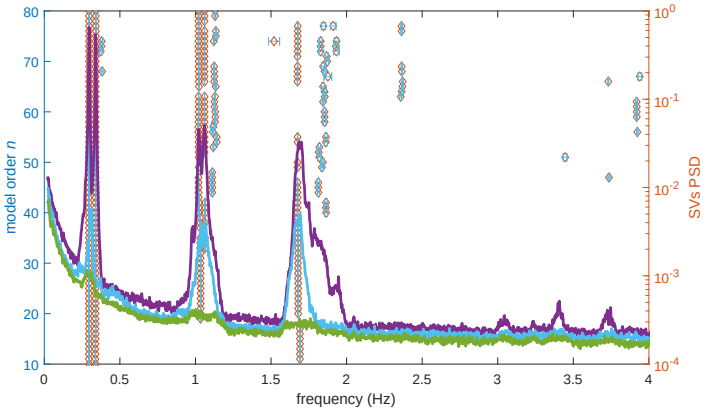

Figure 4.18: Stabilization diagram of natural frequencies of the meteorological mast with a threshold on a maximum deviations of MPC.

It can be observed that after introducing the threshold on the standard deviations of the MPC the modes which are corresponding to the higher order frequencies are discarded from the analysis.

The choice of the approximation framework is discussed based on three data sets of length $N_1 = 18000$, $N_2 = 36000$ and $N_3 = 432000$ and modal parameters estimated at a system order 60. An illustration of the real and imaginary components of the

mode shapes estimated from data set N_3 with their confidence intervals is presented on Figure 4.19.

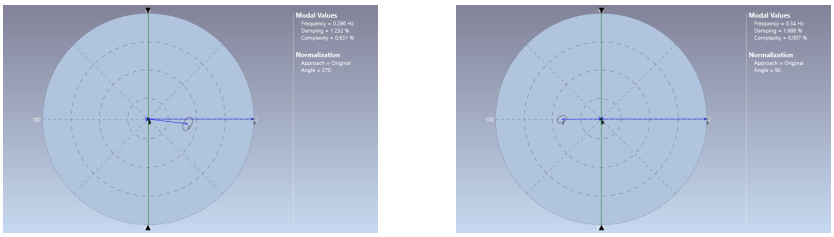

Figure 4.19: Plots of real and imaginary components of the first two mode shapes with their corresponding confidence ellipsoids estimated from data set N_3. Both plots from ARTeMIS Modal Pro 6.0.

It can be observed that the estimated components are aligned around one direction and their dispersion is very low. This indicates that their complexity is also low and consequently the underlying MPC estimates are in the vicinity of 1. Evaluation of the mode shape complexity requires confidence intervals computed either with the Gaussian or the quadratic approximations. Figure 4.22 and Figure 4.23 illustrate respectively the 95% and 99% confidence intervals computed with the Gaussian and the quadratic approximations for both MPC estimates of modes at 0.296Hz and 0.339Hz and the sample length N_1.

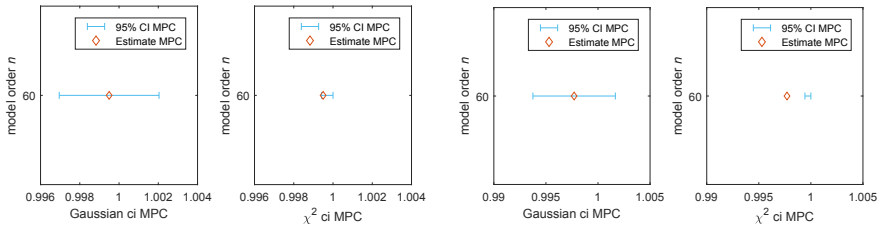

Figure 4.20: MPC_1 (left) and MPC_2 (right) with corresponding 95% confidence intervals. $N_1 = 18000$.

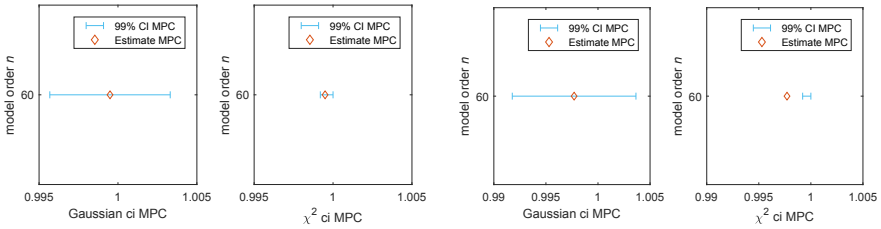

Figure 4.21: MPC_1 (left) and MPC_2 (right) with corresponding 99% confidence intervals. $N_1 = 18000$.

First, it can be observed that in each case the MPC estimates are close to 1. The

confidence bounds for the MPC corresponding to the first mode indicate that there is a probability that these estimates can be approximated both with Gaussian and quadratic distributions, since for both cases the estimates of the MPC are within the computed interval. The confidence bounds computed for the MPC corresponding to the second mode, however, suggest that this mode is most likely Gaussian. Before employing the scheme from Section 4.5 to compute the respective probabilities, the data set with more available samples is tested. Figure 4.20 and Figure 4.21 illustrate respectively the 95% and 99% confidence intervals computed with the Gaussian and the quadratic approximations for both MPC estimates of modes at 0.297Hz and 0.339Hz and the sample length N_3.

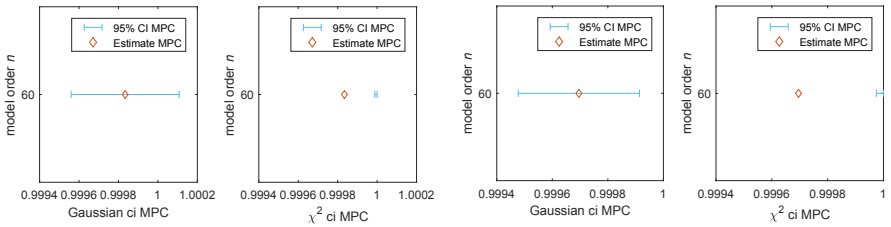

Figure 4.22: MPC_1 (left) and MPC_2 (right) with corresponding 95% confidence intervals. $N_3 = 432000$.

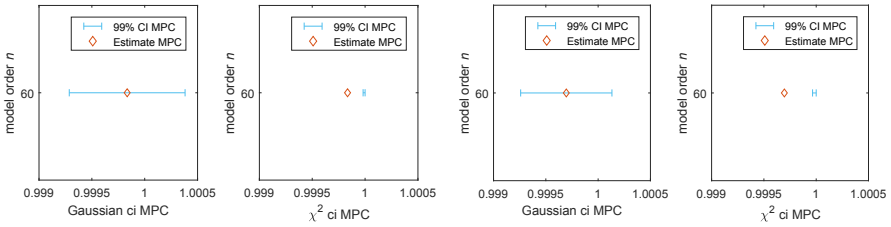

Figure 4.23: MPC_1 (left) and MPC_2 (right) with corresponding 99% confidence intervals. $N_3 = 432000$.

Here it can be observed that the MPC estimates are outside the confidence intervals computed with a quadratic approximation and most of the confidence bounds computed with the Gaussian approximation are well situated in the $(0, 1)$ interval. To establish a quantitative decision about the choice of the approximation framework, the scheme presented in Section 4.5 is used as illustrated on Figure 4.16. The probabilities p_G and p_Q are depicted in Table 4.1. They depend on both the number of samples $N_1 - N_3$, and the level of confidence α. Based on Table 4.1, it can be decided that the two identified mode shapes used for the computation of both MPC estimates are complex valued vectors and the Gaussian distribution is viable to approximate the theoretical distribution of these MPCs.

α	$\Pr^{N_1}$	MPC_1	MPC_2	$\Pr.^{N_2}$	MPC_1	MPC_2	$\Pr.^{N_3}$	MPC_1	MPC_2
95%	p_G	0.60	0.79	p_G	0.72	0.80	p_G	0.80	1
	p_Q	0.14	0	p_Q	0	0	p_Q	0	0
99%	p_G	0.57	0.69	p_G	0.64	0.70	p_G	0.70	0.97
	p_Q	0.37	0	p_Q	0	0	p_Q	0	0

Table 4.1: 95% and 99% level computation of p_G and p_Q using decision scheme of Section 4.5.

4.7 Conclusions

In this chapter we addressed the uncertainty quantification of Modal Phase Collinearity (MPC). For that two statistical frameworks were proposed, depending on the underlying complexity of the mode shape vectors used to compute the MPC. First, a classical Gaussian framework based on the first order Delta method was used to quantify the uncertainty of MPC estimates for complex valued mode shapes. Second, a quadratic framework based on the second order Delta method was used to quantify the uncertainty of MPC estimates for real valued mode shapes. For that case, it was proved that the MPC indicator yields a quadratic form which can be asymptotically approximated by a shifted and scaled χ^2 distribution. The statistical properties of that approximation such as lower and upper bound for its degrees of freedom and its centrality were also proved in the course of this chapter. The proposed approximations were tested on simulations of a chain system and some strategies for their numerical validation were developed and tested based on numerical Monte Carlo simulations. The real-life application of the Gaussian framework was deployed to the full-scale meteorological mast example and consisted of using the estimated variance of MPC as a practical modal indicator to remove the spurious modes from the stabilization diagram of natural frequencies.

4.8 Dissemination

Parts of this chapter have been published in [8, 9]:

[8] S. Gres, M. Döhler, P. Andersen, L. Mevel, Variance computation of MAC and MPC for real-valued mode shapes from the stabilization diagram, in: IOMAC - 8th International Operational Modal Analysis Conference, Copenhagen, Denmark, 2019.

[9] S. Greś, M. Döhler, P. Andersen, L. Mevel, Uncertainty quantification for the modal phase collinearity of complex mode shapes, Mechanical Systems and Signal Processing 152 (2021) 107436.

In addition, the algorithm for uncertainty quantification of MPC for a Gaussian case was implemented in ARTeMIS Modal Pro 6.0 [138].

CHAPTER 5

Uncertainty quantification of Modal Assurance Criterion

In this chapter, a framework to quantify the uncertainty of Modal Assurance Criterion (MAC) is developed. That can be used in a structural design validation to classify whether the mode shape estimates correspond to the same theoretical or estimated mode.

First, different statistical characteristics of estimates of the MAC indicator are observed, which leads to two different frameworks to quantify its uncertainty. The classical Gaussian framework is used to quantify the uncertainty of the MAC computed between the estimates of different mode shapes. The quadratic framework is proposed when the MAC estimates approach their theoretical bounds, namely 0 or 1. That takes places e.g. when the MAC is computed between an exact mode shape from a Finite Element (FE) model and its equivalent estimated from the data. The proposed frameworks are validated numerically, based on the strategy developed in the previous chapter and tested on a experimental example.

In short, this chapter comprises

- illustrative example depicting different empirical distributions of the MAC indicator,
- development of a classic Gaussian approximation of the MAC computed between different mode shape estimates,
- development of a novel approach to approximate a distribution of the MAC computed between an exact mode shape from a Finite Element (FE) model and its equivalent estimated from the data.
- development of a framework to classify whether the mode shape estimates correspond to the same theoretical or estimated mode, based on the confidence intervals of the MAC indicator,
- application of the proposed approach on a real example of an experimental plate.

5.1 Illustrative example

To recall, the MAC computed between two complex valued mode shapes vectors φ and ψ writes

$$g_{mac}(\varphi,\psi) = \frac{|\varphi^H\psi|^2}{\varphi^H\varphi\psi^H\psi} = \frac{\varphi^H\psi\psi^H\varphi}{\varphi^H\varphi\psi^H\psi}. \tag{5.1}$$

For the purpose of this chapter, two general cases of the MAC computation are distinguished, namely

1. $g_{mac}(\hat{\varphi},\hat{\psi})$ where $\hat{\varphi}$ and $\hat{\psi}$ are estimates of two different mode shapes,
2. $g_{mac}(\hat{\varphi},\psi_*)$ where $\hat{\varphi}$ is estimated from the data and ψ_* is an exact mode shape from a model.

The MAC is a data-based indicator with statistical properties. As such, computing it multiple times from independent data sets will yield a histogram approaching the statistical distribution of the MAC. To illustrate it consider a numerical simulation of a 6 DOF chain-like system that, for any consistent set of units, is modeled with a spring stiffness $k_1 = k_3 = k_5 = 100$ and $k_2 = k_4 = k_6 = 200$, mass $m_{1-6} = 1/20$ and a proportional modal damping matrix. The system is excited by a white noise signal in all DOFs and sampled with a frequency of 50Hz for a duration of 2000 seconds. The responses are measured at DOFs numbered 1, 2 and 5. A Gaussian white noise corresponding to 5% of the standard deviation of the output is added to the response at each channel. The computations are performed in a Monte Carlo procedure with $m = 1000$ simulations. Both the SSI-UPC and the variance computation for this algorithm are set up with a system order of 12, time lags of 15 and 200 blocks for the covariance computation of the data Hankel matrix. Six modes are selected in each simulation. The MAC values computed between the mode shapes estimated at model order 12 from one arbitrary data set are depicted on Figure 5.1.

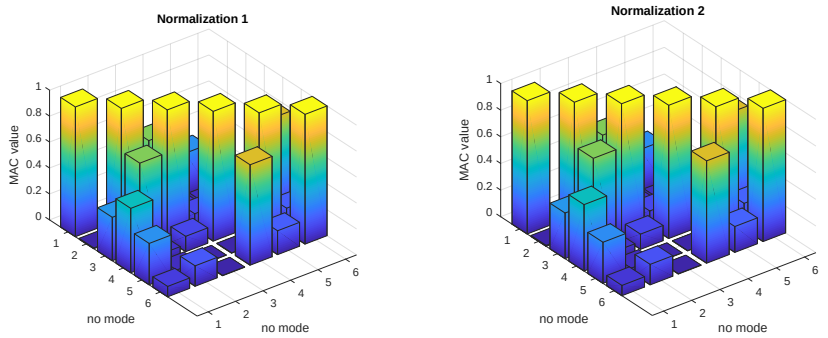

Figure 5.1: MAC values computed for one simulation. Normalization scheme 1 (left) and normalization scheme 2 (right).

As expected, the MAC computed by confronting a mode shape to itself is one. This is represented by the values in the diagonal of Figure 5.1. Denote MAC_{ij} as the MAC computed between i-th and j-th mode shape estimate. Figure 5.2 and Figure

5.3 illustrate four different distributions of the MAC estimates obtained by plotting the respective Monte Carlo simulations.

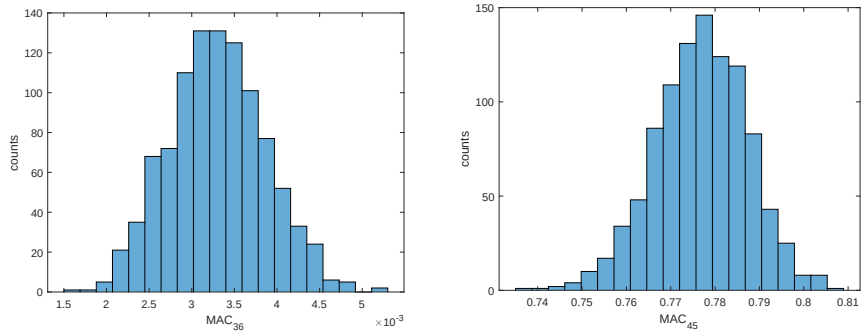

Figure 5.2: Histogram of $g_{mac}(\hat{\varphi}, \hat{\psi})$ computed between two modes from a single model order n- MAC_{36} (left) and MAC_{45} (right).

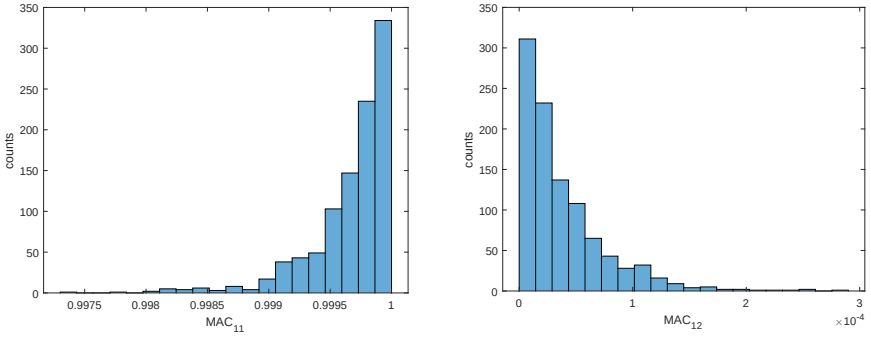

Figure 5.3: Histogram of $g_{mac}(\hat{\varphi}, \psi_*)$ computed between the exact mode shape of first mode from the model and its estimated counterpart- MAC_{11} (left). Histogram of $g_{mac}(\hat{\varphi}, \psi_*)$ computed between two orthogonal mode shapes: exact mode shape of first mode from the model and the estimate of the second mode shape- MAC_{12} (right).

The histograms of MAC_{36}, MAC_{45}, MAC_{11} and MAC_{12} depicted on Figure 5.2 and Figure 5.3 illustrate four distinctively different cases for the MAC distribution (2 Gaussian examples, and 2 distributions resembling a χ^2 shape: one skewed to the left and one skewed to the right). The distribution skewed to the right on the left part of Figure 5.3 refers to the MAC computed between two collinear mode shapes and the distribution skewed to the right refers to the case when the mode shapes are orthogonal. It can be seen that the distribution of MAC appears to be Gaussian in the most simple case and tends to a more skewed distribution when the MAC value gets closer to the border of the MAC interval. Those examples are denoted as base-case examples and will be referred to as such throughout the course of this chapter.

5.2 Gaussian approximation of the MAC distribution

This section is devoted to the simple and classical case of Gaussian approximation for the MAC distribution. This corresponds to the case where two different mode shapes are compared. First, a classical method for Gaussian approximation is recalled. Second, the Gaussian approximation of MAC is formulated. Third, the theoretical result are validated with numerical Monte Carlo simulations.

5.2.1 Delta method for variance estimation of MAC

Assuming that $\hat{\varphi}$ and $\hat{\psi}$ are asymptotically Gaussian variables, the Delta method can be applied to the function $g_{mac}(\hat{\varphi},\hat{\psi})$. The first order perturbation of $g_{mac}(\hat{\varphi},\hat{\psi})$ writes as

$$\Delta g_{mac}(\hat{\varphi},\hat{\psi}) = \hat{\mathcal{J}}^{g_{mac}}_{\hat{\varphi},\hat{\psi}} \begin{bmatrix} \Delta\Re(\hat{\varphi}) \\ \Delta\Im(\hat{\varphi}) \\ \Delta\Re(\hat{\psi}) \\ \Delta\Im(\hat{\psi}) \end{bmatrix} , \tag{5.2}$$

where the Jacobian estimate $\hat{\mathcal{J}}^{g_{mac}}_{\hat{\varphi},\hat{\psi}}$ tends to the the asymptotic Jacobian $\mathcal{J}^{g_{mac}}_{\varphi_*,\psi_*}$. Considering that $\hat{\mathcal{J}}^{g_{mac}}_{\hat{\varphi},\hat{\psi}} \approx \mathcal{J}^{g_{mac}}_{\varphi_*,\psi_*}$ and the joint asymptotic covariance of the mode shapes $\Sigma_{\hat{\varphi},\hat{\psi}} \approx \Sigma_{\varphi_*,\psi_*}$, the covariance of $g_{mac}(\hat{\varphi},\hat{\psi})$, $\Sigma_{g_{mac}(\hat{\varphi},\hat{\psi})}$, is expressed as

$$\begin{aligned} \Sigma_{g_{mac}(\hat{\varphi},\hat{\psi})} &= \mathrm{E}\left(\Delta g_{mac}(\hat{\varphi},\hat{\psi})\Delta g_{mac}(\hat{\varphi},\hat{\psi})^T\right) \approx \hat{\mathcal{J}}^{g_{mac}}_{\hat{\varphi},\hat{\psi}} \Sigma_{\hat{\varphi},\hat{\psi}} (\hat{\mathcal{J}}^{g_{mac}}_{\hat{\varphi},\hat{\psi}})^T \\ &\approx \mathcal{J}^{g_{mac}}_{\varphi_*,\psi_*} \Sigma_{\varphi_*,\psi_*} (\mathcal{J}^{g_{mac}}_{\varphi_*,\psi_*})^T . \end{aligned}$$

Notice that here, g_{mac} being derived analytically, $\hat{\mathcal{J}}^{g_{mac}}_{\hat{\varphi},\hat{\psi}} = \mathcal{J}^{g_{mac}}_{\hat{\varphi},\hat{\psi}}$.

Remark 5.1 (Regarding variance of ψ_*) *Consider ψ_* as a mode shape computed from the finite element model. In that case, ψ_* is an exact mode shape and it has no uncertainty. Therefore the components of the derivatives of $g_{mac}(\hat{\varphi},\psi_*)$ corresponding to ψ_* can be disregarded since their corresponding variance components in $\Sigma_{g_{mac}(\hat{\varphi},\psi_*)}$ are null.*

5.2.2 Gaussian approximation

This section deals with the Gaussian approximation of $g_{mac}(\hat{\varphi},\hat{\psi})$. A consistent estimate of the Jacobian $\mathcal{J}^{g_{mac}}_{\varphi_*,\psi_*}$ can be written as follows

$$\mathcal{J}^{g_{mac}}_{\hat{\varphi},\hat{\psi}} \triangleq \left[\frac{\partial g_{mac}}{\partial\Re(\varphi)}(\hat{\varphi},\hat{\psi}) \quad \frac{\partial g_{mac}}{\partial\Im(\varphi)}(\hat{\varphi},\hat{\psi}) \quad \frac{\partial g_{mac}}{\partial\Re(\psi)}(\hat{\varphi},\hat{\psi}) \quad \frac{\partial g_{mac}}{\partial\Im(\psi)}(\hat{\varphi},\hat{\psi})\right] . \tag{5.3}$$

Its complete derivation can be found in Appendix C.1. The respective partial derivatives of the MAC with respect to the real and imaginary parts of the mode shapes write as

$$\frac{\partial g_{mac}}{\partial\Re(\varphi)}(\varphi,\psi) = \frac{2\Re(\psi\psi^H\varphi)^T}{\varphi^H\varphi\psi^H\psi} - \frac{2\Re(\varphi)^T g_{mac}(\varphi,\psi)}{\varphi^H\varphi} , \tag{5.4}$$

$$\frac{\partial g_{mac}}{\partial\Im(\varphi)}(\varphi,\psi) = \frac{2\Im(\psi\psi^H\varphi)^T}{\varphi^H\varphi\psi^H\psi} - \frac{2\Im(\varphi)^T g_{mac}(\varphi,\psi)}{\varphi^H\varphi} \tag{5.5}$$

and

$$\frac{\partial g_{mac}}{\partial \Re(\psi)}(\varphi,\psi) = \frac{2\Re(\varphi\varphi^H\psi)^T}{\varphi^H\varphi\psi^H\psi} - \frac{2\Re(\psi)^T g_{mac}(\varphi,\psi)}{\psi^H\psi} \ , \tag{5.6}$$

$$\frac{\partial g_{mac}}{\partial \Im(\psi)}(\varphi,\psi) = \frac{2\Im(\varphi\varphi^H\psi)^T}{\varphi^H\varphi\psi^H\psi} - \frac{2\Im(\psi)^T g_{mac}(\varphi,\psi)}{\psi^H\psi} \ . \tag{5.7}$$

To approximate estimates of MAC with a Gaussian distribution, the partial derivatives (5.4)-(5.7) must be non-zero. That is summarized in the following Lemma.

Lemma 5.2 *The necessary and sufficient conditions for the partial derivatives* (5.4)-(5.7) *to be different from zero are*

$$\forall \varphi_*, \psi_* \in \mathbb{C}^r \ \mathcal{J}^{g_{mac}}_{\varphi_*,\psi_*} \neq 0 \Leftrightarrow g_{mac}(\varphi_*,\psi_*) \neq \{0,1\} \ .$$

Proof: See Appendix C.2. □

Consequently, the Gaussian approximation of the MAC writes as follows.

Lemma 5.3 *Assuming that* $g_{mac}(\varphi_*,\psi_*) \neq \{0,1\}$ *and that both mode shapes are jointly Gaussian*

$$\sqrt{N}\left(\begin{bmatrix}\Re(\hat{\varphi})\\ \Im(\hat{\varphi})\\ \Re(\hat{\psi})\\ \Im(\hat{\psi})\end{bmatrix} - \begin{bmatrix}\Re(\varphi_*)\\ \Im(\varphi_*)\\ \Re(\psi_*)\\ \Im(\psi_*)\end{bmatrix}\right) \xrightarrow{\mathcal{L}} \mathcal{N}(0,\Sigma_{\varphi_*,\psi_*}) \ .$$

$g_{mac}(\hat{\varphi},\hat{\psi})$ follows a Gaussian distribution such that

$$\sqrt{N}\left(g_{mac}(\hat{\varphi},\hat{\psi}) - g_{mac}(\varphi_*,\psi_*)\right) \xrightarrow{\mathcal{L}} \mathcal{N}\left(0, \mathcal{J}^{g_{mac}}_{\varphi_*,\psi_*}\Sigma_{\varphi_*,\psi_*}\mathcal{J}^{g_{mac}\,T}_{\varphi_*,\psi_*}\right) \ . \tag{5.8}$$

The estimate of the covariance of $g_{mac}(\hat{\varphi},\hat{\psi})$ writes as

$$\Sigma_{g_{mac}(\hat{\varphi},\hat{\psi})} = \mathcal{J}^{g_{mac}}_{\hat{\varphi},\hat{\psi}}\Sigma_{\hat{\varphi},\hat{\psi}}(\mathcal{J}^{g_{mac}}_{\hat{\varphi},\hat{\psi}})^T \ ,$$

where $\mathcal{J}^{g_{mac}}_{\hat{\varphi},\hat{\psi}} \approx \mathcal{J}^{g_{mac}}_{\varphi_*,\psi_*}$ and $\Sigma_{g_{mac}(\hat{\varphi},\hat{\psi})} \approx \Sigma_{g_{mac}(\varphi_*,\psi_*)}$.

5.2.3 Gaussian approximation validation

In this section a strategy to validate the Gaussian approximation from Lemma 5.3 is devised and applied to estimates of MAC_{36} and MAC_{45}. The following strategy is equivalent to one defined for the MPC in Section 4.2.3.

First consider the Monte Carlo simulations, from which the histogram of MAC estimates is derived based on the estimates of two mode shapes. Denote $\text{MAC}_{MC} \in \mathbb{R}^{m\times 1}$ as the vector of all MAC estimates from all m Monte Carlo simulations. From the histogram, it is straightforward to infer and compute μ_{MC} as its mean and $\sigma_{MC} = \sqrt{\text{var}(\text{MAC}_{MC})}$ as its standard deviation, where var is a variance operator. Both terms are computed as sample means, also called the first two cumulants of the distribution. Considering the Gaussian assumption, both quantities are the only information needed to characterize the stochastic distribution of the considered MAC estimate. Next, let $\overline{\text{MAC}}_{MC}$ be the normalized MAC_{MC}, such that

$$\overline{\text{MAC}}_{MC} = \left(\text{MAC}_{MC} - \mu_{MC}\right)/\sigma_{MC} \ . \tag{5.9}$$

Based on the Monte Carlo independence assumption and its expected Gaussian properties, the vector $\overline{\mathrm{MAC}}_{MC}$ should yield a histogram of the standard Gaussian distribution $\mathcal{N}(0,1)$. Now, consider the computation of variance estimates using the perturbation theory, and denote $\sigma_{PT} \in \mathbb{R}^{m\times 1}$ the vector of all standard deviations computed as in Lemma 5.3, where each component of σ_{PT} is the proposed standard deviation estimate $\sigma_{PT,j}$ based solely on the j-th data set. Then, for $j = 1 \dots m$, define

$$\overline{\mathrm{MAC}}_{PT,j} = \left(\mathrm{MAC}_{MC,j} - \mu_{MC}\right) / \sigma_{PT,j} \tag{5.10}$$

as MAC estimate normalized by parameters computed with the perturbation theory. Based on the Gaussian assumption and the hypothesis that $\sigma_{PT,j}$ is a good estimate of $\mathrm{MAC}_{MC,j}$ variance, $\overline{\mathrm{MAC}}_{PT,j}$ should be a realization of a standard normal distribution $\mathcal{N}(0,1)$. Since all MACs are computed on independent data sets, the collection of all $\overline{\mathrm{MAC}}_{PT,j}$, namely $\overline{\mathrm{MAC}}_{PT} \in \mathbb{R}^{m\times 1}$, should yield a histogram of the Gaussian distribution. Such histograms of MAC_{36} and MAC_{45} estimates along with the CDF of $\overline{\mathrm{MAC}}_{MC}$ and $\mathcal{N}(0,1)$, are presented on Figure 5.4 and Figure 5.5. As expected, the plots illustrate that entries of $\overline{\mathrm{MAC}}_{PT}$ and $\overline{\mathrm{MAC}}_{MC}$ follow $\mathcal{N}(0,1)$ well.

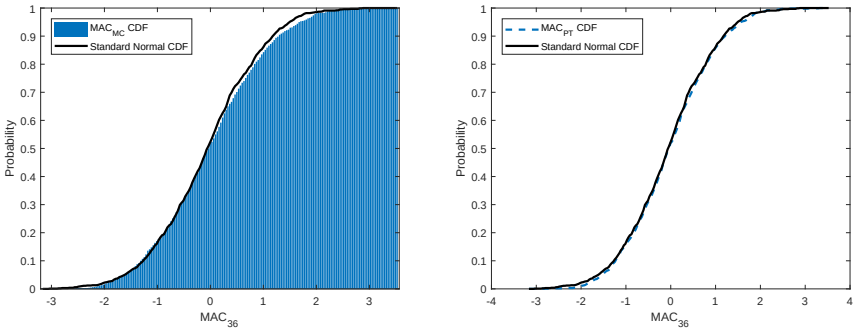

Figure 5.4: CDF of MAC_{MC} (left) and MAC_{PT} (right) computed for MAC_{36}.

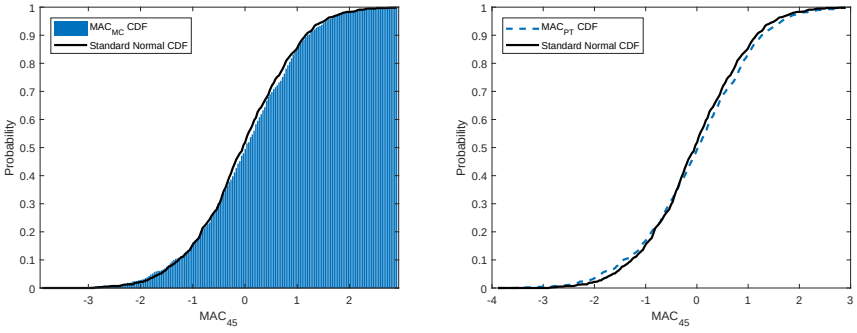

Figure 5.5: CDF of MAC_{MC} (left) and MAC_{PT} (right) computed for MAC_{45}.

Uncertainty is in practice quantified by confidence intervals thus a scheme to

compare the approximated and theoretical confidence intervals is devised. For that define the theoretical two-sided normal cumulative confidence interval (CCI) function as $f_{t,cci} = 2(f_{t,cdf} - 0.5)$, where $f_{t,cdf}(t)$ is the function for the standard normal cumulative distribution and $f_{PT,cci}$ is the similarly defined cumulative function for computing two-sided confidence interval corresponding to $\overline{\text{MAC}}_{PT}$. Function $f_{t,cci}$ is purely theoretical, whereas $f_{PT,cci}$ is derived empirically from the histogram of $\overline{\text{MAC}}_{PT}$. A comparison of both $f_{t,cci}$ and $f_{PT,cci}$ for the MAC_{36} and MAC_{45} estimates is illustrated on Figure 5.6. As expected, both functions coincide well, yielding an accurate approximation of the confidence intervals of both MAC_{36} and MAC_{45} with a Gaussian law. Thus, the proposed characterization of the MAC indicator with a Gaussian law is indeed adequate for mode shapes that are neither collinear nor orthogonal.

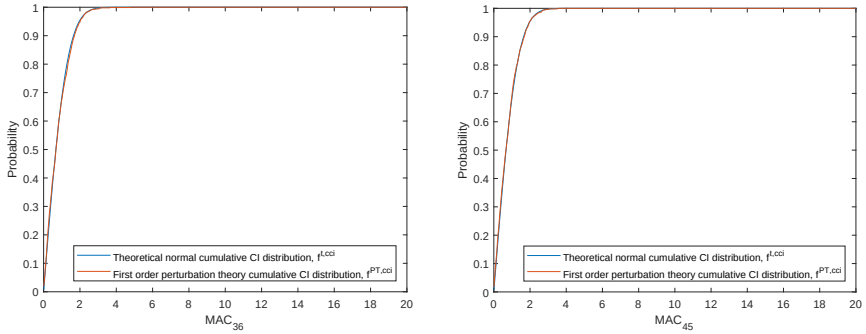

Figure 5.6: $f_{PT,cci}$ and $f_{t,cci}$ computed for MAC_{36} and MAC_{45}.

In practice, the framework proposed in this section is applied to assess uncertainty of one MAC estimate computed solely on a single data set. Until now, this section showed a comparison between the MC histogram and the perturbation-based histogram. Both histograms are mixing all information from all simulations. By proper normalization, it has been possible to compare them to the standard Gaussian Normal distribution, which reveals whether or not the entries of $\overline{\text{MAC}}_{PT}$ and $\overline{\text{MAC}}_{MC}$ are Gaussian and illustrates the dispersion in all the estimated parameters.

A scheme that quantifies the errors in the Gaussian approximation when using just a single data set is now recalled after Section 4.3.2. For each simulation j, assume that the computed standard deviation $\sigma_{PT,j}$ is a correct estimate of the desired σ_{MC}. Then, define a properly normalized vector $\overline{\text{MAC}}^j_{PT}$ as the collection of normalized $\text{MAC}_{MC,k}$ such that $\overline{\text{MAC}}^j_{PT,k} = \left(\text{MAC}_{MC,k} - \mu_{MC}\right)/\sigma_{PT,j}$. Under the Gaussian approximation the histogram derived from $\overline{\text{MAC}}^j_{PT}$ should be close to the histogram of the standard Gaussian distribution. Such closeness can be calculated by classical Pearson Goodness of Fit test, which is defined as

$$P_{\chi^2} = \sum_{i=1}^{b_n} \frac{(O_i - E_i)^2}{E_i} \ , \tag{5.11}$$

where O_i are observations of $\overline{\text{MAC}}^j_{PT}$ within each i-th interval, E_i are counts corresponding to a theoretical $\mathcal{N}(0,1)$ distribution and b_n denotes a number of intervals

used. As such, median, best and worst quantiles of the Pearson statistics can be derived from the approximate histogram of its distribution. Best and worst cases are defined as the 2.5% and 97.5% quantiles of the distribution of P_{χ^2}. The CDFs of the best, the median and the worst quantiles among all $\overline{\text{MAC}}^k PT$ are plotted in the left parts of Figure 5.7 and Figure 5.8 for MAC_{36} and MAC_{45} respectively. The distribution of P_{χ^2} and corresponding marks of the best and the worst fits cases respectively for MAC_{36} and MAC_{45} are displayed on the right parts of Figure 5.7 and 5.8.

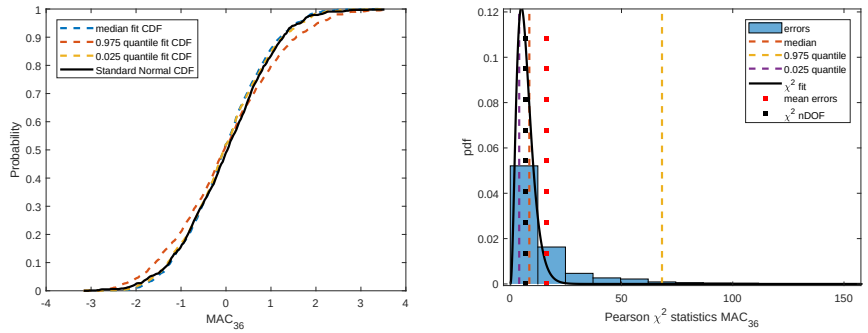

Figure 5.7: Gaussian fits to empirical CDF of MAC_{36} (left) based on median, 0.95 and 0.025 quantiles of Pearson χ^2 statistics. Histogram of Pearson χ^2 statistics with corresponding cases of Gaussian fits to MAC_{36} (right).

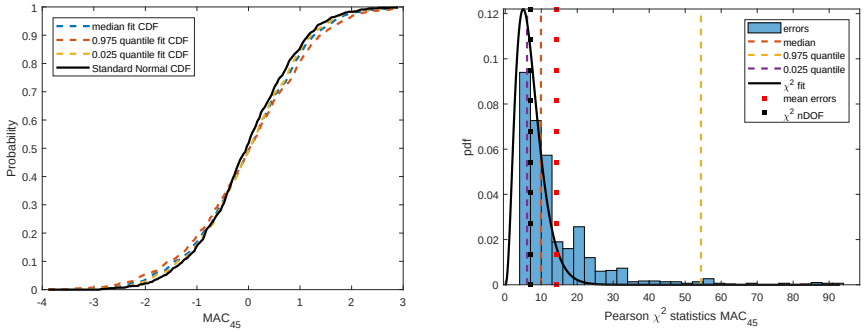

Figure 5.8: Gaussian fits to empirical CDF of MAC_{45} (left) based on median, 0.95 and 0.025 quantiles of Pearson χ^2 statistics. Histogram of Pearson χ^2 statistics with corresponding cases of Gaussian fits to MAC_{45} (right).

Both Figure 5.7 and Figure 5.8 illustrate the performance of the Gaussian approximation for the estimates of MAC_{36} and MAC_{45}. The respective fits to a standard normal CDF show almost a total equivalence even for the worst quantile (97.5%), truly showing the Gaussian characterization of both MACs.

To conclude this section the median, the best and the worst Gaussian fits to all the base-case MACs are illustrated on Figure 5.9 and Figure 5.10.

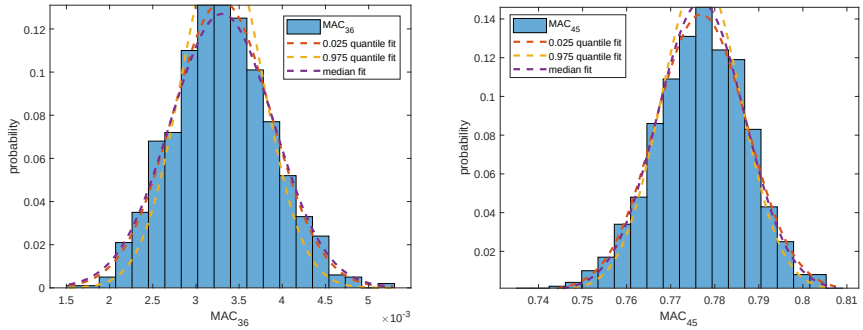

Figure 5.9: Gaussian fits to empirical probability distribution of MAC_{36} and MAC_{45} based on median, 0.95 and 0.025 quantiles of Pearson χ^2 statistics.

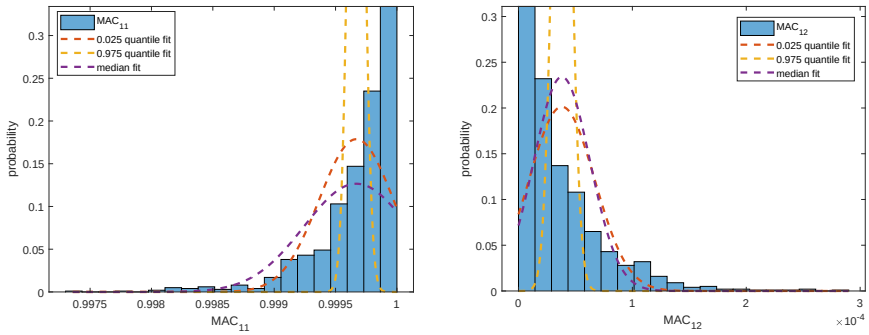

Figure 5.10: Gaussian fits to empirical probability distribution of MAC_{11} and MAC_{12} based on median, 0.95 and 0.025 quantiles of Pearson χ^2 statistics.

Figure 5.9 shows that the Gaussian approximation is good for MAC_{36} (left) and MAC_{45} (right), whereas being inadequate for MAC_{11} (left) and MAC_{12} (right), which is expected from the inspection of the histograms on Figure 5.10. This section is concluded with a study of the behavior of $g_{mac}(\hat{\varphi}, \hat{\psi})$ when the number of samples increases.

5.2.4 Influence of sample length on distribution of $g_{mac}(\hat{\varphi}, \hat{\psi})$: a Gaussian case

The results presented so far were computed for a single data set of length N which is the situation when using such framework for uncertainty quantification in real-life applications. This framework is statistically proved to be adequate for large sample size, due to the theoretical properties of the CLT. Whether it holds for some relatively small data lengths has to be investigated. Analyzing results computed on increasing data lengths provide arguments for deploying it in practice. For that purpose, some quantities derived from the Monte Carlo simulations of the cross MAC are introduced. Let $MAC_{MC,i} \in \mathbb{R}^{m \times 1}$ denote a vector of i-th MAC between different mode shapes

computed for m Monte Carlo simulations, where $i = 1 \dots 30$. Define its empirical standard deviation as

$$\sigma_{\mathrm{MAC_{MC,i}}} = \sqrt{\mathrm{var}\left(\mathrm{MAC_{MC,i}}\right)} \,, \tag{5.12}$$

where $\mathrm{var}\left(\mathrm{MAC_{MC,i}}\right)$ denotes the empirical variance of the i-th MAC from the Monte Carlo histogram. To capture the worst case behavior of the standard deviation computed for all the MAC values, the $\sigma_{\mathrm{MAC_{MC,i}}}$ are summed such that

$$\begin{aligned} \overline{\sigma}_{\mathrm{MAC_{MC}}} &= \sum_{i=1}^{30} \sigma_{\mathrm{MAC_{MC,i}}} \,, \\ \alpha_{\mathrm{MAC_{MC}}} &= \overline{\sigma}_{\mathrm{MAC_{MC}}} \sqrt{N} \,, \end{aligned} \tag{5.13}$$

and constant $\alpha_{\mathrm{MAC_{MC}}}$ denotes the sum of the standard deviations. Now, recall that the proposed perturbation approach computes the variance of the MAC for a single realization j. To mimic the quantities formulated in (5.12) and (5.13), let $\sigma_{\mathrm{MAC_{PT,i}}} \in \mathbb{R}^{m \times 1}$ denote the vector of the standard deviations computed with the perturbation theory for the i-th MAC and $\sigma_{\mathrm{MAC_{PTj,i}}}$ label its j-th realization. The mean standard deviation of the i-th MAC from the perturbation theory writes

$$\overline{\sigma}_{\mathrm{MAC_{PT,i}}} = \frac{1}{m} \sum_{j=1}^{m} \sigma_{\mathrm{MAC_{PTj,i}}} \tag{5.14}$$

and its sum yields

$$\overline{\sigma}_{\mathrm{MAC_{PT}}} = \sum_{i=1}^{30} \overline{\sigma}_{\mathrm{MAC_{PT,i}}} \tag{5.15}$$

$$\alpha_{\mathrm{MAC_{PT}}} = \overline{\sigma}_{\mathrm{MAC_{PT}}} \sqrt{N} \,, \tag{5.16}$$

where $\alpha_{\mathrm{MAC_{PT}}}$ mimics $\alpha_{\mathrm{MAC_{MC}}}$ from (5.13). The histogram of the standard deviations of the i-th MAC is available by means of the Monte Carlo simulations. This histogram reflects the distribution of the i-th MAC, and its own variance can be computed. A sum over the number of computed MAC indicators yields

$$\sigma_{*\mathrm{MAC_{PT}}} = \sum_{i=1}^{30} \sqrt{\mathrm{var}\left(\sigma_{\mathrm{MAC_{PT,i}}}\right)} \,, \tag{5.17}$$

Analysis of the variables in (5.12)-(5.17) computed on data sets with a different sample lengths is depicted on Figure 5.11. First, the 'a' part of Figure 5.11 illustrates that the $\overline{\sigma}_{\mathrm{MAC_{MC}}}$ and $\overline{\sigma}_{\mathrm{MAC_{PT}}}$ are converging to zero. In addition, notice that there is no significant difference between the results obtained by computing the relevant statistics from the histogram based on the Monte Carlo simulations and the mean ones obtained from the perturbation theory. Second, the errors in the variance estimates of the MAC computed with the perturbation approach $\sigma_{*\mathrm{MAC_{PT}}}$ also converge to zero. This is presented in the 'b' part of Figure 5.11. The Coefficient of Variation (CV) $\sigma_{*\mathrm{MAC_{PT}}}/\overline{\sigma}_{\mathrm{MAC_{PT}}}$ computed using perturbation approach converges to a constant value of 5.2%, see 'd' part of Figure 5.11. The obtained value of CV is small and pleads for using the proposed framework, when only one measurement set is available. Finally, the 'c' part of Figure 5.11 illustrates that both $\overline{\sigma}_{\mathrm{MAC_{MC}}}$ and $\overline{\sigma}_{\mathrm{MAC_{PT}}}$ converge with a rate of $\sqrt{N}$ to a similar constant.

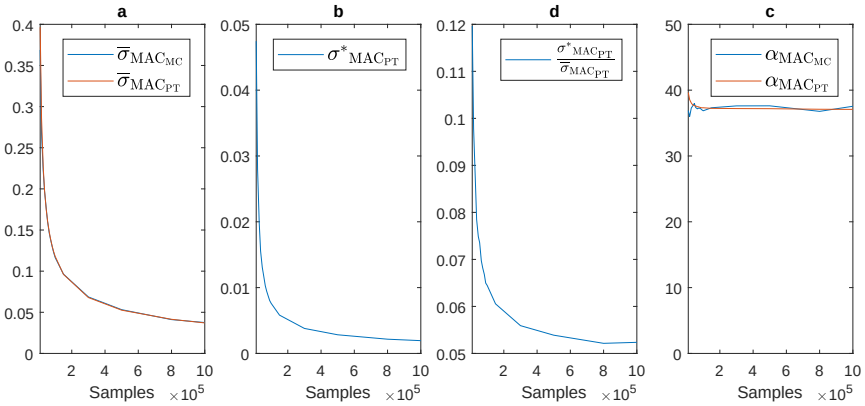

Figure 5.11: Sum of standard deviations of MAC from the Monte Carlo simulation and the mean perturbation theory depending on number of samples (a). Standard deviation of the sum of standard deviations of MAC from the Monte Carlo simulation and the mean perturbation theory (b). Coefficient of Variation of the summed perturbation theory-based standard deviations of the MAC (c). Sum of standard deviations of MAC from the Monte Carlo simulation and the mean perturbation theory scaled with a square root of corresponding data length (d). Normalization 1.

To contextualize the results presented on Figure 5.11 with respect to the validation schemes developed in Section 5.2.3, the median, best and worst Gaussian fits to the estimates of MAC_{36} and MAC_{45} are computed for two different sample lengths. That study is illustrated on Figure 5.12 and Figure 5.13.

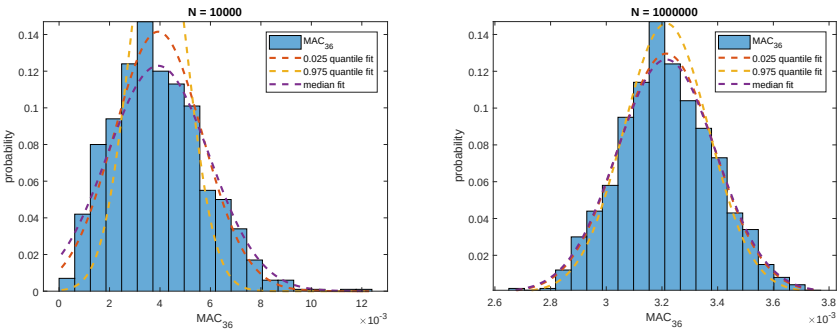

Figure 5.12: Gaussian fits to empirical probability distribution of MAC_{36} based on median, 0.95 and 0.025 quantiles of Pearson χ^2 statistics computed on data sets with different sample size.

As expected the Monte Carlo simulations and the corresponding Gaussian fits computed on the data set with a small sample size exhibit higher variance, and in general, less accurate distribution fits, than the data set generated with more samples. That is in good agreement with Figure 5.11 and it concludes the Gaussian approximation section.

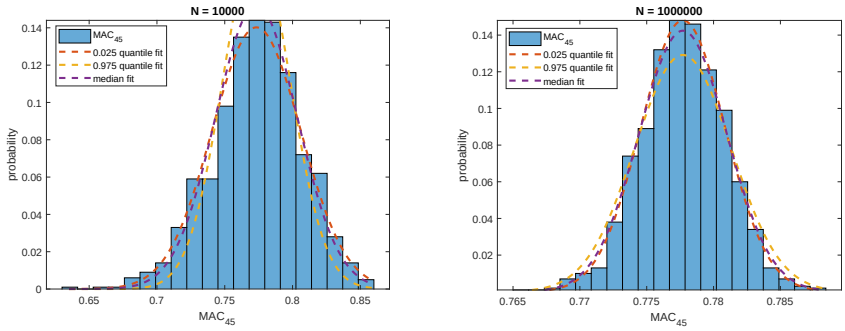

Figure 5.13: Gaussian fits to empirical probability distribution of MAC_{45} based on median, 0.95 and 0.025 quantiles of Pearson χ^2 statistics computed on data sets with different sample size.

5.3 Quadratic approximation of $g_{mac}(\hat{\varphi}, \psi_*)$

This section considers quadratic approximation of the MAC distribution, when it is computed between an exact mode shape from the model and its counterpart estimated from data, namely $g_{mac}(\hat{\varphi}, \psi_*)$. The quadratic approximation applies when the Jacobian (5.3) is null, which, as shown in Lemma 5.2, holds for the cases when $g_{mac}(\varphi_*, \psi_*) = \{0, 1\}$. The following problem and a chosen solution is similar to the one developed in Chapter 4 for the MPC indicator.

Let $g_{mac}(\varphi, \psi)$ be twice differentiable in φ_* and ψ_*. The second order Taylor expansion of $g_{mac}(\hat{\varphi}, \psi_*)$ writes as

$$g_{mac}(\hat{\varphi}, \psi_*) = g_{mac}(\varphi_*, \psi_*) + \hat{X}^T \mathrm{H}_{\varphi_*}^{g_{mac}}/2 \; \hat{X} + o(||\hat{X}||^2) \; , \tag{5.18}$$

where $\hat{X} = \begin{bmatrix} \Re(\hat{\varphi} - \varphi_*)^T & \Im(\hat{\varphi} - \varphi_*)^T \end{bmatrix}^T$ and the Hessian $\mathrm{H}_{\varphi_*}^{g_{mac}}/2 = \tilde{\mathrm{H}}_{\varphi_*}^{g_{mac}} \in \mathbb{R}^{2r \times 2r}$. Also, recall that when N tends to infinity the $\sqrt{N}\hat{X} = \hat{X}_{\mathcal{N}} \to X_{\mathcal{N}}$ which is a Gaussian $\mathcal{N}(0, \Sigma_{\varphi_*})$. The asymptotic properties of $g_{mac}(\hat{\varphi}, \hat{\psi})$ follows

$$N(g_{mac}(\hat{\varphi}, \psi_*) - g_{mac}(\varphi_*, \psi_*)) \approx \hat{X}_{\mathcal{N}}^T \tilde{\mathrm{H}}_{\varphi_*}^{g_{mac}} \hat{X}_{\mathcal{N}} \approx {X_{\mathcal{N}}}^T \tilde{\mathrm{H}}_{\varphi_*}^{g_{mac}} X_{\mathcal{N}} \; . \tag{5.19}$$

The terms in (5.19) suggest that $N(g_{mac}(\hat{\varphi}, \psi_*) - g_{mac}(\varphi_*, \psi_*))$ is asymptotically approximated by a quadratic form whose distribution can be complicated to determine. This chapter utilizes a recent χ^2 approximation using a scaled χ^2 [84] distribution, which was already deployed for the approximation of the quadratic form of the MPC in Section 4.3. Similar to the MPC, in order to use such approximation the matrix $\tilde{\mathrm{H}}_{\varphi_*}^{g_{mac}}$ must be positive semi-definite.

5.3.1 Approximation of the quadratic form

To establish an approximate distribution of the quadratic form in (5.19) first rewrite (5.19) to

$$Q(\hat{X}_{\mathcal{N}}) = \hat{X}_{\mathcal{N}}^T \tilde{\mathrm{H}}_{\hat{\varphi}}^{g_{mac}} \hat{X}_{\mathcal{N}} \approx X_{\mathcal{N}}^T \tilde{\mathrm{H}}_{\varphi_*}^{g_{mac}} X_{\mathcal{N}} \approx N \left(g_{mac}(\hat{\varphi}, \psi_*) - g_{mac}(\varphi_*, \psi_*) \right) \; . \tag{5.20}$$

Temporarily assume that the $\tilde{\mathrm{H}}_{\varphi_*}^{g_{mac}}$ is a positive semi-definite matrix. The distribution of the quadratic form can be approximated, after [84], with a scaled $\chi^2_{l_{PT}}$ distribution

with l_{PT} degrees of freedom. The approximate probability distribution function of $Q(\hat{X}_{\mathcal{N}})$ writes

$$f_Q(y) = \frac{1}{\alpha} f_{\chi^2_{l_{PT}}} \left(\frac{y-\beta}{\alpha} \right) , \tag{5.21}$$

where $y \in [\beta, +\infty]$ and $f_Q(y) = 0$ for $y < \beta$. The respective scaling and shift parameters α and β are defined such that $\alpha = \sigma_Q / \sigma_{\chi^2}$ and $\beta = \mu_Q - (\mu_{\chi^2} \sigma_Q)/\sigma_{\chi^2}$. The mean μ_Q and standard deviation σ_Q of the quadratic form are computed using its asymptotic cumulants, c_1 and c_2, namely $\mu_Q = c_1$ and $\sigma_Q = \sqrt{2c_2}$, where the k-th asymptotic cumulant of $Q(\hat{X}_{\mathcal{N}})$ writes as

$$c_k = \mathrm{tr} \left((\tilde{\mathrm{H}}^{g_{mac}}_{\varphi_*} \Sigma_{\varphi_*})^k \right) . \tag{5.22}$$

The mean μ_{χ^2} and standard deviation σ_{χ^2} of the approximating $\chi^2_{l_{PT}}$ distribution are computed from its number of degrees of freedom l_{PT}, such that $\mu_{\chi^2} = l_{PT}$ and $\sigma_{\chi^2} = \sqrt{2 l_{PT}}$, where $l_{PT} = c_2^3 / c_3^2$.

Corollary 5.4 *Since the quadratic form of MAC is available for $g_{mac}(\varphi_*, \psi_*) = \{0, 1\}$, two cases for approximating its distribution can be distinguished. The first case considers $g_{mac}(\varphi_*, \psi_*) = 1$ and represents two collinear mode shapes namely $\varphi_* = k \cdot \psi_*$. The second case considers $g_{mac}(\varphi_*, \psi_*) = 0$ which corresponds to orthogonal mode shapes $\varphi_*^H \psi_* = 0$. Each case is represented by a different Hessian matrix; the collinear one by $\mathrm{H}^{g_{mac},\mathrm{collinear}}_{\varphi_*}$ and the orthogonal one by $\mathrm{H}^{g_{mac},\mathrm{orthogonal}}_{\varphi_*}$.*

A general formulation for the estimate of the Hessian of $g_{mac}(\hat{\varphi}, \psi_*)$ writes as

$$\mathrm{H}^{g_{mac}}_{\hat{\varphi}} = \begin{bmatrix} \frac{\partial^2 g_{mac}}{\partial \Re(\varphi) \partial \Re(\varphi)} & \frac{\partial^2 g_{mac}}{\partial \Im(\varphi) \partial \Re(\varphi)} \\ \frac{\partial^2 g_{mac}}{\partial \Re(\varphi) \partial \Im(\varphi)} & \frac{\partial^2 g_{mac}}{\partial \Im(\varphi) \partial \Im(\varphi)} \end{bmatrix} . \tag{5.23}$$

Lemma 5.5 *The $\chi^2_{l_{PT,j}}$ distribution used to approximate the distribution of $Q(\hat{X}_{\mathcal{N}})$ (5.20) has $l_{PT,j}$ degrees of freedom that are bounded between $1 \leq l_{PT,j} \leq r-1$ for all j.*

Corollary 5.6 *The $\chi^2_{l_{MC}}$ distribution used to approximate the distribution of the Monte Carlo histogram of all $N(g_{mac}(\hat{\varphi}, \psi_*) - g_{mac}(\varphi_*, \psi_*))$ realizations is assumed to have l_{MC} degrees of freedom that are bounded between $1 \leq l_{MC} \leq r-1$*

5.3.2 Approximation of MAC distribution on the boundary

In this section, the two special cases from Corollary 5.4 are considered, first when the estimated mode shape is collinear and second when the estimated mode shape is orthogonal to the numerical mode shape. In both cases, to apply the aforementioned theory the respective Hessian matrices are analytically developed and their rank is studied.

5.3.2.1 Formulation of the Hessian matrix for collinear mode shapes

The objective of this section is the study of the quadratic form in the case of collinearity between an estimated mode shape and a numerical mode shape. First the Hessian is developed. To simplify the notation of the derivatives define matrices

$$\begin{aligned} M_{xx}^* &= \Re(\psi_*)\Re(\psi_*)^T, \quad M_{yy}^* = \Im(\psi_*)\Im(\psi_*)^T \ , \\ M_{xy}^* &= \Re(\psi_*)\Im(\psi_*)^T, \quad M_{yx}^* = \Im(\psi_*)\Re(\psi_*)^T \ . \end{aligned} \tag{5.24}$$

and scalars $d_* = \psi_*^H \psi_*$ and $e_* = \varphi_*^H \varphi_*$. The derivation of the respective partial derivatives that form a theoretical Hessian (5.23) is enclosed in Appendix C.3. The Hessian is assembled with the derivatives evaluated for the case when $\varphi_* = k \cdot \psi_*$, namely (C.28), (C.31), (C.36), (C.39). Using the simplified notation introduced above, the Hessian (5.23) writes as

$$\mathrm{H}_{\varphi_*}^{g_{mac},\mathrm{collinear}} = \frac{2}{k^2 d_*^2} \begin{bmatrix} M_{xx}^* + M_{yy}^* & M_{xy}^* - M_{yx}^* \\ M_{yx}^* - M_{xy}^* & M_{xx}^* + M_{yy}^* \end{bmatrix} - d_* I_{2r} \ . \tag{5.25}$$

Lemma 5.7 *The Hessian* $\mathrm{H}_{\varphi_*}^{g_{mac},\mathrm{collinear}}$ *has non-positive eigenvalues thus is a negative semi-definite matrix. Its rank is* $\operatorname{rank}\left(\mathrm{H}_{\varphi_*}^{g_{mac},\mathrm{collinear}}\right) = 2r - 2$.

Proof: See Appendix C.4. □

Theorem 5.8 *In the case of collinear mode shapes the quadratic form* $Q(\hat{X}_\mathcal{N})$ *can be formulated as follows*

$$\begin{aligned} Q(\hat{X}_\mathcal{N}) &= \hat{X}_\mathcal{N}^T \tilde{\mathrm{H}}_{\hat{\varphi}}^{g_{mac},\mathrm{collinear}} \hat{X}_\mathcal{N} \approx \hat{X}_\mathcal{N}^T \tilde{\mathrm{H}}_{\varphi_*}^{g_{mac},\mathrm{collinear}} \hat{X}_\mathcal{N} \\ &\approx N\left(1 - g_{mac}(\hat{\varphi}, \psi_*)\right) \ , \end{aligned} \tag{5.26}$$

where $\tilde{\mathrm{H}}_{\varphi_*}^{g_{mac},\mathrm{collinear}} = -\mathrm{H}_{\varphi_*}^{g_{mac},\mathrm{collinear}}/2$.

5.3.2.2 Formulation of the Hessian matrix for the orthogonal mode shapes

The objective of this section is the study of the quadratic form in the case of orthogonality between an estimated mode shape and a numerical mode shape. The Hessian is assembled with the derivatives evaluated for the case when $\varphi_*^H \psi_* = 0$, namely (C.29), (C.32), (C.37), (C.40). Subsequently, the Hessian (5.23) writes as

$$\mathrm{H}_{\varphi_*}^{g_{mac},\mathrm{orthogonal}} = \frac{2}{d_* e_*} \begin{bmatrix} M_{xx}^* + M_{yy}^* & M_{xy}^* - M_{yx}^* \\ M_{yx}^* - M_{xy}^* & M_{xx}^* + M_{yy}^* \end{bmatrix} \ . \tag{5.27}$$

Similar to the collinear case, the respective partial derivatives are enclosed in Appendix C.3.

Lemma 5.9 *The Hessian* $\mathrm{H}_{\varphi_*}^{g_{mac},\mathrm{orthogonal}}$ *has positive eigenvalues thus is a positive semi-definite matrix. Its rank is* $\operatorname{rank}\left(\mathrm{H}_{\varphi_*}^{g_{mac},\mathrm{orthogonal}}\right) = 2r - 2$.

Proof: See Appendix C.5. □

Theorem 5.10 *In the case of orthogonal mode shapes the quadratic form $Q(\hat{X}_{\mathcal{N}})$ can be expressed as*

$$\begin{aligned} Q(\hat{X}_{\mathcal{N}}) &= \hat{X}_{\mathcal{N}}^T \tilde{\mathrm{H}}_{\hat{\varphi}}^{g_{mac},\mathrm{orthogonal}} \hat{X}_{\mathcal{N}} \approx \hat{X}_{\mathcal{N}}^T \tilde{\mathrm{H}}_{\varphi_*}^{g_{mac},\mathrm{orthogonal}} \hat{X}_{\mathcal{N}} \\ &\approx N\left(g_{mac}(\hat{\varphi}, \psi_*)\right) \ , \end{aligned} \tag{5.28}$$

where $\tilde{\mathrm{H}}_{\varphi_*}^{g_{mac},\mathrm{orthogonal}} = \mathrm{H}_{\varphi_*}^{g_{mac},\mathrm{orthogonal}}/2$.

5.3.3 χ_l^2 approximation validation

This section is devoted to the numerical validation of the aforementioned quadratic form approximation. Two strategies recalled in this section validate the χ_l^2 approximation from Theorem 5.26 and Theorem 5.28, and are tested on the cases of MAC_{11} and MAC_{12}. The procedures proposed in this section closely follow Section 4.3.2.

Recall that the estimates of MAC computed from each realization of m Monte Carlo simulations are collected in $\mathrm{MAC}_{MC} \in \mathbb{R}^{m\times 1}$, where each estimate approaches the theoretical boundary of the MAC domain, 0 or 1. Subsequently

$$Q_{\mathrm{MAC}_{MC}} = N\left(\mathrm{MAC}_{MC} - g_{mac}(\varphi_*, \psi_*)\right) \ , \tag{5.29}$$

which, based on Theorems 5.26 and 5.28, is a quadratic form that can be approximated with the χ_l^2 distribution. Notice that $Q_{\mathrm{MAC}_{MC}}$ yields

$$Q_{\mathrm{MAC}_{MC}} = N\left(1 - \mathrm{MAC}_{MC}\right) \ , \tag{5.30}$$

for collinear and

$$Q_{\mathrm{MAC}_{MC}} = N\left(\mathrm{MAC}_{MC}\right) \ , \tag{5.31}$$

for orthogonal cases respectively. The number of degrees of freedom l_{MC} of MAC_{MC} can be derived from the empirical cumulants of the Monte Carlo histogram as described in Section 5.3.1. Note that $1 \leq l_{MC} \leq r-1$, after Lemma 5.5. The density of the χ^2 approximation can be analytically expressed as in (5.21); let $\overline{Q}_{\mathrm{MAC}_{MC}}$ be a scaled and shifted $Q_{\mathrm{MAC}_{MC}}$ such that

$$\overline{Q}_{\mathrm{MAC}_{MC}} = (Q_{\mathrm{MAC}_{MC}} - \bar{\beta})/\bar{\alpha} \ , \tag{5.32}$$

where $\bar{\alpha} = \bar{\sigma}_Q/\bar{\sigma}_{\chi^2}$ and $\bar{\beta} = \bar{\mu}_Q - (\bar{\mu}_{\chi^2}\bar{\sigma}_Q)/\bar{\sigma}_{\chi^2}$. The scalars $\bar{\sigma}_Q$, $\bar{\mu}_Q$, $\bar{\sigma}_{\chi^2}$ and $\bar{\mu}_{\chi^2}$ are computed from the cumulants of $Q_{\mathrm{MAC}_{MC}}$ as in Section 5.3.1. As such, knowing the Monte Carlo histograms, the characterization of the χ^2 approximation is easily performed. That can be achieved by defining a vector $v_1 \in \mathbb{R}^{m\times 1}$ whose j-th entry is drawn from a $\chi^2_{l_{MC}}$ distribution such that $v_j \sim \chi^2_{l_{MC}}$. As such, each entry of v_1 is drawn from a corresponding realization of $\chi^2_{l_{MC}}$ and the resulting aggregated histogram of all components of v_1 should correspond to the theoretical histogram of $\chi^2_{l_{MC}}$. A comparison of the cumulative distribution functions of both $\overline{Q}_{\mathrm{MAC}_{MC}}$ and v_1 is shown in the left parts of Figure 5.14 for the collinear and Figure 5.16 for the orthogonal mode shape cases.

Prior to analyzing the figures, it is illustrated that the perturbation approach is also capable of such approximation. For that define a vector $\overline{Q}_{\mathrm{MAC}_{PT}} \in \mathbb{R}^{m\times 1}$ such that for $j = 1 \ldots m$ its j-th entry writes

$$\overline{Q}_{\mathrm{MAC}_{PT,j}} = (Q_{\mathrm{MAC}_{MC,j}} - \beta_j)/\alpha_j \ , \tag{5.33}$$

where β_j and α_j are the j-th β and α estimated after Section 5.3.1 for the corresponding realization of the Monte Carlo simulation. The main problem here is that each $\overline{Q}_{\mathrm{MAC}_{PT,j}}$ is drawn from some distribution that can be characterized by a different l_j. A common baseline is needed. That is achieved by modifying the approximated distributions to fit with a theoretical χ^2_p distribution, where p will be constant for all realizations and not equal to l_j but $2r-1$ as explained below. Contrary to (5.32), each $Q_{\mathrm{MAC}_{MC,j}}$ is normalized with its own α and β coming from the perturbation theory and not from averaging over the Monte Carlo histogram. In that sense, $Q_{\mathrm{MAC}_{MC,j}}$ is properly following a $\chi^2_{l_{PT,j}}$ distribution, where $l_{PT,j}$ is computed from β_j and α_j. Still, each realization follows its own distinct distribution, which is not optimal for a comparison. This comparison is also more difficult when considering that the Monte Carlo histogram is fitted with its own $\chi^2_{l_{MC}}$ distribution characterized with own l_{MC}. To deal with that the additive property of independent χ^2 distributions is used. Recall from Lemma 5.5 that $1 \leq l_{PT,j} \leq r-1$ for any j. The bounds for l_{MC}, as stated in Corollary 5.6, are $1 \leq l_{MC} \leq r-1$. As such, it exists some complement for all these numbers e.g. one that is equal to $2r-1$, such that both $2r-1-l_{PT,j} > 0$ for all j and $2r-1-l_{MC} > 0$. Now, define random vectors $v_2, v_3 \in \mathbb{R}^{m\times 1}$ such that $v_2 \sim \chi^2_{2r-1-l_{MC}}$, and for $j = 1 \dots m$ each entry of $v_{3,j} \sim \chi^2_{2r-1-l_{PT,j}}$. Consequently using additive property of independent χ^2 distributions define

$$Z_{MC} = \overline{Q}_{\mathrm{MAC}_{MC}} + v_2, \quad Z_{MC} \sim \chi^2_{2r-1} \ , \tag{5.34}$$

$$Z_{PT} = \overline{Q}_{\mathrm{MAC}_{PT}} + v_3, \quad Z_{PT} \sim \chi^2_{2r-1} \ . \tag{5.35}$$

A comparison between CDFs of Z_{MC}, Z_{PT} evaluated for both MAC_{11} and MAC_{12} with a theoretical χ^2_{2r-1} CDF is illustrated in the right parts of Figure 5.14 for collinear and Figure 5.16 for orthogonal mode shapes.

In case when a theoretical reference is known, a statistical measure can be used to quantify the dispersion between the aforementioned distributions. That dispersion can be quantified with Pearson χ^2 statistics between the expected χ^2_{2r-1} distributed variable and the observed $Z^j_{PT} \in \mathbb{R}^{m\times 1}$ vector. It writes as

$$Z^j_{PT} = (Q_{\mathrm{MAC}_{MC}} - \beta_j)/\alpha_j + v_{4,j} \ , \tag{5.36}$$

where $v_{4,j} \sim \chi^2_{2r-1-l_{PT,j}}$. This leads to a collection of histograms that mirror the quality of each α_j, β_j, similarly as in the Gaussian case. The histograms of the Pearson χ^2 statistic for MAC_{11} and MAC_{12} estimates are depicted respectively on the left parts of Figure 5.15 and Figure 5.17. Consequently, a comparison of using the best, median and the worst approximations of MAC_{11} and MAC_{12} estimates, which correspond to respective quantiles of the Pearson χ^2 statistics, is depicted on the respective right parts of Figure 5.15 and Figure 5.17.

5.3.3.1 Collinear mode shapes

Figure 5.14 and Figure 5.15 illustrate the proposed validation scheme applied to the Monte Carlo simulations of MAC_{11}. The left part of the Figure 5.14 illustrates that both CDF coincide meaning that the distribution of the Monte Carlo histogram is well characterized by a quadratic form which distribution is approximated by a χ^2 distribution. The right part of Figure 5.14 shows that the corrected Z_{MC} for Monte Carlo and combined realizations from the perturbation theory Z_{PT} have similar CDF. This shows the validity of the perturbation-based approach to compute the variances

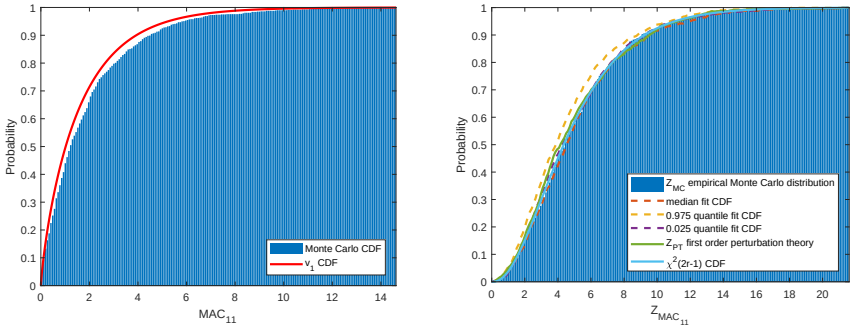

Figure 5.14: $\chi^2_{l_{MC}}$ CDF and CDF of MAC computed between the exact mode shape from the model and estimated one. Theoretical χ^2_{2r-1} CDF compared to CDF of Z_{MC} (5.34) and Z_{PT} (5.35) computed with parameters estimated for MAC between exact mode shape from the model and estimated one (right).

needed to characterize the quadratic distribution and yield similar distribution parameters as the full Monte Carlo histogram. Also, the plots corresponding to the best, median and worst quantiles are all quite similar. They match the Monte Carlo and the perturbation-based Z plots. This means that almost any of the realization among the Monte Carlo experiments can be used to give such variance information.

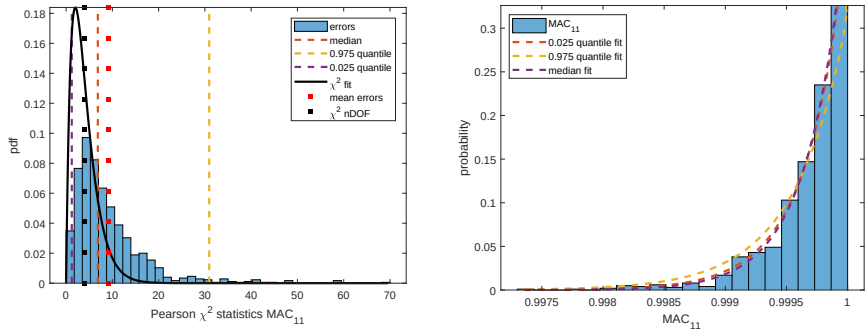

Figure 5.15: Histogram of errors in $\chi^2_{l_{PT}}$ approximation with best, median and worst fits for MAC between exact mode shape from the model and estimated one (left). Scaled and shifted χ^2 fits to empirical probability distribution of MAC between exact mode shape from the model and estimated one based on median, 0.95 and 0.025 quantiles of Pearson χ^2 statistics (right).

Figure 5.15 shows the dispersion of the distance between all the empirical histograms based on the perturbation theory. It can be seen that the empirical mean of the Pearson histogram is close to its theoretical mean. The right part of Figure 5.15 shows the fitting of MAC histogram by the perturbation-based densities corresponding to selected best, median and worst quantiles. It can be seen that the quadratic assumption here is much more adequate for MAC_{11} than the Gaussian approximation depicted on Figure 5.10.

5.3.3.2 Orthogonal mode shapes

Figure 5.16 and Figure 5.17 created for the orthogonal mode shapes case illustrate that both Monte Carlo based histogram of MAC_{12} and the perturbation theory based Z variables are well approximated by a χ^2 law, as expected. They exhibit very similar behavior regarding validity of χ^2 approximation as the results illustrated on Figure 5.14 and Figure 5.15 made for the collinear case, which shows the versatility of the devised validation schemes.

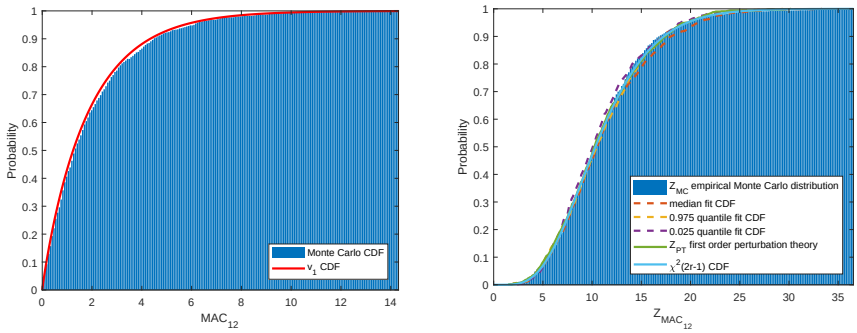

Figure 5.16: $\chi^2(l_{MC})$ CDF and CDF of MAC computed between the exact mode shape from the model and estimated one. Theoretical χ^2_{2r-1} CDF compared to CDF of Z_{MC} (5.34) and Z_{PT} (5.35) computed with parameters estimated for MAC between exact mode shape from the model and estimated one (right).

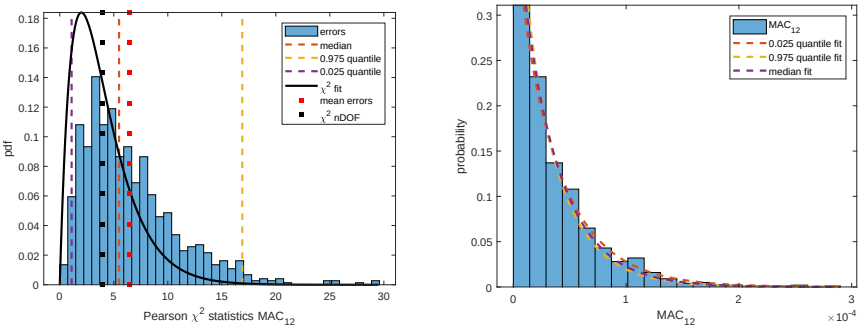

Figure 5.17: Histogram of errors in $\chi^2(l_{PT})$ approximation with best, median and worst fits for MAC between exact mode shape from the model and estimated one (left). Scaled and shifted χ^2 fits to empirical probability distribution of MAC between exact mode shape from the model and estimated one based on median, 0.95 and 0.025 quantiles of Pearson χ^2 statistics (right).

5.3.4 Influence of sample length on distribution of $g_{mac}(\hat{\varphi}, \psi_*)$: a χ^2 case

This section studies the influence of the sample length on the underlying distributions of MAC obtained from Monte Carlo simulations. Two base-cases of MAC

are studied, namely MAC_{11} and MAC_{12} and two sample lengths are tested, namely $N = \{10000, 1000000\}$.

5.3.4.1 Collinear mode shapes

Figure 5.18 illustrates the fitting of Monte Carlo based histograms of MAC_{11} by the perturbation-based densities of the best, the median and the worst quantiles.

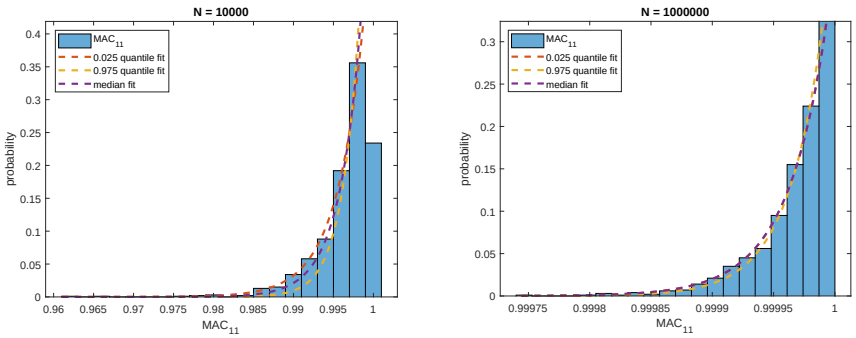

Figure 5.18: Scaled and shifted χ^2 fits to empirical probability distribution of MAC between exact mode shape from the model and estimated one based on median, 0.95 and 0.025 quantiles of Pearson χ^2 statistics.

As expected the best, the median and the worst perturbation-based density fits adequately encompass the Monte Carlo based distribution of MAC_{11} for $N = 10000$ sample case, however, they are less accurate compared to $N = 1000000$ case where even the worst 0.95 quantile fit provides a precise fit to empirical distribution.

5.3.4.2 Orthogonal mode shapes

Figure 5.19 illustrates the fitting of Monte Carlo based histograms of MAC_{12} by the perturbation-based densities of the best, the median and the worst quantiles.

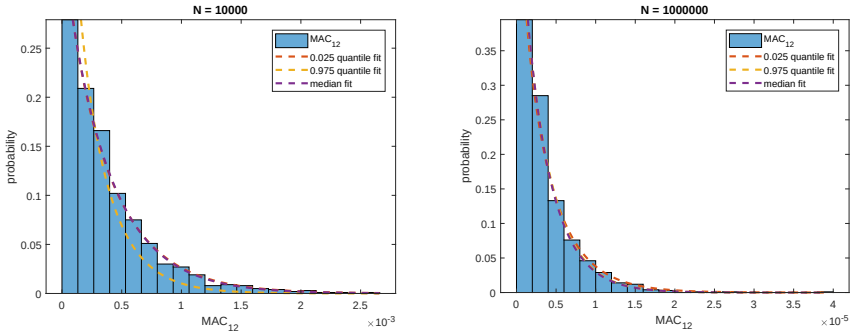

Figure 5.19: Scaled and shifted χ^2 fits to empirical probability distribution of MAC between exact mode shape from the model and estimated one based on median, 0.95 and 0.025 quantiles of Pearson χ^2 statistics.

Distribution fits obtained for MAC between orthogonal mode shapes on Figure 5.19 exhibit similar behavior as ones for the collinear mode shapes on Figure 5.18. The χ^2 approximation of the quadratic form provides a good match for all three selected quantiles of Pearson statistics for both sample lengths.

5.4 Application

This section illustrates the application of the proposed framework to the experimental plate example, which was partly introduced in Section 3.3.1. The MAC computed between a mode shape from the FE model and the corresponding mode shape estimated from the data is considered. The probability of the selected estimates of MAC following Gaussian or quadratic distributions is assessed with the decision framework from Section 4.5.

The FE model of the plate contains 725 4-noded shell elements, 780 nodes and, consequently, 4680 degrees of freedom. The model was created in ANSYS WORKBENCH 17.0. The measurements due to a white noise shaker excitation were sampled with 4096Hz over 120 seconds interval resulting in the total of 491518 samples. The geometry of the plate and the experimental setup are illustrated on Figure 5.20.

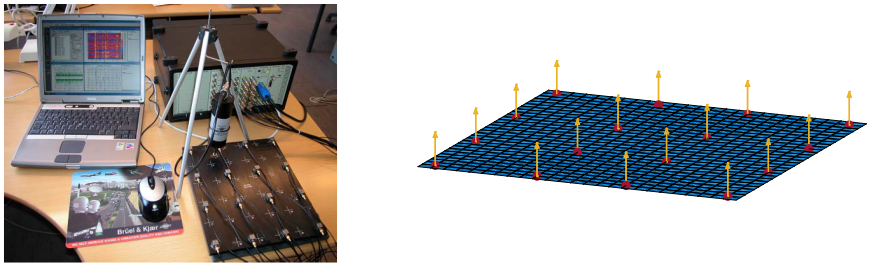

Figure 5.20: The experimental plate model with 16 acceleration channels attached (left). The FE model of the plate with the mapping to 16 output channels (right).

The mode shape corresponding to the first mode of the plate is estimated with SSI-UPC using a system order of 60, time lags of 15 and 200 blocks for the covariance computation of the data Hankel matrix. A comparison of the modal parameter estimates with their exact counterparts from the FE model that correspond to the first mode is presented in Table 5.1.

f_{FE}	f_{exp}	ζ_{exp}	$\mathrm{MAC}(\phi_{\mathrm{FE}}, \phi_{\mathrm{exp}})$
355.63 Hz	339.71 Hz ± 0.04 Hz	0.44 % ± 0.009 %	0.9997

Table 5.1: Comparison of the first mode modal parameters of the plate from the FE model and identified from the experimental data with 491518 samples.

It can be observed that the natural frequency identified from the data is lower then the exact values from the model. That might be caused by the increase in the plate mass due to accelerometers or a shaker, whose masses were not accounted for in the FE model. The estimates of MAC, however, are in the vicinity of 1 indicating high correlation between the estimated and the FE mode shapes. The choice of the

approximation framework for MAC is discussed for the first mode based on two data sets of lengths $N_1 = 12287$ and $N_2 = 491518$. Figure 5.21 and Figure 5.22 illustrate respectively the 95% and 99% confidence intervals computed with the Gaussian and the quadratic approximations for the MAC estimates corresponding to the first mode and the both sample lengths N_1 and N_2.

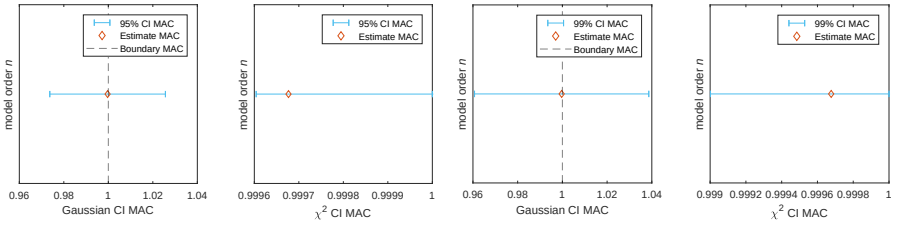

Figure 5.21: MAC estimates with corresponding 95% (left) and 99% (right) confidence intervals. $N_1 = 12287$.

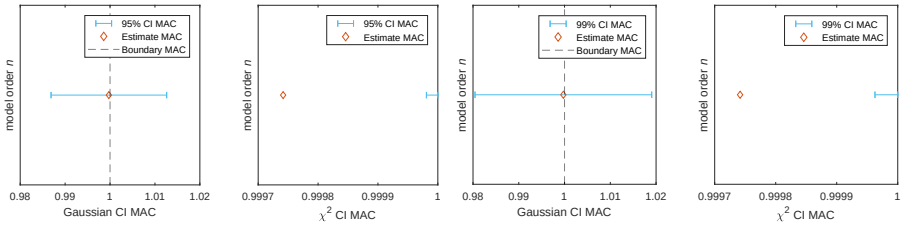

Figure 5.22: MAC estimates with corresponding 95% (left) and 99% (right) confidence intervals. $N_2 = 491518$.

Based on the figures above it can be observed that the low sample approximation of MAC is more likely to be quadratic since its estimates are within the confidence intervals computed with the χ^2 distribution. When the sample size increases the estimates of MAC are more accurate and their confidence intervals shrink. Consequently, they are outside the χ^2 bounds, suggesting that the distribution of the MAC is not longer quadratic, despite its estimate being extremely close to the domain boundary. Table 5.2 shows the probabilities p_G and p_Q introduced earlier in Section 4.5.

α	$\Pr^{N_1}$	$\mathrm{MAC}(\phi_{\mathrm{FE}}, \phi_{\mathrm{exp}})$	$\Pr^{N_2}$	$\mathrm{MAC}(\phi_{\mathrm{FE}}, \phi_{\mathrm{exp}})$
95%	p_G	0.5098	p_G	0.5155
	p_Q	0.1054	p_Q	0
99%	p_G	0.5065	p_G	0.5103
	p_Q	0.6467	p_Q	0

Table 5.2: 95% and 99% level computation of p_G and p_Q using decision scheme of Section 4.5.

By design the $p_G > 0.50$, which is exceeded by the p_Q only in the low sample 99% quantile approximation case. That indicates that for the real data, when the

sample length is sufficiently large, the distribution of the considered MAC is most likely Gaussian, despite the MAC estimate being close to 1. That is most likely caused by the inaccurate FE model, which is not equivalent to the plate used for the experiment. Consequently, the estimated mode shapes do not converge to ones from the FE model, which causes the quadratic approximation to be invalid for the large sample size. For the low sample approximation, however, the quadratic confidence intervals are sufficiently wide to encompass the considered estimates of MAC. It can be concluded that the proposed framework is very sensitive towards the accuracy of the FE model and for its practical use such model should exactly correspond to the experimental data e.g. be appropriately updated.

5.5 Conclusions

In this chapter we addressed the uncertainty quantification of the MAC indicator. Two cases for its computation were distinguished. The first case considered MAC computed between two estimates of the mode shape corresponding to different modes. In the second MAC was computed between a mode shape estimated from the data and an exact mode shape from a model. Two statistical frameworks were used to approximate their underlying distributions. For the first case a classical Gaussian framework based on the first order Delta method was considered. The second case, for which estimates of MAC were in a vicinity of a boarder of their theoretical distribution, involved development of a quadratic framework based on the second order Delta method. Two cases of the quadratic approximations were distinguished, namely first where two mode shapes are collinear and second where the mode shapes are orthogonal. For both it was showed that the MAC estimate asymptotically converges to a quadratic form which can be approximated by a shifted and scaled χ^2 distribution. The statistical properties of both approximations such as bounds for its degrees of freedom were also proved in the course of this chapter. The proposed approximations were tested on a simulations of a chain system and the strategy for their numerical validation were developed based on the numerical Monte Carlo simulation. The proposed framework was applied to the experimental plate case where it was found that the quadratic approximation is adequate to characterize the distribution of MAC computed between the mode shape from the FE model and its counterpart estimated from data with low sample size. When larger sample sizes were considered the estimates of the considered MAC were Gaussian.

5.6 Dissemination

Parts of this chapter have been published in [10, 11]:

[10] S. Gres, M. Döhler, P. Andersen, L. Mevel, Variance computation of the Modal Assurance Criterion, in: International Conference on Noise and Vibration Engineering - KU Leuven, Katholieke Universiteit, Leuven, Belgium, 2018, pp. 2939–2950, proceedings of the ISMA2018 and the USD2018.

[11] S. Greś, M. Döhler, L. Mevel, Uncertainty quantification of the modal assurance criterion in operational modal analysis, Mechanical Systems and Signal Processing 152 (2021) 107457.

In addition, the algorithm for uncertainty quantification of MAC between different estimates of the mode shapes was implemented in ARTeMIS Modal Pro 6.0 [138].

CHAPTER 6

Uncertainty quantification of the MAC from a stabilization diagram

The stabilization diagram is a practical tool used in many engineering applications of system identification to handle bias errors in the estimates of modal parameters, considering the order of the system is unknown. There, the estimates of modal parameters can be clustered into so-called modal alignments by some practical criteria, like the relative difference between the consecutive parameters, and the modal indicators like MAC and MPC. However, no measure yet exists to quantify probability that a modal estimate belongs to a selected modal alignment. In this chapter such statistical measure is developed, based on the confidence intervals of the MAC estimates corresponding to the mode shape estimates within tested alignment. That allows to filter the modal alignments from estimates of modes which do not correspond to the same theoretical mode shape, which should result in an improvement of the global estimates of modal parameters.

In this chapter, a framework to quantify uncertainty of the MAC from a stabilization diagram is developed. Moreover, uncertainty computation of a global mode shape estimate and variance computation of the MPC computed from the global mode shapes is also established. These topics are illustrated based on a numerical simulations of a simple chain system and applied to a real-data from the experimental plate.

6.1 Illustrative example

For numerical simulations consider a theoretical 6 DOF chain-like system that, for any consistent set of units, is modeled with a spring stiffness $k_1 = k_3 = k_5 = 100$ and $k_2 = k_4 = k_6 = 200$, mass $m_{1-6} = 1/20$ and a proportional modal damping matrix. The system is subjected to white noise signal in all DOFs and sampled with a frequency of 50 Hz for 2000 seconds. The responses are measured at 1, 2 and 5 DOF. Gaussian white noise with 5% of the standard deviation of the output is added to the response at each channel. The computations are performed in a

Monte Carlo setup with $m = 1000$ simulations. The SSI-UPC and the corresponding variance computation are set up with time lags of 15 and 200 blocks for the covariance computation of the data Hankel matrix. System orders are in the range between $12 - 40$. Six global modes are established, with the respective modal parameters and their variances, in each simulation. For the formation of each modal alignment the following criteria are used

- difference in two consecutive natural frequencies $\leq 1\%$,
- difference in two consecutive damping ratios $\leq 10\%$,
- MAC level between two consecutive mode shapes $\geq 99\%$,
- standard deviation of natural frequency computed with the perturbation theory $\leq 1\%$.

The results presented first are established based on one realization of the Monte Carlo simulations. Figure 6.1 illustrates the estimates of natural frequency with the corresponding 95% confidence intervals computed for model orders $12 - 40$ together with the estimates of the global natural frequency and its corresponding 95% confidence intervals. Figure 6.2 shows the estimates of the natural frequencies, the damping ratios, the MAC and the MPC from the first modal alignment.

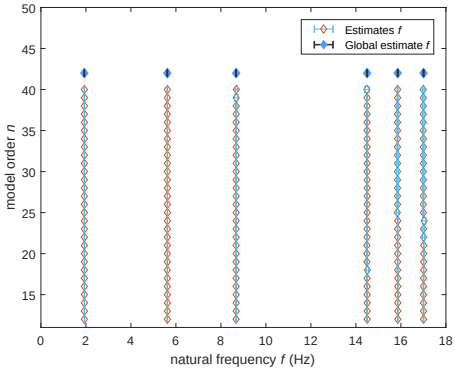

Figure 6.1: Stabilization diagram for natural frequencies with the corresponding 95% confidence intervals.

One can see that the natural frequency of each mode can be tracked along estimated model orders and the estimated variances are small, thus not visible in the scale presented on Figure 6.1. From Figure 6.2 it can be observed that the statistical dispersion of the natural frequencies and damping ratios, represented by the horizontal bars, is small and yields less then 0.1 Hz and 0.15% respectively for the estimates of the natural frequency and the damping ratio. The variation of the natural frequencies and damping ratios in the estimates at different modal orders is reflected by the global estimates as described in the scheme in Appendix A.1.2. The MAC values presented on Figure 6.2 are estimated between the mode shape from model order 12 and the remaining mode shapes of the first alignment. Resultant MAC values tend to 1, meaning that the mode shapes used to compute the MAC belong to the same mode.

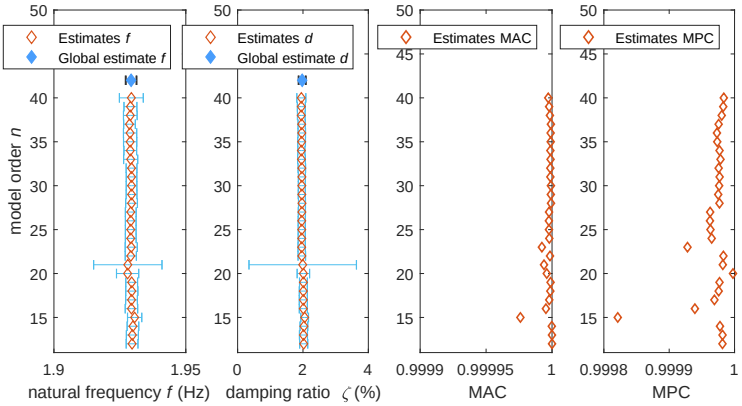

Figure 6.2: Estimates of natural frequencies, damping ratios, MAC and MPC from the first modal alignment.

It also indicates that the estimates of MAC within one modal alignment approach the right boundary of the distribution of the MAC indicator. The quantification of statistical uncertainties for such problems has been investigated for the MPC in Chapter 4 and for the MAC between the estimate of a mode shape and an exact mode shape from a model in Chapter 5. However, a scheme for quantifying the uncertainty of the MAC indicator between two mode shape estimates from the stabilization diagram is missing. For that, three cases of MAC computation can be distinguished, namely

1. $g_{mac}(\hat{\varphi}^{a,n}, \hat{\psi}^{a,n})$ where $\hat{\varphi}^{a,n}$ and $\hat{\psi}^{a,n}$ are estimates of different mode shapes from a modal alignment a and model order n,

2. $g_{mac}(\hat{\varphi}^{a,\text{global}}, \hat{\psi}^{a,n})$ where $\hat{\varphi}^{a,\text{global}}$ is an estimate of a global mode shape from a modal alignment a,

3. $g_{mac}(\hat{\varphi}^{a,\text{global}}, \hat{\psi}^{a,\text{global}})$ where $\hat{\varphi}^{a,\text{global}}$ and $\hat{\psi}^{a,\text{global}}$ are estimates of a orthogonal global mode shapes from two different modal alignments.

Additionally, the global estimates of the MAC and the MPC are functions of the global mode shapes for which the uncertainty scheme is also recalled.

6.1.1 Distribution of MAC from the stabilization diagram

This section illustrates different distributions of MAC between mode shapes corresponding to the modes from the stabilization diagram. The distribution of MAC is made available by Monte Carlo simulations of the numerical system described in Section 6.1. The examples that follow are based on the aforementioned MAC computation cases from the section above

1. $g_{mac}(\hat{\varphi}^{1,12}, \hat{\psi}^{1,14})$ is computed between the mode shapes from first modal alignment at model orders 12 and 14, namely $\hat{\varphi}^{1,12}$ and $\hat{\psi}^{1,14}$. Denote it as the base-case 1.

2. $g_{mac}(\hat{\varphi}^{1,\text{global}}, \hat{\psi}^{1,12})$ is computed between a global mode shape estimate of the first modal alignment and the one at modal order 12, namely $\hat{\varphi}^{1,\text{global}}$ and $\hat{\psi}^{1,12}$. Denote it as the base-case 2.

3. $g_{mac}(\hat{\varphi}^{1,\text{global}}, \hat{\psi}^{3,\text{global}})$ computed between a global mode shape estimate of the first modal alignment and a global mode shape estimate from third alignment, namely $\hat{\varphi}^{1,\text{global}}$ and $\hat{\psi}^{3,\text{global}}$. Denote it as the base-case 3.

These distributions are illustrated on Figure 6.3.

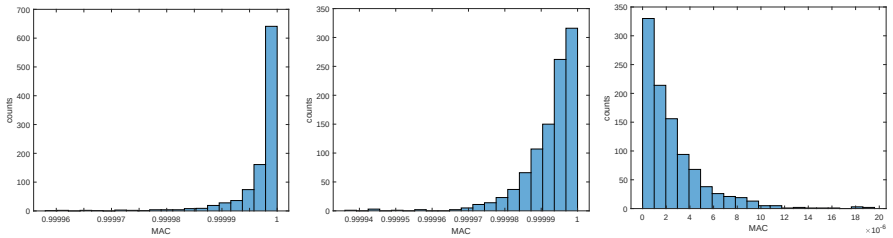

Figure 6.3: Histogram of the base-case 1 MAC (left). Histogram of the base-case 2 MAC (middle). Histogram of the base-case 3 MAC (right).

For the two first cases the MAC indicator is computed between the mode shapes that correspond to the same theoretical mode, hence its value is asymptotically 1. For the third case the MAC is computed between mode shapes that are orthogonal, hence the distribution of its values asymptotically tends to zero. All three cases are inadequate to be approximated by a Gaussian distribution, which was shown on Figure 5.10 from Section 5.2.3, since the Jacobian $\mathcal{J}^{g_{mac}}_{\varphi_*,\psi_*}$ used in that approximation is null, as showed in Lemma 5.2. Also, it is clear that the Gaussian approximation should be symmetrical with respect to its limit mean, which is impossible if the limit is on the boundary of the support. Section 6.3 in this chapter focuses on approximating three aforementioned cases of MAC with a quadratic form, which subsequently is approximated by a scaled χ^2 distribution. Before, however, a strategy to estimate the uncertainty in the global mode shape estimates is established.

6.2 Variance of the global mode shapes

The variance of the global mode shapes can be quantified with a scheme equivalent to the one developed in [79] and recalled for the estimates of the global natural frequencies and the global damping ratios in Appendix A.1.2. Special care should be taken, however, for the different mode shape normalizations, like the ones established in [74] and [81]. Let $\tilde{\varphi}$ denote a mode shape normalized with respect to one of its components labeled here as the *Normalization scheme 1* and $\breve{\varphi}$ be a mode shape rotated such that the imaginary part of one component is 0 and the real part of this component is positive, labeled as the *Normalization scheme 2*. Both normalization schemes are recalled in Appendix A.1.1.1 and A.1.1.2.

To develop a computation scheme for the variance of the global estimate of $\tilde{\varphi}$ first denote $\hat{\tilde{\varphi}}^{a,\text{global}}$ as an estimate of the global mode shape from modal alignment a, normalized by scheme 1. Subsequently, following the lines of [79], the stacked real and

imaginary parts of the global mode shape are expressed by weighting mode shapes at each model order by their covariance matrix, which writes

$$\begin{bmatrix}\Re(\hat{\tilde{\varphi}}^{a,\text{global}})\\ \Im(\hat{\tilde{\varphi}}^{a,\text{global}})\end{bmatrix} = \left(\sum_{i=1}^{n} \Sigma^{-1}_{\Re(\hat{\tilde{\varphi}}^{a,i}),\Im(\hat{\tilde{\varphi}}^{a,i})}\right)^{-1} \left(\sum_{i=1}^{n} \Sigma^{-1}_{\Re(\hat{\tilde{\varphi}}^{a,i}),\Im(\hat{\tilde{\varphi}}^{a,i})} \begin{bmatrix}\Re(\hat{\tilde{\varphi}}^{a,i})\\ \Im(\hat{\tilde{\varphi}}^{a,i})\end{bmatrix}\right) , \tag{6.1}$$

where the development of $\Sigma_{\Re(\hat{\tilde{\varphi}}^{a,i}),\Im(\hat{\tilde{\varphi}}^{a,i})}$ is recalled in Appendix A.1.1. The first order perturbation in $\hat{\tilde{\varphi}}^{a,\text{global}}$ writes as

$$\begin{bmatrix}\Delta\Re(\hat{\tilde{\varphi}}^{a,\text{global}})\\ \Delta\Im(\hat{\tilde{\varphi}}^{a,\text{global}})\end{bmatrix} = \hat{\mathcal{J}}^{\tilde{\varphi}^{a,\text{global}}}_{\hat{\mathcal{R}}} \text{vec}(\Delta\hat{\mathcal{R}}) . \tag{6.2}$$

where

$$\hat{\mathcal{J}}^{\tilde{\varphi}^{a,\text{global}}}_{\hat{\mathcal{R}}} = \left(\sum_{i=1}^{n} \Sigma^{-1}_{\Re(\hat{\tilde{\varphi}}^{a,i}),\Im(\hat{\tilde{\varphi}}^{a,i})}\right)^{-1} \left(\sum_{i=1}^{n} \Sigma^{-1}_{\Re(\hat{\tilde{\varphi}}^{a,i}),\Im(\hat{\tilde{\varphi}}^{a,i})} \begin{bmatrix}\mathcal{J}^{\Re(\tilde{\varphi}^{a,i})}_{\hat{\mathcal{R}}}\\ \mathcal{J}^{\Im(\tilde{\varphi}^{a,i})}_{\hat{\mathcal{R}}}\end{bmatrix}\right) ,$$

which factorize to $\hat{\mathcal{J}}^{\tilde{\varphi}^{a,\text{global}}}_{\hat{\mathcal{R}}} = \left[(\hat{\mathcal{J}}^{\Re(\tilde{\varphi}^{a,\text{global}})}_{\hat{\mathcal{R}}})^T \quad (\hat{\mathcal{J}}^{\Im(\tilde{\varphi}^{a,\text{global}})}_{\hat{\mathcal{R}}})^T\right]^T$ and is a real valued Jacobian matrix.

Remark 6.1 (Regarding the rank deficiency of $\Sigma_{\Re(\hat{\tilde{\varphi}}^{a,i}),\Im(\hat{\tilde{\varphi}}^{a,i})}$) *Since $\tilde{\varphi}$ is defined such that $\tilde{\varphi} = \hat{\varphi}/\varphi_k$, after [74], both $\Re(\varphi_k)$ and $\Im(\varphi_k)$ are deterministic and the covariance of the mode shape is rank deficient where* $\text{rank}\left(\Sigma_{\Re(\hat{\tilde{\varphi}}^{a,i}),\Im(\hat{\tilde{\varphi}}^{a,i})}\right) \leq 2r-2$. *Therefore to avoid inversion problems in* (6.1) *and* (6.2) *the k-th row and column in $\Sigma_{\Re(\hat{\tilde{\varphi}}^{a,i}),\Im(\hat{\tilde{\varphi}}^{a,i})}$ and the k-th row in $\Re(\hat{\tilde{\varphi}}^{a,i})$, $\Im(\hat{\tilde{\varphi}}^{a,i})$, $\mathcal{J}^{\Re(\tilde{\varphi}^{a,i})}_{\hat{\mathcal{R}}}$ and $\mathcal{J}^{\Im(\tilde{\varphi}^{a,i})}_{\hat{\mathcal{R}}}$ are ought to be removed.*

The estimates of the global mode shapes and their corresponding variances from the Normalization scheme 2 follows the lines of the scheme developed for a single mode shape estimate from [81]. That scheme modified for the global mode shapes is summarized below. The estimate of the global mode shape from the Normalization scheme 2 writes as

$$\hat{\tilde{\varphi}}^{a,\text{global}} = \hat{\varphi}^{a,\text{global}}/||\hat{\varphi}^{a,\text{global}}|| . \tag{6.3}$$

Its first order perturbation yields

$$\Delta\hat{\tilde{\varphi}}^{a,\text{global}} = \hat{\mathcal{J}}^{\tilde{\varphi}^{a,\text{global}}}_{\hat{\mathcal{R}}} \text{vec}(\Delta\hat{\mathcal{R}}) . \tag{6.4}$$

where

$$\hat{\mathcal{J}}^{\tilde{\varphi}^{a,\text{global}}}_{\hat{\mathcal{R}}} = \frac{1}{||\hat{\tilde{\varphi}}^{a,\text{global}}||}\left(-\frac{\hat{\tilde{\varphi}}^{a,\text{global}}}{||\hat{\tilde{\varphi}}^{a,\text{global}}||^2}\Re(\hat{\tilde{\varphi}}^{a,\text{global}\,H}\bar{\mathcal{J}}^{\tilde{\varphi}^{a,\text{global}}}_{\hat{\mathcal{R}}}) + \bar{\mathcal{J}}^{\tilde{\varphi}^{a,\text{global}}}_{\hat{\mathcal{R}}}\right) ,$$

and $\bar{\mathcal{J}}^{\tilde{\varphi}^{a,\text{global}}}_{\hat{\mathcal{R}}} = \hat{\mathcal{J}}^{\Re(\tilde{\varphi}^{a,\text{global}})}_{\hat{\mathcal{R}}} + \text{i}\hat{\mathcal{J}}^{\Im(\tilde{\varphi}^{a,\text{global}})}_{\hat{\mathcal{R}}}$ is a complex valued Jacobian matrix. Detailed derivation of (6.4) can be found in Appendix A.1.1.2.

6.2.1 Validation of the global mode shape estimates

This section presents a numerical validation of the global mode shape computation scheme developed above. The results display the histograms of the selected components of the global mode shape which are produced by the Monte Carlo simulation of the chain system introduced in Section 6.1. Two aspects of the global mode shape computation are investigated, namely

- the influence of the number of mode shapes merged in a global mode shape,
- the influence of the length of the data set used for the system identification.

A study of the two cases described above for the $\Re(\hat{\mathring{\varphi}}_1^{1,\text{global}})$ and $\Im(\hat{\mathring{\varphi}}_1^{1,\text{global}})$ is depicted on Figure 6.4.

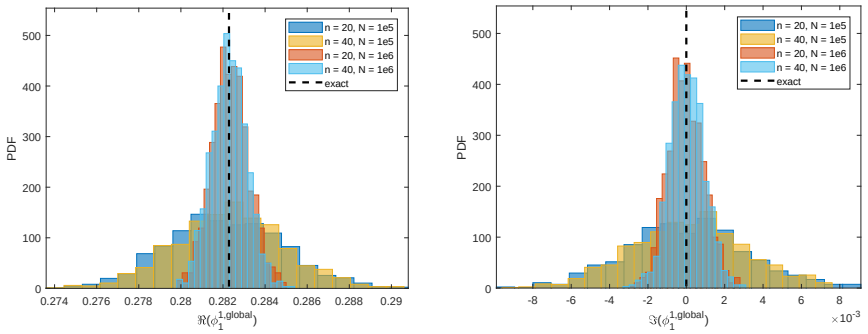

Figure 6.4: Histogram of $\Re(\hat{\mathring{\varphi}}_1^{1,\text{global}})$ (left). Histogram of $\Im(\hat{\mathring{\varphi}}_1^{1,\text{global}})$ (right). Variable maximum model orders and sample length. Normalization scheme 2.

As expected, the histograms of both $\Re(\hat{\mathring{\varphi}}_1^{1,\text{global}})$ and $\Im(\hat{\mathring{\varphi}}_1^{1,\text{global}})$ computed for $N = 1000000$ samples are having less dispersion then the ones computed for $N = 100000$ samples. Also, it can be observed that all four histograms, plotted respectively for the real and the imaginary parts of the investigated mode shape component, are centered around the exact value of that component from the model. That suggests that in this case, on average, the mean value on the global mode shape is not influenced by the number of the mode shapes merged.

Subsequently, because the variance of the global mode shape is computed for each realization of the Monte Carlo simulations based on (6.4), a similar study is conducted for its standard deviations, see Figure 6.5. As expected, the mean values of all four histograms from Figure 6.5 are highly influenced by the length of the data set used. The more samples the less dispersion, as shown on Figure 6.4. In addition, the plots on Figure 6.5 suggest that the number of merged mode shapes influences the standard deviation of its components. The more mode shapes merged, in one modal alignment, the smaller the standard deviation of its components. The next section develops a theoretical basis for approximating the distribution of MAC computed between the mode shape estimates from the stabilization diagram.

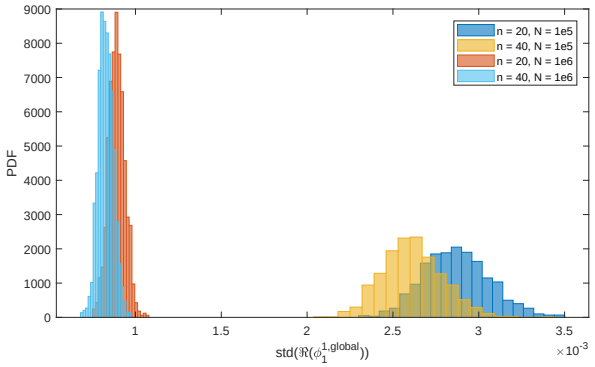

Figure 6.5: Histograms of standard deviations of $\Re(\hat{\varphi}_1^{1,\text{global}})$ computed with the perturbation theory for different model orders and sample lengths. Normalization scheme 2.

6.3 Quadratic approximation of the distribution of $g_{mac}(\hat{\varphi}, \hat{\psi})$

Consider the case when mode shapes $\hat{\varphi}$ and $\hat{\psi}$ are either orthogonal, that is $g_{mac}(\varphi_*, \psi_*) = 0$ and $\varphi_*^H \psi_* = 0$, or collinear $g_{mac}(\varphi_*, \psi_*) = 1$ namely, for some constant k it holds $\varphi_* = k \cdot \psi_*$. For these cases, the first derivative of $g_{mac}(\varphi, \psi)$ with respect to real and imaginary parts of φ and ψ is null, see Lemma 5.2. Consequently, assuming $g_{mac}(\varphi, \psi)$ to be twice differentiable in φ_* and ψ_*, the second order Taylor expansion of $g_{mac}(\hat{\varphi}, \hat{\psi})$ writes as

$$g_{mac}(\hat{\varphi}, \hat{\psi}) = g_{mac}(\varphi_*, \psi_*) + \hat{X}^T \mathrm{H}^{g_{mac}}_{\varphi_*, \psi_*}/2 \; \hat{X} + o(||\hat{X}||^2) \; , \tag{6.5}$$

where $\hat{X} = \begin{bmatrix} \Re(\hat{\varphi} - \varphi_*)^T & \Im(\hat{\varphi} - \varphi_*)^T & \Re(\hat{\psi} - \psi_*)^T & \Im(\hat{\psi} - \psi_*)^T \end{bmatrix}^T$ and the Hessian $\mathrm{H}^{g_{mac}}_{\varphi_*, \psi_*}/2 = \tilde{\mathrm{H}}^{g_{mac}}_{\varphi_*, \psi_*} \in \mathbb{R}^{4r \times 4r}$. Also, recall that when N tends to infinity the $\sqrt{N}\hat{X} = \hat{X}_{\mathcal{N}} \to X_{\mathcal{N}}$ which is a Gaussian $\mathcal{N}(0, \Sigma_{\varphi_*, \psi_*})$, with the covariance matrix $\mathrm{cov}(\hat{\mathrm{X}}) = \Sigma_{\varphi_*, \psi_*}$. The asymptotic properties of $g_{mac}(\hat{\varphi}, \hat{\psi})$ follows

$$N(g_{mac}(\hat{\varphi}, \hat{\psi}) - g_{mac}(\varphi_*, \psi_*)) \approx \hat{X}_{\mathcal{N}}^T \tilde{\mathrm{H}}^{g_{mac}}_{\varphi_*, \psi_*} \hat{X}_{\mathcal{N}} \approx {X_{\mathcal{N}}}^T \tilde{\mathrm{H}}^{g_{mac}}_{\varphi_*, \psi_*} X_{\mathcal{N}} \; . \tag{6.6}$$

The terms in (6.6) suggest that $N(g_{mac}(\hat{\varphi}, \hat{\psi}) - g_{mac}(\varphi_*, \psi_*))$ is asymptotically approximated by a quadratic form, similar to one analyzed in Chapter 4 and Chapter 5.

6.3.1 Approximation of the quadratic form

Rewrite (6.6) to a general expression for the quadratic form $Q(\hat{X}_{\mathcal{N}})$ such that

$$Q(\hat{X}_{\mathcal{N}}) = \hat{X}_{\mathcal{N}}^T \tilde{\mathrm{H}}^{g_{mac}}_{\hat{\varphi}, \hat{\psi}} \hat{X}_{\mathcal{N}} \approx X_{\mathcal{N}}^T \tilde{\mathrm{H}}^{g_{mac}}_{\varphi_*, \psi_*} X_{\mathcal{N}} \approx N \left(g_{mac}(\hat{\varphi}, \hat{\psi}) - g_{mac}(\varphi_*, \psi_*) \right) \; . \tag{6.7}$$

Temporarily assume that the $\tilde{\mathrm{H}}^{g_{mac}}_{\varphi_*, \psi_*}$ is positive semidefinite. The distribution of the quadratic form is approximated, after [84], with a scaled $\chi^2_{l_{PT}}$ distribution with l_{PT}

degrees of freedom. The approximate probability distribution function of $Q(\hat{X}_{\mathcal{N}})$ writes

$$f_Q(y) = \frac{1}{\alpha} f_{\chi^2_{l_{PT}}} \left(\frac{y-\beta}{\alpha} \right) , \tag{6.8}$$

where $y \in [\beta, +\infty]$ and $f_Q(y) = 0$ for $y < \beta$. The respective scaling and shift parameters of the approximate distribution, α and β, are defined such that $\alpha = \sigma_Q/\sigma_{\chi^2}$ and $\beta = \mu_Q - (\mu_{\chi^2}\sigma_Q)/\sigma_{\chi^2}$. The mean μ_Q and standard deviation σ_Q of the quadratic form are computed using its first cumulants, c_1 and c_2, namely $\mu_Q = c_1$ and $\sigma_Q = \sqrt{2c_2}$, where the k-th asymptotic cumulant of $Q(\hat{X}_{\mathcal{N}})$ writes as

$$c_k = \text{tr}\left((\tilde{\text{H}}^g_{\varphi_*,\psi_*} \Sigma_{\varphi_*,\psi_*})^k \right) . \tag{6.9}$$

The mean μ_{χ^2} and standard deviation σ_{χ^2} of the $\chi^2_{l_{PT}}$ distribution are computed from its degrees of freedom l_{PT}, such that $\mu_{\chi^2} = l_{PT}$, $\sigma_{\chi^2} = \sqrt{2l_{PT}}$, where $l_{PT} = c_2^3/c_3^2$.

When both φ and ψ are estimates computed from the data the estimate of Hessian of $g_{mac}(\hat{\varphi}, \hat{\psi})$ writes as

$$\text{H}^{g_{mac}}_{\hat{\varphi},\hat{\psi}} = \begin{bmatrix} \text{H}^{g_{mac}}_{\hat{\varphi},\hat{\psi}_{1,1}} & \text{H}^{g_{mac}}_{\hat{\varphi},\hat{\psi}_{1,2}} \\ \text{H}^{g_{mac}}_{\hat{\varphi},\hat{\psi}_{2,1}} & \text{H}^{g_{mac}}_{\hat{\varphi},\hat{\psi}_{2,2}} \end{bmatrix} , \tag{6.10}$$

where its respective parts are defined as follows

$$\text{H}^{g_{mac}}_{\hat{\varphi},\hat{\psi}_{1,1}} = \begin{bmatrix} \frac{\partial^2 g_{mac}}{\partial\Re(\varphi)\partial\Re(\varphi)} & \frac{\partial^2 g_{mac}}{\partial\Im(\varphi)\partial\Re(\varphi)} \\ \frac{\partial^2 g_{mac}}{\partial\Re(\varphi)\partial\Im(\varphi)} & \frac{\partial^2 g_{mac}}{\partial\Im(\varphi)\partial\Im(\varphi)} \end{bmatrix} ,$$

$$\text{H}^{g_{mac}}_{\hat{\varphi},\hat{\psi}_{1,2}} = \begin{bmatrix} \frac{\partial^2 g_{mac}}{\partial\Re(\psi)\partial\Re(\varphi)} & \frac{\partial^2 g_{mac}}{\partial\Im(\psi)\partial\Re(\varphi)} \\ \frac{\partial^2 g_{mac}}{\partial\Re(\psi)\partial\Im(\varphi)} & \frac{\partial^2 g_{mac}}{\partial\Im(\psi)\partial\Im(\varphi)} \end{bmatrix} ,$$

$$\text{H}^{g_{mac}}_{\hat{\varphi},\hat{\psi}_{2,1}} = \begin{bmatrix} \frac{\partial^2 g_{mac}}{\partial\Re(\varphi)\partial\Re(\psi)} & \frac{\partial^2 g_{mac}}{\partial\Im(\varphi)\partial\Re(\psi)} \\ \frac{\partial^2 g_{mac}}{\partial\Re(\varphi)\partial\Im(\psi)} & \frac{\partial^2 g_{mac}}{\partial\Im(\varphi)\partial\Im(\psi)} \end{bmatrix} ,$$

and

$$\text{H}^{g_{mac}}_{\hat{\varphi},\hat{\psi}_{2,2}} = \begin{bmatrix} \frac{\partial^2 g_{mac}}{\partial\Re(\psi)\partial\Re(\psi)} & \frac{\partial^2 g_{mac}}{\partial\Im(\psi)\partial\Re(\psi)} \\ \frac{\partial^2 g_{mac}}{\partial\Re(\psi)\partial\Im(\psi)} & \frac{\partial^2 g_{mac}}{\partial\Im(\psi)\partial\Im(\psi)} \end{bmatrix} .$$

Notice that $\text{H}^{g_{mac}}_{\hat{\varphi},\hat{\psi}_{1,1}}$ is equal to $\text{H}^{g_{mac}}_{\hat{\varphi}}$ developed in (5.23), see Section 5.3.1. Since two cases for the MAC computation can be distinguished namely, $g_{mac}(\varphi_*, \psi_*) = \{0, 1\}$, the quadratic form in (6.7) can be represented by a different Hessian matrices; collinear by $\text{H}^{g_{mac},\text{collinear}}_{\varphi_*,\psi_*}$ and orthogonal by $\text{H}^{g_{mac},\text{orthogonal}}_{\varphi_*,\psi_*}$.

Lemma 6.2 *The $\chi^2_{l_{PT,j}}$ distribution used to approximate the distribution of $Q(\hat{X}_{\mathcal{N}})$ (6.7) has $l_{PT,j}$ degrees of freedom bounded between $1 \leq l_{PT,j} \leq 2r-2$ for all j.*

6.3.1.1 Collinear mode shapes

The Hessian (6.10), when two mode shapes correspond to the same theoretical mode, writes as

$$\mathrm{H}_{\varphi_*,\psi_*}^{g_{mac},\mathrm{collinear}} = \frac{2}{k^2 d_*} \begin{bmatrix} 1 & -k \\ -k & k^2 \end{bmatrix} \otimes \begin{bmatrix} T_{1,1}^* & T_{1,2}^* \\ T_{2,1}^* & T_{2,2}^* \end{bmatrix} ,$$

where the respective matrices T^* were defined in (D.52) in Appendix D.1. Derivation of the respective partial derivatives is also enclosed in Appendix D.1.

Lemma 6.3 *The Hessian* $\mathrm{H}_{\varphi_*,\psi_*}^{g_{mac},\mathrm{collinear}}$ *has non-positive eigenvalues thus is a negative semi-definite matrix. Its rank is* $\operatorname{rank}\left(\mathrm{H}_{\varphi_*,\psi_*}^{g_{mac},\mathrm{collinear}}\right) = 2r - 2$.

Proof: See Appendix D.2. □

Lemma 6.4 *In the case of collinear mode shapes the quadratic form* $Q(\hat{X}_{\mathcal{N}})$ *is positive semi-definite and can be formulated as follows*

$$Q(\hat{X}_{\mathcal{N}}) = \hat{X}_{\mathcal{N}}^T \tilde{\mathrm{H}}_{\hat{\varphi},\hat{\psi}}^{g,\mathrm{collinear}} \hat{X}_{\mathcal{N}} \approx \hat{X}_{\mathcal{N}}^T \tilde{\mathrm{H}}_{\varphi_*,\psi_*}^{g,\mathrm{collinear}} \hat{X}_{\mathcal{N}} \approx N\left(1 - g_{mac}(\hat{\varphi}, \hat{\psi})\right) ,$$

where $\tilde{\mathrm{H}}_{\varphi_*,\psi_*}^{g,\mathrm{collinear}} = -\mathrm{H}_{\varphi_*,\psi_*}^{g,\mathrm{collinear}}/2$.

Thus, the aforementioned quadratic form can be approximated by χ_l^2 distribution.

6.3.1.2 Orthogonal mode shapes

The Hessian (6.10), when two mode shapes are orthogonal, writes as

$$\mathrm{H}_{\varphi_*,\psi_*}^{g_{mac},\mathrm{orthogonal}} = \frac{2}{d_* e_*} \begin{bmatrix} U_{1,1}^* & U_{1,2}^* \\ (U_{1,2}^*)^T & U_{2,2}^* \end{bmatrix} ,$$

where the respective matrices U^* were defined in (D.54) in Appendix D.1. Derivation of the respective partial derivatives is also enclosed in Appendix D.1.

Lemma 6.5 *The Hessian* $\mathrm{H}_{\varphi_*,\psi_*}^{g_{mac},\mathrm{orthogonal}}$ *has positive eigenvalues thus is a positive semi-definite matrix. Its rank is* $\operatorname{rank}\left(\mathrm{H}_{\varphi_*,\psi_*}^{g_{mac},\mathrm{orthogonal}}\right) = 2r - 2$.

Proof: See Appendix D.3. □

Lemma 6.6 *In the case of orthogonal mode shapes the quadratic form* $Q(\hat{X}_{\mathcal{N}})$ *is positive semi-definite and can be expressed as*

$$\begin{aligned} Q(\hat{X}_{\mathcal{N}}) &= \hat{X}_{\mathcal{N}}^T \tilde{\mathrm{H}}_{\hat{\varphi},\hat{\psi}}^{g_{mac},\mathrm{orthogonal}} \hat{X}_{\mathcal{N}} \approx \hat{X}_{\mathcal{N}}^T \tilde{\mathrm{H}}_{\varphi_*,\psi_*}^{g_{mac},\mathrm{orthogonal}} \hat{X}_{\mathcal{N}} \\ &\approx N\left(g_{mac}(\hat{\varphi}, \hat{\psi})\right) , \end{aligned}$$

where $\tilde{\mathrm{H}}_{\varphi_*,\psi_*}^{g_{mac},\mathrm{orthogonal}} = \mathrm{H}_{\varphi_*,\psi_*}^{g_{mac},\mathrm{orthogonal}}/2$.

Thus, the aforementioned quadratic form can be approximated by χ_l^2 distribution.

6.3.2 χ^2_l approximation validation

In this section we test χ^2_l approximations from Lemma 6.4 and Lemma 6.6 on $g_{mac}(\hat{\varphi}^{1,12}, \hat{\psi}^{1,14})$, $g_{mac}(\hat{\varphi}^{1,\text{global}}, \hat{\psi}^{1,12})$ and $g_{mac}(\hat{\varphi}^{1,\text{global}}, \hat{\psi}^{3,\text{global}})$. As such, the deployed schemes are equivalent to ones depicted in Section 4.3.2 and Section 5.3.3 thus only the numerical results are presented.

A comparison of the CDFs of both $\overline{Q}_{\text{MAC}_{MC}}$ and v_1 is illustrated on the left parts of Figure 6.6 for $g_{mac}(\hat{\varphi}^{1,12}, \hat{\psi}^{1,14})$, Figure 6.7 for $g_{mac}(\hat{\varphi}^{1,\text{global}}, \hat{\psi}^{1,12})$ and Figure 6.8 for $g_{mac}(\hat{\varphi}^{1,\text{global}}, \hat{\psi}^{3,\text{global}})$. A comparison between CDFs of Z_{MC}, Z_{PT} computed for $g_{mac}(\hat{\varphi}^{1,12}, \hat{\psi}^{1,14})$, $g_{mac}(\hat{\varphi}^{1,\text{global}}, \hat{\psi}^{1,12})$ and $g_{mac}(\hat{\varphi}^{1,\text{global}}, \hat{\psi}^{3,\text{global}})$ with a theoretical χ^2_{4r-2} CDF is illustrated on the right parts of Figure 6.6 for the base-case 1, on Figure 6.7 for the base-case 2 and on Figure 6.8 for the base-case 3.

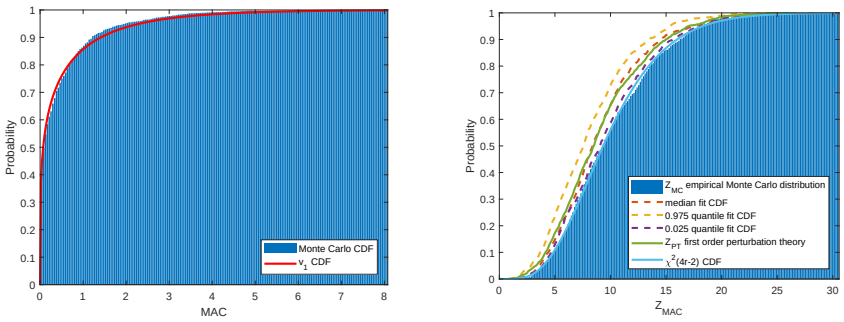

Figure 6.6: $\chi^2_{l_{MC}}$ CDF and CDF of the base-case 1 (left). Theoretical χ^2_{4r-2} CDF compared to CDF of Z_{MC} and Z_{PT} computed for the base-case 1 (right).

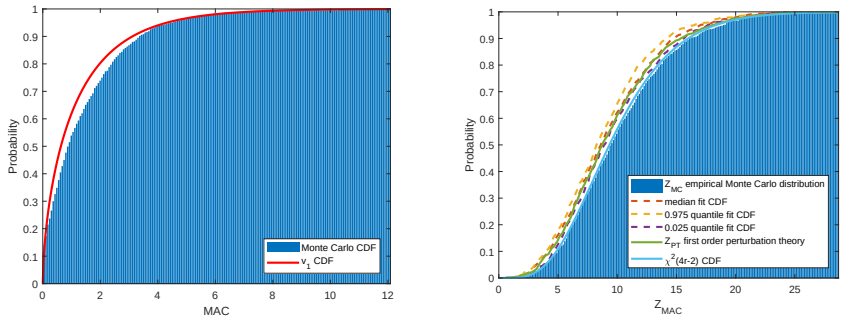

Figure 6.7: $\chi^2_{l_{MC}}$ CDF and CDF of the base-case 2 (left). Theoretical χ^2_{4r-2} CDF compared to CDF of Z_{MC} and Z_{PT} computed for the base-case 2 (right).

The left parts of Figures 6.6-6.8 illustrate that the both CDF of Monte Carlo histogram and its χ^2 approximation coincide, which indicates that the distributions of the investigated base-cases of MAC are well characterized by the quadratic form.

The right parts of Figures 6.6-6.8 show that the corrected Z_{MC} for Monte Carlo and the combined realizations from the perturbation theory Z_{PT} have, in the most of the

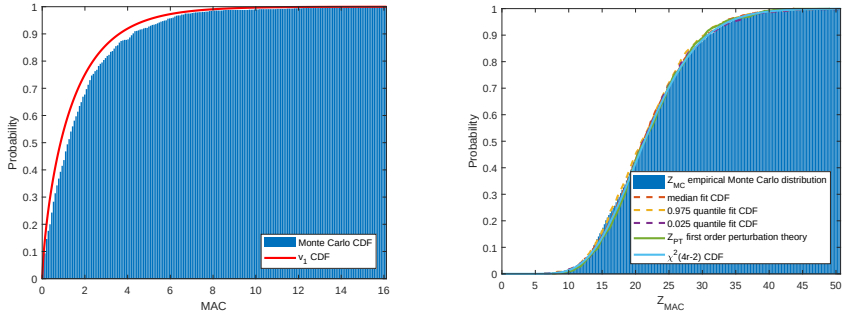

Figure 6.8: $\chi^2_{l_{MC}}$ CDF and CDF of the base-case 3 (left). Theoretical χ^2_{4r-2} CDF compared to CDF of Z_{MC} and Z_{PT} computed for the base-case 3 MAC (right).

cases, a similar CDF. It can be observed that distribution fits for $g_{mac}(\hat{\varphi}^{1,12}, \hat{\psi}^{1,14})$ are the least accurate, all slightly overestimating the quantiles of χ^2_{4r-2} distribution. That can result in a minor underestimation of the confidence bounds for that case of MAC computation. A possible cause for this is a relatively small sample size to characterize the uncertainty of $g_{mac}(\hat{\varphi}^{1,12}, \hat{\psi}^{1,14})$ case. For other cases of MAC computation $g_{mac}(\hat{\varphi}^{1,\text{global}}, \hat{\psi}^{1,12})$ and $g_{mac}(\hat{\varphi}^{1,\text{global}}, \hat{\psi}^{3,\text{global}})$ the CDF fits are accurate. This pleads for the validity of the perturbation theory to compute variances needed to characterize the quadratic distribution and yield similar distribution parameters as the full Monte Carlo histogram. Also, plots corresponding to the best, the median and the worst quantiles are all quite similar. They match the Monte Carlo and the perturbation-based Z plots. This means that almost any of the realizations among the Monte Carlo experiments can be used for the variance computation with the perturbation theory. The resultant variance estimate would be then equivalent to the variance of the Monte Carlo histogram.

The plots of the histograms of the Pearson χ^2 statistics are showed in the left parts of Figure 6.9 for $g_{mac}(\hat{\varphi}^{1,12}, \hat{\psi}^{1,14})$, Figure 6.10 for $g_{mac}(\hat{\varphi}^{1,\text{global}}, \hat{\psi}^{1,12})$ and Figure 6.11 for $g_{mac}(\hat{\varphi}^{1,\text{global}}, \hat{\psi}^{3,\text{global}})$. Consequently, a comparison of using the best, the median and the worst approximations of $g_{mac}(\hat{\varphi}^{1,12}, \hat{\psi}^{1,14})$, $g_{mac}(\hat{\varphi}^{1,\text{global}}, \hat{\psi}^{1,12})$ and $g_{mac}(\hat{\varphi}^{1,\text{global}}, \hat{\psi}^{3,\text{global}})$ to the χ^2_{4r-2} distribution is depicted on the respective right parts of Figure 6.9, Figure 6.10 and on Figure 6.11. The left parts of Figures 6.9-6.11 illustrate the dispersion of the distance between all the empirical histograms based on the perturbation theory. It can be seen that the empirical distribution of the Pearson histogram is close to its theoretical distribution for all the base-cases. The right parts of Figure 6.9-Figure 6.11 show the fitting of the MAC histogram by the perturbation-based densities corresponding to the selected quantiles. It can be seen that the considered distributions fit adequately to the empirical Monte Carlo histogram, even in the worst case of 0.95 quantile of the Pearson statistics.

6.3.3 Influence of sample size on χ^2 approximation

This section presents a study of the influence of the sample length on the underlying distributions of the MAC estimates obtained from the Monte Carlo simulations. All three base-cases of MAC are investigated. Three sample lengths are tested, namely $N = \{10000, 50000, 1000000\}$. The study is illustrated on Figures 6.12-6.14. As

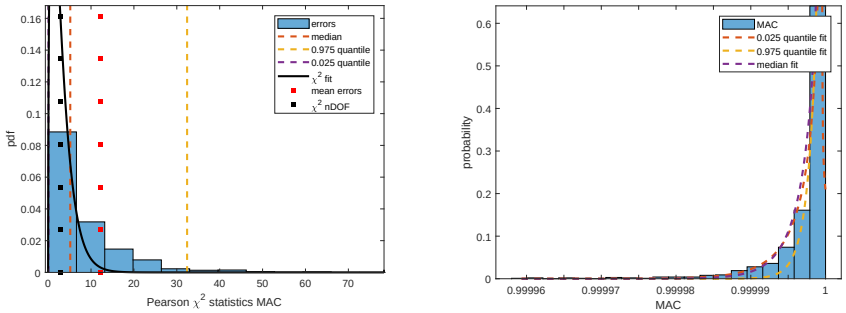

Figure 6.9: Histogram of errors in $\chi^2_{l_{PT}}$ approximation for the base-case 1 MAC (left). χ^2 fits to the empirical PDF of the base-case 1 MAC based on quantiles of Pearson statistics (right).

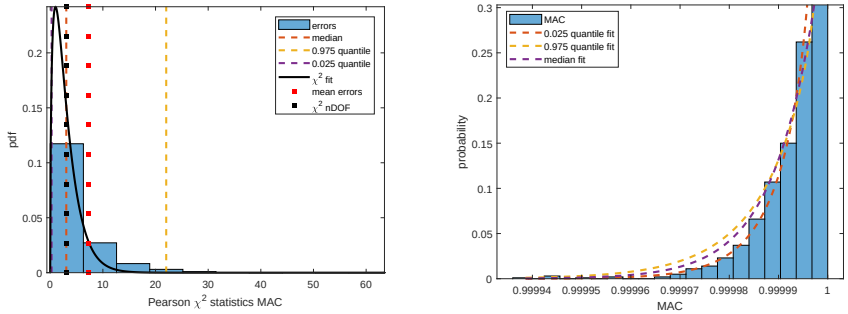

Figure 6.10: Histogram of errors in $\chi^2_{l_{PT}}$ approximation for the base-case 2 MAC (left). χ^2 fits to the empirical PDF of the base-case 2 MAC based on quantiles of Pearson statistics (right).

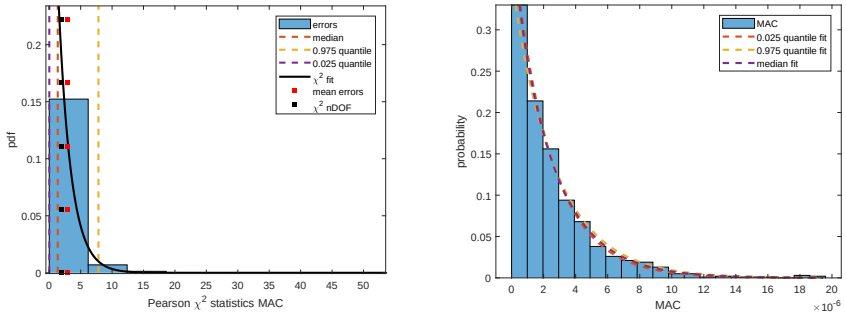

Figure 6.11: Histogram of errors in $\chi^2_{l_{PT}}$ approximation for the base-case 3 MAC (left). χ^2 fits to the empirical PDF of the base-case 3 MAC based on quantiles of Pearson statistics (right).

expected, the accuracy of the best, the median and the worst fits to the Monte Carlo

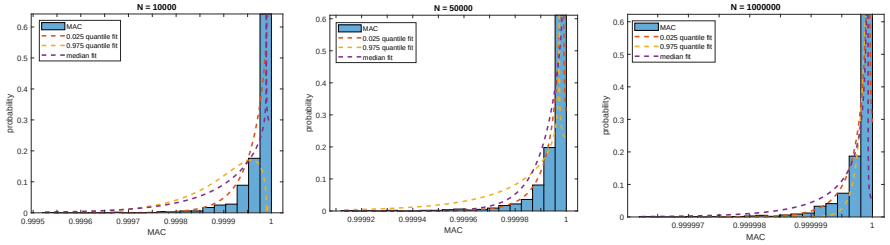

Figure 6.12: Scaled and shifted χ^2 fits to empirical probability distribution of MAC for the base-case 1 based on median, 0.95 and 0.025 quantiles of Pearson χ^2 statistics.

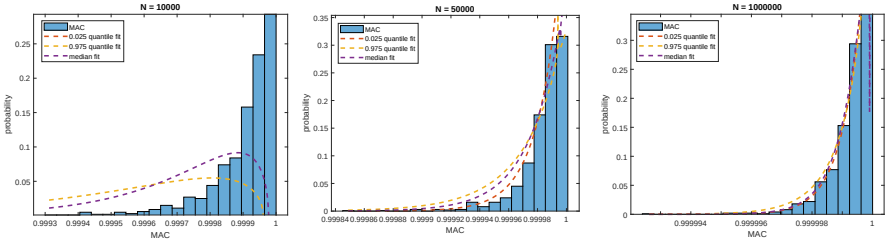

Figure 6.13: Scaled and shifted χ^2 fits to empirical probability distribution of MAC for the base-case 2 based on median, 0.95 and 0.025 quantiles of Pearson χ^2 statistics.

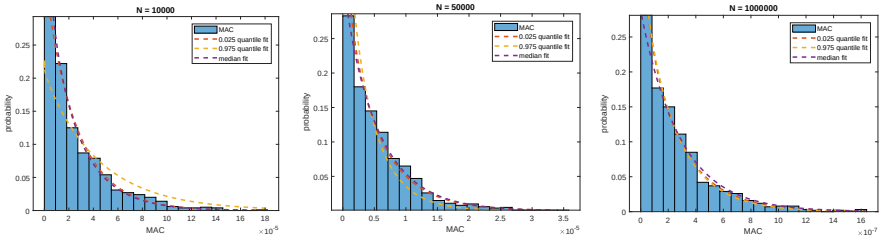

Figure 6.14: Scaled and shifted χ^2 fits to empirical probability distribution of MAC for the base-case 3 based on median, 0.95 and 0.025 quantiles of Pearson χ^2 statistics.

histograms increases with the number of samples used. The worst fits computed for $N = 10000$ samples, are inadequate to approximate the Monte Carlo histogram, in particular for the base-case 2, see Figure 6.13. In all three base-cases the worst fit dramatically improves for $N = 50000$ samples and is similar to the best and median fits in $N = 1000000$ samples case.

6.4 Formation of modal alignments based on the confidence intervals of MAC estimates

The formation of modal alignments can be improved with the information about the uncertainty in the MAC estimates. First, the confidence intervals of the χ^2 distribution approximating the quadratic form of MAC are computed. To avoid

selecting one mode shape from the modal alignment as a reference for the MAC computation, here, the MAC is computed between each mode shape from that alignment and the estimate of the global mode shape computed from the remaining vectors. That is summarized by the pseudo-algorithm presented below.

Algorithm 2: Computing χ^2 confidence intervals for the MAC estimates.

Input : Φ_m^a collection of m mode shapes from modal alignment a, p_Q^t threshold for probability of MAC estimate corresponding to quadratic form approximation.

Output : χ^2 confidence intervals for selected distribution quantile, u number of MAC estimates corresponding to the quadratic approximation with a probability larger then p_Q^t.

for $i = 1 : m$ **do**
- exclude i-th mode shape $\varphi^{a,i}$ from Φ_m^a ;
- compute $\varphi_i^{a,\text{global}}$ from the remaining $m-1$ mode shapes ;
- compute $g_{\text{mac}}(\varphi_i^{a,\text{global}}, \varphi_i^a)$;
- compute μ_Q, σ_Q, μ_{χ^2} and σ_{χ^2} ;
- compute confidence intervals of the approximating χ^2 distribution for selected distribution quantile ;
- compute p_Q as the probability of the approximating distribution to be quadratic, based on the computed χ^2 confidence intervals ;

end

return u based on p_Q^t and the computed collection of p_Q;

return the collection of χ^2 confidence intervals for each mode shape in the modal alignment ;

Subsequently, the estimates of MAC with p_Q lower then a selected threshold can be discarded and the Algorithm 2 can be repeated.

Algorithm 3: Selecting the MAC estimates in the modal alignment that corresponds to the same mode shape.

Input : Φ_m^a collection of m mode shapes from modal alignment a.

Output : Φ_u^a collection of u mode shapes from modal alignment a .

initialize Algorithm 2 with Φ_m^a input ;

retrieve u from the output of Algorithm 2 ;

while $u < m$ **do**
- select Φ_u^a corresponding to u MAC estimates inside the χ^2 confidence intervals ;
- assign $m = u$;
- repeat Algorithm 2 with Φ_u^a input ;
- retrieve u from the output of Algorithm 2 ;

end

return Φ_u^a corresponding to u MAC estimates ;

For an illustration, the proposed schemes are deployed for the realization of the Monte Carlo simulations that corresponds to data set used to establish Figure 6.2 in Section 6.1. A threshold for the probability of quadratic form approximation $p_Q^t = 0.6$ is used. In addition, a global estimate of the MPC $g_{mpc}(\hat{\varphi}^{a,\text{global}})$ is computed. Here the latter Figure is updated by the global estimates of the MPC and their corresponding 95% confidence bounds. The 95% confidence bounds for the MPC

indicator are computed with the strategy developed in Chapter 4, for the real mode shape case.

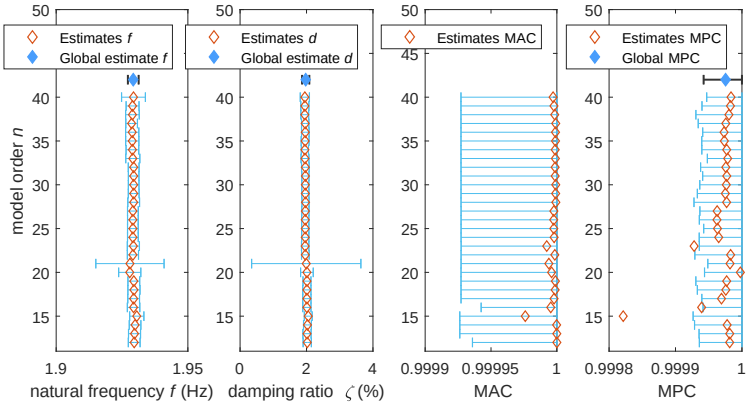

Figure 6.15: Estimates of natural frequencies, damping ratios, MAC and MPC from the first modal alignment with the corresponding 95% confidence intervals.

It can be observed that the estimates of the MAC computed for each model order are within χ^2 confidence intervals, indicating that the underlying mode shapes correspond to the same mode. The estimated uncertainties are small however, apart from illustrating the variances in the estimates of the MAC and MPC, the variances of both indicators reflect the underlying variances of the mode shape estimates.

6.5 Application

This section illustrates the application of the proposed framework to the measurements collected from the experimental plate used previously in Section 3.3.1 and Section 5.4. The data set of 491518 samples is used. The modal parameters are identified with SSI-UPC using 20 time lags to compute the Hankel matrix and 200 blocks for its covariance computation. System orders are in range of $10 - 80$. A threshold of 2.5% on the maximum standard deviation of the estimated natural frequencies is used to reject the uncertain estimates. The stabilization diagram of the natural frequencies with their corresponding confidence intervals is illustrated on Figure 6.16. Nine stable and well excited modes of the plate are tracked based on the criteria given at the beginning of this chapter in Section 6.1. To filter the stabilization diagrams from the estimates of the modes that do not correspond to the same mode shape three iterations of Algorithm 3 are performed. A threshold for the probability of quadratic form approximation $p_Q^t = 0.6$ is used. Figure 6.17 illustrates the stabilization diagram of the MAC values and their corresponding 95% confidence intervals computed for the mode shapes from the first 4 modal alignments for the first iteration of Algorithm 3. It can be observed that some estimates of the MAC at lower system orders are outside the χ^2 confidence bounds. Those will be discarded in the next iteration of Algorithm 3 as showed on Figure 6.18.

After the third iteration the resultant alignments of the MAC estimates are more stable. It is expected that the modification of the modal alignments will change

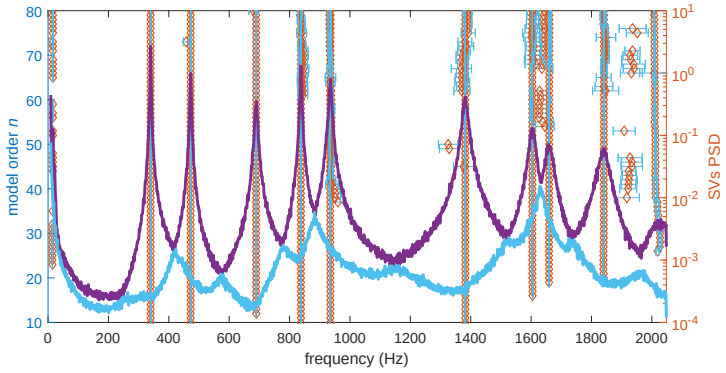

Figure 6.16: Stabilization diagram of the natural frequencies of the experimental plate.

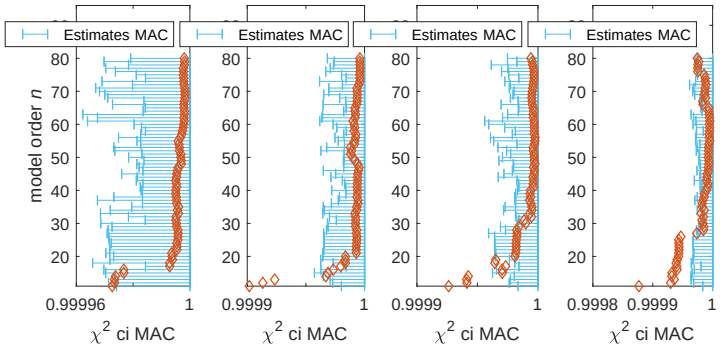

Figure 6.17: Estimates of MAC from the first 4 modal alignments with the corresponding 95% confidence intervals. First iteration of Algorithm 3.

the global estimates of natural frequencies and damping ratios by removing those estimates that do not correspond to the same mode. That is illustrated on Figure 6.19 for the first mode, and on Figure 6.20 for the third mode. For both the first and the third mode of the plate, the proposed approach rejects estimates of modal parameters at low system orders. From Figure 6.19 and Figure 6.20 it can be observed that the discarded estimates were the ones diverging the most from the global estimates of the considered modal parameter.

6.6 Conclusions

In this chapter we addressed the uncertainty quantification of MAC indicator from the stabilization diagram. Two cases for its computation were distinguished. In the first, the MAC was computed between two mode shapes estimated from one modal alignment. The second considered the MAC between a global estimate of a mode shape and a mode shape from the corresponding alignment. In addition, a scheme to compute a global mode shape and its covariance was outlined. In the both considered cases the estimates of MAC are on the boundary of $[0, 1]$ interval, thus the quadratic

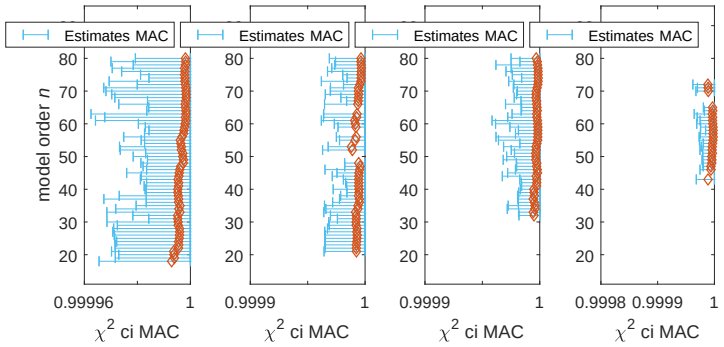

Figure 6.18: Estimates of MAC from the first 4 modal alignments with the corresponding 95% confidence intervals. Last iteration of Algorithm 3.

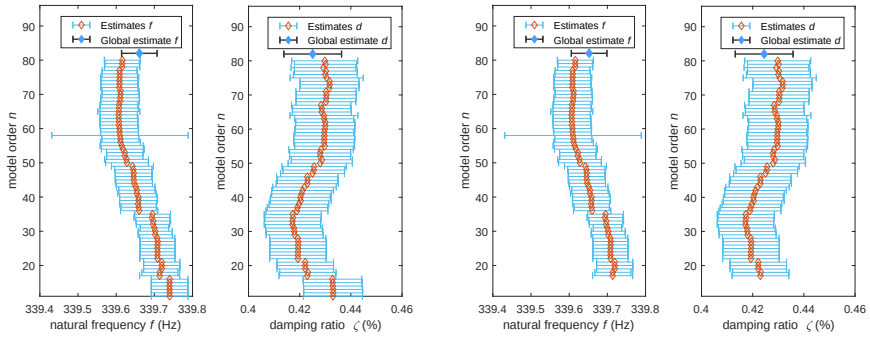

Figure 6.19: Stabilization diagram of natural frequencies and damping ratio estimates from the first mode. Initial diagram (left) and after (right) the rejection of estimates outside the confidence intervals of MAC.

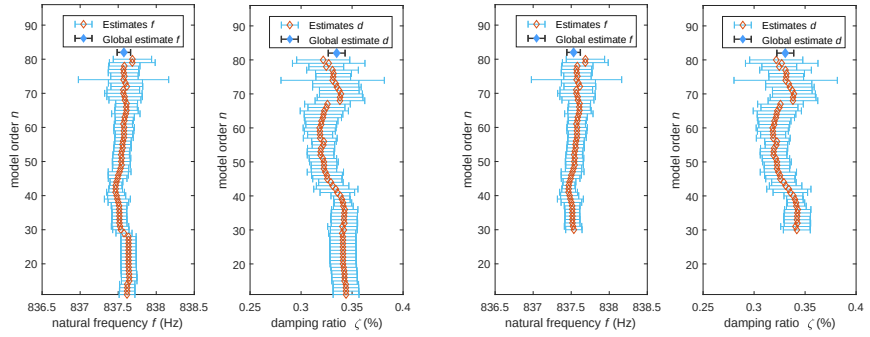

Figure 6.20: Stabilization diagram of natural frequencies and damping ratio estimates from the third mode. Initial diagram (left) and after (right) the rejection of estimates outside the confidence intervals of MAC.

framework for their uncertainty quantification was used. Two general cases of the quadratic approximations were distinguished, namely the first, where the two mode shapes used for MAC computation are collinear and the second, where the mode shapes are orthogonal. For both it was showed that the MAC indicator yields a quadratic form which can be asymptotically approximated by a shifted and scaled χ^2 distribution, whose statistical properties were proved in the course of this chapter. The proposed approximations were tested on simulations of a chain system and some strategies for their numerical validation, similar to ones used in the previous chapters, were applied to the numerical Monte Carlo simulation. The real-life application of the proposed framework was deployed to the experimental plate example where the MAC estimates for different modal alignments were presented together with their underlying confidence intervals.

6.7 Dissemination

Parts of this chapter have been published in:

[8] S. Gres, M. Döhler, P. Andersen, L. Mevel, Variance computation of MAC and MPC for real-valued mode shapes from the stabilization diagram, in: IOMAC - 8th International Operational Modal Analysis Conference, Copenhagen, Denmark, 2019.

Furthermore, this chapter is currently in preparation for the submission to Mechanical Systems and Signal Processing journal.

CHAPTER 7

Hankel matrix normalization for robust damage detection

In this chapter, a new damage detection residual using the difference of the Hankel matrices in the reference state and the excitation normalized Hankel matrix in the tested, potentially damaged state, is derived. The proposed metric can be used in the SHM systems designed for structures subjected to challenging excitation conditions.

As such, the aforementioned residual is evaluated in the local asymptotic approach for Gaussian residuals framework [2] and to decide about the health of the system, the resultant value of the test is compared to a threshold. The robustness of the new approach is achieved via a normalization scheme that is adapted from the multipatch subspace-based damage identification [3]. Its influence on the residual is thoroughly studied from a theoretical point of view. The major result achieved in this chapter is that the mean value of the proposed residual does not depend on the variances of the excitation. Some practical considerations regarding the implementation of the proposed method are given. The proposed approach is tested on numerical simulations, and experimental data from the laboratory and real-data from two full scale bridges.

In short, this chapter comprises

- illustrative example depicting how changes in the covariance of the ambient excitation affect the popular data-based damage detection metrics,
- development of a damage detection residual based on a difference of Hankel matrices in the reference state and the excitation normalized Hankel matrix in the tested states,
- derivation of a damage detection test using statistical properties of the proposed damage detection residual,
- verification of the proposed test on a numerical Monte Carlo simulations,
- application of the proposed approach on the real-life examples of experimental plate, Dogna bridge and Z24 bridge.

7.1 Background and illustrative example

Hankel matrices built from output covariance sequences contain the dynamic behavior of the underlying mechanical system, hence they are often used for damage detection. It is well known that changes in the excitation conditions influence properties of Hankel matrices, which consequently afflicts the performance of the damage detection metrics constructed from such matrices, when no proper normalization is applied, and renders it impossible to use in practice.

In this section, the influence of changing excitation covariance on the Hankel matrix-based damage detection residuals is recalled. First, the expression to compute the Hankel matrices from output covariance sequences and its dependence on the excitation properties are given, based on [134, 17].

Let $R_i = \mathrm{E}(y_k y_{k-i}^{\mathrm{pcT}})$ be the theoretical covariance of the discrete measurements y_k at time lag i, also called *output covariances*, where superscript 'pc' denotes r_0 projection channels. The collection of R_i can be stacked to form a block Hankel matrix $\mathcal{H} \in \mathbb{R}^{(p+1)r \times qr_0}$ of output covariance sequences such that

$$\mathcal{H} = \begin{bmatrix} R_1 & R_2 & \vdots & R_q \\ R_2 & R_3 & \vdots & R_{q+1} \\ \vdots & \vdots & \vdots & \vdots \\ R_{p+1} & R_{p+2} & \vdots & R_{p+q} \end{bmatrix} , \tag{7.1}$$

where p, q are parameters with usually $p = q+1$, r labels the total number of channels. The estimates $\hat{R}_i$ and consequently $\hat{\mathcal{H}}$ can be computed from the sample covariance from past $\mathcal{Y}^+$ and future $\mathcal{Y}^-$ data horizons such that $\hat{\mathcal{H}} = \mathcal{Y}^+ \mathcal{Y}^{-T}$, where both $\mathcal{Y}^+$ and $\mathcal{Y}^-$ were introduced in Section 2.1.1. The theoretical output covariance can be factorized such that

$$R_i = C_n A_n^{i-1} \mathrm{E}(x_{k+1} y_k^T) = C_n A_n^{i-1} G , \tag{7.2}$$

where $x_k \in \mathbb{R}^n$ are the states; $A_n \in \mathbb{R}^{n \times n}$, $C_n \in \mathbb{R}^{r \times n}$ are the state and observation matrices and $G = \mathrm{E}(x_{k+1} y_k^T)$ denotes the cross covariance between the states and the outputs. The Hankel matrix enjoys the factorization property into $\mathcal{H} = \Gamma(C_n, A_n)\mathcal{C}(A_n, G)$ matrix where the observability $\Gamma(C_n, A_n)$ and controlability $\mathcal{C}(A_n, G)$ matrices are defined as

$$\Gamma(C_n, A_n) = \begin{bmatrix} C_n \\ C_n A_n \\ \vdots \\ C_n A_n^p \end{bmatrix} , \quad \mathcal{C}(A_n, G) = \begin{bmatrix} G & A_n G & \dots & A_n^{q-1} G \end{bmatrix} . \tag{7.3}$$

The influence of process (excitation) and output noise properties on the output covariance sequences and consequently on the Hankel matrix can be identified with a formulation of forward stochastic model after [17]

$$\mathrm{E}[x_k \; x_k^T] = \Sigma_s = A_n \Sigma_s A_n^T + Q , \tag{7.4}$$

$$\mathrm{E}[y_k \; y_k^T] = R_0 = C_n \Sigma_s C_n^T + R , \tag{7.5}$$

$$\mathrm{E}[x_{k+1} \; y_k^T] = G = A_n \Sigma_s C_n^T + S . \tag{7.6}$$

The noise covariance matrices are defined as

$$\mathrm{E}\left[\begin{pmatrix} w_m \\ v_m \end{pmatrix} \begin{pmatrix} w_n & v_n \end{pmatrix}\right] = \begin{bmatrix} Q & S \\ S^T & R \end{bmatrix} \delta_{mn} \ . \tag{7.7}$$

A variation in the process noise covariance Q affects the Lyapunov equation for the state covariance (7.4) which both modifies the covariance between the measurements (7.5) and the covariance between measurements and the states (7.5). That leads to a change in the stochastic part of the Hankel matrices build from those output covariance sequences. Therefore a damage detection test employing data sets from different excitation levels should appreciate a change in the variance of the process noise by using a robust features or adopting a proper normalization scheme.

7.1.1 Illustrative example

Here we will set up a numerical experiment to illustrate the effect of changing excitation properties on the empirical damage detection metrics depicted in paragraph 7.1.1.1. This simple numerical example will accompany this chapter for the numerical validation of the investigated methods. It will be illustrated that the empirical methods do not work satisfactory when the covariance of the excitation is varying, thus the following example will be a support of the new scheme for damage detection proposed further in this chapter.

The studied case is a theoretical 6 DOF chain-like system that, for any consistent set of units, is modeled with a proportional damping matrix, spring stiffness $k_1 = k_3 = k_5 = 100$ and $k_2 = k_4 = k_6 = 200$ and mass $m_{1-6} = 1/20$. The system is subjected to a noise signal with a changing excitation covariance Q and acting at all DOFs. Responses are measured at 1, 3 and 6 DOF. The simulation campaign consists of the reference built with $N_0 = 2 \cdot 10^6$ data points and the tested states, each simulated with $N = 10^5$. Different excitation covariance scenarios are considered, namely

- first, the most simple theoretical case, when Q is the diagonal matrix $\mathcal{I}_6$,
- second, where every excitation point is scaled with a random scalar constant a such that $Q = a \cdot \mathcal{I}_6$,
- third, the most general case, where $Q = a \cdot bb^T$ where $b \in \mathbb{R}^{6\times 6}$ is a randomly generated matrix whose entries follow the standard normal distribution.

The damage is modeled as a gradual stiffness reduction of the second (unmeasured) DOF. A Gaussian white noise with a 5% of the standard deviation of the output is added to the response at each measurement channel.

7.1.1.1 Empirical damage detection residuals based on a difference of Hankel matrices

Four empirical countermeasures developed here are based on a Mahalanobis distance [139] computed on the estimates of Hankel matrices from respectively reference $\hat{\mathcal{H}}_{ref}$ and tested states $\hat{\mathcal{H}}_{test}$ with their corresponding covariance matrices $\Sigma_{\hat{\mathcal{H}}_{ref}}$ and $\Sigma_{\hat{\mathcal{H}}_{test}}$. Some empirical normalization of the Hankel matrices is deployed to tests its ability to counter the excitation schemes formulated in the section above. The presented schemes are corresponding to the respective distance metrics d_1 (7.8) - d_4 (7.11).

For the first measure, the variance is computed on the reference data. This is the classical distance formulation as known in the literature which writes as

$$d_1(\hat{\mathcal{H}}_{ref}, \hat{\mathcal{H}}_{test}) = \sqrt{\mathrm{vec}(\hat{\mathcal{H}}_{ref} - \hat{\mathcal{H}}_{test})^T \Sigma^{-1}_{\hat{\mathcal{H}}_{ref}} \mathrm{vec}(\hat{\mathcal{H}}_{ref} - \hat{\mathcal{H}}_{test})} \,. \tag{7.8}$$

For the second, the variance corresponds to the variance of the tested Hankel matrix and is recomputed every time for a new data set to be compared with the reference one

$$d_2(\hat{\mathcal{H}}_{ref}, \hat{\mathcal{H}}_{test}) = \sqrt{\mathrm{vec}(\hat{\mathcal{H}}_{ref} - \hat{\mathcal{H}}_{test})^T \Sigma^{-1}_{\hat{\mathcal{H}}_{test}} \mathrm{vec}(\hat{\mathcal{H}}_{ref} - \hat{\mathcal{H}}_{test})} \,. \tag{7.9}$$

In the third, the data themselves are re-normalized with an estimate of its autocorrelation matrix R_0.

$$d_3(\hat{\mathcal{H}}_{ref}, \hat{\mathcal{H}}_{est}) = \sqrt{\mathrm{vec}(\hat{\mathcal{H}}^W_{ref} - \hat{\mathcal{H}}^W_{test})^T \Sigma^{-1}_{\hat{\mathcal{H}}^W_{ref}} \mathrm{vec}(\hat{\mathcal{H}}^W_{ref} - \hat{\mathcal{H}}^W_{test})} \,, \tag{7.10}$$

where $\hat{\mathcal{H}}^W = W^{-1}\hat{\mathcal{H}}W^{-1}_{\mathrm{pc}}$. The normalization factors W and W_{pc} write as

$$W = \mathcal{I}_{(p+1)r} \otimes W_r, \;\; W_r = (R_0)^{1/2} = \Big(\mathrm{E}(y_k y_k^T)\Big)^{1/2}$$

and

$$W_{\mathrm{pc}} = \mathcal{I}_{(p+1)r} \otimes W_{r,\mathrm{pc}}, \;\; W_{r,\mathrm{pc}} = \Big(\mathrm{E}(y_k^{\mathrm{pc}} y_k^{\mathrm{pc}T})\Big)^{1/2} \,.$$

Notice that quantities W_{pc} and W have to be estimated. Finally, putting the variances of both datasets together is tested

$$d_4(\hat{\mathcal{H}}_{ref}, \hat{\mathcal{H}}_{test}) = \sqrt{\mathrm{vec}(\hat{\mathcal{H}}^W_{ref} - \hat{\mathcal{H}}^W_{test})^T \Sigma^{-1}_{\hat{\mathcal{H}}^W} \mathrm{vec}(\hat{\mathcal{H}}^W_{ref} - \hat{\mathcal{H}}^W_{test})} \,, \tag{7.11}$$

where $\Sigma_{\hat{\mathcal{H}}^W} = \Sigma_{\hat{\mathcal{H}}^W_{ref}} + \Sigma_{\hat{\mathcal{H}}^W_{test}}$ accounts for the uncertainty in both tested and reference data sets.

7.1.1.2 Empirical evaluation of current methods

The distances defined in the section above are tested on the numerical validation example and are depicted on Figures 7.1 - 7.4. In each example the reference data are computed multiple times with a constant noise variance of $Q = I_6$. Subsequently the metrics are evaluated on the reference sets, which is considered to cover a full range of the reference values and any value higher than those is considered as representative for a damaged set. Multiple choices of both Q and damages are considered. Those are color coded and depicted on the legends of the respective plots. Firstly a simple scaling for $Q = \mathcal{I}_6$ is tested. A method failing this variation would fail any other more complicated change.

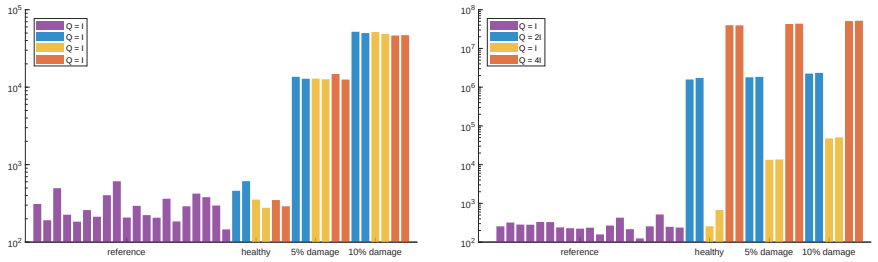

Figure 7.1: Damage detection with residual constructed with unnormalized Hankel matrices and covariance computed once in the reference state. Distance d_1 (7.8).

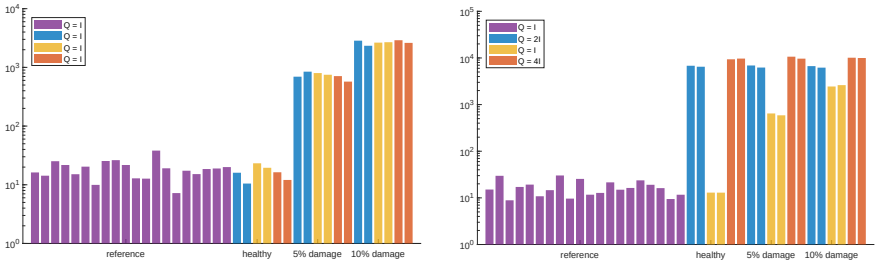

Figure 7.2: Damage detection with residual constructed with unnormalized Hankel matrices and covariance computed only on each tested data set. Distance d_2 (7.9).

Performance of the classical Mahalanobis distances, when the covariance of the reference is computed either in the reference or current state, is good when the input properties are kept constant, which is expected, as seen on Figure 7.1 (left) and Figure 7.2 (left). However, the classical Mahalanobis distance computed on Hankel matrices fails to detect faults or exhibit false alarms as seen both on Figure 7.1 (right) and Figure 7.2 (right) when the variance of the input noise is fluctuating. An empirical attempt to overcome that is by normalizing the measurements by the autocorrelation matrix R_0 as illustrated by d_3 metric (7.10). The results from that scheme are depicted on Figure 7.3. When normalizing with R_0, different scaling for the noise covariance

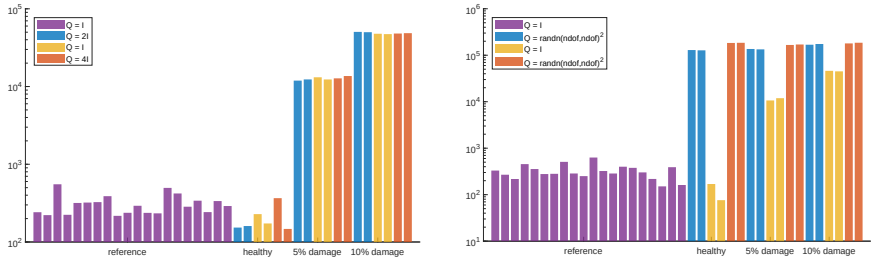

Figure 7.3: Damage detection with residual constructed with Hankel matrices normalized by R_0 and covariance computed once in the reference state. Distance d_3 (7.10).

can be handled as illustrated on Figure 7.3 (left), whereas more complex Q matrices yield false alarms and bad performance for the detection on Figure 7.3 (right). One possible strategy to handle that is to account for the variance of the Hankel matrix both in the reference and the tested states. That is represented by d_4 scheme and depicted on Figure 7.4. Distance d_4 depicted on Figure 7.4 yields similar results to

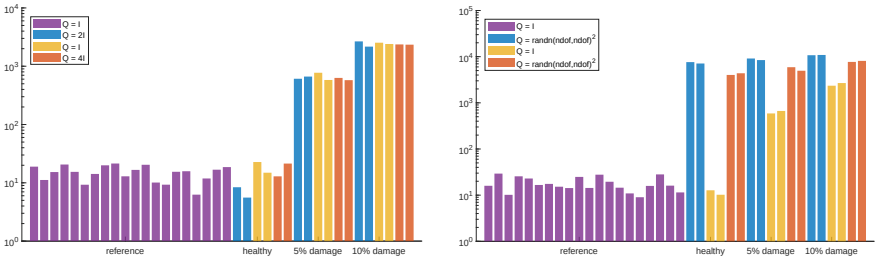

Figure 7.4: Damage detection with residual constructed with unnormalized Hankel matrices and covariance including both the reference and tested states. Distance d_4 (7.11).

ones from Figure 7.3, not handling more complex changes in the excitation covariance, despite taking into account the covariance of both Hankel matrices. Still, it is an idea that will be investigated further in this chapter.

7.2 Damage detection residual based on robust normalization

In this section a new damage detection residual is derived. The proposed metric takes into account the changes in the excitation covariance by a robust normalization scheme. It is shown that the newly developed distance fits in a well-known and previously published, e.g. in [2, 128, 129], local asymptotic approach for change detection. In this framework the distance is a Gaussian residual, whose mean is defined for both safe and damage scenarios. This section outlines the schemes to compute the mean and the variance of the proposed residual. Subsequently, a hypothesis test to distinguish between healthy and damage states is developed. Two versions of the test are proposed. Both tests follow a χ^2 distribution, whose mean is robust to changes in the excitation covariance under a null hypothesis, which is proved in Section 7.3.1. The proposed schemes are validated with a numerical simulation.

7.2.1 Normalization scheme

Let $\mathcal{H}_{ref}$ and $\mathcal{H}_{test}$ be exact Hankel matrices of rank n, computed for a system in the unchanged state, subjected to excitation with different covariances Q_{ref} and Q_{test}. The SVD of juxtaposed $\mathcal{H}_{ref}$ and $\mathcal{H}_{test}$ writes

$$\begin{bmatrix}\mathcal{H}_{ref} & \mathcal{H}_{test}\end{bmatrix} = \begin{bmatrix}U_s & U_{ker}\end{bmatrix} \begin{bmatrix}D_s & 0\\ 0 & 0\end{bmatrix} \begin{bmatrix}V_{s,ref}^T & V_{s,test}^T\\ V_{ker,ref}^T & V_{ker,test}^T\end{bmatrix}, \tag{7.12}$$

where $\text{rank}(\begin{bmatrix}\mathcal{H}_{ref} & \mathcal{H}_{test}\end{bmatrix}) = n$, $U_s \in \mathbb{R}^{(p+1)r\times n}$ are left singular vectors, $D_s \in \mathbb{R}^{n\times n}$ are non-zero singular values and $V_s^T = \begin{bmatrix}V_{s,ref}^T & V_{s,test}^T\end{bmatrix} \in \mathbb{R}^{n\times 2qr_0}$ are right singular

vectors corresponding to $\mathcal{H}_{ref}$ and $\mathcal{H}_{test}$ respectively. Now define $\mathcal{Z}_{ref} = D_s V_{s,ref}^T$ and $\mathcal{Z}_{test} = D_s V_{s,test}^T$, where both $\mathcal{Z}_{ref}$ and $\mathcal{Z}_{test}$ are full row rank. Since the converged Hankel matrices share the same observability matrix in the reference state (independently of the excitation), it holds

$$\begin{bmatrix} \mathcal{H}_{ref} & \mathcal{H}_{test} \end{bmatrix} = U_s \begin{bmatrix} \mathcal{Z}_{ref} & \mathcal{Z}_{test} \end{bmatrix} . \tag{7.13}$$

To compare $\mathcal{H}_{ref}$ with $\mathcal{H}_{test}$ a proper normalization of the later matrix must be deployed, due to a change in the excitation. In order to do so, a normalization scheme is proposed, that is based on a multipatch SSI normalization strategy from [3]. The scheme writes

$$\overline{\mathcal{H}}_{test} = \mathcal{H}_{test} \mathcal{Z}_{test}^{\dagger} \mathcal{Z}_{ref} , \tag{7.14}$$

where $\overline{\mathcal{H}}_{test}$ is a Hankel matrix sharing the same stochastic controlability matrix as $\mathcal{H}_{ref}$. Based on the latter expression a residual for damage detection robust to a changes in the excitation covariance can be defined.

7.2.2 Parametric residual

In order to build a residual that will indicate a change only in the underlying eigenstructure of the system, a parameter that defines the state of the system must be introduced first. Typical parameters in engineering applications are the estimates of modal parameters or stiffness/mass properties of the mechanical system [133].

Definition 7.1 *Let $\theta \in \Theta$ denote a general parameterization of the structural properties of the considered problem in a parameter space Θ. Thus, measured data (Y_k) is generated based on θ, variances of the input (Q) and measurement noise. Call $\mathcal{H}(\theta)$ the exact Hankel matrix corresponding to the structure in state θ and $\hat{\mathcal{H}}^{\theta}$ as the estimate of $\mathcal{H}(\theta)$ based on the measured data $(Y_k)_N$. Note that N here is the sample size of Y. Recall that $\hat{\mathcal{H}}^{\theta}$ converges to $\mathcal{H}(\theta)$ as N goes to infinity.*

There are two residuals defined in this section. The first is an estimate of a non parametric metric that implicitly relies on the system parameters. The second is an asymptotic residual, which depends analytically on the system parameter through an exact Hankel matrices, which can be considered as a function of θ. To describe the former, first assume that $\mathcal{H}_{ref}(\theta_*)$ and $\mathcal{H}_{test}(\theta_*)$ are the Hankel matrices corresponding to the different excitations Q_{ref} and Q_{test}. Here θ_* denotes a nominal system parameter in the reference state. As such, a Singular Value Decomposition of the juxtaposed matrices can be written as

$$\begin{bmatrix} \mathcal{H}_{ref}(\theta_*) & \mathcal{H}_{test}(\theta) \end{bmatrix} = U_s \begin{bmatrix} \mathcal{Z}_{ref}(\theta_*) & \mathcal{Z}_{test}(\theta) \end{bmatrix} \tag{7.15}$$

where, under a healthy state for both matrices, the following relation holds

$$\mathcal{H}_{test}(\theta_*) \mathcal{Z}_{test}^{\dagger} \mathcal{Z}_{ref} - \mathcal{H}_{ref}(\theta_*) = 0 . \tag{7.16}$$

where θ_* is dropped for simplicity in $\mathcal{Z}_{ref}$ and $\mathcal{Z}_{test}$. The theoretical residual is defined as

$$\zeta(\theta) = \operatorname{vec} \left(\mathcal{H}_{test}(\theta) \mathcal{Z}_{test}^{\dagger} \mathcal{Z}_{ref} - \mathcal{H}_{ref}(\theta_*) \right) . \tag{7.17}$$

The estimate of the residual, $\hat{\zeta}^{\theta}$, can be obtained from the estimates of the Hankel matrices $\hat{\mathcal{H}}^{\theta_*}_{ref}$ and $\hat{\mathcal{H}}^{\theta}_{test}$ computed from the measured data and normalized with $\sqrt{N}$. Consequently, the system residual writes as

$$\hat{\zeta}^{\theta} = \sqrt{N}\text{vec}\left(\hat{\mathcal{H}}^{\theta}_{test}\hat{\mathcal{Z}}^{\dagger}_{test}\hat{\mathcal{Z}}_{ref} - \hat{\mathcal{H}}^{\theta_*}_{ref}\right) , \tag{7.18}$$

where $\hat{\mathcal{Z}}_{ref}$ and $\hat{\mathcal{Z}}_{test}$ are derived from the relation

$$\begin{bmatrix}\hat{\mathcal{H}}^{\theta_*}_{ref} & \hat{\mathcal{H}}^{\theta}_{test}\end{bmatrix} \approx \hat{U}_s \begin{bmatrix}\hat{\mathcal{Z}}_{ref} & \hat{\mathcal{Z}}_{test}\end{bmatrix} , \tag{7.19}$$

where $\hat{U}_s$ is of column size n.

Remark 7.2 (Regarding $\hat{\mathcal{H}}^{\theta}$ computed on data with different lengths) *In practice the length of the dataset in the reference state, here denote it as M, may be different than the number of samples in the tested state N. Thus, $\hat{\mathcal{H}}^{\theta_*}_{ref}$ is estimated on M whereas $\hat{\mathcal{H}}^{\theta}_{test}$ is computed on N samples. That is important for the development of the residual covariance, therefore this fact is distinguished by denoting Hankel matrix estimated in the reference state as $\hat{\mathcal{H}}^{\theta_*}_{ref,M}$ and the tested state by $\hat{\mathcal{H}}^{\theta}_{test,N}$.*

Evaluated on the reference state characterized with θ_* the expected value of the theoretical residual in (7.17) is zero. When computed under current (potentially damaged) state characterized with θ, the properties of the residual are unknown, however its distribution can be quantified with the asymptotic local approach for change detection as in e.g. [134]. Knowing the distribution parameters for the respective system states, the decision between the latter is achieved with hypothesis testing.

7.2.3 Asymptotic local approach for change detection

To quantify the distribution of the residual under system parameters θ_* and θ, for some large sample size N, when $N < M$, close hypotheses are assumed

$$\begin{aligned} &\text{H}_0 : \theta = \theta_* \quad \text{(healthy state)} , \\ &\text{H}_1 : \theta = \theta_* + \delta/\sqrt{N} \quad \text{(damaged state)} , \end{aligned} \tag{7.20}$$

where δ is unknown but fixed parameter defined as $\delta = \sqrt{N}(\theta - \theta_*)$ and the null H_0 and alternative H_1 hypotheses are formulated to detect small changes in θ_*. Recall the asymptotic properties of Hankel matrices

$$\begin{aligned} &\text{under H}_0 : \sqrt{M}\text{vec}\left(\hat{\mathcal{H}}^{\theta_*}_{ref,M} - \mathcal{H}_{ref}(\theta_*)\right) \xrightarrow{\mathcal{L}} \mathcal{N}(0, \Sigma_{\mathcal{H}_{ref}(\theta_*)}) , \\ &\text{under H}_0 : \sqrt{N}\text{vec}\left(\hat{\mathcal{H}}^{\theta_*}_{test,N} - \mathcal{H}_{test}(\theta_*)\right) \xrightarrow{\mathcal{L}} \mathcal{N}(0, \Sigma_{\mathcal{H}_{test}(\theta_*)}) , \\ &\text{under H}_1 : \sqrt{N}\text{vec}\left(\hat{\mathcal{H}}^{\theta}_{test,N} - \mathcal{H}_{test}(\theta_*)\right) \xrightarrow{\mathcal{L}} \mathcal{N}(\mathcal{J}^{\mathcal{H}_{test}}_{\theta_*}\delta, \Sigma_{\mathcal{H}_{test}(\theta_*)}) , \end{aligned} \tag{7.21}$$

where $\Sigma_{\mathcal{H}_{ref}(\theta_*)}$ and $\Sigma_{\mathcal{H}_{test}(\theta_*)}$ are respective asymptotic covariance of $\hat{\mathcal{H}}^{\theta_*}_{ref}$ and $\hat{\mathcal{H}}^{\theta}_{test}$. The Jacobian $\mathcal{J}^{\mathcal{H}_{test}}_{\theta_*} = \text{vec}\left(\partial\mathcal{H}_{test}/\partial\theta\ (\theta_*)\right)$ is the derivative of $\mathcal{H}_{test}(\theta)$ with respect to θ evaluated in θ_*. Let $\hat{h} = h_{M,N}$, $h(\theta)$ and h_* be defined as

$$\hat{h} = h_{M,N} = \begin{bmatrix}\text{vec}(\hat{\mathcal{H}}^{\theta_*}_{ref,M}) \\ \text{vec}(\hat{\mathcal{H}}^{\theta}_{test,N})\end{bmatrix} , \ h(\theta) = \begin{bmatrix}\text{vec}(\mathcal{H}_{ref}(\theta_*)) \\ \text{vec}(\mathcal{H}_{test}(\theta))\end{bmatrix} ,$$

where $h_* = h(\theta_*) = \lim_{M,N\to\infty} h_{M,N}$ and $\hat{\mathcal{H}}^{\theta_*}_{ref} = \hat{\mathcal{H}}^{\theta_*}_{ref,M}$, $\hat{\mathcal{H}}^{\theta}_{test} = \hat{\mathcal{H}}^{\theta}_{test,N}$ are computed on statistically independent data sets. To account for different data lengths, N and M, define a scalar c such that $\lim_{N,M\to\infty} M/N = c$. Next, define the function $g_{dd}(\cdot)$ generating residual from (7.18) such that

$$g_{dd}(\hat{h}) = g_{dd}(h_{M,N}) = \text{vec}\left(\hat{\mathcal{H}}^{\theta}_{test}\hat{\mathcal{Z}}^{\dagger}_{test}\hat{\mathcal{Z}}_{ref} - \hat{\mathcal{H}}^{\theta_*}_{ref}\right) , \tag{7.22}$$

$$g_{dd}(h_*) = \text{vec}\left(\mathcal{H}_{test}(\theta_*){\mathcal{Z}_{test}}^{\dagger}\mathcal{Z}_{ref} - \mathcal{H}_{ref}(\theta_*)\right) . \tag{7.23}$$

The normalization matrices $\hat{\mathcal{Z}}_{ref}$ and $\hat{\mathcal{Z}}_{test}$ yield $\hat{\mathcal{Z}}_{ref} = \hat{D}_s\hat{V}^T_{s,ref}$ and $\hat{\mathcal{Z}}_{test} = \hat{D}_s\hat{V}^T_{s,test}$ after (7.19). The residual of the system can be written as

$$\hat{\zeta}^{\theta} = \sqrt{N}\left(g_{dd}(\hat{h}) - g_{dd}(h_*)\right) . \tag{7.24}$$

Notice that albeit both M and N tend to infinity, what matters is the relative speed between M and N, which is described by c. The normalizing term is $\sqrt{N}$, since it relates to the possibly damaged data set, about which a decision has to be made. That is investigated in Lemma 7.3 and subsequently in its proof. The asymptotic properties of (7.24) are derived using the Delta method and summarized in Lemma 7.3. For details on the Delta method see Appendix 2.2.1.

Lemma 7.3 *The residual in* (7.24) *is asymptotically Gaussian with following properties*

$$\text{under } \mathrm{H}_0 : \hat{\zeta}^{\theta_*} \xrightarrow{\mathcal{L}} \mathcal{N}(0, \Sigma_\zeta) , \tag{7.25}$$

$$\text{under } \mathrm{H}_1 : \hat{\zeta}^{\theta} \xrightarrow{\mathcal{L}} \mathcal{N}(\mathcal{J}^{\zeta}_{\theta_*}\delta, \Sigma_\zeta) , \tag{7.26}$$

where $\mathcal{J}^{\zeta}_{\theta_*} = \partial g_{dd}h/\partial\theta\ (\theta_*) = \mathcal{J}^{g_{dd}}_{h_*}\mathcal{J}^{h}_{\theta_*}$ *is the asymptotic sensitivity of residual with respect to parameter* θ *in* θ_* *and* $\Sigma_\zeta = \mathcal{J}^{g_{dd}}_{h_*}\Sigma_{c,h_*}(\mathcal{J}^{g_{dd}}_{h_*})^T$*, where* $\mathcal{J}^{g_{dd}}_{h_*} = \partial g_{dd}/\partial h\ (h_*)$*. The covariance* Σ_{c,h_*} *writes*

$$\Sigma_{c,h_*} = \begin{bmatrix} c^{-1}\Sigma_{\mathcal{H}_{ref}(\theta_*)} & 0 \\ 0 & \Sigma_{\mathcal{H}_{test}(\theta_*)} \end{bmatrix} .$$

Proof: See Appendix E.1. □

In practice, when more data is collected in the reference state $M > N$, which is usually the case, the variance of $\hat{\mathcal{H}}^{\theta_*}_{ref}$ decreases, hence the contribution of $\Sigma_{\mathcal{H}_{ref}(\theta_*)}$ is lower. Naturally, the opposite applies when $M < N$ where the contribution of $\Sigma_{\mathcal{H}_{ref}(\theta_*)}$ in Σ_{c,h_*} becomes predominant. Notice also that the normalization can be done either with M or N.

7.2.4 Hypothesis test

Based on the local approach, the residual in (7.25) is asymptotically Gaussian under both hypotheses, hence a decision between the latter can be achieved by applying the Generalized Likelihood ratio (GLR) test [2], [128]. It is well established that the GLR test statistics for asymptotically Gaussian distributions, like in (7.25)-(7.26), is χ^2 distributed [129].

When no choice on the parametrization is made, a simple test can be defined.

Proposition 7.4 (Non-parametric test) *A non-parametric test writes as*

$$t_{\text{global}}^{\text{np}} = (\hat{\zeta}^{\theta})^T \, \widehat{\Sigma}^{-1} \, \hat{\zeta}^{\theta} \ , \tag{7.27}$$

where $\widehat{\Sigma}$ is a consistent estimate of Σ_ζ. The resultant test value should be compared to a threshold computed empirically from the realizations of the test in the reference state.

When explicit parametrization of the system is made, the parametric version of the test can be defined.

Proposition 7.5 (Parametric test) *A parametric GLR test writes as*

$$t_{\text{global}} = (\hat{\zeta}^{\theta})^T \, \widehat{\Sigma}^{-1} \, \widehat{\mathcal{J}} \left(\widehat{\mathcal{J}}^T \, \widehat{\Sigma}^{-1} \, \widehat{\mathcal{J}} \right)^{-1} \widehat{\mathcal{J}}^T \, \widehat{\Sigma}^{-1} \hat{\zeta}^{\theta} \ , \tag{7.28}$$

where $\widehat{\mathcal{J}}$ and $\widehat{\Sigma}$ are consistent estimates of $\mathcal{J}_{\theta_*}^{\zeta}$ and Σ_ζ.

Assuming Σ_ζ to be invertible, under H_0, t_{global} follows a $\chi^2(\text{rank}(\mathcal{J}_{\theta_*}^{\zeta}))$ distribution. Under H_1, it follows a non central χ^2 distribution of mean $\mu_{\chi^2} = \text{rank}(\mathcal{J}_{\theta_*}^{\zeta}) + \lambda$ and variance $\sigma_{\chi^2}^2 = 2(\text{rank}(\mathcal{J}_{\theta_*}^{\zeta}) + 2\lambda)$, where λ is the noncentrality parameter equal to

$$\lambda = \delta^T (\mathcal{J}_{\theta_*}^{\zeta})^T \, \Sigma_{\zeta}^{-1} \, \mathcal{J}_{\theta_*}^{\zeta} \, \delta \ .$$

Thus, the test value resulting from (7.28) should be compared to a threshold corresponding to a χ^2 distribution whose DOF are corresponding to the mean value of the test in the reference state.

The main result of this chapter is that the value of the test under H_0 does not depend on the variances of the excitation nor on the length of the data sets used for its estimation. The opposite holds for the test computed for increasing with M, N under H_1 hypothesis, as it is shown in the next section.

7.2.5 Application and computation of the damage detection tests

In this section, the computation of the matrices necessary in the evaluation of both $t_{\text{global}}^{\text{np}}$ and t_{global} is addressed. Subsequently, both tests are validated on a numerical example.

7.2.5.1 Covariance of the residual Σ_ζ

First, the covariance of the residual (7.24) is developed. A general expression for the first order perturbation of $\hat{\zeta}$ writes

$$\Delta\hat{\zeta}^{\theta} \approx \sqrt{N} \begin{bmatrix} \mathcal{J}_{\hat{\mathcal{H}}_{ref}^{\theta_*}} & \mathcal{J}_{\hat{\mathcal{H}}_{test}^{\theta}} \end{bmatrix} \begin{bmatrix} \text{vec}(\Delta\hat{\mathcal{H}}_{ref}^{\theta_*}) \\ \text{vec}(\Delta\hat{\mathcal{H}}_{test}^{\theta}) \end{bmatrix} \ . \tag{7.29}$$

A final expression for the covariance of the residual is given in the following Lemma.

Lemma 7.6 *The covariance of the residual yields*

$$\begin{aligned} \Sigma_\zeta &= \lim \mathrm{E} \left((\Delta\hat{\zeta}^{\theta}) \Delta(\hat{\zeta}^{\theta})^T \right) \\ &= \mathcal{J}_{\mathcal{H}_{ref}(\theta_*)} \Sigma_{\mathcal{H}_{ref}(\theta_*)} \mathcal{J}_{\mathcal{H}_{ref}(\theta_*)}^T + \mathcal{J}_{\mathcal{H}_{test}(\theta_*)} \Sigma_{\mathcal{H}_{test}(\theta_*)} \mathcal{J}_{\mathcal{H}_{test}(\theta_*)}^T \ , \end{aligned} \tag{7.30}$$

where $\mathcal{J}_{\mathcal{H}_{ref}(\theta_*)} = I_{(p+1)r} \otimes U_s U_s^T - I_{qr_0} \otimes I_{(p+1)r}$ and $\mathcal{J}_{\mathcal{H}_{test}(\theta_*)} = (\mathcal{Z}_{test}^{\dagger} \mathcal{Z}_{ref})^T \otimes U_{ker} U_{ker}^T$.

Proof: For derivation of the necessary Jacobians, see Appendix E.2. □

An estimate of the asymptotic covariance of the residual $\hat{\Sigma}_\zeta$ can be computed with consistent estimates of matrices used in Lemma 7.6. A consistent estimate of the asymptotic covariance of Hankel matrices can be found e.g. in [140].

7.2.5.2 Example of non-parametric χ^2 test

This section presents the results from the non-parametric test, introduced in Proposition 7.27, evaluated on the numerical simulations of the chain-like system introduced in Section 7.1.1.

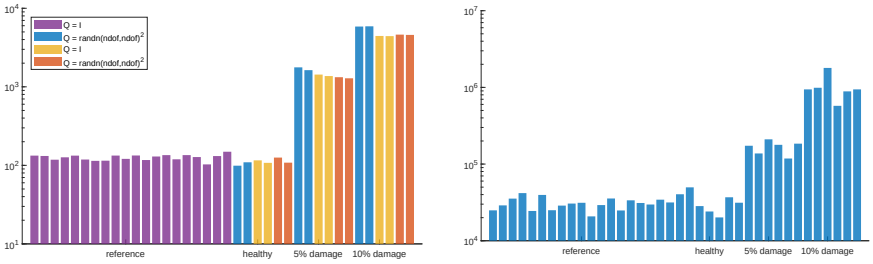

Figure 7.5: Damage detection with non-parametric residual based on robust normalization. Three randomly chosen excitation levels in the tested data sets (left). Random excitation in every data set (right).

Figure 7.5 (left) displays the evolution of the test over time for three different states of the system, namely one healthy and two damage states. As it can be seen, the test is able to separate the different damages despite being computed for different values of the excitation. Figure 7.5 (right) displays the same type of information for Q changing for each simulated data set. That shows that the damage can be identified without any prior knowledge of the excitation properties.

To illustrate the distribution of the test statistics a numerical Monte Carlo simulations are conducted for the considered excitation cases.

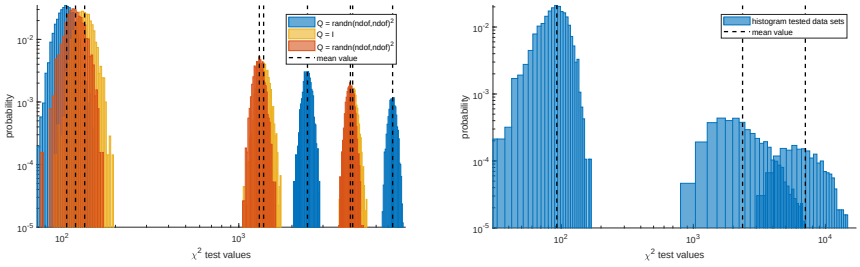

Figure 7.6: Distribution of non-parametric residual based on robust normalization. Three randomly chosen excitation levels in the tested data sets (left). Random excitation in every data set (right).

The Monte Carlo simulations exhibit the distribution of the test for different excitation matrices Q, first for three selected $Q = Q_1, Q_2, Q_3$ illustrated on Figure

7.6 (left). There, in the healthy case, all three distributions are superposed, showing the robustness of the test to the excitation changes. As for the damaged cases, slight changes in the mean of the distribution can be seen between the histograms of the pair Q_2, Q_3 and Q_1, but still different damage levels are visibly separated. Figure 7.6 (right) shows the capability of the test when Q is changing all the time for each simulated data set and is in principal unknown. It can be observed that the distributions of the test for safe and damage states are well separated and different damage levels can be distinguished.

Notice that the mean value of the test distribution when the structure is safe is high and unpredictable. This is due to the lack of Jacobian in the computation of the $t^{\mathrm{np}}_{\mathrm{global}}$ test, see Proposition 7.27. The Jacobian takes into account the sensitivity of the test with respect to each of the system parameters. Therefore, when using such Jacobian the mean value of the test can be predicted, and a threshold for damage can be theoretically established.

In the next section, an analytical derivation of the Jacobian $\mathcal{J}^{\zeta}_{\theta_*}$ is given. This will yield the full expression of t_{global} and its evaluation on the former numerical example.

7.2.5.3 Residual sensitivity with respect to system parameter $\mathcal{J}^{\zeta}_{\theta_*}$

This section is devoted to the derivation of Jacobian $\mathcal{J}^{\zeta}_{\theta_*}$. Let θ' and θ'' be given variables in the parameter space. Define $\begin{bmatrix}\mathcal{H}_{ref}(\theta') & \mathcal{H}_{test}(\theta'')\end{bmatrix} \in \mathbb{R}^{(p+1)r\times 2qr_0}$ as a matrix constructed from juxtaposed exact Hankel matrices, both describing state of the system under respective parameters θ' and θ''. Its SVD writes as

$$\begin{aligned}&\begin{bmatrix}\mathcal{H}_{ref}(\theta') & \mathcal{H}_{test}(\theta'')\end{bmatrix} \\ &= U_s(\theta',\theta'')D_s(\theta',\theta'')\begin{bmatrix}V^T_{s,ref}(\theta',\theta'') & V^T_{s,test}(\theta',\theta'')\end{bmatrix} \\ &+ U_{ker}(\theta',\theta'')D_{ker}(\theta',\theta'')\begin{bmatrix}V^T_{ker,ref}(\theta',\theta'') & V^T_{ker,test}(\theta',\theta'')\end{bmatrix}\ .\end{aligned} \tag{7.31}$$

Now introduce parametrized normalization matrices such that

$$\begin{aligned}\mathcal{Z}_{ref}(\theta',\theta'') &= D_s(\theta',\theta'')V^T_{s,ref}(\theta',\theta'')\ , \\ \mathcal{Z}_{test}(\theta',\theta'') &= D_s(\theta',\theta'')V^T_{s,test}(\theta',\theta'')\ .\end{aligned}$$

Then the theoretical residual can be written as a function of two variables θ' and θ'' as

$$\zeta(\theta',\theta'') = \mathrm{vec}\left(\mathcal{H}_{test}(\theta'')\mathcal{Z}^{\dagger}_{test}(\theta',\theta'')\mathcal{Z}_{ref}(\theta',\theta'') - \mathcal{H}_{ref}(\theta')\right)\ . \tag{7.32}$$

Since the parametrized residual $\zeta(\theta',\theta'')$ is derived with respect to the system parameter the notation of $\mathcal{Z}_{ref}(\theta',\theta'')$ and $\mathcal{Z}_{test}(\theta',\theta'')$ is kept for the clarity of the derivative. The expression of $\zeta(\theta',\theta'')$ yields

$$\forall\theta' = \theta'' = \theta_* \rightarrow \zeta(\theta',\theta'') = 0\ .$$

The derivative of $\zeta(\theta',\theta'')$ with respect to the system parameters θ' and θ'' evaluated at the point (θ_*,θ_*) coincide with the Jacobian matrix $\mathcal{J}^{\zeta}_{\theta_*}$.

Lemma 7.7 *Jacobian* $\mathcal{J}_{\theta_*}^{\zeta}$ *can be expressed as*

$$\mathcal{J}_{\theta_*}^{\zeta} = \left(\left(\mathcal{Z}_{ref}^{\dagger} \mathcal{Z}_{ref} \right)^T \otimes U_{ker} U_{ker}^T \right) \mathcal{J}_{\theta_*}^{\mathcal{H}_{ref}} \ , \tag{7.33}$$

where $\mathcal{J}_{\theta_*}^{\mathcal{H}_{ref}} = \mathrm{vec}\left(\partial \mathcal{H}_{ref} / \partial \theta \ (\theta_*)\right)$, $\mathcal{Z}_{ref} = \mathcal{Z}_{ref}(\theta_*, \theta_*)$, $\mathcal{Z}_{test} = \mathcal{Z}_{test}(\theta_*, \theta_*)$ *and* $U_{ker} = U_{ker}(\theta_*, \theta_*)$. *Consistent estimates of these matrices can be used in the estimation of* $\mathcal{J}_{\theta_*}^{\zeta}$.

Proof: See Appendix E.3. □

Computation of the Jacobian $\mathcal{J}_{\theta_*}^{\mathcal{H}_{ref}}$ can vary based on the chosen parametrization of the structural system, which can be done e.g. with the modal parameters identified through the system identification, modal parameters of an analytic model of the system or any other parameter with a functional relation between, in this case, the parametric Hankel matrix and the system model. A review of different parametrization schemes can be found in [141]. In this chapter the chain system is parametrized with its analytical stiffness, which is connected to the parametric Hankel matrix $\mathcal{H}_{ref}(\theta_*)$ by the following chained sensitivities

$$\mathcal{J}_{\theta_*}^{\mathcal{H}_{ref}} = \mathcal{J}_{\Gamma}^{\mathcal{H}_{ref}} \mathcal{J}_{\lambda,\phi}^{\Gamma} \mathcal{J}_{\mu,\psi}^{\lambda,\phi} \mathcal{J}_{\theta_*}^{\mu,\psi} \ ,$$

where $\mathcal{J}_{\Gamma}^{\mathcal{H}_{ref}}$ is the sensitivity of the Hankel matrix with respect to the parametric observability matrix, $\mathcal{J}_{\lambda,\phi}^{\Gamma}$ is the sensitivity of the parametric observability with respect to the continuous poles of the system, $\mathcal{J}_{\mu,\psi}^{\lambda,\phi}$ is the Jacobian of the eigenvalues of the continuous system with respect to its discrete eigenvalues and $\mathcal{J}_{\theta_*}^{\mu,\psi}$ is the Jacobian of the discrete eigenvalues of the system with respect to the selected system parameter. Computation of the following Jacobians is not elaborated in this chapter. For a detailed computation schemes see [141, 140, 133].

7.2.5.4 Example of parametric χ^2 test

Here the capabilities of the parametric test are investigated on the numerical example. The protocol is very similar to the one in Section 7.2.5.2 and illustrates the test formulated in (7.28).

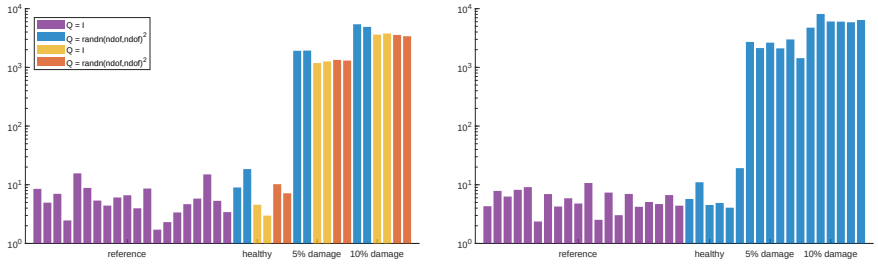

Figure 7.7: Damage detection with parametric residual based on the robust normalization. Three randomly chosen excitation levels in the tested data sets (left). Random excitation in every data set (right).

The results illustrated on Figure 7.7 (left) are also quite similar to the ones depicted on Figure 7.6, where values of the damage detection test for all three different Q

are well separated and the damage is well detected. As expected, no false alarms are present in the reference state. The mean value of the test corresponds to the rank of the Jacobian matrix $\mathcal{J}_{\theta_*}^{\zeta}$ which yields the number of the independent system parameters (in this case equal to 6). The test values for completely unknown and changing Q are plotted on Figure 7.7 (right) and show a good capability for the test to be robust to false alarms in the reference (safe) state and to detect damages in both damage states. For a final depiction of the robustness of the proposed test the Monte Carlo simulations are conducted.

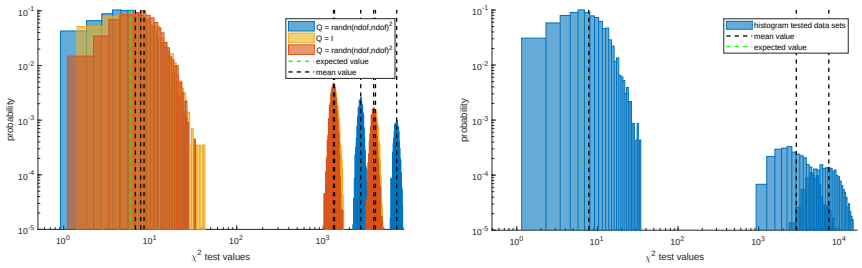

Figure 7.8: Distribution of parametric residual based on robust normalization. Three randomly chosen excitation levels in the tested data sets (left). Random excitation in every data set (right).

Figure 7.8 (left) shows the histograms of the test values obtained from the Monte Carlo simulations. It can be observed that the parametric test is very robust to the changes in the excitation covariance and that the test values from the damaged structure are very well separated from the ones corresponding to the safe structure. Similar information is shown on Figure 7.8 (right), where a good separation between test values computed on the safe structure and the test values due to different level of damages can be observed.

Contrary to the non parametric test, the mean of the distribution of the t_{global} test computed on the safe structure is both stable and very close to its theoretical value equal to 6. In addition to that, a threshold for assessing that damage occurred in the structure can be determined a priori based on the theoretical distribution of the residual under H_0 and its quantiles.

Notice also that the mean of the test is still showing some fluctuations due to Q in the damage states. That is because the covariance of the residual Σ_ζ depends on Q. Albeit not preventing to detect damages, in this case, these fluctuations might affect the ability of the test to separate between different damage levels.

7.3 Practical considerations

The previous sections established the computation of the mean and the variance of the proposed Gaussian residual and deployed it for damage detection via hypothesis testing. Some empirical histograms of the test values under H_0 and H_1 hypotheses were shown, which correspond to an approximate χ^2 distribution of the test values.

To recall, the t_{global} computed under H_0 follows a $\chi^2(\text{rank}(\mathcal{J}_{\theta_*}^{\zeta}))$ distribution. Under H_1, it follows a non central χ^2 distribution of mean $\mu_{\chi^2} = \text{rank}(\mathcal{J}_{\theta_*}^{\zeta}) + \lambda$ and variance $\sigma_{\chi^2}^2 = 2(\text{rank}(\mathcal{J}_{\theta_*}^{\zeta}) + 2\lambda)$. A consistent estimate of the non centrality

parameter λ yields

$$\hat{\lambda} = \delta^T \widehat{\mathcal{J}}^T \widehat{\Sigma}^{-1/2T} \widehat{\Sigma}^{-1/2} \widehat{\mathcal{J}} \delta \ ,$$

where $\delta = \sqrt{N}\Delta\theta$.

In many previous work on a Gaussian residual-based damage detection tests, the reference is considered to be deterministic and the properties of $\hat{\lambda}$ are only dependent on N. The considered distance depends both on N and M hence the effect of both N and M on $\hat{\lambda}$ will be investigated in this section. In addition, since both $\hat{\lambda}$ and t_{global} depend on $\widehat{\mathcal{J}}$, some important properties of this Jacobian are developed. Subsequently, following the lines of [129], an efficient computation scheme for the test based on QR decomposition is presented.

7.3.1 Invariance to a change in the excitation properties

A key result of this chapter is now stated, allowing to prove that on average the proposed residual is robust to changes in the excitation covariance.

Theorem 7.8 *Jacobian* (7.33) $\mathcal{J}^{\zeta}_{\theta_*}$ *is invariant towards a change in the excitation properties of the data.*

Proof: See Appendix E.5. □

Based on Theorem 7.8, the mean of the residual is not impacted by the change in the excitation Q_{test}. As a consequence the Jacobian of the residual is the same under H_0 and H_1. As such, the rank of the Jacobian is a constant under H_0 and H_1, and the test value should be constant under H_0 for different values of Q. However, the mean of the χ^2 test under H_1 is dependent on Σ_ζ, which explains the fluctuations of the test values under H_1 depicted on Figure 7.6 and Figure 7.8.

7.3.2 A numerical study about the non centrality parameter of the damage detection test

As explained at the beginning of this section, the non centrality parameter depends on both N and M, hence, for the purpose of this section, it can be denoted as $\lambda_{N,M}$. For the sake of simplicity, assume N and M are of the same order and recall a scalar $c > 0$, such that M/N tends to c. Also assume that $M > N$, meaning more data is collected under the reference state of the structure then in one tested state. Then, it has been shown in Proof E.1 that the asymptotic variance is

$$\Sigma_\zeta = c^{-1} \mathcal{J}_{\mathcal{H}_{ref}(\theta_*)} \Sigma_{\mathcal{H}_{ref}(\theta_*)} \mathcal{J}^T_{\mathcal{H}_{ref}(\theta_*)} + \mathcal{J}_{\mathcal{H}_{test}(\theta_*)} \Sigma_{\mathcal{H}_{test}(\theta_*)} \mathcal{J}^T_{\mathcal{H}_{test}(\theta_*)} \ .$$

As it can be seen, if more data are available in the reference state, the contribution of $\Sigma_{\mathcal{H}_{ref}(\theta_*)}$ to the variance of the residual is decreasing, since c^{-1} decreases. Then the non centrality parameter yields

$$\begin{aligned}\lambda_{N,M} = \delta^T \mathcal{J}^T_{\theta_*} (&c^{-1} \mathcal{J}_{\mathcal{H}_{ref}(\theta_*)} \Sigma_{\mathcal{H}_{ref}(\theta_*)} \mathcal{J}^T_{\mathcal{H}_{ref}(\theta_*)} \\ &+ \mathcal{J}_{\mathcal{H}_{test}(\theta_*)} \Sigma_{\mathcal{H}_{test}(\theta_*)} \mathcal{J}^T_{\mathcal{H}_{test}(\theta_*)})^{-1} \mathcal{J}_{\theta_*} \delta \ .\end{aligned}$$

As such, the mean value of the test mainly depends on δ with a variance term depending on $\Sigma_{\mathcal{H}_{test}(\theta_*)}$ since M gets very large, as expected in the reference state,

where usually more data are available. When M is much larger than N, then the relation $M/N = c > 0$ does not hold anymore, and $\lambda_{N,M}$ is equal to

$$\lambda_{N,M} = \delta^T \mathcal{J}_{\theta_*}^T (\mathcal{J}_{\mathcal{H}_{test}\theta_*}) \Sigma_{\mathcal{H}_{test}(\theta_*)} \mathcal{J}_{\mathcal{H}_{test}(\theta_*)}^T)^{-1} \mathcal{J}_{\theta_*} \delta \ ,$$

since the reference can be considered deterministic.

The case where $N > M$, however unrealistic, could be treated similarly and shows that the non centrality parameter relies then more on M and the variance of the residual mainly depends on $\Sigma_{\mathcal{H}_{ref}(\theta_*)}$. A study of the non centrality parameter for the case of the 5% stiffness reduction in the 2DOF of the chain system introduced in this chapter and constantly changing load covariance is illustrated on Figure 7.9.

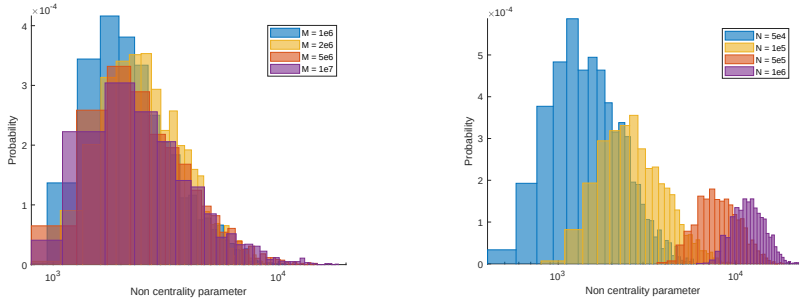

Figure 7.9: Non Centrality Parameter study. Fixed $N = 100000$ samples, varying M (left). Fixed $M = 2000000$ samples, varying N (right).

As expected, the non centrality parameter is dependent on the combination of the variances in both states, with a bigger influence of the variance of the more uncertain Hankel matrix, computed in the state with the fewer measured data, here the tested state with data length N.

7.3.3 Efficient implementation of the damage detection test

In [142] it was shown that the direct computation of parametric test is numerically unstable due to a rank deficiency of the asymptotic covariance matrix Σ_ζ. The developments in this section follow the lines of [129] to deal with its bad conditioning and to derive a numerically stable test.

Corollary 7.9 *Efficient computation of χ^2 test* (7.28) *writes as*

$$t_{\text{global}} = a^T a \ , \tag{7.34}$$

where $a = \mathcal{Q}^T \mathcal{K}^\dagger \mathcal{B}^T \hat{\zeta}^\theta$, $\mathcal{B} = \mathcal{I}_{(p+1)r} \otimes U_{ker}$ and matrix $\mathcal{K}$ yields

$$\mathcal{K} = \left[-\mathcal{B}^T \Sigma_{\mathcal{H}_{ref}(\theta_*)} \quad \left((\mathcal{Z}_{test}^\dagger \mathcal{Z}_{ref})^T \otimes \mathcal{I}_{(p+1)r-n} \right) \mathcal{B}^T \Sigma_{\mathcal{H}_{test}(\theta_*)} \right] \ .$$

Matrix $\mathcal{Q}$ is computed from a thin QR decomposition of $\mathcal{K}^\dagger \mathcal{J}_s = \mathcal{Q}\mathcal{R}$ where $\mathcal{J}_{\theta_*}^\zeta = \mathcal{B}\mathcal{J}_s$. A detailed development of the following is enclosed in Appendix E.6.

7.4 Application

This section is devoted to the application of the proposed residual. First, the new approach is tested on a small-scale experiment conducted on an aluminum plate which is perturbed by an added mass. Second, experimental data from Dogna and Z24 bridges are tested.

7.4.1 Mass perturbation in the aluminum plate

The plate is excited with a random tapping which is supposed to resemble random and broadband excitation conditions. The signal is sampled with a frequency of 4166.67Hz and one measurement comprises 1250000 samples. The experimental campaign consists of 21 measurements in total, 11 conducted in the healthy state, 5 with a 1 mass perturbation and 5 with a perturbation of 2 masses. The perturbation in mass is introduced by placing an aluminum cap, that corresponds to 1.35% of the total mass of the plate, on the top surface of the plate. The measurements are conducted with ARTeMIS Modal Pro 5.3 [138]. The geometry of the plate, the acquisition system and the software recording the measurements are illustrated on Figure 7.10.

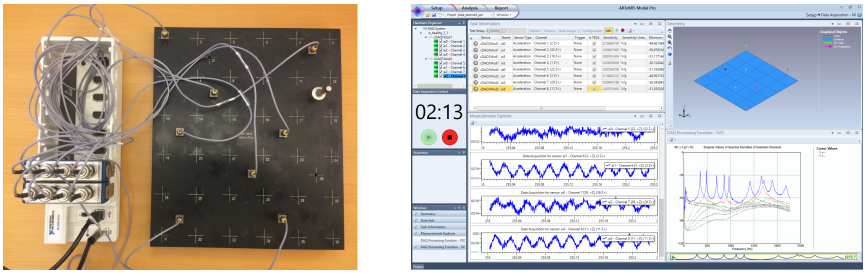

Figure 7.10: Experimental test setup of the plate (left). Data acquisition with ARTeMIS Modal Pro 5.3 (right).

The non-parametric test from Proposition 7.4 is computed. The Hankel matrices are computed with 4 time lags and the normalization factors are computed with a model order of 18. The reference state is computed from 5 measurements in the healthy state. The number of blocks for the covariance of each Hankel matrix is selected to 200. The results from the non-parametric test are depicted on Figure 7.11.

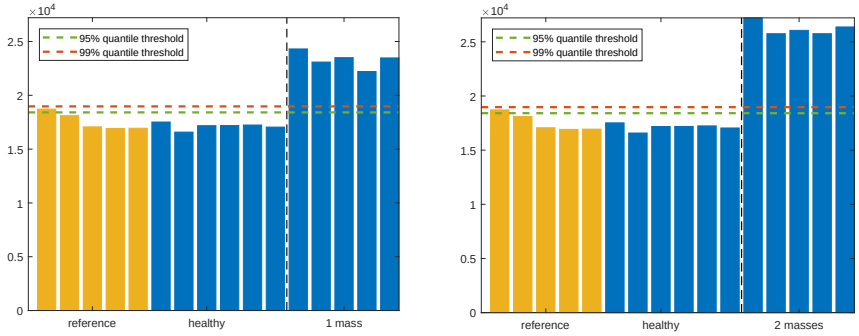

Figure 7.11: Detection of mass change in aluminum plate during ambient excitation with non-parametric damage detection test after Proposition 7.4. Detection of 1 mass (left), detection of 2 masses (right).

The non-parametric test yields similar values for the healthy and reference states, which are clearly separated from both damage states. As a consequence, one can define a detection threshold based on the test values from the reference data sets. In theory, this threshold should correspond to a quantile of the theoretical χ^2 distribution of the test in the reference state. However, in the absence of the Jacobian the number of degrees of freedom of the underlying χ^2 distribution cannot be predicted. Therefore the empirical mean and the variance based on few test values in the reference state are computed and two quantiles, 95% and 99%, of this empirical distribution are chosen to represent this threshold.

Next, the parametric test from Proposition 7.5 is investigated. The system is parameterized with the modal parameters of the plate estimated from the first reference data set. In total 9 modes of the plate in the frequency band $347 - 2095$ Hz are estimated. The computed χ^2 test values for the parametric test are depicted on Figure 7.12.

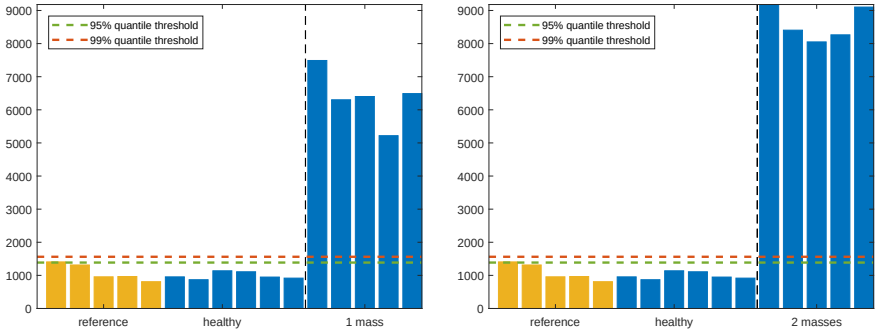

Figure 7.12: Detection of mass change in aluminum plate during ambient excitation with parametric damage detection test after Proposition 7.5. Detection of 1 mass (left), detection of 2 masses (right).

Similarly to Figure 7.11, no false-positive nor false-negative scores can be observed, which illustrates a good practical performance of the proposed test to detect damages

and be robust towards false alarms in the healthy states. The detection threshold computed for the parametric test is higher then in theory, however much lower then in the non-parametric case. That indicates that the distribution of the test values is sharper in the parametric test case, implying a higher probability of detecting damages.

7.4.2 Dogna bridge

The Dogna bridge illustrated on Figure 7.13, was a four-span, single-lane 16m long and 4m wide concrete bridge, which for traffic safety reasons was demolished on May 2008.

Figure 7.13: Dogna bridge, front view.

Before the demolition, a progressive damage campaign was carried out and consisted of a series of an ambient vibration tests conducted while damaging one of the bridge spans. The experimental tests lasted for 54 minutes and were carried out under similar temperature conditions so its influence on the obtained results can be considered insignificant. Figure 7.14 shows the artificial damages induced on the bridge. The damage was introduced in two main blocks, namely the cuts in the beams and the removal of concrete from the center span of the bridge, denoted here as damage 1 and damage 2 respectively.

Figure 7.14: Artificial damage induced to side beams (damage 1) and centerline of the bridge (damage 2).

The bridge was equipped with 10 accelerometers mounted on its deck. The measurements were sampled with the frequency of 400 Hz and each measurement lasted for 147.5 seconds. A total number of 22 data sets were recorded, from which the first 8 measurements are under healthy conditions. Data sets between 9 and 14 are the measurements from the damage state 1 and data sets from 15 to 22 are corresponding to the damage state 2.

The non-parametric version of the proposed test is computed with 7 time lags to create a Hankel matrix and a model order of 8 to compute the normalization matrices. The reference Hankel matrix is computed as an average of the first 4 measurement setups in the healthy state. The number of blocks for the covariance of the reference and the tested Hankel matrices is selected at 100. The results of χ^2 test values from the non-parametric test are depicted on Figure 7.15.

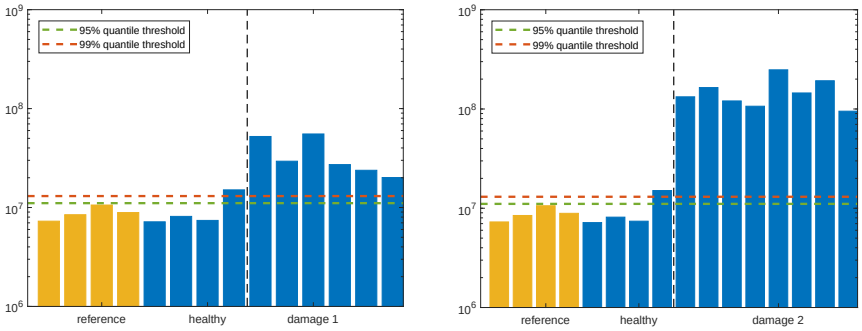

Figure 7.15: Damage detection in the Dogna bridge with non-parametric damage detection test after Proposition 7.4. Damage 1 (right) and damage 2 (left).

As expected, two different damages inflicted on the bridge are clearly detected, despite possible fluctuations in the unknown ambient excitation. Moreover, a clear separation between safe and damaged states, based on the 95% and 99% quantiles of the empirical distribution of the test values in the reference state, can be observed.

7.4.3 Z24 bridge

The Z24 bridge is a benchmark for many studies involving system identification [143], damage detection [144] and removal of the environmental characteristics from the parameters estimated from the data [125]. Before its demolition in 1998, a progressive damage campaign was carried out and consisted of a series of ambient and forced vibration tests conducted while inducing different kinds of damage on the bridge. A complete description of that experimental campaign can be found in [145]. The progressive damage tests took place between August and September where some significant changes in the temperature conditions were experienced during its execution. The approach proposed in this paper doesn't account for the temperature variation. Therefore, only several data sets from the beginning of the experimental campaign are analyzed and assumed not to be significantly perturbed by these temperature changes.

The analyzed measurements correspond to the mix of a forced excitation from two shakers and an ambient excitation from wind and traffic under the bridge. The vibration tests were conducted with 28 moving and 5 fixed sensors measuring vertical,

transverse and lateral accelerations of the bridge. For the purpose of this study only the measurements from 5 fixed senors are analyzed. The data were sampled with the frequency of 100 Hz and each measurement lasted for 655.36 seconds. A total number of 54 data sets were analyzed, from which the first 18 measurements are under healthy conditions. The first 6 data sets are selected for the reference state computation. Data sets between 19 and 36 are the measurements corresponding to damage state 1, namely lowering one of the bridge piers by 20mm, and data sets from 37 to 54 are corresponding to the damage state 2, which labels lowering the same pier by another 20mm. The view on the bridge with positions and directions of the sensors used for this study is shown on Figure 7.16.

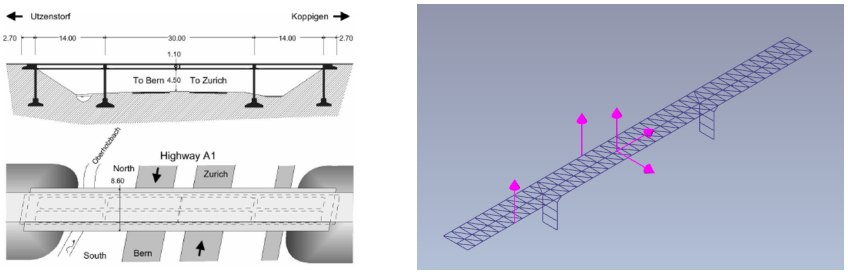

Figure 7.16: Front view and top views of the Z24 bridge (left). Geometry and analyzed sensors of the Z24 bridge ARTeMIS Modal Pro 6.0 (right).

The test from (7.27) is computed with 10 time lags to create a Hankel matrix and model order of 6 to compute the normalization matrices. The reference state is computed from the first 6 measurements in the healthy state. The number of blocks for the covariance of the reference and the tested Hankel matrices is selected to 400. The results are depicted on Figure 7.17.

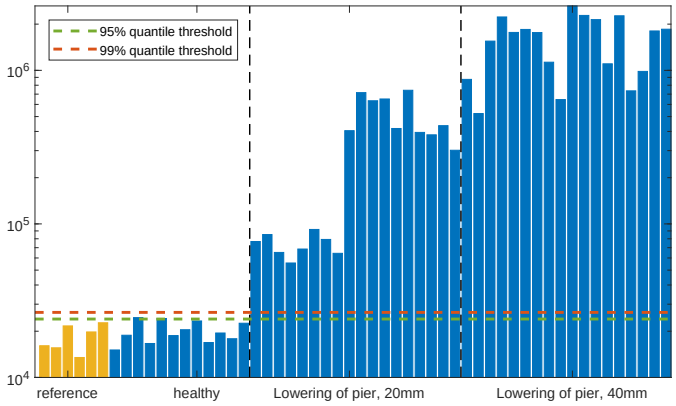

Figure 7.17: Damage detection in the Z24 bridge. Damage detection test after (7.27) .

As expected, the results exhibit no false alarms in the healthy state of the structure. Moreover, two damage levels inflicted on the bridge are clearly detected. Plotted

detection thresholds correspond to two quantiles, 95% and 99%, of the empirical distribution of the test values in the reference state. The two different levels of the χ^2 test for the damage state 1 might indicate lowering the bridge pier two times by 10mm.

7.5 Conclusions

In this chapter we have derived a new Gaussian residual for damage detection. The proposed method is robust towards false alarms in the healthy state of the structure, a feature that is critical for its practical application in structural monitoring systems and one that was not achieved with the previously developed method based on the Mahalanobis distance computed between Hankel matrices in different states of the structure. The robustness of the new approach is achieved via a normalization scheme, inherited from a multipatch subspace identification algorithm. Its influence on the residual is thoroughly studied from both a statistical and a numerical point of view. For the decision about the condition of the system, the residual is evaluated in a hypothesis test, which follows a χ^2 distribution, whose properties in the reference state are independent of the excitation and, depending on the availability of the structural model, can be computed a priori, which is attractive from a practical point of view. In the damaged state, the mean of the proposed residual is also independent of excitation conditions, but not its covariance. In consequence, the resultant test statistics are dependant on the excitation changes under faulty conditions of the structure. The new method has been evaluated on both numerical and experimental data sets.

7.6 Dissemination

Parts of this chapter have been published in [12, 13, 14, 15, 16]:

[12] S. Gres, M. Döhler, P. Andersen, L. Damkilde, L. Mevel, Hankel matrix normalization for robust damage detection, in: IOMAC - 8th International Operational Modal Analysis Conference, Copenhagen, Denmark, 2019.

[13] S. Gres, P. Andersen, R. Johansen, M. Ulriksen, L. Damkilde, A comparison of damage detection methods applied to civil engineering structures, in: Experimental Vibration Analysis for Civil Engineering Structures, Springer, Germany, 2018, pp. 306–316, proceedings of the 7th International Conference on Experimental Vibration Analysis for Civil Engineering Structures.

[14] S. Gres, M. D. Ulriksen, M. Döhler, R. J. Johansen, P. Andersen, L. Damkilde, S. A. Nielsen, Statistical methods for damage detection applied to civil structures, Procedia Engineering 199 (2017) 1919 – 1924, x International Conference on Structural Dynamics, EURODYN 2017.

[15] S. Greś, M. Döhler, L. Mevel, Hankel matrix-based mahalanobis distance for fault detection robust towards changes in process noise covariance, IFAC-PapersOnLine 54 (7) (2021) 73–78, 19th IFAC Symposium on System Identification SYSID 2021.

[16] S. Greś, M. Döhler, P. Andersen, L. Mevel, Subspace-based mahalanobis damage detection robust to changes in excitation covariance, Structural Control and Health Monitoring 28 (8) (2021) e2760.

Conclusions

The methods developed in this thesis account for different aspects of ambient excitation conditions during vibration-based monitoring of structures. That comprises

- removing the periodic components of excitation from the response measurements with the proposed orthogonal projection approach. That enables OMA of structures with rotating machinery onboard when the resultant harmonic-free signals are analyzed with the classical OMA methods.
- classification whether the true mode shapes are real or complex valued vectors, based on the framework to quantify statistical uncertainty in estimates of the Modal Phase Collinearity.
- classification whether the mode shape estimates correspond to the same theoretical or estimated mode, based on the framework to quantify statistical uncertainty in estimates of the Modal Assurance Criterion.
- damage detection invariant towards the intricate influence of ambient excitation conditions based on a robust normalization of Hankel matrices.

The pertinence of the proposed schemes to real-life vibration problems is illustrated based on full-scale structures like an offshore meteorological mast at the North Sea, an operating ferry, Dogna and Z24 bridges and the small-scale plate.

The strengths and the shortcomings of the methods proposed in this thesis are presented in the summary below.

Summary

Here, a short summary, with the merits and weaknesses of the each method is outlined.

1. **Harmonic removal for subspace-based system identification**.

   A method for removing modes of the structure corresponding to harmonic excitation was proposed, based on the orthogonal projection of raw measurements onto their predicted harmonic counterparts. That improves subspace-based system identification for Operational Modal Analysis of structures with rotating machinery onboard. Numerical simulation has shown the consistency of the new method and its deployment to real-life vibration problems was illustrated on the experimental plate and the ferry in-operation. The weakness of the proposed scheme is related to identification of the harmonic modes from the data. That requires selection of an appropriate system order for system identification and

criteria that will classify the estimated mode as harmonic, for example a minimum damping ratio. When appropriate quantities are chosen, the developed method offers better estimates of the underlying structural modes, comparing to classic subspace identification methods under periodic inputs, which is reflected in more accurate estimates of their damping ratios and a reduced statistical uncertainties.

2. **Uncertainty quantification of modal indicators: Modal Phase Collinearity (MPC)**.

   A statistical framework for the uncertainty quantification of the MPC was proposed. The novelty of the proposed approach lies in approximating the distribution of the MPC when its estimates are close to their theoretical boarder, meaning that the underlying mode shape is asymptotically a real-valued vector. A classic Gaussian approximation was shown to be appropriate to infer the distribution of the MPC for complex-valued mode shapes. A quadratic form distribution of the MPC was derived and its χ^2 approximation was developed when the underlying mode shapes are asymptotically real-valued vectors. A framework to decide whether the true mode shape is real or complex-valued was designed based on the confidence bounds of the approximate distributions of the MPC indicator. The proposed approximate distributions were not satisfactory when the MPC estimate is too far from the boarder to be quadratic but still close enough to the boarder where it does not satisfy a Gaussian approximation. In that case it was more adequate to approximate the MPC with a Gaussian, however more samples were required for an accurate computation of the confidence bounds. The proposed quadratic form was successfully used for the approximation of the MPC estimates computed for a low sample lengths.

3. **Uncertainty quantification of modal indicators: Modal Assurance Criterion (MAC)**.

   A statistical framework for the uncertainty quantification of the MAC was proposed. The novelty of the proposed approach lies in the development of the quadratic form approximation, which enables to infer the distribution of MAC estimates when they are close to the boarder of their domain. A classic Gaussian approximation was used to infer the distribution of the MAC computed between the mode shape estimates corresponding to different modes. A quadratic form of the MAC was derived and its χ^2 approximation was developed for the MAC computed between an exact mode shape from a Finite Element (FE) model and its equivalent estimated from the data. A framework, equivalent to the one designed for the MPC, to decide whether the estimated mode shape belongs to the exact mode shape from the FE model was proposed, based on the confidence bounds of the above mentioned approximations. A weakness of the aforementioned scheme is its sensitivity towards errors in the FE modeling. The probability that an estimated mode shape is equivalent to the mode shape from the FE model is based on the location of the considered MAC estimate in the quadratic form confidence intervals, which are based on the second order statistics, and are very small. Some discrepancy between the FE model and the real structure can cause the estimates of MAC to be outside the aforementioned confidence bounds and will result in the rejection of the hypothesis that the estimated mode shape belongs to the considered mode shape from the FE model.

4. **Uncertainty quantification of the MAC from a stabilization diagram**.

A second order statistical framework for the uncertainty quantification of the MAC estimated between mode shapes corresponding to the same modal alignment was developed, and used in the formation of the stabilization diagrams. A quadratic form of the MAC between two mode shape estimates was derived and its χ^2 approximation was developed. It was found that the MAC estimated between mode shapes that correspond to the same mode is well suited in the confidence intervals of the quadratic approximation. The estimates of MAC for which the quadratic form approximation was less probable were discarded from the modal alignments.

5. **Hankel matrix normalization for damage detection robust to excitation changes**.

   The normalization scheme adopted from the multipatch subspace-based system identification was used to design a residual for damage detection, which is robust when the covariance of the ambient excitation changes between the tested data sets. The influence of the excitation properties on the proposed metric was thoroughly studied on numerical simulations and its performance in detecting damages was tested on real data from an experimental plate and two full-scale bridges. To estimate the normalization matrices, the proposed approach requires an SVD of the Hankel matrix built from output covariance sequences and its truncation at a selected model order, which is a drawback since the true order of the system is unknown in practice. For the decision about the condition of the system, the proposed residual was evaluated in a hypothesis test, which follows a χ^2 distribution, whose properties, depending on the availability of the structural model, can, in theory, be computed a priori. The threshold for the parametric test, although according to the parametrization when validated in the numerical simulations, was higher when computed for the experimental plate case. That might have been caused by a bad numerical condition of the covariance of the residual. The residual mean in the damaged state was shown to be independent of changes in the excitation covariance. Consequently, the proposed hypothesis test is robust towards the aforementioned excitation changes in the reference state of the structure, conversely to the faulty state, where the residual mean is robust but the statistics of the proposed test were changing.

Outlook

The methods proposed in this thesis were developed theoretically, validated on numerical simulations and tested on a few examples of real structures. Nevertheless, there are numerous aspects in which their performance could be improved or their scope extended.

For example, the harmonic removal method can be extended by an uncertainty quantification scheme, appreciating that the orthogonally projected harmonic signals are predicted from the stochastic response measurements. The orthogonal projection itself can be reformulated for a better numerical performance with e.g. QR decomposition.

The assumption of approximating the MPC computed from asymptotically real-valued mode shapes with the quadratic form approximation should be verified in a controlled experiment where the nature of the mode shapes of interest is known. A similar suggestion applies to the quadratic form approximation of the MAC computed

between a mode shape estimate and its counterpart from the FE model, where the influence of modeling errors should be studied. A framework that classifies the case where the distribution of the MPC or the MAC estimates is neither Gaussian nor quadratic but in between, and develops its approximation, should be studied.

The performance of the proposed damage detection metric should be tested on a real structure where the excitation is changing in a controlled manner, with e.g. a shaker. Moreover, the assumptions taken to emulate complex changes in the excitation covariance should be verified with real-life excitation cases such as wind, waves and a current. While the residual mean has been shown to be robust to excitation changes, the actual influence of real-life excitation cases on the test statistics in the damaged case should be further evaluated. The proposed metric should also be compared with other Gaussian residuals that have been proposed in the literature [129, 134, 130], and their fusion, to enhance the performance of damage detection, should be studied.

Software transfer

The industrial readiness of the method for harmonic removal and the methods for the Gaussian approximation of the distribution of modal indicators is inferred by their transfer to the commercial software ARTeMIS Modal Pro 6.0 [138].

The use of a quadratic form to approximate the distribution of the parameters at the boarder of their theoretical domain, developed here for the MPC and the MAC, is a novelty in the engineering applications. The proposed approach, however, despite its attractive features to decide about the physical parameters of a structure, does not reached the practical maturity required for a transfer to a commercial software yet, due to the aforementioned sensitivity to modeling errors.

A similar comment applies to the proposed damage detection metric, where for its deployment in a commercial SHM system, the completion of the aforementioned future work is required.

Part III

Appendix

APPENDIX A

Background theory

A.1 Variance of modal parameters

The following section recalls some generic expressions for the covariance computation of the modal parameters.

A.1.1 Variance of modal parameters estimated at single model order

Let $\hat{f}$, $\hat{\zeta}$ and $\hat{\varphi}$ be estimates of natural frequency, damping ratio and mode shape computed from SSI-UPC algorithm for a single model order. A strategy to quantify the variance of $\hat{f}$, $\hat{\zeta}$ and $\hat{\varphi}$ was established in [74, 76, 33]. This section recalls the general principle of that uncertainty quantification scheme.
The first order perturbation of an arbitrary chosen $\hat{f}$, $\hat{\zeta}$ and $\hat{\varphi}$ follows

$$\begin{aligned}
\Delta\hat{f} &= \underbrace{\hat{\mathcal{J}}^{f}_{\hat{A}_n}\hat{\mathcal{J}}^{A_n}_{\hat{\Gamma}}\hat{\mathcal{J}}^{\Gamma}_{\hat{\mathcal{H}}^{\mathrm{dat}}}\hat{\mathcal{J}}^{\mathcal{H}^{\mathrm{dat}}}_{\hat{\mathcal{R}}}}_{=\hat{\mathcal{J}}^{\hat{f}}_{\hat{\mathcal{R}}}}\mathrm{vec}(\Delta\hat{\mathcal{R}}), \qquad (A.1)\\
\Delta\hat{\zeta} &= \underbrace{\hat{\mathcal{J}}^{\zeta}_{\hat{A}_n}\hat{\mathcal{J}}^{A_n}_{\hat{\Gamma}}\hat{\mathcal{J}}^{\Gamma}_{\hat{\mathcal{H}}^{\mathrm{dat}}}\hat{\mathcal{J}}^{\mathcal{H}^{\mathrm{dat}}}_{\hat{\mathcal{R}}}}_{=\hat{\mathcal{J}}^{\hat{\zeta}}_{\hat{\mathcal{R}}}}\mathrm{vec}(\Delta\hat{\mathcal{R}}),\\
\Delta\hat{\varphi} &= \underbrace{\hat{\mathcal{J}}^{\varphi}_{(\hat{A}_n,\hat{C}_n)}\hat{\mathcal{J}}^{(A_n,C_n)}_{\hat{\Gamma}}\hat{\mathcal{J}}^{\Gamma}_{\hat{\mathcal{H}}^{\mathrm{dat}}}\hat{\mathcal{J}}^{\mathcal{H}^{\mathrm{dat}}}_{\hat{\mathcal{R}}}}_{=\hat{\mathcal{J}}^{\hat{\varphi}}_{\hat{\mathcal{R}}}}\mathrm{vec}(\Delta\hat{\mathcal{R}})
\end{aligned}$$

where $\hat{\mathcal{J}}^{f}_{\hat{A}_n}$ is the estimate of the sensitivity of the eigenfrequency with respect to the state transition matrix, $\hat{\mathcal{J}}^{\zeta}_{\hat{A}_n}$ is the estimate of the sensitivity of the damping ratio with respect to the state transition matrix, $\hat{\mathcal{J}}^{\varphi}_{(\hat{A}_n,\hat{C}_n)}$ is the estimate of the sensitivity of the mode shape components with respect to the state transition and the observation matrix, $\hat{\mathcal{J}}^{(A_n,C_n)}_{\hat{\Gamma}}$ is the estimate of the sensitivity of the state transition and the

observation matrix at model order n towards the observability matrix at order n, $\hat{\mathcal{J}}^{\Gamma}_{\hat{\mathcal{H}}^{\text{dat}}}$ is the estimate of the sensitivity of the observability matrix towards Hankel matrix and finally $\hat{\mathcal{J}}^{\mathcal{H}^{\text{dat}}}_{\hat{\mathcal{R}}}$ is the estimate of the sensitivity of the Hankel matrix towards the auto-covariance matrices of the measurements. The stacked auto-covariance matrices $\text{vec}(\Delta\hat{\mathcal{R}}) = \begin{bmatrix}\text{vec}(\Delta\hat{\mathcal{R}}^{+})\\ \text{vec}(\Delta\hat{\mathcal{R}}^{-})\end{bmatrix}$ where $\hat{\mathcal{R}}^{+}$ and $\hat{\mathcal{R}}^{-}$ are respectively the estimated mean of the auto-covariance of each block of the past and future measurements.
An estimate of the covariance of the natural frequency $\Sigma_{\hat{f}}$, damping ratio $\Sigma_{\hat{\zeta}}$ and mode shape $\Sigma_{\hat{\varphi}}$ can be expressed as

$$\begin{aligned}\Sigma_{\hat{f}} &= \hat{\mathcal{J}}^{f}_{\hat{\mathcal{R}}}\Sigma_{\hat{\mathcal{R}}}(\hat{\mathcal{J}}^{f}_{\hat{\mathcal{R}}})^{T},\\ \Sigma_{\hat{\zeta}} &= \hat{\mathcal{J}}^{\zeta}_{\hat{\mathcal{R}}}\Sigma_{\hat{\mathcal{R}}}(\hat{\mathcal{J}}^{\zeta}_{\hat{\mathcal{R}}})^{T},\\ \Sigma_{\hat{\varphi}} &= \hat{\mathcal{J}}^{\varphi}_{\hat{\mathcal{R}}}\Sigma_{\hat{\mathcal{R}}}(\hat{\mathcal{J}}^{\varphi}_{\hat{\mathcal{R}}})^{T}.\end{aligned} \tag{A.2}$$

where $\hat{\mathcal{J}}^{f}_{\hat{\mathcal{R}}}$, $\hat{\mathcal{J}}^{\zeta}_{\hat{\mathcal{R}}}$ and $\hat{\mathcal{J}}^{\varphi}_{\hat{\mathcal{R}}}$ are the respective estimates of a chained sensitivity of $\hat{f}$, $\hat{\zeta}$ and $\hat{\varphi}$ with respect to the estimate of the covariance matrix of the measurements $\hat{\mathcal{R}}$. A detailed developments of (A.1) and (A.2) can be found in [76] and [33].

Remark A.1 (Regarding mode shape normalization schemes) *Two schemes are recalled here, namely*

1. *One mode shape component is set to 1. This k-th component can e.g. be chosen as the component with the maximum amplitude ($k = \arg\max_j\{|\hat{\varphi}_j|\}$), or any other selected entry of $\hat{\varphi}$. The normalized mode shape can be written as*

$$\tilde{\varphi} = \hat{\varphi}/\hat{\varphi}_k. \tag{A.3}$$

   The variance computation of this mode shape normalization scheme is developed in A.1.1.1. Note that the k-th component in this normalized mode shape has, by design, no uncertainty.

2. *The mode shape is rotated such that the imaginary part of one component is 0 and the real part of this component is positive. This k-th component can be chosen as in case 1. Then the mode shape is rotated to the maximum angle of deflection. In addition, the norm of the mode shape is set to 1. Then, the normalized mode shape can be written as*

$$\breve{\varphi} = \tilde{\varphi}/||\tilde{\varphi}||. \tag{A.4}$$

   The variance computation of this mode shape normalization scheme is developed in A.1.1.2. Note that the imaginary part of the k-th component in this normalized mode shape has, by design, no uncertainty.

A.1.1.1 Uncertainty of mode shape normalization scheme 1

To compute the variance of some normalized mode shape, the effect of the normalization must be accounted for. The first order perturbation of the first normalization scheme,

for the estimate $\hat{\varphi}$ of modeshape φ, which was developed in [74], writes as

$$\begin{aligned}\Delta\tilde{\varphi} &= \Delta\left(\frac{1}{\hat{\varphi}_k}\right)\hat{\varphi} + \frac{1}{\hat{\varphi}_k}\Delta\hat{\varphi} \\ &= -\frac{1}{(\hat{\varphi}_k)^2}\Delta(\hat{\varphi}_k)\hat{\varphi} + \frac{1}{\hat{\varphi}_k}\Delta\hat{\varphi} \\ &= \underbrace{\frac{1}{\hat{\varphi}_k}\left(-\frac{1}{\hat{\varphi}_k}\hat{\varphi}e_k^T + I_r\right)}_{=\hat{\mathcal{J}}_{\tilde{\varphi},\hat{\varphi}}}\Delta\hat{\varphi},\end{aligned}$$

using the fact that the (scalar) $\hat{\varphi}_k = e_k^T\hat{\varphi}$ where e_k is the k-th unit vector. The respective covariance of the real and imaginary mode shape part writes thus

$$\operatorname{cov}\left(\begin{bmatrix}\Re(\tilde{\varphi})\\ \Im(\tilde{\varphi})\end{bmatrix}\right) = \begin{bmatrix}\Re(\hat{\mathcal{J}}_{\tilde{\varphi},\hat{\varphi}}\hat{\mathcal{J}}_{\hat{\varphi},\hat{\mathcal{R}}})\\ \Im(\hat{\mathcal{J}}_{\tilde{\varphi},\hat{\varphi}}\hat{\mathcal{J}}_{\hat{\varphi},\hat{\mathcal{R}}})\end{bmatrix}\Sigma_{\hat{\mathcal{R}}}\begin{bmatrix}\Re(\hat{\mathcal{J}}_{\tilde{\varphi},\hat{\varphi}}\hat{\mathcal{J}}_{\hat{\varphi},\hat{\mathcal{R}}})\\ \Im(\hat{\mathcal{J}}_{\tilde{\varphi},\hat{\varphi}}\hat{\mathcal{J}}_{\hat{\varphi},\hat{\mathcal{R}}})\end{bmatrix}^T. \tag{A.5}$$

where $\Sigma_{\hat{\mathcal{R}}}$ can be easily computed as a sample covariance on blocks of the data as in [79] and [33].

A.1.1.2 Uncertainty of mode shape normalization scheme 2

Regarding the second normalization scheme depicted in (A.4), the first order perturbation of $\breve{\varphi}$ writes as

$$\begin{aligned}\Delta\breve{\varphi} &= \Delta\left(\frac{1}{||\tilde{\varphi}||}\right)\tilde{\varphi} + \frac{1}{||\tilde{\varphi}||}\Delta\tilde{\varphi} \\ &= -\frac{\tilde{\varphi}}{2||\tilde{\varphi}||^3}\Delta(||\tilde{\varphi}||^2) + \frac{1}{||\tilde{\varphi}||}\Delta\tilde{\varphi} \\ &= -\frac{\tilde{\varphi}}{||\tilde{\varphi}||^3}\Re(\tilde{\varphi}^H\Delta\tilde{\varphi}) + \frac{1}{||\tilde{\varphi}||}\Delta\tilde{\varphi} \\ &= \underbrace{\frac{1}{||\tilde{\varphi}||}\left(-\frac{\tilde{\varphi}}{||\tilde{\varphi}||^2}\Re(\tilde{\varphi}^H\mathcal{J}_{\tilde{\varphi},\hat{\varphi}}\mathcal{J}_{\hat{\varphi},\hat{\mathcal{R}}}) + \mathcal{J}_{\tilde{\varphi},\hat{\varphi}}\mathcal{J}_{\hat{\varphi},\hat{\mathcal{R}}}\right)}_{=\mathcal{J}_{\breve{\varphi},\hat{\mathcal{R}}}}\operatorname{vec}(\Delta\hat{\mathcal{R}}),\end{aligned}$$

and thus for the covariance of the real and imaginary mode shape parts

$$\operatorname{cov}\left(\begin{bmatrix}\Re(\breve{\varphi})\\ \Im(\breve{\varphi})\end{bmatrix}\right) \approx \begin{bmatrix}\Re(\mathcal{J}_{\breve{\varphi},\hat{\mathcal{R}}})\\ \Im(\mathcal{J}_{\breve{\varphi},\hat{\mathcal{R}}})\end{bmatrix}\Sigma_{\mathcal{R}}\begin{bmatrix}\Re(\mathcal{J}_{\breve{\varphi},\hat{\mathcal{R}}})\\ \Im(\mathcal{J}_{\breve{\varphi},\hat{\mathcal{R}}})\end{bmatrix}^T. \tag{A.6}$$

A.1.2 Variance of global estimates of natural frequencies and damping ratios from the stabilization diagram

Let $\hat{f}^{a,\text{global}}$ and $\hat{\zeta}^{a,\text{global}}$ denote a global estimates of the natural frequency and damping ratio from a model alignment a. Also let $\hat{f}^{a,i}$ and $\hat{\zeta}^{a,i}$ be the i-th estimates of the natural frequency and damping ratio from the same alignment a, where $i = 1 \dots n$

and $\Sigma_{\hat{f}^{a,i},\hat{\zeta}^{a,i}}$ is their joint covariance matrix. Now, the expressions for the global estimates of natural frequencies and damping ratios from [79] write as

$$\begin{bmatrix} \hat{f}^{a,\text{global}} \\ \hat{\zeta}^{a,\text{global}} \end{bmatrix} = \left(\sum_{i=1}^{n} \Sigma^{-1}_{\hat{f}^{a,i},\hat{\zeta}^{a,i}} \right)^{-1} \left(\sum_{i=1}^{n} \Sigma^{-1}_{\hat{f}^{a,i},\hat{\zeta}^{a,i}} \begin{bmatrix} \hat{f}^{a,i} \\ \hat{\zeta}^{a,i} \end{bmatrix} \right) \tag{A.7}$$

and their first order perturbation

$$\begin{bmatrix} \Delta\hat{f}^{a,\text{global}} \\ \Delta\hat{\zeta}^{a,\text{global}} \end{bmatrix} = \left(\sum_{i=1}^{n} \Sigma^{-1}_{\hat{f}^{a,i},\hat{\zeta}^{a,i}} \right)^{-1} \left(\sum_{i=1}^{n} \Sigma^{-1}_{\hat{f}^{a,i},\hat{\zeta}^{a,i}} \begin{bmatrix} \mathcal{J}^{\hat{f}^{a,i}}_{\hat{\mathcal{R}}} \\ \mathcal{J}^{\hat{\zeta}^{a,i}}_{\hat{\mathcal{R}}} \end{bmatrix} \right) \text{vec}(\Delta\hat{\mathcal{R}}) \ . \tag{A.8}$$

APPENDIX B

Uncertainty quantification of Modal Phase Collinearity

B.1 Proof of Lemma 2.4

The eigenvalues λ_1 and λ_2 write

$$\begin{aligned}\lambda_1 &= \frac{(S_{xx}+S_{yy})+\sqrt{(S_{xx}-S_{yy})^2+4S_{xy}^2}}{2}\ ,\\ \lambda_2 &= \frac{(S_{xx}+S_{yy})-\sqrt{(S_{xx}-S_{yy})^2+4S_{xy}^2}}{2}\ .\end{aligned} \tag{B.1}$$

Plugging (B.1) into (2.13) gives

$$\mathrm{MPC} = \frac{(S_{xx}-S_{yy})^2+4(S_{xy})^2}{(S_{xx}+S_{yy})^2}\quad , \tag{B.2}$$

which is identical to expression in (2.14). The MPC can be also expressed as a MAC value between a mode shape and its complex conjugate. It writes as follows

$$\begin{aligned}\mathrm{MAC}(\varphi,\overline{\varphi}) &= \frac{\varphi^H\overline{\varphi}\varphi^T\varphi}{\varphi^H\varphi\varphi^T\overline{\varphi}}\\ &= \frac{\left(S_{xx}-2i\Re(\varphi)^T\Im(\varphi)-S_{yy}\right)\left(S_{xx}+2i\Re(\varphi)^T\Im(\varphi)-S_{yy}\right)}{(S_{xx}+S_{yy})^2}\\ &= \frac{(S_{xx}-S_{yy})^2+4(S_{xy})^2}{(S_{xx}+S_{yy})^2}\ .\end{aligned}$$

B.2 Proof of Lemma 4.1

Evaluated in φ_* the partial derivatives (4.3)-(4.4) yield

$$\frac{\partial g_{mpc}}{\partial \Re(\varphi)} = \frac{4(S^*_{xx} - S^*_{yy})\Re(\varphi_*)^T + 8S^*_{xy}\Im(\varphi_*)^T}{(c_*)^2} - \frac{4g_{mpc}(\varphi_*)\Re(\varphi_*)^T}{c_*} , \tag{B.3}$$

$$\frac{\partial g_{mpc}}{\partial \Im(\varphi)} = \frac{4(S^*_{yy} - S^*_{xx})\Im(\varphi_*)^T + 8S^*_{xy}\Re(\varphi_*)^T}{(c_*)^2} - \frac{4g_{mpc}(\varphi_*)\Im(\varphi_*)^T}{c_*} , \tag{B.4}$$

where the respective scalars S^*_{xx}, S^*_{yy}, S^*_{xy}, S^*_{yx} and c_* correspond to S_{xx}, S_{yy}, S_{xy}, S_{yx} and c evaluated on φ_*.

First it is proved that $g_{mpc}(\varphi_*) = \{0, 1\} \Rightarrow \mathcal{J}^{g_{mpc}}_{\varphi_*} = 0$. First consider the case $g_{mpc}(\varphi_*) = 1$. Equating the numerator and denominator of the fraction from (2.14) yields

$$\begin{aligned} &\left(S^*_{xx} - S^*_{yy}\right)^2 + 4\left(S^*_{xy}\right)^2 = \left(S^*_{xx} + S^*_{yy}\right)^2 , \\ &\Rightarrow 4S^*_{xx}S^*_{yy} = 4S^{*2}_{xy} , \\ &\Rightarrow ||\Re(\varphi_*)||^2||\Im(\varphi_*)||^2 = ||\Re(\varphi_*)||^2||\Im(\varphi_*)||^2\cos^2(\Re(\varphi_*), \Im(\varphi_*)) , \\ &\Rightarrow \cos^2(\Re(\varphi_*), \Im(\varphi_*)) = 1 . \end{aligned} \tag{B.5}$$

As such, (B.5) implies that the angle between the real and imaginary part of φ_* is 0. Thus, assuming without loss of generality that the real part is non-zero, then the imaginary part is a multiple of the real part, $a \cdot \Re(\varphi_*) = \Im(\varphi_*)$ where a is a scalar constant. Consequently, $\mathcal{J}^{g_{mpc}}_{\varphi_*}$ writes as

$$\begin{aligned} \frac{\partial g_{mpc}}{\partial \Re(\varphi)} &= \frac{4(S^*_{xx} - a^2 S^*_{xx})\Re(\varphi_*)^T + 8a^2 S^*_{xx}\Re(\varphi_*)^T}{c_*^2} \\ &\quad - \frac{4g_{mpc}(\varphi_*)(S^*_{xx} + a^2 S^*_{xx})\Re(\varphi_*)^T}{c_*^2} \\ &= \frac{4(S^*_{xx} + a^2 S^*_{xx})\Re(\varphi_*)^T - 4(S^*_{xx} + a^2 S^*_{xx})\Re(\varphi_*)^T}{c_*^2} = 0 \end{aligned}$$

and

$$\begin{aligned} \frac{\partial g_{mpc}}{\partial \Im(\varphi)} &= \frac{4(a^2 S^*_{xx} - S^*_{xx})a\Re(\varphi_*)^T + 8aS^*_{xx}\Re(\varphi_*)^T}{c_*^2} \\ &\quad - \frac{4g_{mpc}(\varphi_*)(S^*_{xx} + a^2 S^*_{xx})a\Re(\varphi_*)^T}{c_*^2} \\ &= \frac{8aS^*_{xx}\Re(\varphi_*)^T - 8aS^*_{xx}\Re(\varphi_*)^T}{c_*^2} = 0 . \end{aligned}$$

Similarly, assuming that $g_{mpc}(\varphi_*) = 0$, it results that

$$\begin{aligned} &\left(S^*_{xx} - S^*_{yy}\right)^2 + 4\left(S^*_{xy}\right)^2 = 0 \ , \\ &\Rightarrow \left(S^*_{xx} - S^*_{yy}\right)^2 = -4S^*_{xx}S^*_{yy}\cos^2(\Re(\varphi_*), \Im(\varphi_*)) \ , \end{aligned} \tag{B.6}$$

where $S^{*2}_{xy} = S^*_{xx}S^*_{yy}\cos^2(\Re(\varphi_*), \Im(\varphi_*))$. Since the right side of (B.6) is less than or equal to zero and the left side of (B.6) is greater than or equal to zero, both sides are zero, hence $S^*_{xx} = S^*_{yy}$ and $\cos^2(\Re(\varphi_*), \Im(\varphi_*)) = 0$. Plugging this into (4.3) and (4.4) yields

$$\frac{\partial g_{mpc}}{\partial \Re(\varphi)} = \frac{4(S^*_{xx} - S^*_{xx})\Re(\varphi_*)^T + 0}{c_*^2} - \frac{0}{c_*} = 0$$

and

$$\frac{\partial g_{mpc}}{\partial \Im(\varphi)} = \frac{4(S^*_{xx} - S^*_{xx})\Im(\varphi_*)^T + 0}{c_*^2} - \frac{0}{c_*} = 0 \ ,$$

which concludes the first part of the proof. Second it is shown that $\mathcal{J}^{g_{mpc}}_{\varphi_*} = 0 \Rightarrow g_{mpc}(\varphi_*) = \{0, 1\}$. Equating the numerator of (4.3) to zero yields

$$\begin{aligned} &4(S^*_{xx} - S^*_{yy})\Re(\varphi_*)^T + 8S^*_{xy}\Im(\varphi_*)^T \\ &\qquad - 4g_{mpc}(\varphi_*)\Re(\varphi_*)^T \left(S^*_{xx} + S^*_{yy}\right) = 0 \ . \end{aligned} \tag{B.7}$$

Consider two cases, depending whether $S^*_{xy} \neq 0$ or $S^*_{xy} = 0$. In the first case, multiplying (B.7) with $\Im(\varphi_*)$ yields to

$$\begin{aligned} &4(S^*_{xx} - S^*_{yy})\Re(\varphi_*)^T + 8S^*_{xy}\Im(\varphi_*)^T \\ &= 4g_{mpc}(\varphi_*)\Re(\varphi_*)^T \left(S^*_{xx} + S^*_{yy}\right) \ , \\ &\Rightarrow 4(S^*_{xx} - S^*_{yy})S^*_{xy} + 8S^*_{xy}S^*_{yy} = 4S^*_{xy}g_{mpc}(\varphi_*)\left(S^*_{xx} + S^*_{yy}\right) \ , \\ &\Rightarrow 4(S^*_{xx} - S^*_{yy}) + 8S^*_{yy} = 4g_{mpc}(\varphi_*)\left(S^*_{xx} + S^*_{yy}\right) \ , \\ &\Rightarrow 4(S^*_{xx} + S^*_{yy}) = 4g_{mpc}(\varphi_*)\left(S^*_{xx} + S^*_{yy}\right) \ , \\ &\Rightarrow g_{mpc}(\varphi_*) = 1 \ . \end{aligned} \tag{B.8}$$

In the second case when $S^*_{xy} = 0$, multiplying (B.7) with $\Re(\varphi_*)$, where $\Re(\varphi_*) \neq 0$ and $S^*_{xx} \neq 0$, leads to

$$\begin{aligned} &4(S^*_{xx} - S^*_{yy})\Re(\varphi_*)^T + 8S^*_{xy}\Im(\varphi_*)^T \\ &= 4g_{mpc}(\varphi_*)\Re(\varphi_*)^T \left(S^*_{xx} + S^*_{yy}\right) \ , \\ &\Rightarrow 4(S^*_{xx} - S^*_{yy})S^*_{xx} = 4S^*_{xx}g_{mpc}(\varphi_*)\left(S^*_{xx} + S^*_{yy}\right) \ , \\ &\Rightarrow S^*_{xx} - S^*_{yy} = \frac{\left(S^*_{xx} - S^*_{yy}\right)^2}{S^*_{xx} + S^*_{yy}} \ . \end{aligned} \tag{B.9}$$

Consequently, distinguish two solutions. First consider $S^*_{xx} = S^*_{yy}$, which together with $S^*_{xy} = 0$ yields

$$g_{mpc}(\varphi_*) = \frac{0}{\left(S^*_{xx} + S^*_{yy}\right)^2} = 0 \ .$$

Second, suppose that $S_{xx}^* \neq S_{yy}^*$, which gives

$$\begin{aligned} &S_{xx}^* - S_{yy}^* = S_{xx}^* + S_{yy}^* \ , \\ &\Rightarrow S_{yy}^* = 0 \ . \end{aligned} \tag{B.10}$$

Plugging $S_{yy}^* = 0$ together with $S_{xy}^* = 0$ into (2.14) yields

$$g_{mpc}(\varphi_*) = S_{xx}^{*2}/S_{xx}^{*2} = 1 \ .$$

Thus, based on (B.8) and the roots of (B.9) it holds that $\mathcal{J}_{\varphi_*}^{g_{mpc}} = 0 \Rightarrow g_{mpc}(\varphi_*) = \{0, 1\}$. That leads to the assertion in Lemma 4.1.

B.3 Hessian derivation

In the following the respective parts of the Hessian are developed and evaluated considering that the imaginary part of the mode shape is a multiple of its real part, $a \cdot \Re(\varphi_*) = \Im(\varphi_*)$. The partial derivatives introduced in (4.14) can be computed such that

$$\frac{\partial^2 g_{mpc}}{\partial \Re(\varphi) \partial \Re(\varphi)} = \frac{\partial}{\partial \Re(\varphi)} \left(\frac{\partial g_{mpc}}{\partial \Re(\varphi)} \right)^T \ , \tag{B.11}$$

$$\frac{\partial^2 g_{mpc}}{\partial \Im(\varphi) \partial \Re(\varphi)} = \frac{\partial}{\partial \Im(\varphi)} \left(\frac{\partial g_{mpc}}{\partial \Re(\varphi)} \right)^T \ , \tag{B.12}$$

$$\frac{\partial^2 g_{mpc}}{\partial \Re(\varphi) \partial \Im(\varphi)} = \frac{\partial}{\partial \Re(\varphi)} \left(\frac{\partial g_{mpc}}{\partial \Im(\varphi)} \right)^T \ , \tag{B.13}$$

$$\frac{\partial^2 g_{mpc}}{\partial \Im(\varphi) \partial \Im(\varphi)} = \frac{\partial}{\partial \Im(\varphi)} \left(\frac{\partial g_{mpc}}{\partial \Im(\varphi)} \right)^T \ . \tag{B.14}$$

Notice that $\frac{\partial^2 g_{mpc}}{\partial \Im(\varphi) \partial \Re(\varphi)} = \frac{\partial^2 g_{mpc}}{\partial \Re(\varphi) \partial \Im(\varphi)}^T$. Based on (4.3), (B.11) writes as

$$\begin{aligned} \frac{\partial^2 g_{mpc}}{\partial \Re(\varphi) \partial \Re(\varphi)} &= \frac{\partial}{\partial \Re(\varphi)} \frac{4\Re(\varphi)(S_{xx} - S_{yy}) + 8\Im(\varphi) S_{xy}}{c^2} \\ &\quad - \frac{\partial}{\partial \Re(\varphi)} \frac{4\Re(\varphi) g_{mpc}(\varphi)}{c} \\ &= \underbrace{\frac{\partial}{\partial \Re(\varphi)} \frac{4\Re(\varphi)(S_{xx} - S_{yy}) + 8\Im(\varphi) S_{xy}}{c^2}}_{=\mathrm{A}_{1,1}(\varphi)} \\ &\quad + \underbrace{\frac{\partial}{\partial \Re(\varphi)} \frac{-4\Re(\varphi) g_{mpc}(\varphi)}{c}}_{=\mathrm{B}_{1,1}(\varphi)} \ . \end{aligned} \tag{B.15}$$

Matrix $\mathrm{A}_{1,1}$ from (B.15) evaluated at φ_* follows

$$\begin{aligned}\mathrm{A}_{1,1}(\varphi_*) &= \frac{4I_r(S^*_{xx}-S^*_{yy})+8\left(\Re(\varphi_*)\Re(\varphi_*)^T+\Im(\varphi_*)\Im(\varphi_*)^T\right)}{c_*^2} \\ &- \frac{\left(4\Re(\varphi_*)(S^*_{xx}-S^*_{yy})+8\Im(\varphi_*)S^*_{xy}\right)\left(4\Re(\varphi_*)^T(S^*_{xx}+S^*_{yy})\right)}{c_*^4} \\ &= \frac{4I_r(S^*_{xx}-S^*_{yy})+8(\Re(\varphi_*)\Re(\varphi_*)^T+\Im(\varphi_*)\Im(\varphi_*)^T)}{c_*^2} \\ &- \frac{16\Re(\varphi_*)\Re(\varphi_*)^T(S^*_{xx}-S^*_{yy})+32\Im(\varphi_*)\Re(\varphi_*)^TS^*_{xy}}{c_*^3}\ .\end{aligned} \tag{B.16}$$

Since $\partial g_{mpc}/\partial\Re(\varphi)\ (\varphi_*)=0$, matrix $\mathrm{B}_{1,1}$ from (B.15) evaluated at φ_* writes as

$$\mathrm{B}_{1,1}(\varphi_*) = \frac{-4c_*I_r+8\Re(\varphi_*)\Re(\varphi_*)^T}{c_*^2}\ . \tag{B.17}$$

Combining (B.16) and (B.17) with the simplified notation from (4.15) yields

$$\begin{aligned}\mathrm{A}_{1,1}(\varphi_*)+\mathrm{B}_{1,1}(\varphi_*) &= \frac{-8S^*_{yy}I_r+8(2M^*_{xx}+M^*_{yy})}{c_*^2} \\ &- \frac{16b_*M^*_{xx}+32M^*_{yx}S^*_{xy}}{c_*^3}\ ,\end{aligned} \tag{B.18}$$

where $b_*=S^*_{xx}-S^*_{yy}$. Deploying $a\cdot\Re(\varphi_*)=\Im(\varphi_*)$, the expression in (B.18) gives

$$\begin{aligned}\mathrm{A}_{1,1}(\varphi_*)+\mathrm{B}_{1,1}(\varphi_*) &= \frac{-8a^2S^*_{xx}I_r+8(2M^*_{xx}+a^2M^*_{xx})}{(1+a^2)^2S^{*2}_{xx}} \\ &- \frac{16(1-a^2)S^*_{xx}M^*_{xx}+32a^2M^*_{xx}S^*_{xx}}{(1+a^2)^3S^{*3}_{xx}} \\ &= \frac{8a^2\left(M^*_{xx}+a^2M^*_{xx}-I_rS^*_{xx}-a^2I_rS^*_{xx}\right)}{(1+a^2)^3S^{*2}_{xx}} \\ &= \frac{8a^2\left(M^*_{xx}-I_rS^*_{xx}\right)}{(1+a^2)^2S^{*2}_{xx}}\ .\end{aligned} \tag{B.19}$$

Second, after (4.4), (B.14) writes as

$$\begin{aligned}\frac{\partial^2 g_{mpc}}{\partial\Im(\varphi)\partial\Im(\varphi)} &= \frac{\partial}{\partial\Im(\varphi)}\frac{4\Im(\varphi)(S_{yy}-S_{xx})+8\Re(\varphi)S_{xy}}{c^2} \\ &- \frac{\partial}{\partial\Im(\varphi)}\frac{4\Im(\varphi)g_{mpc}(\varphi)}{c} \\ &= \underbrace{\frac{\partial}{\partial\Im(\varphi)}\frac{4\Im(\varphi)(S_{yy}-S_{xx})+8\Re(\varphi)S_{xy}}{c^2}}_{=\mathrm{A}_{2,2}(\varphi)} \\ &+ \underbrace{\frac{\partial}{\partial\Im(\varphi)}\frac{-4\Im(\varphi)g_{mpc}(\varphi)}{c}}_{=\mathrm{B}_{2,2}(\varphi)}\ .\end{aligned} \tag{B.20}$$

Matrix $\mathrm{A}_{2,2}$ from (B.20) evaluated at φ_* follows

$$\begin{aligned}\mathrm{A}_{2,2}(\varphi_*) = &\frac{4I_r(S^*_{yy}-S^*_{xx})+8(\Re(\varphi_*)\Re(\varphi_*)^T+\Im(\varphi_*)\Im(\varphi_*)^T)}{c_*^2}\\ &-\frac{16\Im(\varphi_*)\Im(\varphi_*)^T(S^*_{yy}-S^*_{xx})+32\Re(\varphi_*)\Im(\varphi_*)^T S^*_{xy}}{c_*^3}\ .\end{aligned} \tag{B.21}$$

Matrix $\mathrm{B}_{2,2}$ from (B.20) evaluated at φ_* writes as

$$\mathrm{B}_{2,2}(\varphi_*) = \frac{-4c_*I_r+8\Im(\varphi_*)\Im(\varphi_*)^T}{c_*^2}\ . \tag{B.22}$$

Combining (B.21) and (B.22) with the simplified notation from (4.15) yields

$$\begin{aligned}\mathrm{A}_{2,2}(\varphi_*)+\mathrm{B}_{2,2}(\varphi_*) = &\frac{-8S^*_{xx}I_r+8(M^*_{xx}+2M^*_{yy})}{c_*^2}\\ &-\frac{-16b_*M^*_{yy}+32M^*_{xy}S^*_{xy}}{c_*^3}\end{aligned} \tag{B.23}$$

and deploying $a\cdot\Re(\varphi_*)=\Im(\varphi_*)$ the expression in (B.23) gives

$$\begin{aligned}\mathrm{A}_{2,2}(\varphi_*)+\mathrm{B}_{2,2}(\varphi_*) &= \frac{-8S^*_{xx}I_r+8(M^*_{xx}+2a^2M^*_{xx})}{(1+a^2)^2S^{*2}_{xx}}\\ &\quad-\frac{-16(1-a^2)a^2S^*_{xx}M^*_{xx}+32a^2M^*_{xx}S^*_{xx}}{(1+a^2)^3S^{*3}_{xx}}\\ &= \frac{8\left(M^*_{xx}+a^2M^*_{xx}-I_rS^*_{xx}-a^2I_rS^*_{xx}\right)}{(1+a^2)^3S^{*2}_{xx}}\\ &= \frac{8\left(M^*_{xx}-I_rS^*_{xx}\right)}{(1+a^2)^2S^{*2}_{xx}}\ .\end{aligned} \tag{B.24}$$

The cross derivative $\frac{\partial^2 g_{mpc}}{\partial\Im(\varphi)\partial\Re(\varphi)}$ from (B.12) writes as

$$\frac{\partial^2 g_{mpc}}{\partial\Im(\varphi)\partial\Re(\varphi)} = \frac{\partial}{\partial\Im(\varphi)}\frac{4\Re(\varphi)(S_{xx}-S_{yy})+8\Im(\varphi)S_{xy}}{c^2} \tag{B.25}$$

$$\begin{aligned}&-\frac{\partial}{\partial\Im(\varphi)}\frac{4\Re(\varphi)g_{mpc}(\varphi)}{c}\\ &=\underbrace{\frac{\partial}{\partial\Im(\varphi)}\frac{4\Re(\varphi)(S_{xx}-S_{yy})+8\Im(\varphi)S_{xy}}{c^2}}_{=\mathrm{A}_{1,2}(\varphi)}\\ &+\underbrace{\frac{\partial}{\partial\Im(\varphi)}\frac{-4\Re(\varphi)g_{mpc}(\varphi)}{c}}_{=\mathrm{B}_{1,2}(\varphi)}\ .\end{aligned}$$

Matrix $\mathrm{A}_{1,2}$ from (B.25) evaluated at φ_* follows

$$\begin{aligned}\mathrm{A}_{1,2}(\varphi_*) &= \frac{8\left(\Im(\varphi_*)\Re(\varphi_*)^T - \Re(\varphi_*)\Im(\varphi_*)^T\right) + 8I_r S_{xy}^*}{c_*^2} \\ &- \frac{\left(4\Re(\varphi_*)(S_{xx}^* - S_{yy}^*) + 8\Im(\varphi_*)S_{xy}^*\right)\left(4\Im(\varphi_*)^T(S_{xx}^* + S_{yy}^*)\right)}{c_*^4} \\ &= \frac{8\left(\Im(\varphi_*)\Re(\varphi_*)^T - \Re(\varphi_*)\Im(\varphi_*)^T\right) + 8I_r S_{xy}^*}{c_*^2} \\ &- \frac{16\Re(\varphi_*)\Im(\varphi_*)^T(S_{xx}^* - S_{yy}^*) + 32\Im(\varphi_*)\Im(\varphi_*)^T S_{xy}^*}{c_*^3} \ .\end{aligned} \tag{B.26}$$

Matrix $\mathrm{B}_{1,2}$ from (B.25) evaluated at φ_* writes as

$$\mathrm{B}_{1,2}(\varphi_*) = \frac{8\Re(\varphi_*)\Im(\varphi_*)^T}{c_*^2} \ . \tag{B.27}$$

Combining (B.26) and (B.27) with the simplified notation from (4.15) yields

$$\mathrm{A}_{1,2}(\varphi_*) + \mathrm{B}_{1,2}(\varphi_*) = \frac{8M_{xy}^* + 8I_r S_{xy}^*}{c_*^2} - \frac{16b_* M_{xy}^* + 32M_{yy}^* S_{xy}^*}{c_*^3} \tag{B.28}$$

and deploying $a \cdot \Re(\varphi_*) = \Im(\varphi_*)$ the expression in (B.28) gives

$$\begin{aligned}\mathrm{A}_{1,2}(\varphi_*) + \mathrm{B}_{1,2}(\varphi_*) &= \frac{8aM_{xx}^* + 8aI_r S_{xx}^*}{(1+a^2)^2 S_{xx}^{*2}} \\ &- \frac{16(1-a^2)aS_{xx}^* M_{xx}^* + 32a^3 M_{xx}^* S_{xx}^*}{(1+a^2)^3 S_{xx}^{*3}} \\ &= \frac{8a\left(I_r S_{xx}^* + a^2 I_r S_{xx}^* - M_{xx}^* - a^2 M_{xx}^*\right)}{(1+a^2)^3 S_{xx}^{*2}} \\ &= \frac{8a\left(I_r S_{xx}^* - M_{xx}^*\right)}{(1+a^2)^2 S_{xx}^{*2}} \ .\end{aligned} \tag{B.29}$$

Lastly, from (B.13), it writes as

$$\begin{aligned}\frac{\partial^2 g_{mpc}}{\partial\Re(\varphi)\partial\Im(\varphi)} &= \frac{\partial}{\partial\Re(\varphi)}\frac{4\Im(\varphi)(S_{yy} - S_{xx}) + 8\Re(\varphi)S_{xy}}{c^2} \\ &- \frac{\partial}{\partial\Re(\varphi)}\frac{4\Im(\varphi)g_{mpc}(\varphi)}{c} \\ &= \underbrace{\frac{\partial}{\partial\Re(\varphi)}\frac{4\Im(\varphi)(S_{yy} - S_{xx}) + 8\Re(\varphi)S_{xy}}{c^2}}_{=\mathrm{A}_{2,1}(\varphi)} \\ &+ \underbrace{\frac{\partial}{\partial\Re(\varphi)}\frac{-4\Im(\varphi)g_{mpc}(\varphi)}{c}}_{=\mathrm{B}_{2,1}(\varphi)} \ .\end{aligned} \tag{B.30}$$

Matrix $\mathrm{A}_{2,1}$ from (B.30) evaluated at φ_* follows

$$\begin{aligned}\mathrm{A}_{2,1}(\varphi_*) &= \frac{8\left(\Re(\varphi_*)\Im(\varphi_*)^T - \Im(\varphi_*)\Re(\varphi_*)^T\right) + 8I_r S_{xy}^*}{c_*^2} \\ &- \frac{\left(4\Im(\varphi_*)(S_{yy}^* - S_{xx}^*) + 8\Re(\varphi_*)S_{xy}^*\right)\left(4\Re(\varphi_*)^T(S_{xx}^* + S_{yy}^*)\right)}{c_*^4} \\ &= \frac{8\left(\Re(\varphi_*)\Im(\varphi_*)^T - \Im(\varphi_*)\Re(\varphi_*)^T\right) + 8I_r S_{xy}^*}{c_*^2} \\ &- \frac{16\Im(\varphi_*)\Re(\varphi_*)^T(S_{yy}^* - S_{xx}^*) + 32\Re(\varphi_*)\Re(\varphi_*)^T S_{xy}^*}{c_*^3} \ .\end{aligned} \tag{B.31}$$

Matrix $\mathrm{B}_{2,1}(\varphi_*)$ from (B.30) evaluated at φ_* writes as

$$\begin{aligned}\mathrm{B}_{2,1}(\varphi_*) &= \frac{\left(\frac{\partial\left(-4\Im(\varphi)g_{mpc}(\varphi)\right)}{\partial\Re(\varphi)}\right)c_* + 8\Im(\varphi_*)\Re(\varphi_*)^T}{c_*^2} \\ &= \frac{8\Im(\varphi_*)\Re(\varphi_*)^T}{c_*^2} \ .\end{aligned} \tag{B.32}$$

Combining (B.31) and (B.32) with the simplified notation from (4.15) yields

$$\mathrm{A}_{2,1}(\varphi_*) + \mathrm{B}_{2,1}(\varphi_*) = \frac{8M_{xy}^* + 8I_r S_{xy}^*}{c_*^2} + \frac{16b_* M_{yx}^* - 32M_{xx}^* S_{xy}^*}{c_*^3} \tag{B.33}$$

and deploying $a \cdot \Re(\varphi_*) = \Im(\varphi_*)$ the expression in (B.33) gives

$$\begin{aligned}\mathrm{A}_{2,1}(\varphi_*) + \mathrm{B}_{2,1}(\varphi_*) &= \frac{8aM_{xx}^* + 8aI_r S_{xx}^*}{(1+a^2)^2 S_{xx}^{*2}} \\ &- \frac{-16(1-a^2)aS_{xx}^* M_{xx}^* + 32aM_{xx}^* S_{xx}^*}{(1+a^2)^3 S_{xx}^{*3}} \\ &= \frac{8a\left(I_r S_{xx}^* + a^2 I_r S_{xx}^* - M_{xx}^* - a^2 M_{xx}^*\right)}{(1+a^2)^3 S_{xx}^{*2}} \\ &= \frac{8a\left(I_r S_{xx}^* - M_{xx}^*\right)}{(1+a^2)^2 S_{xx}^{*2}} \ .\end{aligned} \tag{B.34}$$

B.4 Proof of Lemma 4.4

First it is shown that $\mathrm{H}_{\varphi_*}^{g_{mpc}}$ is negative semi-definite. Let λ_1, λ_2 be the eigenvalues of M_a and $\mu_1 \dots \mu_r$ the eigenvalues of K_x. The eigenvalues of the Kronecker product $M_a \otimes K_x$ can be written as a product of the eigenvalues of corresponding matrices $\lambda_i \cdot \mu_j$ where $i = \{1, 2\}$ and $j = 1 \dots r$. First, start with computing λ which satisfies

$$(\lambda - a^2)(\lambda - 1) - a^2 = \lambda^2 + a^2 - \lambda - a^2\lambda - a^2 = \lambda(\lambda - 1 - a^2) = 0 \ . \tag{B.35}$$

Thus, $\lambda_1 = 0$ and $\lambda_2 = a^2 + 1 > 0$. Second, for any vector $y \in \mathbb{R}^r$ matrix K_x satisfies

$$\begin{aligned} y^T K_x y &= y^T \left(M^*_{xx} - I_r S^*_{xx}\right) y \qquad \text{(B.36)} \\ &= y^T \left(\Re(\varphi_*)\Re(\varphi_*)^T - I_r \Re(\varphi_*)^T \Re(\varphi_*)\right) y \\ &= y^T \Re(\varphi_*)\Re(\varphi_*)^T y - y^T y \Re(\varphi_*)^T \Re(\varphi_*) \\ &= ||\Re(\varphi_*)||^2 ||y||^2 \cos(\Re(\varphi_*), y) - ||y||^2 ||\Re(\varphi_*)||^2 \leq 0 \ , \end{aligned}$$

which implies that for all $\mu_1 \dots \mu_r \leq 0$. The expression in (B.36) is equal to zero if and only if $\cos(\Re(\varphi_*), y) = 1$, e.g. if and only if y is a multiple of $\Re(\varphi_*)$. Subsequently the eigenvalues of the Kronecker product $M_a \otimes K_x$ are smaller than or equal to zero, and since the scalar $n_{xx} = 8/(1+a^2)^2 S^2_{xx} > 0$, it can be concluded that the matrix $\mathrm{H}^{g_{mpc}}_{\varphi_*}$ is negative semi-definite.

Next, based on the property of the Kronecker product which states that $\mathrm{rank}(A \otimes B) = \mathrm{rank}(A) \cdot \mathrm{rank}(B)$, it is shown that $\mathrm{rank}\left(\mathrm{H}^{g_{mpc}}_{\varphi_*}\right) = r - 1$. First, examine the rank of K_x. Based on (B.36), one eigenvalue of K_x and the corresponding eigenvector writes as $\mu_1 = 0$ and $\tilde{x} = \Re(\varphi_*)/||\Re(\varphi_*)||^2$ respectively. The computation of the remaining $r-1$ eigenvalues is as follows: It exists $r-1$ linearly independent vectors $q_1, \dots, q_{r-1} \in \mathbb{R}^r$, such that $\{\tilde{x}, q_1 \dots q_{r-1}\}$ is an orthonormal basis of $\mathbb{R}^r$ that satisfies $q_i^T \tilde{x} = 0$ for $i = 1 \dots r-1$, $q_i^T q_j = 0$, $i \neq j$ and $q_i^T q_i = 1$. To show that the (q_i) are actually the eigenvectors of K_x, and to deduce its eigenvalues, write

$$\begin{aligned} K_x q_i &= \left(\Re(\varphi_*)\Re(\varphi_*)^T - I_r \Re(\varphi_*)^T \Re(\varphi_*)\right) q_i \qquad \text{(B.37)} \\ &= ||\Re(\varphi_*)||^2 \left(\tilde{x}\tilde{x}^T - I_r \underbrace{\tilde{x}^T \tilde{x}}_{=1}\right) q_i \\ &= ||\Re(\varphi_*)||^2 \left(\tilde{x} \underbrace{\tilde{x}^T q_i}_{=0} - q_i\right) \\ &= -||\Re(\varphi_*)||^2 q_i = \mu_i q_i \ . \end{aligned}$$

Therefore $L = \begin{bmatrix} \tilde{x} & q_1 & \dots & q_{r-1} \end{bmatrix}$ are the eigenvectors that satisfy the eigenvalue decomposition

$$L^T K_x L = M \text{ with } \mathrm{M} = \begin{bmatrix} 0 & & & \\ & -||\Re(\varphi_*)||^2 & & \\ & & \ddots & \\ & & & -||\Re(\varphi_*)||^2 \end{bmatrix}$$

and hence $\mathrm{rank}(K_x) = r - 1$. That, together with $\mathrm{rank}(M_a) = 1$, inferred from (B.35), concludes the second part of the proof.

B.5 Proof of Theorem 4.5

Theorem 4.5 describes the approximation of the quadratic form $Q(\hat{X}_{\mathcal{N}})$, where $\hat{X}_{\mathcal{N}}$ is an *asymptotically* Gaussian vector, by a scaled χ^2 distribution based on

[84]. However, in [84] the quadratic form is defined using a Gaussian vector. Since $Q(\hat{X}_\mathcal{N}) \to X_\mathcal{N}^T \overline{\mathrm{H}}_{\varphi_*}^{g_{mpc}} X_\mathcal{N}$, the following proof can be carried out using the Gaussian vector $X_\mathcal{N} \sim \mathcal{N}(0, \Sigma_{\varphi_*})$ and the asymptotic quadratic form $X_\mathcal{N}^T \overline{\mathrm{H}}_{\varphi_*}^{g_{mpc}} X_\mathcal{N}$, and all the results hold asymptotically.

This proof contains three parts. The first part details the development of the asymptotic quadratic form of $X_\mathcal{N}^T \overline{\mathrm{H}}_{\varphi_*}^{g_{mpc}} X_\mathcal{N}$ into a weighted sum of χ_1^2-distributed variables, while neither $\overline{\mathrm{H}}_{\varphi_*}^{g_{mpc}}$ nor Σ_{φ_*} are of full rank. This particular case has not been detailed in [84]. Then, the subsequent approximation of this sum by a scaled $\chi_{l_{PT}}^2$ distribution can be made based on [84], where two cases for the computation of l_{PT} are described. The second part of the proof justifies the choice $l_{PT} = c_2^3/c_3^2$ in [84]. Finally, the third part details the scaling of the $\chi_{l_{PT}}^2$ distribution based on [84].

B.5.1 Part 1: development of quadratic form with degenerate Gaussian vector into sum of χ_1^2 distributions

First, introduce the inverse square root of Σ_{φ_*}, which is computed from the SVD

$$\Sigma_{\varphi_*} = \begin{bmatrix} U_1 & U_2 \end{bmatrix} \begin{bmatrix} D_1 & 0 \\ 0 & 0 \end{bmatrix} \begin{bmatrix} U_1^T \\ U_2^T \end{bmatrix} \ . \tag{B.38}$$

The square root matrix can be defined as $\Sigma_{\varphi_*}^{1/2} = U_1 D_1^{1/2} \in \mathbb{R}^{2r \times d}$, $d = \mathrm{rank}\,(\Sigma_{\varphi_*}) \leq r-1$, and its pseudo-inverse is defined as $\Sigma_{\varphi_*}^{-1/2} = D_1^{-1/2} U_1^T \in \mathbb{R}^{d \times 2r}$. From the properties of SVD it holds that $\Sigma_{\varphi_*}^{-1/2} \Sigma_{\varphi_*}^{1/2} = I_d$ and $\Sigma_{\varphi_*}^{1/2} \Sigma_{\varphi_*}^{-1/2} = U_1 U_1^T$. Since $X_\mathcal{N} \sim \mathcal{N}(0, \Sigma_{\varphi_*})$ it follows that $\Sigma_{\varphi_*}^{-1/2} \tilde{X}_* \sim \mathcal{N}(0, I_d)$. Similarly, define the matrix square root $\overline{\mathrm{H}}_{\varphi_*}^{g_{mpc}^{1/2}} \in \mathbb{R}^{2r \times r-1}$ of $\overline{\mathrm{H}}_{\varphi_*}^{g_{mpc}}$, where $\overline{\mathrm{H}}_{\varphi_*}^{g_{mpc}} = \overline{\mathrm{H}}_{\varphi_*}^{g_{mpc}^{1/2}} \overline{\mathrm{H}}_{\varphi_*}^{g_{mpc}^{T/2}}$. Note that $\mathrm{rank}\left(\overline{\mathrm{H}}_{\varphi_*}^{g_{mpc}}\right) = r-1$. Now, introduce a positive semi-definite matrix $B = {\Sigma_{\varphi_*}^{1/2}}^T {\overline{\mathrm{H}}_{\varphi_*}^{g_{mpc}^{1/2}}}^T \overline{\mathrm{H}}_{\varphi_*}^{g_{mpc}^{T/2}} \Sigma_{\varphi_*}^{1/2}$, whose eigenvalue decomposition writes

$$V \Lambda V^T = V \Lambda^{1/2} \Lambda^{1/2} V^T, \quad \Lambda = \begin{bmatrix} \Lambda_1 & 0 \\ 0 & 0 \end{bmatrix} \ , \tag{B.39}$$

where $V, \Lambda \in \mathbb{R}^{d \times d}$, $\Lambda_1 = \mathrm{diag}(\lambda_1, \ldots, \lambda_{r^*}) \in \mathbb{R}^{r^* \times r^*}$, $r^* = \mathrm{rank}\,(B) \leq \min\{d, r-1\}$. Note that in case when $d = r-1$ and when no vector of the column space of $\overline{\mathrm{H}}_{\varphi_*}^{g_{mpc}}$ lies in the null space of Σ_{φ_*}, then $\mathrm{rank}\,(B) = r-1$. First, suppose that $d = r-1$. Since both $\overline{\mathrm{H}}_{\varphi_*}^{g_{mpc}^{T/2}} \Sigma_{\varphi_*}^{1/2}$ and $\Lambda^{1/2} V^T$ are matrix square roots of the same matrix B, there exist an orthogonal matrix M and

$$M \overline{\mathrm{H}}_{\varphi_*}^{g_{mpc}} \Sigma_{\varphi_*}^{1/2} = \Lambda^{1/2} V^T \ . \tag{B.40}$$

If $d < r-1$ then for (B.40) to hold some null vectors are added to the eigenvalue decomposition of B such that

$$B = \begin{bmatrix} V & 0_{r-1-d} \end{bmatrix} \begin{bmatrix} \Lambda & 0 \\ 0 & 0 \end{bmatrix} \begin{bmatrix} V_1^T \\ 0_{r-1-d}^T \end{bmatrix} = \tilde{V} \tilde{\Lambda} \tilde{V}^T \ , \tag{B.41}$$

where $\tilde{\Lambda} \in \mathbb{R}^{r-1 \times r-1}$ and $\tilde{V}$ with $\tilde{\Lambda}$ are used instead of V and Λ. The quadratic form $\hat{X}^T \overline{\mathrm{H}}_{\varphi_*}^{g_{mpc}} \hat{X}$ can be expressed as

$$X_\mathcal{N}^T \overline{\mathrm{H}}_{\varphi_*}^{g_{mpc}} X_\mathcal{N} = \tilde{X}_*^T \overline{\mathrm{H}}_{\varphi_*}^{g_{mpc}^{1/2}} M^T M \overline{\mathrm{H}}_{\varphi_*}^{g_{mpc}^{T/2}} X_\mathcal{N} \ . \tag{B.42}$$

To show that (B.42) is, in fact, the product of two weighted Gaussian variables write

$$M\overline{\mathrm{H}}_{\varphi_*}^{g_{mpc}}\tilde{X}_* = M\overline{\mathrm{H}}_{\varphi_*}^{g_{mpc}} \underbrace{\left(\Sigma_{\varphi_*}^{1/2}\Sigma_{\varphi_*}^{-1/2} + U_2U_2^T\right)}_{=I_{2r}} X_{\mathcal{N}} \tag{B.43}$$
$$= M\overline{\mathrm{H}}_{\varphi_*}^{g_{mpc}} \left(\Sigma_{\varphi_*}^{1/2}\Sigma_{\varphi_*}^{-1/2}\right)\tilde{X}_* + M\overline{\mathrm{H}}_{\varphi_*}^{g_{mpc}} \left(U_2U_2^T\right) X_{\mathcal{N}} \ .$$

Since U_2 is a left kernel of Σ_{φ_*} (B.38), the $U_2^T\tilde{X}_* \sim \mathcal{N}(0, U_2^T\Sigma_{\varphi_*}U_2^T) = \mathcal{N}(0,0) = 0$ and the product

$$M\overline{\mathrm{H}}_{\varphi_*}^{g_{mpc}} \left(U_2U_2^T\right) X_{\mathcal{N}} \sim 0.$$

Consequently (B.43) boils down to

$$M\overline{\mathrm{H}}_{\varphi_*}^{g_{mpc}}\tilde{X}_* = \underbrace{M\overline{\mathrm{H}}_{\varphi_*}^{g_{mpc}}\Sigma_{\varphi_*}^{1/2}}_{=\Lambda_1^{1/2}V^T} \underbrace{\Sigma_{\varphi_*}^{-1/2}X_{\mathcal{N}}}_{\sim\mathcal{N}(0,I_d)} \ . \tag{B.44}$$

Matrix V is orthonormal thus, $M\overline{\mathrm{H}}_{\varphi_*}^{g_{mpc}}X_{\mathcal{N}} \sim \Lambda^{1/2}\mathcal{N}(0,I_d)$. Thus, after (B.42), the quadratic form can be expressed as a sum of weighted $\chi_1^2(0)$ distributions

$$\tilde{X}_*^T\overline{\mathrm{H}}_{\varphi_*}^{g_{mpc}}X_{\mathcal{N}} \sim \sum_{i=1}^{r^*}\lambda_i\chi_{l_i}^2(0) \ , \tag{B.45}$$

where $l_i = 1$, which is the basis of the scaled χ^2 approximation in [84].

B.5.2 Part 2: number of degrees of freedom of $\chi^2_{l_{PT}}$ distribution

In [84], the approximation with a scaled $\chi^2_{l_{PT}}$ distribution is given with $l_{PT} = c_2^3/c_3^2$ degrees of freedom under the condition that $s_1^2 \leq s_2$, where

$$s_1 = \frac{c_3}{c_2^{3/2}}, \quad s_2 = \frac{c_4}{c_2^2} \ . \tag{B.46}$$

The following developments show that, for the case of MPC indicator, this condition is always satisfied. Recall that the k-th asymptotic cumulant of $Q(\hat{X}_{\mathcal{N}})$ writes as

$$c_k = \mathrm{tr}\left((\overline{\mathrm{H}}_{\varphi_*}^{g_{mpc}}\Sigma_{\varphi_*})^k\right) = \sum_{i=1}^{r^*}\lambda_i^k \ , \tag{B.47}$$

where r^* is the number of non-zero eigenvalues λ_i of $\Sigma_{\varphi_*}^{T/2}\overline{\mathrm{H}}_{\varphi_*}^{g_{mpc}}\Sigma_{\varphi_*}^{1/2}$ (see (B.39)). For the considered collection of $\lambda_i \in \mathbb{R}$ it holds the Cauchy-Schwarz inequality

$$c_3^2 = \left(\sum_{i=1}^{r^*}\lambda_i\lambda_i^2\right)^2 \leq \sum_{i=1}^{r^*}\lambda_i^2\sum_{i=1}^{r^*}\lambda_i^4 = c_2c_4 \ ,$$

thus $c_3^2/c_2^3 \leq c_4/c_2^2$ which is equivalent to $s_1^2 \leq s_2$.

B.5.3 Part 3: derivation of scaled $\chi^2_{l_{PT}}$ distribution function

In the last part of this proof, the distribution function of the quadratic form $Q(\tilde{X})$ is derived. First, recall that for some given random variable X there exist a function $\Phi_X : \mathbb{R} \to \mathbb{C}$ which is called a characteristic function of X. Assume, the probability distribution function of X writes as f_X, then $\Phi_X(t)$ can be formulated as

$$\Phi_X(t) = \mathrm{E}\left(\exp(\mathrm{i}tX)\right) = \int_{\mathbb{R}} \exp(\mathrm{i}tx) f_X(x) dx \ . \tag{B.48}$$

The proof will follow from the derivation of the asymptotic probability density function of the quadratic form $Q(\tilde{X})$. From [84], recall that the approximation of the tail probability writes as

$$\Pr\left(Q(\tilde{X}) > t\right) \approx \Pr\left(\chi^2_{l_{PT}} > \sigma_{\chi^2} t^* + \mu_{\chi^2}\right) \ , \tag{B.49}$$

where $t^* = (t - \mu_Q)/\sigma_Q$. Also denote $\alpha = \sigma_Q/\sigma_{\chi^2}$, $\beta = \mu_Q - (\mu_{\chi^2}\sigma_Q)/\sigma_{\chi^2}$. For simplicity, denote the variable $\chi^2_{l_{PT}}$ as $\mathcal{X}$. Then define, the linear combination $\mathcal{Y} = \alpha\mathcal{X} + \beta$. Then the law of $\mathcal{Y}$ can be derived from the law of $\mathcal{X}$. After plugging the expression for $\mathcal{Y}$, the characteristic function $\Phi_{\mathcal{Y}}(t) = \mathrm{E}\left(\exp(it\mathcal{Y})\right)$ writes as

$$\begin{aligned}\Phi_{\mathcal{Y}}(t) &= \exp(\mathrm{i}t\beta)\mathrm{E}\left(\exp(\mathrm{i}t\alpha\mathcal{X})\right) = \int_{x_0}^{\infty} \exp(\mathrm{i}t\beta)\exp\left(\mathrm{i}t\alpha x\right) f_{\mathcal{X}}(x) dx \\ &= \int_{y_0}^{\infty} \exp(\mathrm{i}ty) \underbrace{\frac{1}{\alpha} f_{\mathcal{X}}\left(\frac{y-\beta}{\alpha}\right)}_{=f_{\mathcal{Y}}(y)} dy \ ,\end{aligned} \tag{B.50}$$

where $x_0 = 0$ and $y_0 = \beta$. From Equation (B.49), the density of $f_{\mathcal{Y}}(y)$ on $[y_0, \infty]$ is an approximate of the density of $Q(\tilde{X})$. It can be interpreted as a scaled and translated $\chi^2_{l_{PT}}$ probability density function. That concludes the proof.

B.6 Proof of Lemma 4.7

It is proved that l_{PT} is bounded as $1 \leq l_{PT} \leq r^*$, where

$$r^* \leq \min(\mathrm{rank}(\Sigma_{\varphi_*}), \mathrm{rank}(\overline{\mathrm{H}}^{g_{mpc}}_{\varphi_*})) \leq r - 1 \ .$$

Recall that $l_{PT} = c_2^3/c_3^2$. The upper bound r^* holds from the Jensen inequality which for the real convex function $f(x) = x^{3/2}$ and $x_i = \lambda_i^2$ writes

$$\begin{aligned}&\left(\frac{\sum_{i=1}^{r^*}\lambda_i^2}{r^*}\right)^{3/2} \leq \frac{\sum_{i=1}^{r^*}\left(\lambda_i^2\right)^{3/2}}{r^*} \ , \\ &\Rightarrow \frac{\left(\sum_{i=1}^{r^*}\lambda_i^2\right)^{3/2}}{r^{*3/2}} \leq \frac{\sum_{i=1}^{r^*}\lambda_i^3}{r^*} \ , \\ &\Rightarrow \frac{\left(\sum_{i=1}^{r^*}\lambda_i^2\right)^{3}}{r^{*3}} \leq \frac{\left(\sum_{i=1}^{r^*}\lambda_i^3\right)^{2}}{r^{*2}} \ , \\ &\Rightarrow \frac{\left(\sum_{i=1}^{r^*}\lambda_i^2\right)^{3}}{\left(\sum_{i=1}^{r^*}\lambda_i^3\right)^{2}} \leq r^* \Rightarrow l_{PT} \leq r^* \ .\end{aligned}$$

The lower bound is proved with the Cauchy-Schwarz inequality and the relation $\sum_{i=1}^{r^*} \lambda_i^4 \leq \left(\sum_{i=1}^{r^*} \lambda_i^2\right)^2$. It holds

$$c_3^2 = \left(\sum_{i=1}^{r^*} \lambda_i \lambda_i^2\right)^2 \leq \sum_{i=1}^{r^*} \lambda_i^2 \sum_{i=1}^{r^*} \lambda_i^4 \leq \sum_{i=1}^{r^*} \lambda_i^2 \left(\sum_{i=1}^{r^*} \lambda_i^2\right)^2 = c_2^3 \ ,$$
$$\Rightarrow \quad l_{PT} \geq 1 \ .$$

This concludes the proof.

APPENDIX C

Uncertainty quantification of Modal Assurance Criterion

C.1 Jacobian derivation

To compute the $\mathcal{J}^{g_{mac}}_{\varphi_*,\psi_*}$ the partial derivatives with respect to real and imaginary parts of respective mode shapes are derived by using the total derivative of (2.9). Recall that for any function $f(\theta)$, $df(\theta) = f'(\theta)d\theta$. Then

$$dg_{mac}(\varphi,\psi) = \frac{d(\varphi^H\psi\psi^H\varphi)}{\varphi^H\varphi\psi^H\psi} - \frac{\varphi^H\psi\psi^H\varphi}{(\varphi^H\varphi\psi^H\psi)^2}d(\varphi^H\varphi\psi^H\psi)\ . \tag{C.1}$$

Since both the φ and ψ are column vectors the product $\varphi^H\psi$ is a complex scalar. Expressing the first term from (C.1) it holds

$$d(\varphi^H\psi\psi^H\varphi) = d(\varphi^H)\psi\psi^H\varphi + \varphi^H d(\psi)\psi^H\varphi + \varphi^H\psi d(\psi^H)\varphi + \varphi^H\psi\psi^H d(\varphi)\ . \tag{C.2}$$

The terms $d(\varphi^H)\psi\psi^H\varphi$ and $\varphi^H\psi\psi^H d(\varphi)$ are conjugates of each other, and so are $\varphi^H d(\psi)\psi^H\varphi$ and $\varphi^H\psi d(\psi^H)\varphi$. Thus, it follows

$$d(\varphi^H\psi\psi^H\varphi) = 2\Re(\varphi^H d(\psi)\psi^H\varphi) + 2\Re(\varphi^H\psi\psi^H d(\varphi)) \tag{C.3}$$

$$= 2\Re(\psi^H\varphi\varphi^H d\psi) + 2\Re(\varphi^H\psi\psi^H d\varphi)\ . \tag{C.4}$$

Finally, for every complex vectors y and x the real part of the inner product writes $\Re(y^Hx) = \Re((\Re(y) + \mathrm{i}\Im(y))^H(\Re(x) + \mathrm{i}\Im(x))) = \Re(y)^T\Re(x) + \Im(y)^T\Im(x)$, hence it holds

$$\Re(\psi^H\varphi\varphi^H d\psi) = \begin{bmatrix}\Re(\varphi\varphi^H\psi)^T & \Im(\varphi\varphi^H\psi)^T\end{bmatrix}\begin{bmatrix}d\Re(\psi)\\ d\Im(\psi)\end{bmatrix} \tag{C.5}$$

and

$$\Re(\varphi^H \psi\psi^H d\varphi) = \begin{bmatrix} \Re(\psi\psi^H\varphi)^T & \Im(\psi\psi^H\varphi)^T \end{bmatrix} \begin{bmatrix} d\Re(\varphi) \\ d\Im(\varphi) \end{bmatrix} . \tag{C.6}$$

The second term of (C.1) is derived with a scheme analogous to the one depicted in (C.2)-(C.6). It follows

$$\Re(\varphi^H \psi\psi^H d\varphi) = \begin{bmatrix} \Re(\psi\psi^H\varphi)^T & \Im(\psi\psi^H\varphi)^T \end{bmatrix} \begin{bmatrix} d\Re(\varphi) \\ d\Im(\varphi) \end{bmatrix} . \tag{C.7}$$

Looking on the second term of (C.7),

$$d(\varphi^H \varphi\psi^H \psi) = d(\varphi^H)\varphi\psi^H\psi + \varphi^H d(\varphi)\psi^H\psi + \varphi^H\varphi d(\psi^H)\psi + \varphi^H\varphi\psi^H d(\psi) .$$

After sorting the complex conjugates,

$$\begin{aligned} d(\varphi^H \varphi\psi^H \psi) &= 2\Re(\varphi^H d(\varphi)\psi^H\psi) + 2\Re(\varphi^H\varphi\psi^H d(\psi)) \\ &= 2\Re(\psi^H\psi\varphi^H d\varphi) + 2\Re(\varphi^H\varphi\psi^H d(\psi)) . \end{aligned}$$

Finally, computing the real part of the inner products

$$\Re(\psi^H \psi\varphi^H d\varphi) = \begin{bmatrix} \Re(\varphi\psi^H\psi)^T & \Im(\varphi\psi^H\psi)^T \end{bmatrix} \begin{bmatrix} d\Re(\varphi) \\ d\Im(\varphi) \end{bmatrix} \tag{C.8}$$

and

$$\Re(\varphi^H \varphi\psi^H d(\psi)) = \begin{bmatrix} \Re(\psi\varphi^H\varphi)^T & \Im(\psi\varphi^H\varphi)^T \end{bmatrix} \begin{bmatrix} d\Re(\psi) \\ d\Im(\psi) \end{bmatrix} . \tag{C.9}$$

C.2 Proof of Lemma 5.2

First it is proved that when $g_{mac}(\varphi_*, \psi_*) = \{0, 1\}$ the partial derivatives (5.4)-(5.7) are equal to zero. Since MAC measures degree of linearity between two vectors, the case $g_{mac}(\varphi_*, \psi_*) = 1$ indicates that the vectors ψ_* and φ_* are collinear. The opposite $g_{mac}(\varphi_*, \psi_*) = 0$ indicates that two vectors are orthogonal. First case can be encompassed by $\varphi_* = k \cdot \psi_*$ where k is some constant scalar. Plugging it to the

derivatives (5.4)-(5.7) yields

$$\frac{\partial g_{mac}}{\partial \Re(\varphi)}(\varphi_*, \psi_*) = \frac{2\Re(\psi_*\psi_*^H\varphi_*)^T}{\varphi_*^H\varphi_*\psi_*^H\psi_*} - \frac{2\Re(\varphi_*)^T g_{mac}(\varphi,\psi)}{\varphi_*^H\varphi_*} \tag{C.10}$$
$$= \frac{2k\Re(\psi_*\psi_*^H\psi_*)^T}{k^2\psi_*^H\psi_*\psi_*^H\psi_*} - \frac{2k\Re(\psi_*)^T}{k^2\psi_*^H\psi_*} = 0 \ ,$$
$$\frac{\partial g_{mac}}{\partial \Im(\varphi)}(\varphi_*, \psi_*) = \frac{2\Im(\psi_*\psi_*^H\varphi_*)^T}{\varphi_*^H\varphi_*\psi_*^H\psi_*} - \frac{2\Im(\varphi)^T g_{mac}(\varphi_*,\psi_*)}{\varphi^H\varphi} \tag{C.11}$$
$$= \frac{2k\Im(\psi_*\psi_*^H\psi_*)^T}{k^2\psi_*^H\psi_*\psi_*^H\psi_*} - \frac{2k\Im(\psi_*)^T}{k^2\psi_*^H\psi_*} = 0 \ ,$$
$$\frac{\partial g_{mac}}{\partial \Re(\psi)}(\varphi_*, \psi_*) = \frac{2\Re(\varphi_*\varphi_*^H\psi_*)^T}{\varphi_*^H\varphi_*\psi_*^H\psi_*} - \frac{2\Re(\psi_*)^T g_{mac}(\varphi_*,\psi_*)}{\psi_*^H\psi_*} \tag{C.12}$$
$$= \frac{2k^2\Re(\psi_*\psi_*^H\psi_*)^T}{k^2\psi_*^H\psi_*\psi_*^H\psi_*} - \frac{2\Re(\psi_*)^T}{\psi_*^H\psi_*} = 0 \ ,$$
$$\frac{\partial g_{mac}}{\partial \Im(\psi)}(\varphi_*, \psi_*) = \frac{2\Im(\varphi_*\varphi_*^H\psi_*)^T}{\varphi_*^H\varphi_*\psi_*^H\psi_*} - \frac{2\Im(\psi_*)^T g_{mac}(\varphi_*,\psi_*)}{\psi_*^H\psi_*} \tag{C.13}$$
$$= \frac{2k^2\Im(\psi_*\psi_*^H\psi_*)^T}{k^2\psi_*^H\psi_*\psi_*^H\psi_*} - \frac{2\Im(\psi_*)^T}{\psi_*^H\psi_*} = 0 \ .$$

Considering the case when two mode shape vectors are orthogonal yields

$$\frac{\partial g_{mac}}{\partial \Re(\varphi)}(\varphi_*, \psi_*) = \frac{2\Re(\psi_*\psi_*^H\varphi_*)^T}{\varphi_*^H\varphi_*\psi_*^H\psi_*} - \frac{2\Re(\varphi_*)^T g_{mac}(\varphi_*,\psi_*)}{\varphi_*^H\varphi_*} = 0 \ , \tag{C.14}$$
$$\frac{\partial g_{mac}}{\partial \Im(\varphi)}(\varphi_*, \psi_*) = \frac{2\Im(\psi_*\psi_*^H\varphi_*)^T}{\varphi_*^H\varphi_*\psi_*^H\psi_*} - \frac{2\Im(\varphi_*)^T g_{mac}(\varphi_*,\psi_*)}{\varphi_*^H\varphi_*} = 0 \ , \tag{C.15}$$
$$\frac{\partial g_{mac}}{\partial \Re(\psi)}(\varphi_*, \psi_*) = \frac{2\Re(\varphi_*\varphi_*^H\psi_*)^T}{\varphi_*^H\varphi_*\psi_*^H\psi_*} - \frac{2\Re(\psi_*)^T g_{mac}(\varphi_*,\psi_*)}{\psi_*^H\psi_*} = 0 \ , \tag{C.16}$$
$$\frac{\partial g_{mac}}{\partial \Im(\psi)}(\varphi_*, \psi_*) = \frac{2\Im(\varphi_*\varphi_*^H\psi_*)^T}{\varphi_*^H\varphi_*\psi_*^H\psi_*} - \frac{2\Im(\psi_*)^T g_{mac}(\varphi_*,\psi_*)}{\psi_*^H\psi_*} = 0 \ , \tag{C.17}$$

which concludes the first part of the proof. Second, the following condition is shown

$$\left[\frac{\partial g_{mac}}{\partial \Re(\varphi)} \quad \frac{\partial g_{mac}}{\partial \Im(\varphi)} \quad \frac{\partial g_{mac}}{\partial \Re(\psi)} \quad \frac{\partial g_{mac}}{\partial \Im(\psi)}\right] = 0$$
$$\Rightarrow g_{mac}(\varphi_*, \psi_*) = \{0, 1\} \ .$$

Equating the partial derivatives (5.4)-(5.7) to zero yields

$$\frac{\partial g_{mac}}{\partial \Re(\varphi)}(\varphi_*, \psi_*) + \frac{\partial g_{mac}}{\partial \Im(\varphi)}(\varphi_*, \psi_*) = 0 \ , \tag{C.18}$$
$$\frac{\partial g_{mac}}{\partial \Re(\psi)}(\varphi_*, \psi_*) + \frac{\partial g_{mac}}{\partial \Im(\psi)}(\varphi_*, \psi_*) = 0 \ . \tag{C.19}$$

Developing (C.18) writes

$$\begin{aligned}\frac{\partial g_{mac}}{\partial \Re(\varphi)}(\varphi_*,\psi_*)+\frac{\partial g_{mac}}{\partial \Im(\varphi)}(\varphi_*,\psi_*) &= \frac{2\Re(\psi_*\psi_*^H\varphi_*)^T+2\Im(\psi_*\psi_*^H\varphi_*)^T}{\varphi_*^H\varphi_*\psi_*^H\psi_*} \\ &- \frac{g_{mac}(\varphi_*,\psi_*)}{\varphi_*^H\varphi_*}\left(2\Re(\varphi_*)^T+2\Im(\varphi_*)^T\right) \\ &= \frac{2(\psi_*\psi_*^H\varphi_*)^T}{\varphi_*^H\varphi_*\psi_*^H\psi_*}-\frac{2\varphi_*^T g_{mac}(\varphi_*,\psi_*)}{\varphi_*^H\varphi_*} \\ &= \psi_*\psi_*^H\varphi_*-g_{mac}(\varphi_*,\psi_*)\varphi_*\psi_*^H\psi_*=0\ .\end{aligned} \tag{C.20}$$

Here distinguish two solutions namely, first when $\psi_*^H\varphi_*\neq 0$ and the opposite when $\psi_*^H\varphi_*=0$. Concerning the first solution, multiplying (C.20) with ψ_*^H from the left yields

$$\psi_*^H\psi_*\psi_*^H\varphi_*=g_{mac}(\varphi_*,\psi_*)\psi_*^H\varphi_*\psi_*^H\psi_*\Rightarrow g_{mac}(\varphi_*,\psi_*)=\frac{\psi_*^H\psi_*\psi_*^H\varphi_*}{\psi_*^H\varphi_*\psi_*^H\psi_*}=1\ .$$

As for the second solution, when $\psi_*^H\varphi_*=0$ (C.20) writes as

$$\begin{aligned}&\psi_*\psi_*^H\varphi_*-g_{mac}(\varphi_*,\psi_*)\varphi_*\psi_*^H\psi_*=0\ ,\\ &g_{mac}(\varphi_*,\psi_*)\varphi_*=0\Rightarrow g_{mac}(\varphi_*,\psi_*)=0\ .\end{aligned}$$

Similarly, developing (C.19) writes

$$\begin{aligned}\frac{\partial g_{mac}}{\partial \Re(\psi)}(\varphi_*,\psi_*)+\frac{\partial g_{mac}}{\partial \Im(\psi)}(\varphi_*,\psi_*) &= \frac{2\Re(\varphi_*\varphi_*^H\psi_*)^T+2\Im(\varphi_*\varphi_*^H\psi_*)^T}{\varphi_*^H\varphi_*\psi_*^H\psi_*} \\ &- \frac{g_{mac}(\varphi_*,\psi_*)}{\psi_*^H\psi_*}\left(2\Re(\psi_*)^T+2\Im(\psi_*)^T\right) \\ &= \frac{2(\varphi_*\varphi_*^H\psi_*)^T}{\varphi_*^H\varphi_*\psi_*^H\psi_*}-\frac{2g_{mac}(\varphi_*,\psi_*)\psi_*^T}{\psi_*^H\psi_*} \\ &= \varphi_*\varphi_*^H\psi_*-g_{mac}(\varphi_*,\psi_*)\psi_*\varphi_*^H\varphi_*=0\ .\end{aligned} \tag{C.21}$$

Assuming that $\varphi_*^H\psi_*\neq 0$ and multiplying (C.21) with φ_*^H from the left yields

$$\varphi_*^H\varphi_*\varphi_*^H\psi_*=g_{mac}(\varphi_*,\psi_*)\varphi_*^H\psi_*\varphi_*^H\varphi_*\Rightarrow g_{mac}(\varphi_*,\psi_*)=\frac{\varphi_*^H\varphi_*\varphi_*^H\psi_*}{\varphi_*^H\psi_*\varphi_*^H\varphi_*}=1\ .$$

Now, considering that $\varphi_*^H\psi_*=0$ (C.21) writes as

$$\begin{aligned}&\varphi_*\varphi_*^H\psi_*-g_{mac}(\varphi_*,\psi_*)\psi_*\varphi_*^H\varphi_*=0\Rightarrow g_{mac}(\varphi_*,\psi_*)\psi_*=0\\ &\Rightarrow g_{mac}(\varphi_*,\psi_*)=0\ .\end{aligned}$$

That leads to the assertion in Lemma 5.2.

C.3 Hessian derivation for $g_{mac}(\hat{\varphi},\psi_*)$

In the following the respective parts of the Hessian are developed and evaluated considering two cases namely, first when both mode shapes, φ and ψ, belong to the same theoretical mode

$$\varphi_*=k\cdot\psi_* \tag{C.22}$$

and second when two mode shapes φ and ψ are orthogonal

$$\varphi_*^H \psi_* = 0 \ . \tag{C.23}$$

In order to obtain the first row of (5.23) the total derivative of (5.4) is computed, which yields

$$\begin{aligned} d\left[\frac{\partial g_{mac}(\varphi,\psi)}{\partial \Re(\varphi)}\right] &= d\left(\frac{2\Re(\psi\psi^H\varphi)}{\varphi^H\varphi\psi^H\psi} - \frac{2g_{mac}(\varphi,\psi)\Re(\varphi)}{\varphi^H\varphi}\right) \\ &= \frac{2d(\Re(\psi\psi^H\varphi))}{\varphi^H\varphi\psi^H\psi} - \frac{2\Re(\psi\psi^H\varphi)d(\varphi^H\varphi\psi^H\psi)}{(\varphi^H\varphi\psi^H\psi)^2} \\ &\quad - \frac{2d\left(g_{mac}(\varphi,\psi)\Re(\varphi)\right)}{\varphi^H\varphi} + \frac{2g_{mac}(\varphi,\psi)\Re(\varphi)d(\varphi^H\varphi)}{(\varphi^H\varphi)^2} \ . \end{aligned} \tag{C.24}$$

The development of the first term in (C.24) holds

$$\begin{aligned} d(\Re(\psi\psi^H\varphi)) &= d\Re\left(\left(\Re(\psi)+\mathrm{i}\Im(\psi)\right)\left(\Re(\psi)+\mathrm{i}\Im(\psi)\right)^H\left(\Re(\varphi)+\mathrm{i}\Im(\varphi)\right)\right) \\ &= d\Re(\psi)\Re(\psi)^T\Re(\varphi) + \Re(\psi)d\Re(\psi)^T\Re(\varphi) + \Re(\psi)\Re(\psi)^T d\Re(\varphi) \\ &+ d\Re(\psi)\Im(\psi)^T\Im(\varphi) + \Re(\psi)d\Im(\psi)^T\Im(\varphi) + \Re(\psi)\Im(\psi)^T d\Im(\varphi) \\ &+ d\Im(\psi)\Im(\psi)^T\Re(\varphi) + \Im(\psi)d\Im(\psi)^T\Re(\varphi) + \Im(\psi)\Im(\psi)^T d\Re(\varphi) \\ &- d\Im(\psi)\Re(\psi)^T\Im(\varphi) - \Im(\psi)d\Re(\psi)^T\Im(\varphi) - \Im(\psi)\Re(\psi)^T d\Im(\varphi) \\ &= \Re(\varphi)^T\Re(\psi)I_r d\Re(\psi) + \Re(\psi)\Re(\varphi)^T d\Re(\psi) + \Re(\psi)\Re(\psi)^T d\Re(\varphi) \\ &+ \Im(\varphi)^T\Im(\psi)I_r d\Re(\psi) + \Re(\psi)\Im(\varphi)^T d\Im(\psi) + \Re(\psi)\Im(\psi)^T d\Im(\varphi) \\ &+ \Re(\varphi)^T\Im(\psi)I_r d\Im(\psi) + \Im(\psi)\Re(\varphi)^T d\Im(\psi) + \Im(\psi)\Im(\psi)^T d\Re(\varphi) \\ &- \Im(\varphi)^T\Re(\psi)I_r d\Im(\psi) - \Im(\psi)\Im(\varphi)^T d\Re(\psi) - \Im(\psi)\Re(\psi)^T d\Im(\varphi) \ . \end{aligned} \tag{C.25}$$

The development of the last term in (C.24) yields

$$\begin{aligned} d(\varphi^H\varphi) = d\left(\Re(\varphi)^T\Re(\varphi) + \Im(\varphi)^T\Im(\varphi)\right) &= 2\Re(\varphi)^T d\Re(\varphi) \\ &\quad + 2\Im(\varphi)^T d\Im(\varphi) \ . \end{aligned} \tag{C.26}$$

After (C.25), (C.26) and (C.8), the first term in the first row of (5.23) writes as

$$\begin{aligned} \frac{\partial^2 g_{mac}}{\partial\Re(\varphi)\partial\Re(\varphi)} &= \frac{2\Re(\psi)\Re(\psi)^T + 2\Im(\psi)\Im(\psi)^T}{\varphi^H\varphi\psi^H\psi} \\ &+ \frac{4g_{mac}(\varphi,\psi)\Re(\varphi)\Re(\varphi)^T - 2g_{mac}(\varphi,\psi)I_r\varphi^H\varphi}{(\varphi^H\varphi)^2} \\ &- \frac{4\Re(\psi\psi^H\varphi)\Re(\varphi\psi^H\psi)^T}{(\varphi^H\varphi\psi^H\psi)^2} \ . \end{aligned} \tag{C.27}$$

Inserting (C.22) to (C.27) (mode shapes are collinear) and using the simplified notation from (5.24) yields

$$\begin{aligned}\frac{\partial^2 g_{mac}}{\partial\Re(\varphi)\partial\Re(\varphi)} &= \frac{2\Re(\psi_*)\Re(\psi_*)^T + 2\Im(\psi_*)\Im(\psi_*)^T}{k^2(\psi_*^H\psi_*)^2} \\ &+ \frac{4\Re(\psi_*)\Re(\psi_*)^T - 2I_r\psi_*^H\psi_*}{k^2(\psi_*^H\psi_*)^2} - \frac{4\Re(\psi_*)\Re(\psi_*)^T}{k^2(\psi_*^H\psi_*)^2} \\ &= \frac{2\Re(\psi_*)\Re(\psi_*)^T + 2\Im(\psi_*)\Im(\psi_*)^T - 2I_r\psi_*^H\psi_*}{k^2(\psi_*^H\psi_*)^2} \ .\end{aligned} \tag{C.28}$$

Inserting (C.23) to (C.27) (mode shapes are orthogonal) and using the simplified notation from (5.24) yields

$$\frac{\partial^2 g_{mac}}{\partial\Re(\varphi)\partial\Re(\varphi)} = \frac{2\Re(\psi_*)\Re(\psi_*)^T + 2\Im(\psi_*)\Im(\psi_*)^T}{\varphi_*^H\varphi_*\psi_*^H\psi_*} \ . \tag{C.29}$$

After (C.25), (C.26) and (C.8), the second term in the first row of (5.23) writes as

$$\begin{aligned}\frac{\partial^2 g_{mac}}{\partial\Im(\varphi)\partial\Re(\varphi)} &= \frac{2\Re(\psi)\Im(\psi)^T - 2\Im(\psi)\Re(\psi)^T}{\varphi^H\varphi\psi^H\psi} \\ &+ \frac{4g_{mac}(\varphi,\psi)\Re(\varphi)\Im(\varphi)^T}{(\varphi^H\varphi)^2} - \frac{4\Re(\psi\psi^H\varphi)\Im(\varphi\psi^H\psi)^T}{(\varphi^H\varphi\psi^H\psi)^2} \ .\end{aligned} \tag{C.30}$$

Inserting (C.22) to (C.30) (mode shapes are collinear) and using the simplified notation from (5.24) yields

$$\begin{aligned}\frac{\partial^2 g_{mac}}{\partial\Im(\varphi)\partial\Re(\varphi)} &= \frac{2\Re(\psi_*)\Im(\psi_*)^T - 2\Im(\psi_*)\Re(\psi_*)^T}{k^2(\psi_*^H\psi_*)^2} \\ &+ \frac{4\Re(\psi_*)\Im(\psi_*)^T}{k^2(\psi_*^H\psi_*)^2} - \frac{4\Re(\psi_*)\Im(\psi_*)^T}{k^2(\psi_*^H\psi_*)^2} \\ &= \frac{2\Re(\psi_*)\Im(\psi_*)^T - 2\Im(\psi_*)\Re(\psi_*)^T}{k^2(\psi_*^H\psi_*)^2} \ .\end{aligned} \tag{C.31}$$

Inserting (C.23) to (C.30) (mode shapes are orthogonal) and using the simplified notation from (5.24) yields

$$\frac{\partial^2 g_{mac}}{\partial\Im(\varphi)\partial\Re(\varphi)} = \frac{2\Re(\psi_*)\Im(\psi_*)^T - 2\Im(\psi_*)\Re(\psi_*)^T}{\varphi_*^H\varphi_*\psi_*^H\psi_*} \ . \tag{C.32}$$

To obtain the second row of (5.23) the total derivative of (5.5) is computed, which yields

$$\begin{aligned}d\left[\frac{\partial g_{mac}(\varphi,\psi)}{\partial\Im(\varphi)}\right] &= d\left(\frac{2\Im(\psi\psi^H\varphi)}{\varphi^H\varphi\psi^H\psi} - \frac{2g_{mac}(\varphi,\psi)\Im(\varphi)}{\varphi^H\varphi}\right) \\ &= \frac{2d(\Im(\psi\psi^H\varphi))}{\varphi^H\varphi\psi^H\psi} - \frac{2\Im(\psi\psi^H\varphi)d(\varphi^H\varphi\psi^H\psi)}{(\varphi^H\varphi\psi^H\psi)^2} \\ &- \frac{2d(g_{mac}(\varphi,\psi)\Im(\varphi))}{\varphi^H\varphi} + \frac{2g_{mac}(\varphi,\psi)\Im(\varphi)d(\varphi^H\varphi)}{(\varphi^H\varphi)^2} \ .\end{aligned} \tag{C.33}$$

The development of the first term in (C.33) holds

$$\begin{aligned} d(\Im(\psi\psi^H\varphi)) &= d\Im\left(\left(\Re(\psi)+\mathrm{i}\Im(\psi)\right)\left(\Re(\psi)+\mathrm{i}\Im(\psi)\right)^H\left(\Re(\varphi)+\mathrm{i}\Im(\varphi)\right)\right) \qquad \text{(C.34)}\\ &= d\Im(\psi)\Re(\psi)^T\Re(\varphi) + \Im(\psi)d\Re(\psi)^T\Re(\varphi) + \Im(\psi)\Re(\psi)^T d\Re(\varphi)\\ &+ d\Im(\psi)\Im(\psi)^T\Im(\varphi) + \Im(\psi)d\Im(\psi)^T\Im(\varphi) + \Im(\psi)\Im(\psi)^T d\Im(\varphi)\\ &+ d\Re(\psi)\Re(\psi)^T\Im(\varphi) + \Re(\psi)d\Re(\psi)^T\Im(\varphi) + \Re(\psi)\Re(\psi)^T d\Im(\varphi)\\ &- d\Re(\psi)\Im(\psi)^T\Re(\varphi) - \Re(\psi)d\Im(\psi)^T\Re(\varphi) - \Re(\psi)\Im(\psi)^T d\Re(\varphi)\\ &= \Re(\varphi)^T\Re(\psi)I_r d\Im(\psi) + \Im(\psi)\Re(\varphi)^T d\Re(\psi) + \Im(\psi)\Re(\psi)^T d\Re(\varphi)\\ &+ \Im(\varphi)^T\Im(\psi)I_r d\Im(\psi) + \Im(\psi)\Im(\varphi)^T d\Im(\psi) + \Im(\psi)\Im(\psi)^T d\Im(\varphi)\\ &+ \Im(\varphi)^T\Re(\psi)I_r d\Re(\psi) + \Re(\psi)\Im(\varphi)^T d\Re(\psi) + \Re(\psi)\Re(\psi)^T d\Im(\varphi)\\ &- \Re(\varphi)^T\Im(\psi)I_r d\Re(\psi) - \Re(\psi)\Re(\varphi)^T d\Im(\psi) - \Re(\psi)\Im(\psi)^T d\Re(\psi)\ . \end{aligned}$$

After (C.34), (C.26) and (C.8), the first term in the second row of (5.23) writes as

$$\begin{aligned} \frac{\partial^2 g_{mac}}{\partial\Re(\varphi)\partial\Im(\varphi)} &= \frac{2\Im(\psi)\Re(\psi)^T - 2\Re(\psi)\Im(\psi)^T}{\varphi^H\varphi\psi^H\psi} \qquad \text{(C.35)}\\ &+ \frac{4g_{mac}(\varphi,\psi)\Im(\varphi)\Re(\varphi)^T}{(\varphi^H\varphi)^2} - \frac{4\Im(\psi\psi^H\varphi)\Re(\varphi\psi^H\psi)^T}{(\varphi^H\varphi\psi^H\psi)^2}\ . \end{aligned}$$

Inserting (C.22) to (C.35) (mode shapes are collinear) and using the simplified notation from (5.24) yields

$$\begin{aligned} \frac{\partial^2 g_{mac}}{\partial\Re(\varphi)\partial\Im(\varphi)} &= \frac{2\Im(\psi_*)\Re(\psi_*)^T - 2\Re(\psi_*)\Im(\psi_*)^T}{k^2(\psi_*^H\psi_*)^2} \qquad \text{(C.36)}\\ &+ \frac{4\Im(\psi_*)\Re(\psi_*)^T}{k^2(\psi_*^H\psi_*)^2} - \frac{4\Im(\psi_*)\Re(\psi_*)^T}{k^2(\psi_*^H\psi_*)^2}\\ &= \frac{2\Im(\psi_*)\Re(\psi_*)^T - 2\Re(\psi_*)\Im(\psi_*)^T}{k^2(\psi_*^H\psi_*)^2}\ . \end{aligned}$$

Inserting (C.23) to (C.35) (mode shapes are orthogonal) and using the simplified notation from (5.24) yields

$$\frac{\partial^2 g_{mac}}{\partial\Re(\varphi)\partial\Im(\varphi)} = \frac{2\Im(\psi_*)\Re(\psi_*)^T - 2\Re(\psi_*)\Im(\psi_*)^T}{\varphi_*^H\varphi_*\psi_*^H\psi_*}\ . \qquad \text{(C.37)}$$

After (C.34), (C.26) and (C.8), the second term in the second row of (5.23) writes as

$$\begin{aligned} \frac{\partial^2 g_{mac}}{\partial\Im(\varphi)\partial\Im(\varphi)} &= \frac{2\Re(\psi)\Re(\psi)^T + 2\Im(\psi)\Im(\psi)^T}{\varphi^H\varphi\psi^H\psi} \qquad \text{(C.38)}\\ &+ \frac{4g_{mac}(\varphi,\psi)\Im(\varphi)\Im(\varphi)^T - 2g_{mac}(\varphi,\psi)I_r\varphi^H\varphi}{(\varphi^H\varphi)^2}\\ &- \frac{4\Im(\psi\psi^H\varphi)\Im(\varphi\psi^H\psi)^T}{(\varphi^H\varphi\psi^H\psi)^2}\ . \end{aligned}$$

Inserting (C.22) to (C.38) (mode shapes are collinear) and using the simplified notation from (5.24) yields

$$\begin{aligned}\frac{\partial^2 g_{mac}}{\partial\Im(\varphi)\partial\Im(\varphi)} &= \frac{2\Re(\psi_*)\Re(\psi_*)^T + 2\Im(\psi_*)\Im(\psi_*)^T}{k^2(\psi_*^H\psi_*)^2} \\ &+ \frac{4\Im(\psi_*)\Im(\psi_*)^T - 2I_r\psi_*^H\psi_*}{k^2(\psi_*^H\psi_*)^2} - \frac{4\Im(\psi_*)\Im(\psi_*)^T}{k^2(\psi_*^H\psi_*)^2} \\ &= \frac{2\Re(\psi_*)\Re(\psi_*)^T + 2\Im(\psi_*)\Im(\psi_*)^T - 2I_r\psi_*^H\psi_*}{k^2(\psi_*^H\psi_*)^2} \ .\end{aligned} \tag{C.39}$$

Inserting (C.23) to (C.38) (mode shapes are orthogonal) and using the simplified notation from (5.24) yields

$$\frac{\partial^2 g_{mac}}{\partial\Im(\varphi)\partial\Im(\varphi)} = \frac{2\Re(\psi_*)\Re(\psi_*)^T + 2\Im(\psi_*)\Im(\psi_*)^T}{\varphi_*^H\varphi_*\psi_*^H\psi_*} \ . \tag{C.40}$$

C.4 Proof of Lemma 5.7

First recall the expression for $\mathrm{H}_{\varphi_*}^{g_{mac},\mathrm{collinear}}$ from (5.25)

$$\mathrm{H}_{\varphi_*}^{g_{mac},\mathrm{collinear}} = \frac{2}{k^2 d_*^2} \underbrace{\begin{bmatrix} M_{xx}^* + M_{yy}^* & M_{xy}^* - M_{yx}^* \\ M_{yx}^* - M_{xy}^* & M_{xx}^* + M_{yy}^* \end{bmatrix} - d_* I_{2r}}_{=K_x} \ . \tag{C.41}$$

In order to show that $\mathrm{H}_{\varphi_*}^{g_{mac},\mathrm{collinear}}$ is negative semidefinite it is proved that K_x is a negative semidefinite matrix. Let $\mu_1 \dots \mu_{2r}$ be the eigenvalues of K_x. It writes

$$\begin{aligned} K_x &= \begin{bmatrix} M_{xx}^* + M_{yy}^* & M_{xy}^* - M_{yx}^* \\ M_{yx}^* - M_{xy}^* & M_{xx}^* + M_{yy}^* \end{bmatrix} - d_* I_{2r} \\ &= \begin{bmatrix} \Re(\psi_*) & -\Im(\psi_*) \\ \Im(\psi_*) & \Re(\psi_*) \end{bmatrix} \begin{bmatrix} \Re(\psi_*) & -\Im(\psi_*) \\ \Im(\psi_*) & \Re(\psi_*) \end{bmatrix}^T - d_* I_{2r} \\ &= \frac{1}{\sqrt{d_*}} \underbrace{\begin{bmatrix} \Re(\psi_*) & -\Im(\psi_*) \\ \Im(\psi_*) & \Re(\psi_*) \end{bmatrix}}_{=L} \underbrace{\begin{bmatrix} d_* & 0 \\ 0 & d_* \end{bmatrix}}_{=M_b} \begin{bmatrix} \Re(\psi_*) & -\Im(\psi_*) \\ \Im(\psi_*) & \Re(\psi_*) \end{bmatrix}^T \frac{1}{\sqrt{d_*}} - d_* I_{2r} \ , \end{aligned} \tag{C.42}$$

where

$$\tilde{L} = \frac{1}{\sqrt{d_*}} L = \frac{1}{\sqrt{d_*}} \begin{bmatrix} \Re(\psi_*) & -\Im(\psi_*) \\ \Im(\psi_*) & \Re(\psi_*) \end{bmatrix} = \begin{bmatrix} L_1 & L_2 \end{bmatrix} \ . \tag{C.43}$$

Notice that the square root of the scalar product $\sqrt{d_*} = \sqrt{\Re(\psi_*)^T\Re(\psi_*) + \Im(\psi_*)^T\Im(\psi_*)}$ is equivalent to the norm of each column of matrix L, and vectors L_1 and L_2 are of norm 1 and orthogonal. Furthermore there exists $2r-2$ linearly independent vectors $q_1, \dots, q_{2r-2} \in \mathbb{R}^r$, such that matrix

$\begin{bmatrix} L_1 & L_2 & q_1 & \dots & q_{2r-2} \end{bmatrix}$ is an orthonormal basis in $\mathbb{R}^{2r}$, satisfying $q_i^T L_1 = 0$ and $q_i^T L_2 = 0$ for $i = 1 \dots 2r-2$, $q_i^T q_j = 0$, $i \neq j$ and $q_i^T q_i = 1$. Now, (C.42) writes as

$$\begin{aligned} K_x &= \begin{bmatrix} L_1 & L_2 & q_1 & \dots & q_{2r-2} \end{bmatrix} \begin{bmatrix} d_* & & & & & \\ & d_* & & & & \\ & & 0 & & & \\ & & & \ddots & & \\ & & & & 0 \end{bmatrix} \begin{bmatrix} L_1^T \\ L_2^T \\ q_1^T \\ \vdots \\ q_{2r-2}^T \end{bmatrix} - aI_{2r} \\ &= \begin{bmatrix} L_1 & L_2 & q_1 & \dots & q_{2r-2} \end{bmatrix} \begin{bmatrix} 0 & & & & & \\ & 0 & & & & \\ & & -d_* & & & \\ & & & \ddots & & \\ & & & & -d_* \end{bmatrix} \begin{bmatrix} L_1^T \\ L_2^T \\ q_1^T \\ \vdots \\ q_{2r-2}^T \end{bmatrix} , \end{aligned}$$

which is by definition the eigenvalue decomposition of K_x. Since K_x has non positive eigenvalues, based on the expression above, it is negative semidefinite matrix of $\text{rank}(K_x) = 2r-2$. That, with the fact that the fraction $2/k^2 d_*^2 > 0$, concludes this proof.

C.5 Proof of Lemma 5.9

First recall the expression for $\mathrm{H}_{\varphi_*}^{g_{mac},\text{orthogonal}}$ from (5.27)

$$\mathrm{H}_{\varphi_*}^{g_{mac},\text{orthogonal}} = \frac{2}{d_* e_*} \underbrace{\begin{bmatrix} M_{xx}^* + M_{yy}^* & M_{xy}^* - M_{yx}^* \\ M_{yx}^* - M_{xy}^* & M_{xx}^* + M_{yy}^* \end{bmatrix}}_{=K_x} . \tag{C.44}$$

In order to show that $\mathrm{H}_{\varphi_*}^{g_{mac},\text{orthogonal}}$ is positive semidefinite it is proved that K_x is a positive semidefinite matrix. Let $\mu_1 \dots \mu_{2r}$ be the eigenvalues of K_x. It writes

$$\begin{aligned} K_x &= \begin{bmatrix} M_{xx}^* + M_{yy}^* & M_{xy}^* - M_{yx}^* \\ M_{yx}^* - M_{xy}^* & M_{xx}^* + M_{yy}^* \end{bmatrix} \\ &= \begin{bmatrix} \Re(\psi_*) & -\Im(\psi_*) \\ \Im(\psi_*) & \Re(\psi_*) \end{bmatrix} \begin{bmatrix} \Re(\psi_*) & -\Im(\psi_*) \\ \Im(\psi_*) & \Re(\psi_*) \end{bmatrix}^T \\ &= \frac{1}{\sqrt{d_*}} \underbrace{\begin{bmatrix} \Re(\psi_*) & -\Im(\psi_*) \\ \Im(\psi_*) & \Re(\psi_*) \end{bmatrix}}_{=L} \underbrace{\begin{bmatrix} d_* & 0 \\ 0 & d_* \end{bmatrix}}_{=M_b} \begin{bmatrix} \Re(\psi_*) & -\Im(\psi_*) \\ \Im(\psi_*) & \Re(\psi_*) \end{bmatrix}^T \frac{1}{\sqrt{d_*}} , \end{aligned} \tag{C.45}$$

where

$$\tilde{L} = \frac{1}{\sqrt{d_*}} L = \frac{1}{\sqrt{d_*}} \begin{bmatrix} \Re(\psi_*) & -\Im(\psi_*) \\ \Im(\psi_*) & \Re(\psi_*) \end{bmatrix} = \begin{bmatrix} L_1 & L_2 \end{bmatrix} . \tag{C.46}$$

Notice that the square root of the scalar product $\sqrt{d_*} = \sqrt{\Re(\psi_*)^T\Re(\psi_*) + \Im(\psi_*)^T\Im(\psi_*)}$ is equivalent to the norm of each column of matrix L, and vectors L_1 and L_2 are of norm 1 and orthogonal. Furthermore there exists $2r-2$ linearly independent vectors $q_1, \ldots, q_{2r-2} \in \mathbb{R}^r$, such that matrix $\begin{bmatrix} L_1 & L_2 & q_1 & \ldots & q_{2r-2} \end{bmatrix}$ is an orthonormal basis in $\mathbb{R}^{2r}$, satisfying $q_i^T L_1 = 0$ and $q_i^T L_2 = 0$ for $i = 1 \ldots 2r-2$, $q_i^T q_j = 0$, $i \neq j$ and $q_i^T q_i = 1$. Now, (C.45) writes as

$$K_x = \begin{bmatrix} L_1 & L_2 & q_1 & \ldots & q_{2r-2} \end{bmatrix} \begin{bmatrix} d_* & & & & \\ & d_* & & & \\ & & 0 & & \\ & & & \ddots & \\ & & & & 0 \end{bmatrix} \begin{bmatrix} L_1^T \\ L_2^T \\ q_1^T \\ \vdots \\ q_{2r-2}^T \end{bmatrix},$$

which is by definition the eigenvalue decomposition of K_x. Since K_x has positive eigenvalues, based on the expression above, it is positive semidefinite matrix of $\operatorname{rank}(K_x) = 2r-2$. That, with the fact that the fraction $2/d_* e_* > 0$, concludes this proof.

APPENDIX D

Uncertainty quantification of the MAC from a stabilization diagram

D.1 Hessian derivation for $g_{mac}(\hat{\varphi}, \hat{\psi})$

The computation of the second order partial derivatives of $g_{mac}(\varphi, \psi)$ with respect to $\Re(\varphi)$ and $\Im(\varphi)$ was conducted in Appendix C.3. The following section illustrates the derivation of the remaining components of $\mathrm{H}^{g}_{\hat{\varphi},\hat{\psi}}$ namely the second order partial derivatives of $g_{mac}(\varphi, \psi)$ with respect to $\Re(\psi)$ and $\Im(\psi)$. Two cases are considered namely, first when both mode shapes used for MAC computation, φ_* and ψ_*, belong the the same mode

$$\varphi_* = k \cdot \psi_* \tag{D.1}$$

and second when two mode shapes φ and ψ are orthogonal

$$\varphi_*^H \psi_* = 0 \ . \tag{D.2}$$

For clarity this section is divided into two sub-parts, one containing the derivations of remaining partial derivatives and second containing their assembly into two Hessian matrices.

Derivation

To obtain the mixed derivatives from the first row of (6.10) the total derivative of (5.4) is computed

$$\begin{aligned} d\left[\frac{\partial g_{mac}(\varphi,\psi)}{\partial \Re(\varphi)}\right] &= d\left(\frac{2\Re(\psi\psi^H\varphi)}{\varphi^H\varphi\psi^H\psi} - \frac{2g_{mac}(\varphi,\psi)\Re(\varphi)}{\varphi^H\varphi}\right) \\ &= \frac{2d(\Re(\psi\psi^H\varphi))}{\varphi^H\varphi\psi^H\psi} - \frac{2\Re(\psi\psi^H\varphi)d(\varphi^H\varphi\psi^H\psi)}{(\varphi^H\varphi\psi^H\psi)^2} \\ &\quad - \frac{2d\left(g_{mac}(\varphi,\psi)\Re(\varphi)\right)}{\varphi^H\varphi} + \frac{2g_{mac}(\varphi,\psi)\Re(\varphi)d(\varphi^H\varphi)}{(\varphi^H\varphi)^2} \ . \end{aligned} \tag{D.3}$$

The development of the first term in (D.3) holds

$$\begin{aligned} d(\Re(\psi\psi^H\varphi)) &= d\Re\left((\Re(\psi)+\mathrm{i}\Im(\psi))\,(\Re(\psi)+\mathrm{i}\Im(\psi))^H\,(\Re(\varphi)+\mathrm{i}\Im(\varphi))\right) \\ &= d\Re(\psi)\Re(\psi)^T\Re(\varphi) + \Re(\psi)d\Re(\psi)^T\Re(\varphi) + \Re(\psi)\Re(\psi)^T d\Re(\varphi) \\ &+ d\Re(\psi)\Im(\psi)^T\Im(\varphi) + \Re(\psi)d\Im(\psi)^T\Im(\varphi) + \Re(\psi)\Im(\psi)^T d\Im(\varphi) \\ &+ d\Im(\psi)\Im(\psi)^T\Re(\varphi) + \Im(\psi)d\Im(\psi)^T\Re(\varphi) + \Im(\psi)\Im(\psi)^T d\Re(\varphi) \\ &- d\Im(\psi)\Re(\psi)^T\Im(\varphi) - \Im(\psi)d\Re(\psi)^T\Im(\varphi) - \Im(\psi)\Re(\psi)^T d\Im(\varphi) \\ &= \Re(\varphi)^T\Re(\psi)I_r d\Re(\psi) + \Re(\psi)\Re(\varphi)^T d\Re(\psi) + \Re(\psi)\Re(\psi)^T d\Re(\varphi) \\ &+ \Im(\varphi)^T\Im(\psi)I_r d\Re(\psi) + \Re(\psi)\Im(\varphi)^T d\Im(\psi) + \Re(\psi)\Im(\psi)^T d\Im(\varphi) \\ &+ \Re(\varphi)^T\Im(\psi)I_r d\Im(\psi) + \Im(\psi)\Re(\varphi)^T d\Im(\psi) + \Im(\psi)\Im(\psi)^T d\Re(\varphi) \\ &- \Im(\varphi)^T\Re(\psi)I_r d\Im(\psi) - \Im(\psi)\Im(\varphi)^T d\Re(\psi) - \Im(\psi)\Re(\psi)^T d\Im(\varphi)\ . \end{aligned} \tag{D.4}$$

The second term in (D.3) was developed in Appendix C.3 and yields

$$\begin{aligned} d(\varphi^H\varphi\psi^H\psi) &= 2\Re(\varphi^H d(\varphi)\psi^H\psi) + 2\Re(\varphi^H\varphi\psi^H d(\psi)) \\ &= 2\Re(\psi^H\psi\varphi^H d\varphi) + 2\Re(\varphi^H\varphi\psi^H d(\psi))\ , \end{aligned}$$

where

$$\Re(\psi^H\psi\varphi^H d\varphi) = \begin{bmatrix}\Re(\varphi\psi^H\psi)^T & \Im(\varphi\psi^H\psi)^T\end{bmatrix}\begin{bmatrix}d\Re(\varphi)\\ d\Im(\varphi)\end{bmatrix}\ , \tag{D.5}$$

and

$$\Re(\varphi^H\varphi\psi^H d(\psi)) = \begin{bmatrix}\Re(\psi\varphi^H\varphi)^T & \Im(\psi\varphi^H\varphi)^T\end{bmatrix}\begin{bmatrix}d\Re(\psi)\\ d\Im(\psi)\end{bmatrix}\ . \tag{D.6}$$

The development of the last term in (D.3) yields

$$\begin{aligned} d(\varphi^H\varphi) = d\left(\Re(\varphi)^T\Re(\varphi) + \Im(\varphi)^T\Im(\varphi)\right) &= 2\Re(\varphi)^T d\Re(\varphi) \\ &+ 2\Im(\varphi)^T d\Im(\varphi)\ . \end{aligned} \tag{D.7}$$

After (D.4) and (D.6), the third term in the first row of (6.10) writes as

$$\begin{aligned} \frac{\partial^2 g_{mac}}{\partial\Re(\psi)\partial\Re(\varphi)} &= \frac{2\Re(\varphi)^T\Re(\psi)I_r + 2\Im(\varphi)^T\Im(\psi)I_r}{\varphi^H\varphi\psi^H\psi} \\ &+ \frac{2\Re(\psi)\Re(\varphi)^T - 2\Im(\psi)\Im(\varphi)^T}{\varphi^H\varphi\psi^H\psi} - \frac{4\Re(\psi\psi^H\varphi)\Re(\psi\varphi^H\varphi)^T}{(\varphi^H\varphi\psi^H\psi)^2}\ . \end{aligned} \tag{D.8}$$

Inserting (D.1) to (D.8) (mode shapes are collinear) yields

$$\begin{aligned} \frac{\partial^2 g_{mac}}{\partial\Re(\psi)\partial\Re(\varphi)} &= \frac{2\Re(\psi_*)^T\Re(\psi_*)I_r + 2\Im(\psi_*)^T\Im(\psi_*)I_r}{k(\psi_*^H\psi_*)^2} \\ &+ \frac{2\Re(\psi_*)\Re(\psi_*)^T - 2\Im(\psi_*)\Im(\psi_*)^T}{k(\psi_*^H\psi_*)^2} - \frac{4\Re(\psi_*)\Re(\psi_*)^T}{k(\psi_*^H\psi_*)^2} \\ &= \frac{2\Re(\psi_*)^T\Re(\psi_*)I_r + 2\Im(\psi_*)^T\Im(\psi_*)I_r}{k(\psi_*^H\psi_*)^2} \\ &- \frac{2\Re(\psi_*)\Re(\psi_*)^T + 2\Im(\psi_*)\Im(\psi_*)^T}{k(\psi_*^H\psi_*)^2}\ . \end{aligned} \tag{D.9}$$

Inserting (D.2) to (D.8) (mode shapes are orthogonal) yields

$$\frac{\partial^2 g_{mac}}{\partial \Re(\psi) \partial \Re(\varphi)} = \frac{2\Re(\psi_*)\Re(\varphi_*)^T - 2\Im(\psi_*)\Im(\varphi_*)^T}{\varphi_*^H \varphi_* \psi_*^H \psi_*} \ . \tag{D.10}$$

After (D.4) and (D.6), the last term in the first row of (6.10) writes as

$$\begin{aligned} \frac{\partial^2 g_{mac}}{\partial \Im(\psi) \partial \Re(\varphi)} &= \frac{2\Re(\varphi)^T \Im(\psi) I_r - 2\Im(\varphi)^T \Re(\psi) I_r}{\varphi^H \varphi \psi^H \psi} \\ &+ \frac{2\Re(\psi)\Im(\varphi)^T + 2\Im(\psi)\Re(\varphi)^T}{\varphi^H \varphi \psi^H \psi} - \frac{4\Re(\psi\psi^H\varphi)\Im(\psi\varphi^H\varphi)^T}{(\varphi^H \varphi \psi^H \psi)^2} \ . \end{aligned} \tag{D.11}$$

Inserting (D.1) to (D.11) (mode shapes are collinear) yields

$$\begin{aligned} \frac{\partial^2 g_{mac}}{\partial \Im(\psi) \partial \Re(\varphi)} &= \frac{2\Re(\psi_*)^T \Im(\psi_*) I_r - 2\Im(\psi_*)^T \Re(\psi_*) I_r}{k(\psi_*^H \psi_*)^2} \\ &+ \frac{2\Re(\psi_*)\Im(\psi_*)^T + 2\Im(\psi_*)\Re(\psi_*)^T}{k(\psi_*^H \psi_*)^2} - \frac{4\Re(\psi_*)\Im(\psi_*)^T}{k(\psi_*^H \psi_*)^2} \\ &= \frac{2\Re(\psi_*)^T \Im(\psi_*) I_r - 2\Im(\psi_*)^T \Re(\psi_*) I_r}{k(\psi_*^H \psi_*)^2} \\ &+ \frac{2\Im(\psi_*)\Re(\psi_*)^T - 2\Re(\psi_*)\Im(\psi_*)^T}{k(\psi_*^H \psi_*)^2} \ . \end{aligned} \tag{D.12}$$

Inserting (D.2) to (D.11) (mode shapes are orthogonal) yields

$$\frac{\partial^2 g_{mac}}{\partial \Im(\psi) \partial \Re(\varphi)} = \frac{2\Re(\psi_*)\Im(\varphi_*)^T + 2\Im(\psi_*)\Re(\varphi_*)^T}{\varphi_*^H \varphi_* \psi_*^H \psi_*} \ . \tag{D.13}$$

To obtain the mixed derivatives from the second row of (6.10) the total derivative of (5.5) is computed, which yields

$$\begin{aligned} d\left[\frac{\partial g_{mac}(\varphi,\psi)}{\partial \Im(\varphi)}\right] &= d\left(\frac{2\Im(\psi\psi^H\varphi)}{\varphi^H\varphi\psi^H\psi} - \frac{2g_{mac}(\varphi,\psi)\Im(\varphi)}{\varphi^H\varphi}\right) \\ &= \frac{2d(\Im(\psi\psi^H\varphi))}{\varphi^H\varphi\psi^H\psi} - \frac{2\Im(\psi\psi^H\varphi)d(\varphi^H\varphi\psi^H\psi)}{(\varphi^H\varphi\psi^H\psi)^2} \\ &- \frac{2d(g_{mac}(\varphi,\psi)\Im(\varphi))}{\varphi^H\varphi} + \frac{2g_{mac}(\varphi,\psi)\Im(\varphi)d(\varphi^H\varphi)}{(\varphi^H\varphi)^2} \ . \end{aligned} \tag{D.14}$$

The development of the first term in (D.14) holds

$$\begin{aligned} d(\Im(\psi\psi^H\varphi)) &= d\Im\left((\Re(\psi)+\mathrm{i}\Im(\psi))\,(\Re(\psi)+\mathrm{i}\Im(\psi))^H\,(\Re(\varphi)+\mathrm{i}\Im(\varphi))\right) \\ &= d\Im(\psi)\Re(\psi)^T\Re(\varphi) + \Im(\psi)d\Re(\psi)^T\Re(\varphi) + \Im(\psi)\Re(\psi)^T d\Re(\varphi) \\ &+ d\Im(\psi)\Im(\psi)^T\Im(\varphi) + \Im(\psi)d\Im(\psi)^T\Im(\varphi) + \Im(\psi)\Im(\psi)^T d\Im(\varphi) \\ &+ d\Re(\psi)\Re(\psi)^T\Im(\varphi) + \Re(\psi)d\Re(\psi)^T\Im(\varphi) + \Re(\psi)\Re(\psi)^T d\Im(\varphi) \\ &- d\Re(\psi)\Im(\psi)^T\Re(\varphi) - \Re(\psi)d\Im(\psi)^T\Re(\varphi) - \Re(\psi)\Im(\psi)^T d\Re(\varphi) \\ &= \Re(\varphi)^T\Re(\psi)I_r d\Im(\psi) + \Im(\psi)\Re(\varphi)^T d\Re(\psi) + \Im(\psi)\Re(\psi)^T d\Re(\varphi) \\ &+ \Im(\varphi)^T\Im(\psi)I_r d\Im(\psi) + \Im(\psi)\Im(\varphi)^T d\Im(\psi) + \Im(\psi)\Im(\psi)^T d\Im(\varphi) \\ &+ \Im(\varphi)^T\Re(\psi)I_r d\Re(\psi) + \Re(\psi)\Im(\varphi)^T d\Re(\psi) + \Re(\psi)\Re(\psi)^T d\Im(\varphi) \\ &- \Re(\varphi)^T\Im(\psi)I_r d\Re(\psi) - \Re(\psi)\Re(\varphi)^T d\Im(\psi) - \Re(\psi)\Im(\psi)^T d\Re(\varphi) \ . \end{aligned} \tag{D.15}$$

After (D.15) and (D.6), the third term in the second row of (6.10) writes as

$$\frac{\partial^2 g_{mac}}{\partial \Re(\psi) \partial \Im(\varphi)} = \frac{2\Im(\varphi)^T \Re(\psi) I_r - 2\Re(\varphi)^T \Im(\psi) I_r}{\varphi^H \varphi \psi^H \psi} + \frac{2\Im(\psi)\Re(\varphi)^T + 2\Re(\psi)\Im(\varphi)^T}{\varphi^H \varphi \psi^H \psi} - \frac{4\Im(\psi\psi^H\varphi)\Re(\psi\varphi^H\varphi)^T}{(\varphi^H \varphi \psi^H \psi)^2} . \tag{D.16}$$

Inserting (D.1) to (D.16) (mode shapes are collinear) yields

$$\begin{aligned} \frac{\partial^2 g_{mac}}{\partial \Re(\psi) \partial \Im(\varphi)} &= \frac{2\Im(\psi_*)^T \Re(\psi_*) I_r - 2\Re(\psi_*)^T \Im(\psi_*) I_r}{k(\psi_*^H \psi_*)^2} \\ &+ \frac{2\Im(\psi_*)\Re(\psi_*)^T + 2\Re(\psi_*)\Im(\psi_*)^T}{k(\psi_*^H \psi_*)^2} - \frac{4\Im(\psi_*)\Re(\psi_*)^T}{k(\psi_*^H \psi_*)^2} \\ &= \frac{2\Im(\psi_*)^T \Re(\psi_*) I_r - 2\Re(\psi_*)^T \Im(\psi_*) I_r}{k(\psi_*^H \psi_*)^2} \\ &+ \frac{2\Re(\psi_*)\Im(\psi_*)^T - 2\Im(\psi_*)\Re(\psi_*)^T}{k(\psi_*^H \psi_*)^2} . \end{aligned} \tag{D.17}$$

Inserting (D.2) to (D.16) (mode shapes are orthogonal) yields

$$\frac{\partial^2 g_{mac}}{\partial \Re(\psi) \partial \Im(\varphi)} = \frac{2\Im(\psi_*)\Re(\varphi_*)^T + 2\Re(\psi_*)\Im(\varphi_*)^T}{\varphi_*^H \varphi_* \psi_*^H \psi_*} . \tag{D.18}$$

After (D.15) and (D.6), the last term in the second row of (6.10) writes as

$$\frac{\partial^2 g_{mac}}{\partial \Im(\psi) \partial \Im(\varphi)} = \frac{2\Re(\varphi)^T \Re(\psi) I_r + 2\Im(\varphi)^T \Im(\psi) I_r}{\varphi^H \varphi \psi^H \psi} + \frac{2\Im(\psi)\Im(\varphi)^T - 2\Re(\psi)\Re(\varphi)^T}{\varphi^H \varphi \psi^H \psi} - \frac{4\Im(\psi\psi^H\varphi)\Im(\psi\varphi^H\varphi)^T}{(\varphi^H \varphi \psi^H \psi)^2} . \tag{D.19}$$

Inserting (D.1) to (D.19) (mode shapes are collinear) yields

$$\begin{aligned} \frac{\partial^2 g_{mac}}{\partial \Im(\psi) \partial \Im(\varphi)} &= \frac{2\Re(\psi_*)^T \Re(\psi_*) I_r + 2\Im(\psi_*)^T \Im(\psi_*) I_r}{k(\psi_*^H \psi_*)^2} \\ &+ \frac{2\Im(\psi_*)\Im(\psi_*)^T - 2\Re(\psi_*)\Re(\psi_*)^T}{k(\psi_*^H \psi_*)^2} - \frac{4\Im(\psi_*)\Im(\psi_*)^T}{k(\psi_*^H \psi_*)^2} \\ &= \frac{2\Re(\psi_*)^T \Re(\psi_*) I_r + 2\Im(\psi_*)^T \Im(\psi_*) I_r}{k(\psi_*^H \psi_*)^2} \\ &- \frac{2\Im(\psi_*)\Im(\psi_*)^T + 2\Re(\psi_*)\Re(\psi_*)^T}{k(\psi_*^H \psi_*)^2} . \end{aligned} \tag{D.20}$$

Inserting (D.2) to (D.19) (mode shapes are orthogonal) yields

$$\frac{\partial^2 g_{mac}}{\partial \Im(\psi) \partial \Im(\varphi)} = \frac{2\Im(\psi_*)\Im(\varphi_*)^T - 2\Re(\psi_*)\Re(\varphi_*)^T}{\varphi_*^H \varphi_* \psi_*^H \psi_*} . \tag{D.21}$$

In order to compute the third row of (6.10) the total derivative of (5.6) is computed, which yields

$$\begin{aligned} d\left[\frac{\partial g_{mac}(\varphi,\psi)}{\partial \Re(\psi)}\right] &= d\left(\frac{2\Re(\varphi\varphi^H\psi)}{\varphi^H\varphi\psi^H\psi} - \frac{2g_{mac}(\varphi,\psi)\Re(\psi)}{\psi^H\psi}\right) \\ &= \frac{2d(\Re(\varphi\varphi^H\psi))}{\varphi^H\varphi\psi^H\psi} - \frac{2\Re(\varphi\varphi^H\psi)d(\varphi^H\varphi\psi^H\psi)}{(\varphi^H\varphi\psi^H\psi)^2} \\ &\quad - \frac{2d(g_{mac}(\varphi,\psi)\Re(\psi))}{\psi^H\psi} + \frac{2g_{mac}(\varphi,\psi)\Re(\psi)d(\psi^H\psi)}{(\psi^H\psi)^2} \ . \end{aligned} \tag{D.22}$$

The development of the first term in (D.22) holds

$$\begin{aligned} d(\Re(\varphi\varphi^H\psi)) &= d\Re\left((\Re(\varphi)+\mathrm{i}\Im(\varphi))\left(\Re(\varphi)+\mathrm{i}\Im(\varphi)\right)^H(\Re(\psi)+\mathrm{i}\Im(\psi))\right) \\ &= d\Re(\varphi)\Re(\varphi)^T\Re(\psi) + \Re(\varphi)d\Re(\varphi)^T\Re(\psi) + \Re(\varphi)\Re(\varphi)^T d\Re(\psi) \\ &+ d\Re(\varphi)\Im(\varphi)^T\Im(\psi) + \Re(\varphi)d\Im(\varphi)^T\Im(\psi) + \Re(\varphi)\Im(\varphi)^T d\Im(\psi) \\ &+ d\Im(\varphi)\Im(\varphi)^T\Re(\psi) + \Im(\varphi)d\Im(\varphi)^T\Re(\psi) + \Im(\varphi)\Im(\varphi)^T d\Re(\psi) \\ &- d\Im(\varphi)\Re(\varphi)^T\Im(\psi) - \Im(\varphi)d\Re(\varphi)^T\Im(\psi) - \Im(\varphi)\Re(\varphi)^T d\Im(\psi) \\ &= \Re(\psi)^T\Re(\varphi)I_r d\Re(\varphi) + \Re(\varphi)\Re(\psi)^T d\Re(\varphi) + \Re(\varphi)\Re(\varphi)^T d\Re(\psi) \\ &+ \Im(\psi)^T\Im(\varphi)I_r d\Re(\varphi) + \Re(\varphi)\Im(\psi)^T d\Im(\varphi) + \Re(\varphi)\Im(\varphi)^T d\Im(\psi) \\ &+ \Re(\psi)^T\Im(\varphi)I_r d\Im(\varphi) + \Im(\varphi)\Re(\psi)^T d\Im(\varphi) + \Im(\varphi)\Im(\varphi)^T d\Re(\psi) \\ &- \Im(\psi)^T\Re(\varphi)I_r d\Im(\varphi) - \Im(\varphi)\Im(\psi)^T d\Re(\varphi) - \Im(\varphi)\Re(\varphi)^T d\Im(\psi) \ . \end{aligned} \tag{D.23}$$

The development of the last term in (D.22) writes as

$$\begin{aligned} d(\psi^H\psi) = d\left(\Re(\psi)^T\Re(\psi) + \Im(\psi)^T\Im(\psi)\right) &= 2\Re(\psi)^T d\Re(\psi) \\ &\quad + 2\Im(\psi)^T d\Im(\psi) \ . \end{aligned} \tag{D.24}$$

After (D.23) and (D.5), the first term in the third row of (6.10) writes as

$$\begin{aligned} \frac{\partial^2 g_{mac}}{\partial\Re(\varphi)\partial\Re(\psi)}(\varphi_*,\psi_*) &= \frac{2\Re(\psi)^T\Re(\varphi)I_r + 2\Im(\psi)^T\Im(\varphi)I_r}{\varphi^H\varphi\psi^H\psi} \\ &\quad + \frac{2\Re(\varphi)\Re(\psi)^T - 2\Im(\varphi)\Im(\psi)^T}{\varphi^H\varphi\psi^H\psi} \\ &\quad - \frac{4\Re(\varphi\varphi^H\psi)\Re(\varphi\psi^H\psi)^T}{(\varphi^H\varphi\psi^H\psi)^2} \ . \end{aligned} \tag{D.25}$$

Inserting (D.1) to (D.25) (mode shapes are collinear) yields

$$\begin{aligned} \frac{\partial^2 g_{mac}}{\partial\Re(\varphi)\partial\Re(\psi)} &= \frac{2\Re(\psi_*)^T\Re(\psi_*)I_r + 2\Im(\psi_*)^T\Im(\psi_*)I_r}{k(\psi_*^H\psi_*)^2} \\ &\quad + \frac{2\Re(\psi_*)\Re(\psi_*)^T - 2\Im(\psi_*)\Im(\psi_*)^T}{k(\psi_*^H\psi_*)^2} - \frac{4\Re(\psi_*)\Re(\psi_*)^T}{k(\psi_*^H\psi_*)^2} \\ &= \frac{2\Re(\psi_*)^T\Re(\psi_*)I_r + 2\Im(\psi_*)^T\Im(\psi_*)I_r}{k(\psi_*^H\psi_*)^2} \\ &\quad - \frac{2\Re(\psi_*)\Re(\psi_*)^T + 2\Im(\psi_*)\Im(\psi_*)^T}{k(\psi_*^H\psi_*)^2} \ . \end{aligned} \tag{D.26}$$

Inserting (D.2) to (D.25) (mode shapes are orthogonal) yields

$$\frac{\partial^2 g_{mac}}{\partial \Re(\varphi) \partial \Re(\psi)} = \frac{2\Re(\varphi_*)\Re(\psi_*)^T - 2\Im(\varphi_*)\Im(\psi_*)^T}{\varphi_*^H \varphi_* \psi_*^H \psi_*} \ . \tag{D.27}$$

After (D.23) and (D.5), the second term in the third row of (6.10) writes as

$$\begin{aligned} \frac{\partial^2 g_{mac}}{\partial \Im(\varphi) \partial \Re(\psi)} &= \frac{2\Re(\psi)^T \Im(\varphi) I_r - 2\Im(\psi)^T \Re(\varphi) I_r}{\varphi^H \varphi \psi^H \psi} \\ &+ \frac{2\Re(\varphi)\Im(\psi)^T + 2\Im(\varphi)\Re(\psi)^T}{\varphi^H \varphi \psi^H \psi} - \frac{4\Re(\varphi\varphi^H\psi)\Im(\varphi\psi^H\psi)^T}{(\varphi^H \varphi \psi^H \psi)^2} \ . \end{aligned} \tag{D.28}$$

Inserting (D.1) to (D.28) (mode shapes are collinear) yields

$$\begin{aligned} \frac{\partial^2 g_{mac}}{\partial \Im(\varphi) \partial \Re(\psi)} &= \frac{2\Re(\psi_*)^T \Im(\psi_*) I_r - 2\Im(\psi_*)^T \Re(\psi_*) I_r}{k(\psi_*^H \psi_*)^2} \\ &+ \frac{2\Re(\psi_*)\Im(\psi_*)^T + 2\Im(\psi_*)\Re(\psi_*)^T}{k(\psi_*^H \psi_*)^2} - \frac{4\Re(\psi_*)\Im(\psi_*)^T}{k(\psi_*^H \psi_*)^2} \\ &= \frac{2\Re(\psi_*)^T \Im(\psi_*) I_r - 2\Im(\psi_*)^T \Re(\psi_*) I_r}{k(\psi_*^H \psi_*)^2} \\ &+ \frac{2\Im(\psi_*)\Re(\psi_*)^T - 2\Re(\psi_*)\Im(\psi_*)^T +}{k(\psi_*^H \psi_*)^2} \ . \end{aligned} \tag{D.29}$$

Inserting (D.2) to (D.28) (mode shapes are orthogonal) yields

$$\frac{\partial^2 g_{mac}}{\partial \Im(\varphi) \partial \Re(\psi)} = \frac{2\Re(\varphi_*)\Im(\psi_*)^T + 2\Im(\varphi_*)\Re(\psi_*)^T}{\varphi_*^H \varphi_* \psi_*^H \psi_*} \ . \tag{D.30}$$

After (D.23), (D.24) and (D.6), the third term in the third row of (6.10) writes as

$$\begin{aligned} \frac{\partial^2 g_{mac}}{\partial \Re(\psi) \partial \Re(\psi)} &= \frac{2\Re(\varphi)\Re(\varphi)^T + 2\Im(\varphi)\Im(\varphi)^T}{\varphi^H \varphi \psi^H \psi} \\ &+ \frac{4 g_{mac}(\varphi,\psi)\Re(\psi)\Re(\psi)^T - 2 g_{mac}(\varphi,\psi) I_r \psi^H \psi}{(\psi^H \psi)^2} \\ &- \frac{4\Re(\varphi\varphi^H\psi)\Re(\psi\varphi^H\varphi)^T}{(\varphi^H \varphi \psi^H \psi)^2} \ . \end{aligned} \tag{D.31}$$

Inserting (D.1) to (D.31) (mode shapes are collinear) yields

$$\begin{aligned} \frac{\partial^2 g_{mac}}{\partial \Re(\psi) \partial \Re(\psi)} &= \frac{2\Re(\psi_*)\Re(\psi_*)^T + 2\Im(\psi_*)\Im(\psi_*)^T}{(\psi_*^H \psi_*)^2} \\ &+ \frac{4\Re(\psi_*)\Re(\psi_*)^T - 2 I_r \psi_*^H \psi_*}{(\psi_*^H \psi_*)^2} - \frac{4\Re(\psi_*)\Re(\psi_*)^T}{(\psi_*^H \psi_*)^2} \\ &= \frac{2\Re(\psi_*)\Re(\psi_*)^T + 2\Im(\psi_*)\Im(\psi_*)^T - 2 I_r \psi_*^H \psi_*}{(\psi_*^H \psi_*)^2} \ . \end{aligned} \tag{D.32}$$

Inserting (D.2) to (D.31) (mode shapes are orthogonal) yields

$$\frac{\partial^2 g_{mac}}{\partial \Re(\psi) \partial \Re(\psi)} = \frac{2\Re(\varphi_*)\Re(\varphi_*)^T + 2\Im(\varphi_*)\Im(\varphi_*)^T}{\varphi_*^H \varphi_* \psi_*^H \psi_*} \ . \tag{D.33}$$

After (D.23), (D.24) and (D.6), the last term in the third row of (6.10) writes as

$$\begin{aligned}\frac{\partial^2 g_{mac}}{\partial \Im(\psi) \partial \Re(\psi)} &= \frac{2\Re(\varphi)\Im(\varphi)^T - 2\Im(\varphi)\Re(\varphi)^T}{\varphi^H \varphi \psi^H \psi} \\ &+ \frac{4 g_{mac}(\varphi,\psi)\Re(\psi)\Im(\psi)^T}{(\psi^H\psi)^2} - \frac{4\Re(\varphi\varphi^H\psi)\Im(\psi\varphi^H\varphi)^T}{(\varphi^H\varphi\psi^H\psi)^2} \ .\end{aligned} \tag{D.34}$$

Inserting (D.1) to (D.34) (mode shapes are collinear) yields

$$\begin{aligned}\frac{\partial^2 g_{mac}}{\partial \Im(\psi) \partial \Re(\psi)} &= \frac{2\Re(\psi_*)\Im(\psi_*)^T - 2\Im(\psi_*)\Re(\psi_*)^T}{(\psi_*^H\psi_*)^2} \\ &+ \frac{4\Re(\psi_*)\Im(\psi_*)^T}{(\psi_*^H\psi_*)^2} - \frac{4\Re(\psi_*)\Im(\psi_*)^T}{(\psi_*^H\psi_*)^2} \\ &= \frac{2\Re(\psi_*)\Im(\psi_*)^T - 2\Im(\psi_*)\Re(\psi_*)^T}{(\psi_*^H\psi_*)^2} \ .\end{aligned} \tag{D.35}$$

Inserting (D.2) to (D.34) (mode shapes are orthogonal) yields

$$\frac{\partial^2 g_{mac}}{\partial \Im(\psi) \partial \Re(\psi)} = \frac{2\Re(\varphi_*)\Im(\varphi_*)^T - 2\Im(\varphi_*)\Re(\varphi_*)^T}{\varphi_*^H \varphi_* \psi_*^H \psi_*} \ . \tag{D.36}$$

Finally, to compute the last row of (6.10) the total derivative of (5.7) is computed, which yields

$$\begin{aligned} d\left[\frac{\partial g_{mac}}{\partial \Im(\psi)}\right] &= d\left(\frac{2\Im(\varphi\varphi^H\psi)}{\varphi^H\varphi\psi^H\psi} - \frac{2 g_{mac}(\varphi,\psi)\Im(\psi)}{\psi^H\psi}\right) \\ &= \frac{2d(\Im(\varphi\varphi^H\psi))}{\varphi^H\varphi\psi^H\psi} - \frac{2\Im(\varphi\varphi^H\psi)d(\varphi^H\varphi\psi^H\psi)}{(\varphi^H\varphi\psi^H\psi)^2} \\ &- \frac{2d(g_{mac}(\varphi,\psi)\Im(\psi))}{\psi^H\psi} + \frac{2 g_{mac}(\varphi,\psi)\Im(\psi)d(\psi^H\psi)}{(\psi^H\psi)^2} \ . \end{aligned} \tag{D.37}$$

The development of the first term in (D.37) writes as

$$\begin{aligned} d(\Im(\varphi\varphi^H\psi)) &= d\Im\left((\Re(\varphi)+\mathrm{i}\Im(\varphi))\,(\Re(\varphi)+\mathrm{i}\Im(\varphi))^H\,(\Re(\psi)+\mathrm{i}\Im(\psi))\right) \\ &= d\Im(\varphi)\Re(\varphi)^T\Re(\psi) + \Im(\varphi)d\Re(\varphi)^T\Re(\psi) + \Im(\varphi)\Re(\varphi)^T d\Re(\psi) \\ &+ d\Im(\varphi)\Im(\varphi)^T\Im(\psi) + \Im(\varphi)d\Im(\varphi)^T\Im(\psi) + \Im(\varphi)\Im(\varphi)^T d\Im(\psi) \\ &+ d\Re(\varphi)\Re(\varphi)^T\Im(\psi) + \Re(\varphi)d\Re(\varphi)^T\Im(\psi) + \Re(\varphi)\Re(\varphi)^T d\Im(\psi) \\ &- d\Re(\varphi)\Im(\varphi)^T\Re(\psi) - \Re(\varphi)d\Im(\varphi)^T\Re(\psi) - \Re(\varphi)\Im(\varphi)^T d\Re(\psi) \\ &= \Re(\psi)^T\Re(\varphi)I_r d\Im(\varphi) + \Im(\varphi)\Re(\psi)^T d\Re(\varphi) + \Im(\varphi)\Re(\varphi)^T d\Re(\psi) \\ &+ \Im(\psi)^T\Im(\varphi)I_r d\Im(\varphi) + \Im(\varphi)\Im(\psi)^T d\Im(\varphi) + \Im(\varphi)\Im(\varphi)^T d\Im(\psi) \\ &+ \Im(\psi)^T\Re(\varphi)I_r d\Re(\varphi) + \Re(\varphi)\Im(\psi)^T d\Re(\varphi) + \Re(\varphi)\Re(\varphi)^T d\Im(\psi) \\ &- \Re(\psi)^T\Im(\varphi)I_r d\Re(\varphi) - \Re(\varphi)\Re(\psi)^T d\Im(\varphi) - \Re(\varphi)\Im(\varphi)^T d\Re(\psi) \ . \end{aligned} \tag{D.38}$$

After (D.38) and (D.5), the first term in the last row of (6.10) writes as

$$\begin{aligned}\frac{\partial^2 g_{mac}}{\partial \Re(\varphi) \partial \Im(\psi)} &= \frac{2\Im(\psi)^T\Re(\varphi)I_r - 2\Re(\psi)^T\Im(\varphi)I_r}{\varphi^H\varphi\psi^H\psi} \\ &+ \frac{2\Im(\varphi)\Re(\psi)^T + 2\Re(\varphi)\Im(\psi)^T}{\varphi^H\varphi\psi^H\psi} - \frac{4\Im(\varphi\varphi^H\psi)\Re(\varphi\psi^H\psi)^T}{(\varphi^H\varphi\psi^H\psi)^2} \ .\end{aligned} \tag{D.39}$$

Inserting (D.1) to (D.39) (mode shapes are collinear) yields

$$\begin{aligned}\frac{\partial^2 g_{mac}}{\partial\Re(\varphi)\partial\Im(\psi)} &= \frac{2\Im(\psi_*)^T\Re(\psi_*)I_r - 2\Re(\psi_*)^T\Im(\psi_*)I_r}{k(\psi_*^H\psi_*)^2} \\ &+ \frac{2\Im(\psi_*)\Re(\psi_*)^T + 2\Re(\psi_*)\Im(\psi_*)^T}{k(\psi_*^H\psi_*)^2} - \frac{4\Im(\psi_*)\Re(\psi_*)^T}{k(\psi_*^H\psi_*)^2} \\ &= \frac{2\Im(\psi_*)^T\Re(\psi_*)I_r - 2\Re(\psi_*)^T\Im(\psi_*)I_r}{k(\psi_*^H\psi_*)^2} \\ &+ \frac{2\Re(\psi_*)\Im(\psi_*)^T - 2\Im(\psi_*)\Re(\psi_*)^T}{k(\psi_*^H\psi_*)^2} \ .\end{aligned} \tag{D.40}$$

Inserting (D.2) to (D.39) (mode shapes are orthogonal) yields

$$\frac{\partial^2 g_{mac}}{\partial\Re(\varphi)\partial\Im(\psi)} = \frac{2\Im(\varphi_*)\Re(\psi_*)^T + 2\Re(\varphi_*)\Im(\psi_*)^T}{\varphi_*^H\varphi_*\psi_*^H\psi_*} \ . \tag{D.41}$$

After (D.38) and (D.5), the second term in the last row of (6.10) writes as

$$\begin{aligned}\frac{\partial^2 g_{mac}}{\partial\Im(\varphi)\partial\Im(\psi)} &= \frac{2\Re(\psi)^T\Re(\varphi)I_r + 2\Im(\psi)^T\Im(\varphi)I_r}{\varphi^H\varphi\psi^H\psi} \\ &+ \frac{2\Im(\varphi)\Im(\psi)^T - 2\Re(\varphi)\Re(\psi)^T}{\varphi^H\varphi\psi^H\psi} - \frac{4\Im(\varphi\varphi^H\psi)\Im(\varphi\psi^H\psi)^T}{(\varphi^H\varphi\psi^H\psi)^2} \ .\end{aligned} \tag{D.42}$$

Inserting (D.1) to (D.42) (mode shapes are collinear) yields

$$\begin{aligned}\frac{\partial^2 g_{mac}}{\partial\Im(\varphi)\partial\Im(\psi)} &= \frac{2\Re(\psi_*)^T\Re(\psi_*)I_r + 2\Im(\psi_*)^T\Im(\psi_*)I_r}{k(\psi_*^H\psi_*)^2} \\ &+ \frac{2\Im(\psi_*)\Im(\psi_*)^T - 2\Re(\psi_*)\Re(\psi_*)^T}{k(\psi_*^H\psi_*)^2} - \frac{4\Im(\psi_*)\Im(\psi_*)^T}{k(\psi_*^H\psi_*)^2} \\ &= \frac{2\Re(\psi_*)^T\Re(\psi_*)I_r + 2\Im(\psi_*)^T\Im(\psi_*)I_r}{k(\psi_*^H\psi_*)^2} \\ &- \frac{2\Im(\psi_*)\Im(\psi_*)^T + 2\Re(\psi_*)\Re(\psi_*)^T}{k(\psi_*^H\psi_*)^2} \ .\end{aligned} \tag{D.43}$$

Inserting (D.2) to (D.42) (mode shapes are orthogonal) yields

$$\frac{\partial^2 g_{mac}}{\partial\Im(\varphi)\partial\Im(\psi)} = \frac{2\Im(\varphi_*)\Im(\psi_*)^T - 2\Re(\varphi_*)\Re(\psi_*)^T}{\varphi_*^H\varphi_*\psi_*^H\psi_*} \ . \tag{D.44}$$

After (D.38), (D.24) and (D.6), the third term in the last row of (6.10) writes as

$$\begin{aligned}\frac{\partial^2 g_{mac}}{\partial\Re(\psi)\partial\Im(\psi)} &= \frac{2\Im(\varphi)\Re(\varphi)^T - 2\Re(\varphi)\Im(\varphi)^T}{\varphi^H\varphi\psi^H\psi} \\ &+ \frac{4g_{mac}(\varphi,\psi)\Im(\psi)\Re(\psi)^T}{(\psi^H\psi)^2} - \frac{4\Im(\varphi\varphi^H\psi)\Re(\psi\varphi^H\varphi)^T}{(\varphi^H\varphi\psi^H\psi)^2} \ .\end{aligned} \tag{D.45}$$

Inserting (D.1) to (D.45) (mode shapes are collinear) yields

$$\begin{aligned}\frac{\partial^2 g_{mac}}{\partial \Re(\psi)\partial \Im(\psi)} &= \frac{2\Im(\psi_*)\Re(\psi_*)^T - 2\Re(\psi_*)\Im(\psi_*)^T}{(\psi_*^H\psi_*)^2} \\ &+ \frac{4\Im(\psi_*)\Re(\psi_*)^T}{(\psi_*^H\psi_*)^2} - \frac{4\Im(\psi_*)\Re(\psi_*)^T}{(\psi_*^H\psi_*)^2} \\ &= \frac{2\Im(\psi_*)\Re(\psi_*)^T - 2\Re(\psi_*)\Im(\psi_*)^T}{(\psi_*^H\psi_*)^2} \ .\end{aligned} \tag{D.46}$$

Inserting (D.2) to (D.45) (mode shapes are orthogonal) yields

$$\frac{\partial^2 g_{mac}}{\partial \Re(\psi)\partial \Im(\psi)} = \frac{2\Im(\varphi_*)\Re(\varphi_*)^T - 2\Re(\varphi_*)\Im(\varphi_*)^T}{\varphi_*^H\varphi_*\psi_*^H\psi_*} \ . \tag{D.47}$$

After (D.38), (D.24) and (D.6), the last term in the last row of (6.10) writes as

$$\begin{aligned}\frac{\partial^2 g_{mac}}{\partial \Im(\psi)\partial \Im(\psi)} &= \frac{2\Re(\varphi)\Re(\varphi)^T + 2\Im(\varphi)\Im(\varphi)^T}{\varphi^H\varphi\psi^H\psi} \\ &+ \frac{4g_{mac}(\varphi,\psi)\Im(\psi)\Im(\psi)^T - 2g_{mac}(\varphi,\psi)I_r\psi^H\psi}{(\psi^H\psi)^2} \\ &- \frac{4\Im(\varphi\varphi^H\psi)\Im(\psi\varphi^H\varphi)^T}{(\varphi^H\varphi\psi^H\psi)^2} \ .\end{aligned} \tag{D.48}$$

Inserting (D.1) to (D.48) (mode shapes are collinear) yields

$$\begin{aligned}\frac{\partial^2 g_{mac}}{\partial \Im(\psi)\partial \Im(\psi)} &= \frac{2\Re(\psi_*)\Re(\psi_*)^T + 2\Im(\psi_*)\Im(\psi_*)^T}{(\psi_*^H\psi_*)^2} \\ &+ \frac{2\Im(\psi_*)\Im(\psi_*)^T - 2I_r\psi_*^H\psi_*}{(\psi_*^H\psi_*)^2} - \frac{2\Im(\psi_*)\Im(\psi_*)^T}{(\psi_*^H\psi_*)^2} \\ &= \frac{2\Re(\psi_*)\Re(\psi_*)^T + 2\Im(\psi_*)\Im(\psi_*)^T - 2I_r\psi_*^H\psi_*}{(\psi_*^H\psi_*)^2} \ .\end{aligned} \tag{D.49}$$

Inserting (D.2) to (D.48) (mode shapes are orthogonal) yields

$$\frac{\partial^2 g_{mac}}{\partial \Im(\psi)\partial \Im(\psi)} = \frac{2\Re(\varphi_*)\Re(\varphi_*)^T + 2\Im(\varphi_*)\Im(\varphi_*)^T}{\varphi_*^H\varphi_*\psi_*^H\psi_*} \ . \tag{D.50}$$

Assembly of the derivatives

To simplify the notation of the derivatives recall the definition of matrices M and define matrices K such that

$$\begin{aligned}M_{xx}^* &= \Re(\psi_*)\Re(\psi_*)^T, \quad K_{xx}^* = \Re(\psi_*)^T\Re(\psi_*)I_r \ , \\ M_{yy}^* &= \Im(\psi_*)\Im(\psi_*)^T, \quad K_{yy}^* = \Im(\psi_*)^T\Im(\psi_*)I_r \ , \\ M_{xy}^* &= \Re(\psi_*)\Im(\psi_*)^T, \quad K_{xy}^* = \Re(\psi_*)^T\Im(\psi_*)I_r \ , \\ M_{yx}^* &= \Im(\psi_*)\Re(\psi_*)^T, \quad K_{yx}^* = \Im(\psi_*)^T\Re(\psi_*)I_r \ .\end{aligned}$$

and scalars $d_* = \psi_*^H\psi_*$ and $e_* = \varphi_*^H\varphi_*$. First all the derivatives evaluated for the case when $\varphi_* = k \cdot \psi_*$ are combined (D.9), (D.12), (D.17), (D.20), (D.26), (D.29), (D.32),

(D.35) ,(D.40), (D.43), (D.46) and (D.49) with the derivatives evaluated for the same case from (C.28), (C.31), (C.36), (C.39). Using the simplified notation introduced above, the Hessian (6.10), when two mode shapes belong to the same theoretical mode, writes as

$$\mathrm{H}_{\varphi_*,\psi_*}^{g_{mac},\text{collinear}} = \frac{2}{k^2 d_*} \begin{bmatrix} T_{1,1}^* & T_{1,2}^* & T_{1,3}^* & T_{1,4}^* \\ T_{2,1}^* & T_{2,2}^* & T_{2,3}^* & T_{2,4}^* \\ T_{3,1}^* & T_{3,2}^* & T_{3,3}^* & T_{3,4}^* \\ T_{4,1}^* & T_{4,2}^* & T_{4,3}^* & T_{4,4}^* \end{bmatrix} = \frac{2}{k^2 d_*} \begin{bmatrix} 1 & -k \\ -k & k^2 \end{bmatrix} \otimes \begin{bmatrix} T_{1,1}^* & T_{1,2}^* \\ T_{2,1}^* & T_{2,2}^* \end{bmatrix} , \tag{D.51}$$

where

$$\begin{aligned} T_{1,1}^* &= M_{xx}^* + M_{yy}^* - aI_r , \\ T_{2,1}^* &= M_{yx}^* - M_{xy}^* , \\ T_{3,1}^* &= k(K_{xx}^* + K_{yy}^* - M_{xx}^* - M_{yy}^*) = -k(M_{xx}^* + M_{yy}^* - aI_r) , \\ T_{4,1}^* &= k(K_{yx}^* - K_{xy}^* + M_{xy}^* - M_{yx}^*) = k(M_{xy}^* - M_{yx}^*) , \\ T_{1,2}^* &= M_{xy}^* - M_{yx}^* , \\ T_{2,2}^* &= M_{xx}^* + M_{yy}^* - aI_r , \\ T_{3,2}^* &= k(K_{xy}^* - K_{yx}^* + M_{yx}^* - M_{xy}^*) = -k(M_{xy}^* - M_{yx}^*) , \\ T_{4,2}^* &= k(K_{xx}^* + K_{yy}^* - M_{xx}^* - M_{yy}^*) = -k(M_{xx}^* + M_{yy}^* - aI_r) , \\ T_{1,3}^* &= k(K_{xx}^* + K_{yy}^* - M_{xx}^* - M_{yy}^*) = -k(M_{xx}^* + M_{yy}^* - aI_r) , \\ T_{2,3}^* &= k(K_{yx}^* - K_{xy}^* + M_{xy}^* - M_{yx}^*) = k(M_{xy}^* - M_{yx}^*) , \\ T_{3,3}^* &= k^2(M_{xx}^* + M_{yy}^* - aI_r) , \\ T_{4,3}^* &= k^2(M_{yx}^* - M_{xy}^*) , \\ T_{1,4}^* &= k(K_{xy}^* - K_{yx}^* + M_{yx}^* - M_{xy}^*) = -k(M_{xy}^* - M_{yx}^*) , \\ T_{2,4}^* &= k(K_{xx}^* + K_{yy}^* - M_{xx}^* - M_{yy}^*) = -k(M_{xx}^* + M_{yy}^* - aI_r) , \\ T_{3,4}^* &= k^2(M_{xy}^* - M_{yx}^*) , \\ T_{4,4}^* &= k^2(M_{xx}^* + M_{yy}^* - aI_r) . \end{aligned} \tag{D.52}$$

Second all the derivatives evaluated for the case when $\varphi^H \psi = 0$ are combined, (D.10), (D.13), (D.18), (D.21), (D.27), (D.30), (D.33), (D.36) ,(D.41), (D.44), (D.47) and (D.50) with the respective derivatives evaluated for the same case from (C.29), (C.32), (C.37), (C.40). To simplify the notation define the following matrices

$$\begin{aligned} N_{xx}^* &= \Re(\psi_*)\Re(\varphi_*)^T, \quad P_{xx}^* = \Re(\varphi_*)\Re(\varphi_*)^T , \\ N_{yy}^* &= \Im(\psi_*)\Im(\varphi_*)^T, \quad P_{yy}^* = \Im(\varphi_*)\Im(\varphi_*)^T , \\ N_{xy}^* &= \Re(\psi_*)\Im(\varphi_*)^T, \quad P_{xy}^* = \Re(\varphi_*)\Im(\varphi_*)^T , \\ N_{yx}^* &= \Im(\psi_*)\Re(\varphi_*)^T, \quad P_{yx}^* = \Im(\varphi_*)\Re(\varphi_*)^T . \end{aligned}$$

The Hessian (6.10), when two mode shapes are orthogonal, writes as

$$\mathrm{H}_{\varphi_*,\psi_*}^{g_{mac},\text{orthogonal}} = \frac{2}{d_* e_*} \begin{bmatrix} U_{1,1}^* & U_{1,2}^* \\ (U_{1,2}^*)^T & U_{2,2}^* \end{bmatrix} , \tag{D.53}$$

where

$$U^*_{1,1} = \begin{bmatrix} M^*_{xx} + M^*_{yy} & M^*_{xy} - M^*_{yx} \\ M^*_{yx} - M^*_{xy} & M^*_{xx} + M^*_{yy} \end{bmatrix} , \tag{D.54}$$

$$U^*_{1,2} = \begin{bmatrix} N^*_{xx} - N^*_{yy} & N^*_{xy} + N^*_{yx} \\ N^*_{yx} + N^*_{xy} & N^*_{yy} - N^*_{xx} \end{bmatrix} ,$$

$$U^*_{2,2} = \begin{bmatrix} P^*_{xx} + P^*_{yy} & P^*_{xy} - P^*_{yx} \\ P^*_{yx} - P^*_{xy} & P^*_{xx} + P^*_{yy} \end{bmatrix} .$$

D.2 Proof of Lemma 6.3

First recall the expression for $\mathrm{H}^{g_{mac},\mathrm{collinear}}_{\varphi_*,\psi_*}$ from (D.51)

$$\mathrm{H}^{g_{mac},\mathrm{collinear}}_{\varphi_*,\psi_*} = \frac{2}{k^2 d_*} \underbrace{\begin{bmatrix} 1 & -k \\ -k & k^2 \end{bmatrix}}_{=M_a} \otimes \underbrace{\begin{bmatrix} T^*_{1,1} & T^*_{1,2} \\ T^*_{2,1} & T^*_{2,2} \end{bmatrix}}_{=K_x} . \tag{D.55}$$

In order to show that $\mathrm{H}^{g_{mac},\mathrm{collinear}}_{\varphi_*,\psi_*}$ is negative semidefinite it is proved that respective M_a and K_x are positive and negative semidefinite matrices. Let λ_1, λ_2 be the eigenvalues of M_a and $\mu_1 \dots \mu_{2r}$ the eigenvalues of K_x. The eigenvalues of the Kronecker product $M_a \otimes K_x$ can be written as a product of the eigenvalues of corresponding matrices $\lambda_i \cdot \mu_j$ where $i = \{1, 2\}$ and $j = 1 \dots 2r$. First, start with computing λ which satisfies

$$(\lambda - 1)(\lambda - k^2) - k^2 = \lambda^2 + k^2 - \lambda - k^2\lambda - k^2 = \lambda(\lambda - 1 - k^2) = 0 . \tag{D.56}$$

Thus, $\lambda_1 = 0$ and $\lambda_2 = k^2 + 1 > 0$. Second, K_x writes as

$$\begin{aligned} K_x &= \begin{bmatrix} T^*_{1,1} & T^*_{1,2} \\ T^*_{2,1} & T^*_{2,2} \end{bmatrix} - aI_{2r} \qquad (D.57) \\ &= \begin{bmatrix} \Re(\psi_*) & -\Im(\psi_*) \\ \Im(\psi_*) & \Re(\psi_*) \end{bmatrix} \begin{bmatrix} \Re(\psi_*) & -\Im(\psi_*) \\ \Im(\psi_*) & \Re(\psi_*) \end{bmatrix}^T - aI_{2r} \\ &= \frac{1}{\sqrt{a}} \underbrace{\begin{bmatrix} \Re(\psi_*) & -\Im(\psi_*) \\ \Im(\psi_*) & \Re(\psi_*) \end{bmatrix}}_{=L} \underbrace{\begin{bmatrix} a & 0 \\ 0 & a \end{bmatrix}}_{=M_b} \begin{bmatrix} \Re(\psi_*) & -\Im(\psi_*) \\ \Im(\psi_*) & \Re(\psi_*) \end{bmatrix}^T \frac{1}{\sqrt{a}} - aI_{2r} , \end{aligned}$$

where

$$\tilde{L} = \frac{1}{\sqrt{a}} L = \frac{1}{\sqrt{a}} \begin{bmatrix} \Re(\psi_*) & -\Im(\psi_*) \\ \Im(\psi_*) & \Re(\psi_*) \end{bmatrix} = \begin{bmatrix} L_1 & L_2 \end{bmatrix} . \tag{D.58}$$

Notice that the square root of the scalar product $\sqrt{a} = \sqrt{\Re(\psi_*)^T \Re(\psi_*) + \Im(\psi_*)^T \Im(\psi_*)}$ is equivalent to the norm of each column of matrix L, and vectors L_1 and L_2 are of norm 1 and orthogonal. Furthermore there exists $2r - 2$ linearly independent vectors $q_1, \dots, q_{2r-2} \in \mathbb{R}^r$, such that matrix

$\begin{bmatrix} L_1 & L_2 & q_1 & \dots & q_{2r-2} \end{bmatrix}$ is an orthonormal basis in $\mathbb{R}^{2r}$, satisfying $q_i^T L_1 = 0$ and $q_i^T L_2 = 0$ for $i = 1 \dots 2r-2$, $q_i^T q_j = 0$, $i \neq j$ and $q_i^T q_i = 1$. Now, (D.57) writes as

$$K_x = \begin{bmatrix} L_1 & L_2 & q_1 & \dots & q_{2r-2} \end{bmatrix} \begin{bmatrix} a & & & & \\ & a & & & \\ & & 0 & & \\ & & & \ddots & \\ & & & & 0 \end{bmatrix} \begin{bmatrix} L_1^T \\ L_2^T \\ q_1^T \\ \vdots \\ q_{2r-2}^T \end{bmatrix} - aI_{2r} \quad \text{(D.59)}$$

$$= \begin{bmatrix} L_1 & L_2 & q_1 & \dots & q_{2r-2} \end{bmatrix} \begin{bmatrix} 0 & & & & \\ & 0 & & & \\ & & -a & & \\ & & & \ddots & \\ & & & & -a \end{bmatrix} \begin{bmatrix} L_1^T \\ L_2^T \\ q_1^T \\ \vdots \\ q_{2r-2}^T \end{bmatrix} ,$$

which is by definition the eigenvalue decomposition of K_x. Since K_x has non positive eigenvalues, based on the expression above, it is negative semidefinite matrix of $\text{rank}(K_x) = 2r-2$. That, with the fact that the fraction $2/k^2 d_* > 0$, concludes this proof.

D.3 Proof of Lemma 6.5

First recall the expression for $\text{H}_{\varphi_*,\psi_*}^{g_{mac},\text{orthogonal}}$ from (D.53)

$$\text{H}_{\varphi_*,\psi_*}^{g_{mac},\text{orthogonal}} = \frac{2}{d_* e_*} \begin{bmatrix} U_{1,1}^* & U_{1,2}^* \\ (U_{1,2}^*)^T & U_{2,2}^* \end{bmatrix} .$$

To simplify the notation in the proof let $A = U_{1,1}^*$, $B = U_{1,2}^*$ and $C = U_{2,2}^*$. The $\text{H}_{\varphi_*,\psi_*}^{g_{mac},\text{orthogonal}}$ (D.53) is positive semi-definite iff

$$\begin{aligned} &C \geq 0 \ , \\ &(I - CC^\dagger)B^T = 0 \ , \\ &\text{H}_{\varphi_*,\psi_*}^{g_{mac},\text{orthogonal}} / C = A - B^T C^\dagger B \geq 0 \ , \end{aligned}$$

where $\text{H}_{\varphi_*,\psi_*}^{g_{mac},\text{orthogonal}} / C$ denotes the Schur complement of block C on matrix $\text{H}_{\varphi_*,\psi_*}^{g_{mac},\text{orthogonal}}$.
The first condition $C \geq 0$, follows from the lines of the proof in Appendix D.2. It

writes

$$C = \begin{bmatrix} \Re(\varphi_*)\Re(\varphi_*)^T + \Im(\varphi_*)\Im(\varphi_*)^T & \Re(\varphi_*)\Im(\varphi_*)^T - \Im(\varphi_*)\Re(\varphi_*)^T \\ -\Re(\varphi_*)\Im(\varphi_*)^T + \Im(\varphi_*)\Re(\varphi_*)^T & \Re(\varphi_*)\Re(\varphi_*)^T + \Im(\varphi_*)\Im(\varphi_*)^T \end{bmatrix} \tag{D.60}$$

$$= \begin{bmatrix} \Re(\varphi_*) & -\Im(\varphi_*) \\ \Im(\varphi_*) & \Re(\varphi_*) \end{bmatrix} \begin{bmatrix} \Re(\varphi_*) & -\Im(\varphi_*) \\ \Im(\varphi_*) & \Re(\varphi_*) \end{bmatrix}^T$$

$$= \frac{1}{\sqrt{a}} \underbrace{\begin{bmatrix} \Re(\varphi_*) & -\Im(\varphi_*) \\ \Im(\varphi_*) & \Re(\varphi_*) \end{bmatrix}}_{=L} \underbrace{\begin{bmatrix} a & 0 \\ 0 & a \end{bmatrix}}_{=M_b} \begin{bmatrix} \Re(\varphi_*) & -\Im(\varphi_*) \\ \Im(\varphi_*) & \Re(\varphi_*) \end{bmatrix}^T \frac{1}{\sqrt{a}} ,$$

where

$$\tilde{L} = \frac{1}{\sqrt{a}} L = \frac{1}{\sqrt{a}} \begin{bmatrix} \Re(\varphi_*) & -\Im(\varphi_*) \\ \Im(\varphi_*) & \Re(\varphi_*) \end{bmatrix} = \begin{bmatrix} L_1 & L_2 \end{bmatrix} . \tag{D.61}$$

Notice that the square root of the scalar product $\sqrt{a} = \sqrt{\Re(\varphi_*)^T\Re(\varphi_*) + \Im(\varphi_*)^T\Im(\varphi_*)}$ is equivalent to the norm of each column of matrix L, and vectors L_1 and L_2 are of norm 1 and orthogonal. Furthermore there exists $2r-2$ linearly independent vectors $q_1, \ldots, q_{2r-2} \in \mathbb{R}^r$, such that matrix $\begin{bmatrix} L_1 & L_2 & q_1 & \ldots & q_{2r-2} \end{bmatrix}$ is an orthonormal basis in $\mathbb{R}^{2r}$, satisfying $q_i^T L_1 = 0$ and $q_i^T L_2 = 0$ for $i = 1 \ldots 2r-2$, $q_i^T q_j = 0$, $i \neq j$ and $q_i^T q_i = 1$. Now, (D.60) writes as

$$C = \begin{bmatrix} L_1 & L_2 & q_1 & \ldots & q_{2r-2} \end{bmatrix} \begin{bmatrix} a & & & & \\ & a & & & \\ & & 0 & & \\ & & & \ddots & \\ & & & & 0 \end{bmatrix} \begin{bmatrix} L_1^T \\ L_2^T \\ q_1^T \\ \vdots \\ q_{2r-2}^T \end{bmatrix} , \tag{D.62}$$

which is by definition the eigenvalue decomposition of C. Since C has positive eigenvalues, based on the expression above, it is positive semi-definite matrix of $\operatorname{rank}(C) = 2r-2$.

The second and third conditions write as follow. First matrices B and C are factorized such that

$$B = \begin{bmatrix} \Re(\psi_*)\Re(\varphi_*)^T - \Im(\psi_*)\Im(\varphi_*)^T & \Re(\psi_*)\Im(\varphi_*)^T + \Im(\psi_*)\Re(\varphi_*)^T \\ \Re(\psi_*)\Im(\varphi_*)^T + \Im(\psi_*)\Re(\varphi_*)^T & -\Re(\psi_*)\Re(\varphi_*)^T + \Im(\psi_*)\Im(\varphi_*)^T \end{bmatrix}$$

$$= \underbrace{\begin{bmatrix} \Re(\psi_*) & -\Im(\psi_*) \\ \Im(\psi_*) & \Re(\psi_*) \end{bmatrix}}_{B_1} \underbrace{\begin{bmatrix} \Re(\varphi_*) & \Im(\varphi_*) \\ \Im(\varphi_*) & -\Re(\varphi_*) \end{bmatrix}^T}_{=B_2} = B_1 B_2 ,$$

$$C = \begin{bmatrix} \Re(\varphi_*)\Re(\varphi_*)^T + \Im(\varphi_*)\Im(\varphi_*)^T & \Re(\varphi_*)\Im(\varphi_*)^T - \Im(\varphi_*)\Re(\varphi_*)^T \\ -\Re(\varphi_*)\Im(\varphi_*)^T + \Im(\varphi_*)\Re(\varphi_*)^T & \Re(\varphi_*)\Re(\varphi_*)^T + \Im(\varphi_*)\Im(\varphi_*)^T \end{bmatrix}$$

$$= \underbrace{\begin{bmatrix} \Re(\varphi_*) & \Im(\varphi_*) \\ \Im(\varphi_*) & -\Re(\varphi_*) \end{bmatrix}}_{=C_1} \begin{bmatrix} \Re(\varphi_*) & \Im(\varphi_*) \\ \Im(\varphi_*) & -\Re(\varphi_*) \end{bmatrix}^T = C_1 C_1^T .$$

Note that $C_1 = B_2^T$ and that both C_1 and B_2 have orthogonal columns. The second condition writes

$$\begin{aligned}(I - CC^\dagger)B^T &= (I - C_1C_1^T(C_1C_1^T)^\dagger)B_2^T B_1^T = (I - C_1C_1^T(C_1^T)^\dagger C_1^\dagger)B_2^T B_1^T \\ &= B_2^T B_1^T - C_1(C_1^\dagger C_1)^T C_1^\dagger C_1 B_1^T \\ &= B_2^T B_1^T - C_1 B_1^T = B_2^T B_1^T - B_2^T B_1^T = 0 \ .\end{aligned}$$

The Schur complement $\mathrm{H}^{g_{mac},\mathrm{orthogonal}}_{\varphi_*,\psi_*}/C$ yields

$$\begin{aligned}\mathrm{H}^{g_{mac},\mathrm{orthogonal}}_{\varphi_*,\psi_*}/C &= A - B_1B_2(C_1C_1^T)^\dagger B_2^T B_1^T = A - B_1B_2(C_1^T)^\dagger C_1^\dagger B_2^T B_1^T \\ &= A - B_1C_1^T(C_1^T)^\dagger C_1^\dagger C_1 B_1^T = A - B_1(C_1^\dagger C_1)^T C_1^\dagger C_1 B_1^T \\ &= A - B_1B_1^T \ .\end{aligned}$$

Using the fact that $A = B_1B_1^T$, see Appendix D.2, the expression above writes

$$\mathrm{H}^{g_{mac},\mathrm{orthogonal}}_{\varphi_*,\psi_*}/C = A - B_1B_1^T = B_1B_1^T - B_1B_1^T = 0 \ .$$

That together with the fact that the fraction $2/d_*e_* > 0$ concludes that $\mathrm{H}^{g_{mac},\mathrm{orthogonal}}_{\varphi_*,\psi_*}$ is positive semi-definite.
Second, the rank of $\mathrm{H}^{g_{mac},\mathrm{orthogonal}}_{\varphi_*,\psi_*}$ is established. It writes

$$\mathrm{rank}(\mathrm{H}^{g_{mac},\mathrm{orthogonal}}_{\varphi_*,\psi_*}) = \mathrm{rank}(C) + \mathrm{rank}(A - BC^\dagger B^T) \ .$$

Since $A - BC^\dagger B^T = 0$ the $\mathrm{rank}(\mathrm{H}^{g_{mac},\mathrm{orthogonal}}_{\varphi_*,\psi_*}) = \mathrm{rank}(C) = 2r - 2$. That concludes the proof.

APPENDIX E

Hankel matrix normalization for robust damage detection

E.1 Proof of Lemma 7.3

As such, computation of the residual (7.24) depends on $h_{M,N}$ and h_* that are constructed from Hankel matrices estimated under different parameters θ, varying process noise covariance Q and different sample sizes M and N. First assume that $M = N$ hence $\hat{h} = h_{M,N} = h_{N,N} = h_N$. In addition, to simplify the notation drop the subscripts denoting the sample size in the respective estimates of the Hankel matrices. Denote $\Sigma_{h_*} = \begin{bmatrix} \Sigma_{\mathcal{H}_{ref}(\theta_*)} & 0 \\ 0 & \Sigma_{\mathcal{H}_{test}(\theta_*)} \end{bmatrix}$. Then $\hat{\mathcal{H}}_{ref}^{\theta_*}$ and $\hat{\mathcal{H}}_{test}^{\theta}$ in $\hat{h}$ are approximated with joint Gaussian distribution as

$$\begin{aligned} &\text{under } \mathrm{H}_0 : \sqrt{N}\left(\hat{h} - h_*\right) \xrightarrow{\mathcal{L}} \mathcal{N}(0, \Sigma_{h_*}) \ , \\ &\text{under } \mathrm{H}_1 : \sqrt{N}\left(\hat{h} - h_*\right) \xrightarrow{\mathcal{L}} \mathcal{N}(\mathcal{J}_{\theta_*}^{h}\delta, \Sigma_{h_*}) \ , \end{aligned} \tag{E.1}$$

where $\mathcal{J}_{\theta_*}^{h} = \frac{\partial h}{\partial \theta}$. The first order Taylor expansion of $g_{dd}(\hat{h})$ writes

$$\sqrt{N}\left(g_{dd}(\hat{h}) - g_{dd}(h_*)\right) = \mathcal{J}_{h_*}^{g_{dd}}\sqrt{N}(\hat{h} - h_*) + \sqrt{N}o(\left\|\hat{h} - h_*\right\|^2) \ . \tag{E.2}$$

Since $\sqrt{N}(\hat{h} - h_*)$ is Gaussian, it holds $\sqrt{N}\left\|\hat{h} - h_*\right\|^2 = O(1/\sqrt{N}) \xrightarrow{a.s.} 0$. Thus $g_{dd}(h_*) = 0$, after using the (7.16) property. The proof of convergence under both H_0 and H_1 follows the properties of the local approach in [146], which yields to equation (7.21), where implicitly under H_1, $\lim_{N\to\infty}\left(\hat{\mathcal{H}}_{test}^{\theta}\right) = \mathcal{H}_{test}(\theta_*)$. Consequently, $g_{dd}(h_*)$ writes as

$$g_{dd}(h_*) = \mathrm{vec}\left(\mathcal{H}_{test}(\theta_*)\mathcal{Z}_{test}^{\dagger}\mathcal{Z}_{ref} - \mathcal{H}_{ref}(\theta_*)\mathrm{vec}\right) = 0 \ , \tag{E.3}$$

and $\sqrt{N}\left(g_{dd}(\hat{h}) - g_{dd}(h_*)\right) = \sqrt{N} g_{dd}(\hat{h}) = \hat{\zeta}^{\theta}$. The asymptotic properties of the residual yield

$$\begin{aligned} &\text{under } \mathrm{H}_0 : \hat{\zeta}^{\theta_*} \xrightarrow{\mathcal{L}} \mathcal{N}(0, \Sigma_\zeta) \ , \\ &\text{under } \mathrm{H}_1 : \hat{\zeta}^{\theta} \xrightarrow{\mathcal{L}} \mathcal{N}(\mathcal{J}^{\zeta}_{\theta_*}\delta, \Sigma_\zeta) \ , \end{aligned} \tag{E.4}$$

where $\Sigma_\zeta = \mathcal{J}^{g_{dd}}_{h_*} \begin{bmatrix} \Sigma_{\mathcal{H}_{ref}(\theta_*)} & 0 \\ 0 & \Sigma_{\mathcal{H}_{test}(\theta_*)} \end{bmatrix} (\mathcal{J}^{g_{dd}}_{h_*})^T$ and $\mathcal{J}^{\zeta}_{\theta_*} = \mathcal{J}^{g_{dd}}_{h_*}\mathcal{J}^{h}_{\theta_*}$. This concludes the first part of the proof.
Second part considers the case when the matrices $\hat{\mathcal{H}}^{\theta_*}_{ref}$ and $\hat{\mathcal{H}}^{\theta}_{test}$ are computed on data sets of different lengths M and N. Assume that $M > N$. Recall $\hat{h} = h_{M,N} = \mathrm{vec}\begin{bmatrix} \hat{\mathcal{H}}^{\theta_*}_{ref,M} \\ \hat{\mathcal{H}}^{\theta}_{test,N} \end{bmatrix}$ and $h(\theta_*) = \mathrm{vec}\begin{bmatrix} \mathcal{H}_{ref}(\theta_*) \\ \mathcal{H}_{test}(\theta_*) \end{bmatrix}$. The proof of the asymptotic normality of the residual $\sqrt{N}\left(g_{dd}(\hat{h}) - g_{dd}(h_*)\right)$ follows the $M = N$ case, however a proper scheme to compute the joint covariance should be addressed. For that, recall definition of $c = \lim_{N,M\to\infty} M/N$ which normalize the residual covariance such that $\mathrm{cov}\left(\sqrt{N}\mathrm{vec}(\hat{\mathcal{H}}^{\theta_*}_{ref,M})\right) = \mathrm{cov}\left(\sqrt{\frac{N}{M}}(\sqrt{M}\mathrm{vec}(\hat{\mathcal{H}}^{\theta_*}_{ref,M}))\right) \approx c^{-1}\Sigma_{\mathcal{H}_{ref}(\theta_*)}$. Subsequently, the asymptotic distribution of the residual follows

$$\text{under } \mathrm{H}_0 : \hat{\zeta}^{\theta_*} \xrightarrow{\mathcal{L}} \mathcal{N}(0, \Sigma_\zeta) \ , \tag{E.5}$$

$$\text{under } \mathrm{H}_1 : \hat{\zeta}^{\theta} \xrightarrow{\mathcal{L}} \mathcal{N}(\mathcal{J}^{\zeta}_{\theta_*}\delta, \Sigma_\zeta) \ , \tag{E.6}$$

where $\Sigma_\zeta = \mathcal{J}^{g_{dd}}_{h_*}\Sigma_{c,h_*}(\mathcal{J}^{g_{dd}}_{h_*})^T$. The covariance Σ_{c,h_*} writes

$$\Sigma_{c,h_*} = \begin{bmatrix} c^{-1}\Sigma_{\mathcal{H}_{ref}(\theta_*)} & 0 \\ 0 & \Sigma_{\mathcal{H}_{test}(\theta_*)} \end{bmatrix} \ .$$

This concludes the proof.

E.2 Proof of Lemma 7.6

perturbation of the residual (7.18) writes as

$$\begin{aligned} \Delta\hat{\zeta}^{\theta} &= \sqrt{N}\Delta\left(\mathrm{vec}\left(\hat{\mathcal{H}}^{\theta}_{test}\hat{\mathcal{Z}}^{\dagger}_{test}\hat{\mathcal{Z}}_{ref} - \hat{\mathcal{H}}^{\theta_*}_{ref}\right)\right) \\ &= \sqrt{N}\Delta\left(\mathrm{vec}\left(\hat{\mathcal{H}}^{\theta}_{test}\hat{\mathcal{Z}}^{\dagger}_{test}\hat{\mathcal{Z}}_{ref}\right)\right) - \sqrt{N}\mathrm{vec}\left(\Delta\hat{\mathcal{H}}^{\theta_*}_{ref}\right) \ . \end{aligned} \tag{E.7}$$

Now, a consistent estimates of the sensitivities $\mathcal{J}_{\mathcal{H}_{ref}(\theta_*)}$ and $\mathcal{J}_{\mathcal{H}_{test}(\theta)}$ will be factored from (E.7). Development of the first segment of (E.7) writes as follows

$$\begin{aligned}\operatorname{vec}\left(\Delta\left(\hat{\mathcal{H}}^{\theta}_{test}\hat{\mathcal{Z}}^{\dagger}_{test}\hat{\mathcal{Z}}_{ref}\right)\right) &= \operatorname{vec}\left(\Delta\hat{\mathcal{H}}^{\theta}_{test}\hat{\mathcal{Z}}^{\dagger}_{test}\hat{\mathcal{Z}}_{ref}\right) \\ &+ \operatorname{vec}\left(\hat{\mathcal{H}}^{\theta}_{test}\Delta\hat{\mathcal{Z}}^{\dagger}_{test}\hat{\mathcal{Z}}_{ref}\right) \\ &+ \operatorname{vec}\left(\hat{\mathcal{H}}^{\theta}_{test}\hat{\mathcal{Z}}^{\dagger}_{test}\Delta\hat{\mathcal{Z}}_{ref}\right) \\ &= \left((\hat{\mathcal{Z}}^{\dagger}_{test}\hat{\mathcal{Z}}_{ref})^{T}\otimes I_{(p+1)r}\right)\operatorname{vec}\left(\Delta\hat{\mathcal{H}}^{\theta}_{test}\right) \\ &+ \left(\hat{\mathcal{Z}}^{T}_{ref}\otimes\hat{\mathcal{H}}^{\theta}_{test}\right)\operatorname{vec}\left(\Delta\hat{\mathcal{Z}}^{\dagger}_{test}\right) \\ &+ \left(I_{(p+1)r}\otimes\hat{\mathcal{H}}^{\theta}_{test}\hat{\mathcal{Z}}^{\dagger}_{test}\right)\operatorname{vec}\left(\Delta\hat{\mathcal{Z}}_{ref}\right)\ .\end{aligned} \tag{E.8}$$

The perturbation of $\operatorname{vec}\left(\hat{\mathcal{Z}}^{\dagger}_{test}\right)$ can be expressed as

$$\Delta\hat{\mathcal{Z}}^{\dagger}_{test} = \mathcal{J}_{\hat{\mathcal{Z}}^{\dagger}_{test},\hat{\mathcal{Z}}_{test}}\operatorname{vec}\left(\Delta\hat{\mathcal{Z}}_{test}\right)$$

where $\mathcal{J}_{\hat{\mathcal{Z}}^{\dagger}_{test},\hat{\mathcal{Z}}_{test}}$ after [147], yields

$$\begin{aligned}\mathcal{J}_{\hat{\mathcal{Z}}^{\dagger}_{test},\hat{\mathcal{Z}}_{test}} &= \left((\hat{\mathcal{Z}}^{\dagger}_{test})^{T}\otimes -\hat{\mathcal{Z}}^{\dagger}_{test}\right) \\ &+ \left(((\hat{\mathcal{Z}}^{\dagger}_{test})^{T}\hat{\mathcal{Z}}^{\dagger}_{test})^{T}\otimes(I_{qr}-\hat{\mathcal{Z}}^{\dagger}_{test}\hat{\mathcal{Z}}_{test})\right)P_{n,qr_0}\ .\end{aligned} \tag{E.9}$$

Note that $\hat{\mathcal{Z}}_{test}$ is expected to be full row rank, namely $\hat{\mathcal{Z}}_{test}\hat{\mathcal{Z}}^{\dagger}_{test} = I_n$ and $P_{n,qr_0}\in\mathbb{R}^{nqr_0\times nqr_0}$ is a permutation matrix such that $P_{n,qr_0}\operatorname{vec}(\Delta\hat{\mathcal{Z}}_{test}) = \operatorname{vec}(\Delta\hat{\mathcal{Z}}_{test})^{T}$. Computation of normalization matrices $\hat{\mathcal{Z}}_{ref}$ and $\hat{\mathcal{Z}}_{test}$ is linked to $\hat{\mathcal{Z}} = \begin{bmatrix}\hat{\mathcal{Z}}_{ref} & \hat{\mathcal{Z}}_{test}\end{bmatrix}$, and consequently to $\hat{\mathcal{H}} = \begin{bmatrix}\hat{\mathcal{H}}^{\theta_*}_{ref} & \hat{\mathcal{H}}^{\theta}_{test}\end{bmatrix}$, via respective selection matrices $S_{\mathcal{Z}_{ref},\mathcal{Z}}$ and $S_{\mathcal{Z}_{test},\mathcal{Z}}$ such that

$$\hat{\mathcal{Z}}_{ref} = S_{\mathcal{Z}_{ref},\mathcal{Z}}\hat{\mathcal{Z}} = S_{\mathcal{Z}_{ref},\mathcal{Z}}\hat{D}_s\hat{V}_s^{T}\ , \tag{E.10}$$

$$\hat{\mathcal{Z}}_{test} = S_{\mathcal{Z}_{test},\mathcal{Z}}\hat{\mathcal{Z}} = S_{\mathcal{Z}_{test},\mathcal{Z}}\hat{D}_s\hat{V}_s^{T}\ , \tag{E.11}$$

where $S_{\mathcal{Z}_{ref},\mathcal{Z}} = \begin{bmatrix}I_m & 0_m\end{bmatrix}$, $S_{\mathcal{Z}_{test},\mathcal{Z}} = \begin{bmatrix}0_m & I_m\end{bmatrix}$ and $m = (p+1)rqr_0$. Thus, the perturbation of respective $\hat{\mathcal{Z}}_{ref}$ and $\hat{\mathcal{Z}}_{test}$ yields

$$\begin{aligned}\operatorname{vec}(\Delta\hat{\mathcal{Z}}_{ref}) &= \operatorname{vec}\left(\Delta(S_{\hat{\mathcal{Z}}_{ref},\hat{\mathcal{Z}}}\hat{D}_s\hat{V}_s^{T})\right) = S_{\hat{\mathcal{Z}}_{ref},\hat{\mathcal{Z}}}\operatorname{vec}\left(\Delta(\hat{D}_s\hat{V}_s^{T})\right) \\ &= S_{\hat{\mathcal{Z}}_{ref},\hat{\mathcal{Z}}}\left(\left(\hat{V}_s\otimes I_n\right)\operatorname{vec}(\Delta\hat{D}_s) + \operatorname{vec}(\hat{D}_s\Delta\hat{V}_s^{T})\right)\ ,\end{aligned} \tag{E.12}$$

$$\begin{aligned}\operatorname{vec}(\Delta\hat{\mathcal{Z}}_{test}) &= \operatorname{vec}\left(\Delta(S_{\hat{\mathcal{Z}}_{test},\hat{\mathcal{Z}}}\hat{D}_s\hat{V}_s^{T})\right) = S_{\hat{\mathcal{Z}}_{test},\hat{\mathcal{Z}}}\operatorname{vec}\left(\Delta(\hat{D}_s\hat{V}_s^{T})\right) \\ &= S_{\hat{\mathcal{Z}}_{test},\hat{\mathcal{Z}}}\left(\left(\hat{V}_s\otimes I_n\right)\operatorname{vec}(\Delta\hat{D}_s) + \operatorname{vec}(\hat{D}_s\Delta\hat{V}_s^{T})\right)\ .\end{aligned} \tag{E.13}$$

The sensitivity of $\operatorname{vec}(\Delta\hat{D}_s\hat{V}_s^{T})$ is derived from $\operatorname{vec}(\Delta\hat{V}_s)$ based on [148] and writes as follows

$$\begin{aligned}&\operatorname{vec}(\Delta\hat{V}_s) = \operatorname{vec}(\hat{V}_s\hat{R} + \hat{V}_{ker}\hat{V}_{ker}^{T}\Delta(\hat{\mathcal{H}}^{T})\hat{U}_s\hat{D}_s^{-1})\ , \\ &\operatorname{vec}(\hat{D}_s\Delta\hat{V}_s^{T}) = \operatorname{vec}(-\hat{D}_s\hat{R}\hat{V}_s^{T} + \hat{U}_s^{T}\Delta(\hat{\mathcal{H}})\hat{V}_{ker}\hat{V}_{ker}^{T})\ ,\end{aligned} \tag{E.14}$$

where $\hat{R} \in \mathbb{R}^{n \times n}$ is canceled out in the future computations and $\hat{R}^T = -\hat{R}$ [148]. To keep the notation compact the sensitivity of $\hat{\zeta}$ can be segmented such that

$$\Delta\hat{\zeta}^{\theta} = \sqrt{N}\left(\hat{K}_1 + \hat{K}_2 + \hat{P}_1 + \hat{T}_1 + \hat{T}_2\right) , \tag{E.15}$$

where the respective terms combine (E.8)-(E.14) and yield

$$\hat{K}_1 = (-(\hat{\mathcal{Z}}_{test}^{\dagger}\hat{\mathcal{Z}}_{ref})^T \otimes \hat{\mathcal{H}}_{test}^{\theta}\hat{\mathcal{Z}}_{test}^{\dagger})S_{\mathcal{Z}_{test},\mathcal{Z}}\left(\hat{V}_s \otimes I_n\right)\mathrm{vec}(\Delta\hat{D}_s) , \tag{E.16}$$

$$\hat{K}_2 = \left(\left(-(\hat{\mathcal{Z}}_{test}^{\dagger}\hat{\mathcal{Z}}_{ref})^T \otimes \hat{\mathcal{H}}_{test}^{\theta}\hat{\mathcal{Z}}_{test}^{\dagger}\right)S_{\mathcal{Z}_{test},\mathcal{Z}}\mathrm{vec}(\hat{D}_s\Delta\hat{V}_s^T)\right) , \tag{E.17}$$

$$\begin{aligned}\hat{P}_1 &= ((\hat{\mathcal{Z}}_{test}^{\dagger}\hat{\mathcal{Z}}_{ref})^T\hat{\mathcal{Z}}_{test}^{\dagger} \otimes \hat{\mathcal{H}}_{test}^{\theta}(I_{qr_0} - \hat{\mathcal{Z}}_{test}^{\dagger}\hat{\mathcal{Z}}_{test}))P_{n,qr_0}\Delta\hat{\mathcal{Z}}_{test} \\ &= \mathcal{J}_{\hat{P}_1}\Delta\hat{\mathcal{Z}}_{test} ,\end{aligned} \tag{E.18}$$

$$\begin{aligned}\hat{T}_1 &= \left(I_{(p+1)r} \otimes \hat{\mathcal{H}}_{test}^{\theta}\hat{\mathcal{Z}}_{test}^{\dagger}\right)S_{\mathcal{Z}_{ref},\mathcal{Z}}\left(\hat{V}_s \otimes I_n\right)\mathrm{vec}(\Delta\hat{D}_s) \\ &+ \left(I_{(p+1)r} \otimes \hat{\mathcal{H}}_{test}^{\theta}\hat{\mathcal{Z}}_{test}^{\dagger}\right)S_{\mathcal{Z}_{ref},\mathcal{Z}}\left(\hat{V}_s \otimes I_n\right)\mathrm{vec}(-\hat{D}_s\hat{R}) \\ &+ \left(\left(I_{(p+1)r} \otimes \hat{\mathcal{H}}_{test}^{\theta}\hat{\mathcal{Z}}_{test}^{\dagger}\right)S_{\mathcal{Z}_{ref},\mathcal{Z}}\left(\hat{V}_{ker}\hat{V}_{ker}^T \otimes \hat{U}_s^T\right)\mathrm{vec}(\Delta\hat{\mathcal{H}})\right) ,\end{aligned} \tag{E.19}$$

$$\hat{T}_2 = \left((\hat{\mathcal{Z}}_{test}^{\dagger}\hat{\mathcal{Z}}_{ref})^T \otimes I_{(p+1)r}\right)\mathrm{vec}\left(\Delta\hat{\mathcal{H}}_{test}^{\theta}\right) - \mathrm{vec}\left(\Delta\hat{\mathcal{H}}_{ref}^{\theta_*}\right) . \tag{E.20}$$

First, $\hat{K}_1$ (E.16) is developed, namely

$$\begin{aligned}\hat{K}_1 &= (-(\hat{\mathcal{Z}}_{test}^{\dagger}\hat{\mathcal{Z}}_{ref})^T \otimes \hat{\mathcal{H}}_{test}^{\theta}\hat{\mathcal{Z}}_{test}^{\dagger})\begin{bmatrix}0_m & I_m\end{bmatrix}(\hat{V}_s \otimes I_n)\mathrm{vec}(\Delta\hat{D}_s) \\ &= \begin{bmatrix}0 & -(\hat{\mathcal{Z}}_{test}^{\dagger}\hat{\mathcal{Z}}_{ref})^T \otimes \hat{\mathcal{H}}_{test}^{\theta}\hat{\mathcal{Z}}_{test}^{\dagger}\end{bmatrix}\left(\begin{bmatrix}\hat{V}_{s,ref} \\ \hat{V}_{s,test}\end{bmatrix} \otimes I_n\right)\mathrm{vec}(\Delta\hat{D}_s) \\ &= \left(\left(-(\hat{\mathcal{Z}}_{test}^{\dagger}\hat{\mathcal{Z}}_{ref})^T\hat{V}_{s,test}\right) \otimes \hat{\mathcal{H}}_{test}^{\theta}\hat{\mathcal{Z}}_{test}^{\dagger}\right)\mathrm{vec}(\Delta\hat{D}_s) \\ &= \left(\left(-\hat{\mathcal{Z}}_{ref}^T\hat{D}_s^{-1}\hat{V}_{s,test}^{\dagger}\hat{V}_{s,test}\right) \otimes \hat{\mathcal{H}}_{test}^{\theta}\hat{\mathcal{Z}}_{test}^{\dagger}\right)\mathrm{vec}(\Delta\hat{D}_s) \\ &= \left(-\hat{V}_{s,ref} \otimes \hat{\mathcal{H}}_{test}^{\theta}\hat{\mathcal{Z}}_{test}^{\dagger}\right)\mathrm{vec}(\Delta\hat{D}_s) .\end{aligned} \tag{E.21}$$

Second, plugging (E.14) to $\hat{K}_2$ yields

$$\begin{aligned}
\hat{K}_2 &= -(\hat{\mathcal{Z}}_{test}^{\dagger}\hat{\mathcal{Z}}_{ref})^T \otimes \hat{\mathcal{H}}_{test}^{\theta}\hat{\mathcal{Z}}_{test}^{\dagger} \begin{bmatrix} 0_m & I_m \end{bmatrix} \hat{V}_s \otimes I_n \mathrm{vec}(-\hat{D}_s\hat{R}) \\
&+ \left(-(\hat{\mathcal{Z}}_{test}^{\dagger}\hat{\mathcal{Z}}_{ref})^T \otimes \hat{\mathcal{H}}_{test}^{\theta}\hat{\mathcal{Z}}_{test}^{\dagger}\right) \begin{bmatrix} 0_m & I_m \end{bmatrix} \left(\hat{V}_{ker}\hat{V}_{ker}^T \otimes \hat{U}_s^T\right) \mathrm{vec}\Delta\hat{\mathcal{H}} \\
&= \begin{bmatrix} 0 & -(\hat{\mathcal{Z}}_{test}^{\dagger}\hat{\mathcal{Z}}_{ref})^T \otimes \hat{\mathcal{H}}_{test}^{\theta}\hat{\mathcal{Z}}_{test}^{\dagger} \end{bmatrix} \left(\begin{bmatrix} \hat{V}_{s,ref} \\ \hat{V}_{s,test} \end{bmatrix} \otimes I_n \right) \mathrm{vec}(-\hat{D}_s\hat{R}) \\
&+ \begin{bmatrix} 0 & -(\hat{\mathcal{Z}}_{test}^{\dagger}\hat{\mathcal{Z}}_{ref})^T \otimes \hat{\mathcal{H}}_{test}^{\theta}\hat{\mathcal{Z}}_{test}^{\dagger} \end{bmatrix} \begin{bmatrix} \hat{V}_{ker,ref}\hat{V}_{ker}^T \otimes \hat{U}_s^T \\ \hat{V}_{ker,test}\hat{V}_{ker}^T \otimes \hat{U}_s^T \end{bmatrix} \mathrm{vec}(\Delta\hat{\mathcal{H}}) \\
&= \left(\hat{V}_{s,ref} \otimes \hat{\mathcal{H}}_{test}^{\theta}\hat{\mathcal{Z}}_{test}^{\dagger}\right) \mathrm{vec}(\hat{D}_s\hat{R}) \\
&- \left((\hat{\mathcal{Z}}_{test}^{\dagger}\hat{\mathcal{Z}}_{ref})^T\hat{V}_{ker,test}\hat{V}_{ker}^T \otimes \hat{\mathcal{H}}_{test}^{\theta}\hat{\mathcal{Z}}_{test}^{\dagger}\hat{U}_s^T\right) \mathrm{vec}\Delta\hat{\mathcal{H}} \\
&= \left(\hat{V}_{s,ref} \otimes \hat{\mathcal{H}}_{test}^{\theta}\hat{\mathcal{Z}}_{test}^{\dagger}\right) \mathrm{vec}(\hat{D}_s\hat{R}) \\
&- \left(\hat{V}_{s,ref}\hat{V}_{s,test}^{\dagger}\hat{V}_{ker,test}\hat{V}_{ker,ref}^T \otimes \hat{\mathcal{H}}_{test}^{\theta}\hat{\mathcal{Z}}_{test}^{\dagger}\hat{U}_s^T\right) \mathrm{vec}(\Delta\hat{\mathcal{H}}_{ref}^{\theta_*}) \\
&- \left(\hat{V}_{s,ref}\hat{V}_{s,test}^{\dagger}\hat{V}_{ker,test}\hat{V}_{ker,test}^T \otimes \hat{\mathcal{H}}_{test}^{\theta}\hat{\mathcal{Z}}_{test}^{\dagger}\hat{U}_s^T\right) \mathrm{vec}(\Delta\hat{\mathcal{H}}_{test}^{\theta}) \ .
\end{aligned} \tag{E.22}$$

Next, $\hat{T}_1$ boils down to

$$\begin{aligned}
\hat{T}_1 &= \left(\hat{V}_{s,ref} \otimes \hat{\mathcal{H}}_{test}^{\theta}\hat{\mathcal{Z}}_{test}^{\dagger}\right) \mathrm{vec}(\Delta\hat{D}_s) \\
&- \left(\hat{V}_{s,ref} \otimes \hat{\mathcal{H}}_{test}^{\theta}\hat{\mathcal{Z}}_{test}^{\dagger}\right) \mathrm{vec}(\hat{D}_s\hat{R}) \\
&+ \left(\hat{V}_{ker,ref}\hat{V}_{ker,ref}^T \otimes \hat{\mathcal{H}}_{test}^{\theta}\hat{\mathcal{Z}}_{test}^{\dagger}\hat{U}_s^T\right) \mathrm{vec}(\Delta\hat{\mathcal{H}}_{ref}^{\theta_*}) \\
&+ \left(\hat{V}_{ker,ref}\hat{V}_{ker,test}^T \otimes \hat{\mathcal{H}}_{test}^{\theta}\hat{\mathcal{Z}}_{test}^{\dagger}\hat{U}_s^T\right) \mathrm{vec}(\Delta\hat{\mathcal{H}}_{test}^{\theta}) \ .
\end{aligned} \tag{E.23}$$

After grouping the terms (E.20)-(E.23), the estimate of the residual (E.15) yields

$$\begin{aligned}
\Delta\hat{\zeta}^{\theta}/\sqrt{N} &= \left(\hat{V}_{ker,ref}\hat{V}_{ker,ref}^T \otimes \hat{\mathcal{H}}_{test}^{\theta}\hat{\mathcal{Z}}_{test}^{\dagger}\hat{U}_s^T\right) \mathrm{vec}(\Delta\hat{\mathcal{H}}_{ref}^{\theta_*}) \\
&+ \left(\hat{V}_{ker,ref}\hat{V}_{ker,test}^T \otimes \hat{\mathcal{H}}_{test}^{\theta}\hat{\mathcal{Z}}_{test}^{\dagger}\hat{U}_s^T\right) \mathrm{vec}(\Delta\hat{\mathcal{H}}_{test}^{\theta}) \\
&+ \left(\hat{V}_{s,ref}\hat{V}_{s,test}^{\dagger}\hat{V}_{ker,test}\hat{V}_{ker,test}^T \otimes \hat{\mathcal{H}}_{test}^{\theta}\hat{\mathcal{Z}}_{test}^{\dagger}\hat{U}_s^T\right) \mathrm{vec}(\Delta\hat{\mathcal{H}}_{ref}^{\theta_*}) \\
&- \left(\hat{V}_{s,ref}\hat{V}_{s,test}^{\dagger}\hat{V}_{ker,test}\hat{V}_{ker,test}^T \otimes \hat{\mathcal{H}}_{test}^{\theta}\hat{\mathcal{Z}}_{test}^{\dagger}\hat{U}_s^T\right) \mathrm{vec}(\Delta\hat{\mathcal{H}}_{test}^{\theta}) \\
&+ \mathcal{J}_{\hat{P}_1}\Delta\hat{\mathcal{Z}}_{test} + \left((\hat{\mathcal{Z}}_{test}^{\dagger}\hat{\mathcal{Z}}_{ref})^T \otimes I_{(p+1)r}\right) \mathrm{vec}\left(\Delta\hat{\mathcal{H}}_{test}^{\theta}\right) - \mathrm{vec}\left(\Delta\hat{\mathcal{H}}_{ref}^{\theta_*}\right) \ .
\end{aligned} \tag{E.24}$$

Consistent estimate of the residual sensitivity is not trivial to factor due to complex formulation of $\mathcal{J}_{\hat{P}_1}\Delta\hat{\mathcal{Z}}_{test}$. However, asymptotic sensitivity of residual is straightforward to derive due to some favorable properties of converged matrices e.g. $\mathcal{H}_{test}(\theta_*)\mathcal{Z}_{test}^{\dagger} = U_s$. Letting the matrices in (E.24) converge to their limits makes the term $\mathcal{J}_{\hat{P}_1} \to \mathcal{J}_{P_1}$ cancels out since

$$\mathcal{J}_{P_1} = \left((\mathcal{Z}_{test}^{\dagger}\mathcal{Z}_{ref})^T\mathcal{Z}_{test}^{\dagger} \otimes \mathcal{H}_{test}(\theta_*)(I_{qr_0} - \mathcal{Z}_{test}^{\dagger}\mathcal{Z}_{test})\right) P_{n,qr_0} \tag{E.25}$$

$$= \left((\mathcal{Z}_{test}^{\dagger}\mathcal{Z}_{ref})^T\mathcal{Z}_{test}^{\dagger} \otimes (\mathcal{H}_{test}(\theta_*) - \mathcal{H}_{test}(\theta_*))\right) P_{n,qr_0} \ , \tag{E.26}$$

since $\left(\mathcal{Z}_{test}^{\dagger}\mathcal{Z}_{ref}\right)^{T}\mathcal{Z}_{test}^{\dagger}$ is bounded, and $\sqrt{N}\Delta\hat{\mathcal{Z}}_{test}$ can be proved to be asymptotically Gaussian due to the Delta method, thus bounded in moments. Then $\mathcal{J}_{\hat{P}_1} \to \mathcal{J}_{P_1} = 0$. Furthermore, since $\operatorname{rank}(\begin{bmatrix}\mathcal{H}_{ref}(\theta_*) & \mathcal{H}_{test}(\theta_*)\end{bmatrix}) = n$ the following property of singular vectors can be deployed, namely

$$\begin{bmatrix}V_{s,ref}\\V_{s,test}\end{bmatrix}\begin{bmatrix}V_{s,ref}^T & V_{s,test}^T\end{bmatrix} + \begin{bmatrix}V_{ker,ref}\\V_{ker,test}\end{bmatrix}\begin{bmatrix}V_{ker,ref}^T & V_{ker,test}^T\end{bmatrix} = I_{2n} \ . \tag{E.27}$$

Consequently, the left parts of the first four terms of (E.24) are simplified. That writes as

$$\begin{aligned}
&\left(V_{ker,ref}V_{ker,ref}^T + \hat{V}_{s,ref}\hat{V}_{s,test}^{\dagger}\hat{V}_{ker,test}\hat{V}_{ker,test}^T\right)\otimes\mathcal{H}_{test}(\theta_*)\mathcal{Z}_{test}^{\dagger}U_s^T\\
&= \left(V_{ker,ref}V_{ker,ref}^T + V_{s,ref}V_{s,ref}^T\right)\otimes\mathcal{H}_{test}(\theta_*)\mathcal{Z}_{test}^{\dagger}U_s^T\\
&= \left(V_{ker,ref}V_{ker,ref}^T + I_{(p+1)r} - V_{ker,ref}V_{ker,ref}^T\right)\otimes\mathcal{H}_{test}(\theta_*)\mathcal{Z}_{test}^{\dagger}U_s^T\\
&= I_n\otimes\mathcal{H}_{test}(\theta_*)\mathcal{Z}_{test}^{\dagger}U_s^T
\end{aligned}$$

and

$$\begin{aligned}
&\left(V_{ker,ref}V_{ker,test}^T - V_{s,ref}V_{s,test}^{\dagger}V_{ker,test}V_{ker,test}^T\right)\otimes\mathcal{H}_{test}(\theta_*)\mathcal{Z}_{test}^{\dagger}U_s^T\\
&= \left(V_{ker,ref}V_{ker,test}^T - V_{s,ref}V_{s,test}^{\dagger} + V_{s,ref}V_{s,test}^T\right)\otimes\mathcal{H}_{test}(\theta_*)\mathcal{Z}_{test}^{\dagger}U_s^T\\
&= \left(-V_{s,ref}V_{s,test}^{\dagger}\right)\otimes\mathcal{H}_{test}(\theta_*)\mathcal{Z}_{test}^{\dagger}U_s^T \ .
\end{aligned}$$

The perturbation in the residual yields

$$\begin{aligned}
\Delta\hat{\zeta}^{\theta}/\sqrt{N} \approx &\left(I_{(p+1)r}\otimes U_sU_s^T\right)\operatorname{vec}(\Delta\hat{\mathcal{H}}_{ref}^{\theta_*}) - \operatorname{vec}\left(\Delta\hat{\mathcal{H}}_{ref}^{\theta_*}\right)\\
&- \left(\left(\mathcal{Z}_{test}^{\dagger}\mathcal{Z}_{ref}\right)^T\otimes U_sU_s^T\right)\operatorname{vec}(\Delta\hat{\mathcal{H}}_{test}^{\theta})\\
&+ \left(\left(\mathcal{Z}_{test}^{\dagger}\mathcal{Z}_{ref}\right)^T\otimes I_{(p+1)r}\right)\operatorname{vec}\left(\Delta\hat{\mathcal{H}}_{test}^{\theta}\right) \ .
\end{aligned} \tag{E.28}$$

After grouping the terms the expression above is simplified to

$$\Delta\hat{\zeta}^{\theta} \approx \sqrt{N}\begin{bmatrix}\mathcal{J}_{\mathcal{H}_{ref}(\theta_*)} & \mathcal{J}_{\mathcal{H}_{test}(\theta_*)}\end{bmatrix}\begin{bmatrix}\operatorname{vec}(\Delta\hat{\mathcal{H}}_{ref}^{\theta_*})\\\operatorname{vec}(\Delta\hat{\mathcal{H}}_{test}^{\theta})\end{bmatrix} \ , \tag{E.29}$$

where

$$\mathcal{J}_{\mathcal{H}_{ref}(\theta_*)} = I_{(p+1)r}\otimes U_sU_s^T - I_{qr_0}\otimes I_{(p+1)r} \ , \tag{E.30}$$

$$\begin{aligned}
\mathcal{J}_{\mathcal{H}_{test}(\theta_*)} &= \left(\mathcal{Z}_{test}^{\dagger}\mathcal{Z}_{ref}\right)^T\otimes I_{(p+1)r} - \left(\mathcal{Z}_{test}^{\dagger}\mathcal{Z}_{ref}\right)^T\otimes U_sU_s^T\\
&= \left(\mathcal{Z}_{test}^{\dagger}\mathcal{Z}_{ref}\right)^T\otimes U_{ker}U_{ker}^T \ .
\end{aligned} \tag{E.31}$$

E.3 Proof of Lemma 7.7

The following proof outlines the derivation of the parametric residual function

$$\zeta(\theta', \theta'') = \underbrace{\text{vec}\left(\mathcal{H}_{test}(\theta'')\mathcal{Z}_{test}^{\dagger}(\theta', \theta'')\mathcal{Z}_{ref}(\theta', \theta'')\right)}_{=A} - \underbrace{\text{vec}\left(\mathcal{H}_{ref}(\theta')\right)}_{=B} \ .$$

with respect to the parameter θ'' evaluated on $\theta'' = \theta' = \theta_*$. The partial derivative of $\zeta(\theta', \theta'')$ writes as

$$\mathcal{J}_{\theta_*}^{\zeta} = \frac{\partial \zeta}{\partial \theta''} = \frac{\partial A}{\partial \theta''} + \underbrace{\frac{\partial B}{\partial \theta''}}_{=0} = \frac{\partial A}{\partial \mathcal{H}_{test}(\theta'')} \mathcal{J}_{\theta_*}^{\mathcal{H}_{test}} \ ,$$

where $\mathcal{J}_{\theta_*}^{\mathcal{H}_{test}} = \text{vec}(\partial \mathcal{H}_{test}/\partial \theta'' \ (\theta_*))$. The derivative of both terms of the SVD of the Hankel matrices are continuous in θ'', see Lemma E.1 in Appendix E.4. Therefore, following the same lines as in Appendix E.2, it yields to an expression similar to (E.31) namely

$$\mathcal{J}_{\theta_*}^{\zeta} = (\mathcal{Z}_{test}^{\dagger}(\theta_*, \theta_*)\mathcal{Z}_{ref}(\theta_*, \theta_*))^T \otimes U_{ker}(\theta_*, \theta_*) U_{ker}^T(\theta_*, \theta_*) \mathcal{J}_{\theta_*}^{\mathcal{H}_{test}} \ .$$

To ease the notation drop θ_* from $U_{ker}(\theta_*, \theta_*)$ and $\mathcal{Z}_{ref/test}(\theta_*, \theta_*)$. The expression for $\mathcal{J}_{\theta_*}$ writes as

$$\begin{aligned} \mathcal{J}_{\theta_*}^{\zeta} &= \left((\mathcal{Z}_{test}^{\dagger}\mathcal{Z}_{ref})^T \otimes U_{ker}U_{ker}^T\right) \mathcal{J}_{\theta_*}^{\mathcal{H}_{test}} \\ &= \left((\mathcal{Z}_{test}^{\dagger}\mathcal{Z}_{ref})^T \otimes U_{ker}U_{ker}^T\right) \mathcal{J}_{\theta_*}^{\mathcal{H}_{test}} \ . \end{aligned} \tag{E.32}$$

Now, to reformulate (E.32) consider $\theta = \theta'' = \theta'$. It holds

$$\begin{bmatrix} \mathcal{H}_{ref}(\theta) & \mathcal{H}_{test}(\theta) \end{bmatrix} = U_s(\theta) \begin{bmatrix} \mathcal{Z}_{ref}(\theta) & \mathcal{Z}_{test}(\theta) \end{bmatrix} \ , \tag{E.33}$$

where $\mathcal{Z}_{ref}(\theta) = \mathcal{Z}_{ref}(\theta, \theta)$ for any θ. Same comment applies to $\mathcal{Z}_{test}(\theta) = \mathcal{Z}_{test}(\theta, \theta)$ and $U_s(\theta) = U_s(\theta, \theta)$, hence $\mathcal{H}_{ref}(\theta) = \mathcal{H}_{test}(\theta)\mathcal{Z}_{test}(\theta)^{\dagger}\mathcal{Z}_{ref}(\theta)$ and $\mathcal{H}_{test}(\theta) = \mathcal{H}_{ref}(\theta)\mathcal{Z}_{ref}(\theta)^{\dagger}\mathcal{Z}_{test}(\theta)$. The Jacobian $\mathcal{J}_{\theta_*}^{\zeta}$ (E.32) writes as

$$\begin{aligned} \mathcal{J}_{\theta_*}^{\zeta} &= \left((\mathcal{Z}_{test}^{\dagger}\mathcal{Z}_{ref})^T \otimes U_{ker}U_{ker}^T\right) \text{vec}\left(\frac{\partial \mathcal{H}_{ref}}{\partial \theta} \mathcal{Z}_{ref}^{\dagger}\mathcal{Z}_{test}\right) \\ &\quad + \underbrace{\left((\mathcal{Z}_{test}^{\dagger}\mathcal{Z}_{ref})^T \otimes U_{ker}U_{ker}^T\right) \text{vec}\left(\mathcal{H}_{ref}(\theta_*) \frac{\partial \mathcal{Z}_{ref}^{\dagger}}{\partial \theta} \mathcal{Z}_{test}\right)}_{=0} \\ &\quad + \underbrace{\left((\mathcal{Z}_{test}^{\dagger}\mathcal{Z}_{ref})^T \otimes U_{ker}U_{ker}^T\right) \text{vec}\left(\mathcal{H}_{ref}(\theta_*) \mathcal{Z}_{ref}^{\dagger} \frac{\partial \mathcal{Z}_{test}}{\partial \theta}\right)}_{=0} \\ &= \text{vec}\left(U_{ker}U_{ker}^T \frac{\partial \mathcal{H}_{ref}}{\partial \theta} \mathcal{Z}_{ref}^{\dagger}\mathcal{Z}_{test}\mathcal{Z}_{test}^{\dagger}\mathcal{Z}_{ref}\right) \\ &= \left((\mathcal{Z}_{ref}^{\dagger}\mathcal{Z}_{ref})^T \otimes U_{ker}U_{ker}^T\right) \mathcal{J}_{\theta_*}^{\mathcal{H}_{ref}} \ . \end{aligned} \tag{E.34}$$

E.4 Continuity of the derivatives of the SVD of a matrix

Lemma E.1 *Let $X(\theta)$ be a matrix. Assume θ tends to θ_*, where* $\text{rank}(X(\theta)) = 2n$, *for $\theta \neq \theta_*$ and* $\text{rank}(X(\theta_*)) = n$. *Then the derivative of any singular vector of $X(\theta)$ is continuous around θ_*.*

Proof: The SVD of X writes as

$$X = \begin{bmatrix} U_1 & \tilde{U}_1 & \check{U}_2 \end{bmatrix} \begin{bmatrix} D_1 & 0 & 0 \\ 0 & \tilde{D}_1 & 0 \\ 0 & 0 & D_2 \end{bmatrix} \begin{bmatrix} V_1^T \\ \tilde{V}_1^T \\ \check{V}_2^T \end{bmatrix} ,$$

where U_1 and V_1 denote the first $1 \dots n$ left and right singular vectors. D_1 are the first $1 \dots n$ non-zero singular values. Matrices $\tilde{U}_1$ and $\tilde{V}_1$ denote $n+1 \dots 2n$ left and right singular vectors, and $\tilde{D}_1$ corresponds to $n+1 \dots 2n$ non-zero singular values. Matrices $\check{U}_2$ and $\check{V}_2^T$ are left and right nullspace of X respectively. Let u_f denote f-th left singular vector of $\begin{bmatrix} U_1 & \tilde{U}_1 \end{bmatrix}$ where $f = 1 \dots 2n$. First order perturbation of u_f, developed in [148], writes as

$$\begin{aligned} \Delta u_f = & \begin{bmatrix} U_1 & \tilde{U}_1 \end{bmatrix} \begin{bmatrix} D_f & 0 \\ 0 & \tilde{D}_f \end{bmatrix} \begin{bmatrix} U_1^T \\ \tilde{U}_1^T \end{bmatrix} \Delta X v_f d_f \\ & + \begin{bmatrix} U_1 & \tilde{U}_1 \end{bmatrix} \begin{bmatrix} D_f & 0 \\ 0 & \tilde{D}_f \end{bmatrix} \begin{bmatrix} D_1 & 0 \\ 0 & \tilde{D}_1 \end{bmatrix} \begin{bmatrix} V_1^T \\ \tilde{V}_1^T \end{bmatrix} \Delta X^H u_f + \check{U}_2 \check{U}_2^T \Delta X v_f d_f^{-1} , \end{aligned} \tag{E.35}$$

where $D_f \in \mathbb{C}^{f \times f}$ and for $g = 1 \dots f$ the (f,g)-th element of D_f is $D_f(f,g) = 1/\left(d_f^2 - d_g^2\right)$ and $D_f(f,f) = 0$. Suppose non-zero singular values $d_{n+1} \dots d_{2n}$ converge to zero, $\tilde{D}_1 \to 0$. Then $\tilde{D}_f \to \mathcal{I}_k \sigma_f^2$ and $\tilde{U}_2 = \tilde{U}_1$ are now vectors spanning the left nullspace U_2 of X, such that $U_2 = \begin{bmatrix} \tilde{U}_2 & \check{U}_2 \end{bmatrix}$. Thus, the first order perturbation of u_f (E.35) follows

$$\begin{aligned} \Delta u_f = & \left(U_1 D_f U_1^T + \tilde{U}_2 \mathcal{I}_k \sigma_f^2 \tilde{U}_2^T \right) \Delta X v_f d_f + U_1 D_f D_1 V_1^T \Delta X^H u_f \\ & + \check{U}_2 \check{U}_2^T \Delta X v_f d_f^{-1} \\ = & U_1 D_f U_1^T \Delta X v_f d_f + \tilde{U}_2 \tilde{U}_2^T \Delta X v_f d_f^{-1} + U_1 D_f D_1 V_1^T \Delta X^H u_f \\ & + \check{U}_2 \check{U}_2^T \Delta X v_f d_f^{-1} \\ = & U_1 D_f U_1^T \Delta X v_f d_f + U_1 D_f D_1 V_1^T \Delta X^H u_f + U_2 U_2^T \Delta X v_f d_f^{-1} , \end{aligned} \tag{E.36}$$

which corresponds to the sensitivity of f-th left singular vector of matrix X with $\text{rank}(X) = n$. □

E.5 Proof of Theorem 7.8

Let $\mathcal{H}_{ref}(\theta_*)$ and $\mathcal{H}_{test}(\theta_*)$ be the Hankel matrices of the system computed with the data of the same length under different excitation conditions. Their SVD partitioned at order n yields

$$\begin{bmatrix} \mathcal{H}_{ref}(\theta_*) & \mathcal{H}_{test}(\theta_*) \end{bmatrix} = U_s \begin{bmatrix} \mathcal{Z}_{ref} & \mathcal{Z}_{test} \end{bmatrix} ,$$

where $\mathcal{H}_{ref}(\theta_*) = U_s Z_{ref}$. Since U_s, $\mathcal{Z}_{ref}$ and $\mathcal{Z}_{test}$ are computed from the joint SVD of $\mathcal{H}_{ref}(\theta_*)$ and $\mathcal{H}_{test}(\theta_*)$, they may depend on the excitation properties related to the latter matrices. Let the partitioned SVD of $\mathcal{H}_{ref}(\theta_*)$ be $\mathcal{H}_{ref}(\theta_*) = \tilde{U}_s \tilde{D}_s \tilde{V}_s^T$. Since both U_s and $\tilde{U}_s$ define an orthogonal basis of the column space of $\mathcal{H}_{ref}(\theta_*)$, there exists a matrix T with $U_s = \tilde{U}_s T$. It holds

$$I_n = U_s^T U_s = (\tilde{U}_s T)^T \tilde{U}_s T = T^T T \ ,$$

hence T is orthogonal. Partitioned SVD of $\mathcal{H}_{ref}(\theta_*)$ can be redefined as

$$\mathcal{H}_{ref}(\theta_*) = \tilde{U}_s T \underbrace{T^T \tilde{D}_s \tilde{V}_s^T}_{=\mathcal{Z}_{ref}} \ .$$

Then, $\mathcal{Z}_{ref}^\dagger \mathcal{Z}_{ref}$ simplifies to

$$\mathcal{Z}_{ref}^\dagger \mathcal{Z}_{ref} = \tilde{V}_s \tilde{D}_s^{-1} T T^T \tilde{D}_s \tilde{V}_s^T = \tilde{V}_s \tilde{V}_s^T \ ,$$

which depends only on $\mathcal{H}_{ref}(\theta_*)$ (the reference matrix), but not on potentially different noise properties of the tested matrix $\mathcal{H}_{test}(\theta_*)$.

E.6 Practical implementation of parametric χ^2 test

First the computation of Σ_ζ (7.30) is reformulated. For that define $\mathcal{B} \in \mathbb{R}^{s_1 \times s_2}$ and $\mathcal{K} \in \mathbb{R}^{s_2 \times n_{b,t}}$ such that

$$\mathcal{B} = \mathcal{I}_{(p+1)r} \otimes U_{ker}$$

and

$$\mathcal{K} = \left[-\mathcal{B}^T \Sigma_{\mathcal{H}_{ref}(\theta_*)} \quad \left((\mathcal{Z}_{test}^\dagger \mathcal{Z}_{ref})^T \otimes \mathcal{I}_{(p+1)r-n} \right) \mathcal{B}^T \Sigma_{\mathcal{H}_{test}(\theta_*)} \right] \ ,$$

where $s_2 = ((p+1)r)((p+1)r-n)$ and $n_{b,t} = n_{b,1} + n_{b,2}$. Note that $\mathcal{B}$ is a matrix with orthogonal columns, $\mathcal{B}^T \mathcal{B} = \mathcal{I}_{s_2}$. The expression for the covariance of the residual follows $\Sigma_\zeta = \mathcal{B}\mathcal{K}(\mathcal{B}\mathcal{K})^T$ and its inverse can be written as $\Sigma_\zeta^{-1} = \mathcal{B}\mathcal{K}^{\dagger T} \mathcal{K}^\dagger \mathcal{B}^T$. Second, matrix $\mathcal{B}$ is factored from Jacobian (7.33) such that

$$\begin{aligned} \mathcal{J}_{\theta_*}^\zeta &= \left((\mathcal{Z}_{ref}^\dagger \mathcal{Z}_{ref})^T \otimes U_{ker} U_{ker}^T \right) \operatorname{vec} \left(\frac{\partial \mathcal{H}_{ref}}{\partial \theta} \right) \\ &= \mathcal{B} \left((\mathcal{Z}_{ref}^\dagger \mathcal{Z}_{ref})^T \otimes U_{ker}^T \right) \operatorname{vec} \left(\frac{\partial \mathcal{H}_{ref}}{\partial \theta} \right) = \mathcal{B} \mathcal{J}_s \ . \end{aligned}$$

Now, from the definition of χ^2 test (7.28) it holds

$$\begin{aligned} t_{\text{global}} &= (\hat{\zeta}^\theta)^T \Sigma_\zeta^{-1} \mathcal{J}_{\theta_*} \left(\mathcal{J}_{\theta_*}^T \Sigma_\zeta^{-1} \mathcal{J}_{\theta_*} \right)^\dagger \mathcal{J}_{\theta_*}^T \Sigma_\zeta^{-1} \hat{\zeta}^\theta \\ &= (\hat{\zeta}^\theta)^T \mathcal{B}\mathcal{K}^{\dagger T} \mathcal{K}^\dagger \mathcal{B}^T \mathcal{B} \mathcal{J}_s \left((\mathcal{B}\mathcal{J}_s)^T \mathcal{B}\mathcal{K}^{\dagger T} \mathcal{K}^\dagger \mathcal{B}^T \mathcal{B} \mathcal{J}_s \right) (\mathcal{B}\mathcal{J}_s)^T \mathcal{B}\mathcal{K}^{\dagger T} \mathcal{K}^\dagger \mathcal{B}^T \hat{\zeta}^\theta \\ &= (\hat{\zeta}^\theta)^T \mathcal{B}\mathcal{K}^{\dagger T} \mathcal{K}^\dagger \mathcal{J}_s \left(\mathcal{J}_s^T \mathcal{K}^{\dagger T} \mathcal{K}^\dagger \mathcal{J}_s \right) \mathcal{J}_s^T \mathcal{K}^{\dagger T} \mathcal{K}^\dagger \mathcal{B}^T \hat{\zeta}^\theta \ . \end{aligned}$$

Using thin QR decomposition of $\mathcal{K}^{\dagger}\mathcal{J}_s = \mathcal{Q}\mathcal{R}$, after [142] and [129], the test boils down to

$$\begin{aligned} t_{\text{global}} &= (\hat{\zeta}^{\theta})^T \mathcal{B}{\mathcal{K}^{\dagger}}^T \mathcal{Q}\mathcal{R} \left((\mathcal{Q}\mathcal{R})^T \mathcal{Q}\mathcal{R} \right)^{\dagger} (\mathcal{Q}\mathcal{R})^T \mathcal{K}^{\dagger} \mathcal{B}^T \hat{\zeta}^{\theta} \\ &= (\hat{\zeta}^{\theta})^T \mathcal{B}{\mathcal{K}^{\dagger}}^T \mathcal{Q}\mathcal{R} \left(\mathcal{R}^{\dagger} \mathcal{Q}^T \mathcal{Q} {\mathcal{R}^T}^{\dagger} \right) \mathcal{R}^T \mathcal{Q}^T \mathcal{K}^{\dagger} \mathcal{B}^T \hat{\zeta}^{\theta} \\ &= (\hat{\zeta}^{\theta})^T \mathcal{B}{\mathcal{K}^{\dagger}}^T \mathcal{Q}\mathcal{Q}^T \mathcal{K}^{\dagger} \mathcal{B}^T \hat{\zeta}^{\theta} \ . \end{aligned}$$

In a more compact form it can be written as

$$t_{\text{global}} = a^T a \ , \tag{E.37}$$

where $a = \mathcal{Q}^T \mathcal{K}^{\dagger} \mathcal{B}^T \hat{\zeta}^{\theta}$.

Resume in Danish

Vibrationsbaseret strukturel overvågning er en tværfaglig disciplin indeholdt i fagområdet omhandlende Structural Health Monitoring (SHM). Disciplinen referer til implementeringen af en strategi der overvåger integriteten af en struktur baseret på målinger af vibrationer i strukturen under drift. Den praktiske implementering består af flere sammenkoblede opgaver, såsom design af overvågningssystemet, hvilket inkluderer sensorer arrangeret i en specifik opsætning, samt valg eller design af passende signalbehandlingsmetoder til analyse af målingerne. Sådanne overvågningssystemer er anvendt på forskellige tekniske strukturer, f.eks. vindmøller, offshore-strukturer (Figur 1), broer, højhushuse, gearkasser, rotorer og motorer.

Den nylige vækst indenfor området er drevet af en efterspørgsel fra industrien, samt den teknologiske udvikling i det krævede hardware og software til lagring og analysering af målinger. Industriens motivation hidrører ikke alene fra drift- og vedligeholdelsesbesparelser, eksempelvis ved inspektionsplanlægning baseret på målinger, men også fra ønsket om at reducere risiko for fatale svigt ved hjælp af tidlig fejldetektering samt forbedringer af designrutiner ved inkorporering af målinger i virtuelle modeller. Alle disse faktorer leder hen mod en reduktion af den såkaldte *menneskelige* faktor, der spænder fra ingeniørens analyse af målinger til dykkere og klatres visuelle inspektioner af offshore-strukturer hvilket resulterer i betragtelige omkostninger.

Metoder der analyserer vibrationsmålinger og de faktiske oplysninger om strukturens tilstand er kernen i SHM. I praksis overvåges strukturens integritet under drift, deraf under ukendte samt umålelige omgivende eksciteringer. Disse særlige tilstande medfører udfordringer for førnævnte metoder, som kan resultere i ukorrekte fejlrapporteringer under fejldetektering samt upræcise estimater af modalparametre, hvis de ikke behandles korrekt. I denne afhandling betragtes tre problemstillinger omhandlende disse forhold. Den første problemstilling omhandler undersøgelse og behandling af effekten af periodisk ekscitering på estimeringen af vibrationskarakteristika. Den anden problemstilling omhandler kvantificering af usikkerhed i forbindelse med støjende data i forhold til modalindikatorer. Den tredje problemstilling omhandler redegørelse af ændringer i de naturlige eksciteringstilstande til design af en robust metode til skadedetektering. Indholdet af problemstillingerne er drøftet i det følgende.

En standard antagelse i mange anvendte metoder er stationariteten af ukendte omgivende eksciteringer. Denne antagelser er dog sommertider overskredet, eksempelvis ved periodisk ekscitering stammende fra roterende komponenter under strukturens drift. Sådanne eksterne forstyrrelser har indflydelse på de opsamlede målinger såsom accelerationer, forskydninger, hastigheder og tøjninger, hvilke er strukturelle reaktioner på ukendte eksciteringer. Derfor benyttes disse målinger til at identificere

modalparametre, navnlig egenfrekvenser, dæmpningsforhold samt tilstandsformer som er hovedkarakteristika i en struktur. Disse estimeres i Operational Modal Analysis (OMA) gennem systemidentifikationstekniker hvor egen-strukturen af et lineært system er identificeret fra målingerne. Periodisk ekscitering kan besværliggøre udførelsen af OMA i praksis, da egen-strukturen i så fald indeholder en blanding af strukturelle og periodiske tilstandsformer, hvilke kan være svære at adskille. Derudover, når de strukturelle og periodiske tilstandsformer ligger tæt, kan det blive umuligt korrekt identificerer de strukturelle tilstandsformer med klassiske metoder.

Estimater af modalparametre er upræcis grundet statistiske usikkerheder, da de er regnet fra en begrænset mængde målinger af omgivende vibrationer, som ofte er præget af støj. De er derfor aldrig lig strukturens faktiske fysiske parametre. Disse usikkerheder skal kvantificeres eller kompenseres for, hvilket ofte er afgørende i praksis, når resultaterne fra systemidentifikationsmetoderne fortolkes. Desuden kan sådanne fortolkninger forbedres af såkaldte modalindikatorer. Modalindikatorerne afspejler nogle af de fysiske aspekter af de estimerede tilstandsformer. Disse modalindikatorer, Modal Assurance Criterion (MAC) and Modal Phase Collinearity (MPC), indeholder de statistiske usikkerheder fra de underliggende tilstandsformsestimeringer. Den statistiske struktur i forhold til modalparametre er velkendt og udviklet i sammenhæng med understruktur-baseret systemidentifikationsmetoder, hvorimod usikkerhedskvantificering af modalindikatorer endnu ikke er blevet udviklet. En særlig udfordring i denne analyse, er modalindikatorernes begrænsning til værdier mellem 0 og 1, for hvilke, ved endepunkterne af dette interval, den klassiske gaussiske struktur for usikkerhedskvantificering, som benyttes i OMA, er utilstrækkelig.

Monitorering af strukturelleintegriteten baseret på målinger kan henføres til detektering af ændringer i visse skade-overfølsomme egenskaber udledt af disse målinger. Egenskaberne, ligesom alle andre estimerede parametre, er notorisk påvirket af usikkerheder, hvis der ikke tages hensyn til disse, kan de skjule små ændringer der påføres systemet. Modalparametre er ofte brugt som sådanne egenskaber, da de bliver påvirket af ændringer i stivheden grundet skader. Ydeevnen af modalparametre-baserede metoder afhænger imidlertid af flere faktorer, såsom kvaliteten af målinger vedrørende estimerede parametre, samt evnen til at spore de udvalgte estimeringer efter de er identificeret fra den sunde tilstand af systemet. Derfor er det ønskværdigt at udregne disse egenskaber direkte fra målingerne uden behovet for estimeringen af modalparametre. Dette, sammen med statistiske evalueringer af ovennævnte egenskaber, kan lede til automatiseret skadedetektering. Som tillæg til den statistiske variabilitet, er de målingsbaserede skadesegenskaber notorisk afhængige de naturlige ændringer i de omkringliggende eksciterings betingelser. Dette udgør en stor udfordring i evalueringen af sådanne indikatorer, da eksciterings betingelserne principielt er ukendte og ikke målte, en ændring grundet dette kan derfor ukorrekt blive klarificeret som en skade. En løsning af problemet ligger i designet af et skadesdetekteringsresidual, hvis middelværdi er uafhængig af ændringer i eksciterings betingelser. En sådan robusthed overfor ændringer i eksciteringsegenskaber er en forudsætning for benyttelse af et hver residual i praktisk anvendelse til skadesdetektering,

Bibliography

[1] G. Casella, R. L. Berger, Statistical inference, 2nd Edition, Cengage Learning, 2001.

[2] A. Benveniste, M. Basseville, G. Moustakides, The asymptotic local approach to change detection and model validation, IEEE Transactions on Automatic Control 32 (7) (1987) 583–592.

[3] M. Döhler, L. Mevel, Modular subspace-based system identification from multi-setup measurements, IEEE Transactions on Automatic Control 57 (11) (2012) 2951–2956. doi:10.1109/TAC.2012.2193711.

[4] L. Mevel, A. Benveniste, M. Basseville, M. Goursat, Blind subspace-based eigenstructure identification under nonstationary excitation using moving sensors, IEEE Transactions on Signal Processing 50 (1) (2002) 41–48.

[5] S. Gres, P. Andersen, C. Hoen, L. Damkilde, Orthogonal projection-based harmonic signal removal for operational modal analysis, in: IMAC - XXXVI International Modal Analysis Conference, Orlando, USA, 2018.

[6] S. Gres, P. Andersen, L. Damkilde, Operational modal analysis of rotating machinery, in: IMAC - XXXVI International Modal Analysis Conference, Orlando, USA, 2018.

[7] S. Greś, M. Döhler, P. Andersen, L. Mevel, Kalman filter-based subspace identification for operational modal analysis under unmeasured periodic excitation, Mechanical Systems and Signal Processing 146 (2021) 106996.

[8] S. Gres, M. Döhler, P. Andersen, L. Mevel, Variance computation of MAC and MPC for real-valued mode shapes from the stabilization diagram, in: IOMAC - 8th International Operational Modal Analysis Conference, Copenhagen, Denmark, 2019.

[9] S. Greś, M. Döhler, P. Andersen, L. Mevel, Uncertainty quantification for the modal phase collinearity of complex mode shapes, Mechanical Systems and Signal Processing 152 (2021) 107436.

[10] S. Gres, M. Döhler, P. Andersen, L. Mevel, Variance computation of the Modal Assurance Criterion, in: International Conference on Noise and Vibration Engineering - KU Leuven, Katholieke Universiteit, Leuven, Belgium, 2018, pp. 2939–2950, proceedings of the ISMA2018 and the USD2018.

[11] S. Greś, M. Döhler, L. Mevel, Uncertainty quantification of the modal assurance criterion in operational modal analysis, Mechanical Systems and Signal Processing 152 (2021) 107457.

[12] S. Gres, M. Döhler, P. Andersen, L. Damkilde, L. Mevel, Hankel matrix normalization for robust damage detection, in: IOMAC - 8th International Operational Modal Analysis Conference, Copenhagen, Denmark, 2019.

[13] S. Gres, P. Andersen, R. Johansen, M. Ulriksen, L. Damkilde, A comparison of damage detection methods applied to civil engineering structures, in: Experimental Vibration Analysis for Civil Engineering Structures, Springer, Germany, 2018, pp. 306–316, proceedings of the 7th International Conference on Experimental Vibration Analysis for Civil Engineering Structures.

[14] S. Gres, M. D. Ulriksen, M. Döhler, R. J. Johansen, P. Andersen, L. Damkilde, S. A. Nielsen, Statistical methods for damage detection applied to civil structures, Procedia Engineering 199 (2017) 1919 – 1924, x International Conference on Structural Dynamics, EURODYN 2017.

[15] S. Greś, M. Döhler, L. Mevel, Hankel matrix-based mahalanobis distance for fault detection robust towards changes in process noise covariance, IFAC-PapersOnLine 54 (7) (2021) 73–78, 19th IFAC Symposium on System Identification SYSID 2021.

[16] S. Greś, M. Döhler, P. Andersen, L. Mevel, Subspace-based mahalanobis damage detection robust to changes in excitation covariance, Structural Control and Health Monitoring 28 (8) (2021) e2760.

[17] P. van Overschee, B. de Moor, Subspace Identification for Linear Systems, 1st Edition, Springer, 1996.

[18] P. Guillaume, T. De Troyer, C. Devriendt, G. De Sitter, Omax - operational modal analysis in presence of exogenous inputs, in: P. Sas, M. D. Munck (Eds.), Proceedings of ISMA2006, KU Leuven, Department of Mechanical Engineering, PMA, 2006, pp. 2985–2996.

[19] H. S. Ward, R. Crawford, Wind-induced vibrations and building modes, Bulletin of the Seismological Society of America 56 (4) (1966) 793.

[20] N.-M. To, Ph.D. thesis, British Columbia, Canada (1982).

[21] A. J. Felber, Development of a hybrid bridge evaluation system, Theses, University of British Columbia (December 1993).

[22] A. M. Abdel-Ghaffar, R. H. Scanlan, Ambient vibration studies of golden gate bridge: I. suspended structure, Journal of Engineering Mechanics 111 (4) (1985) 463–482. doi:10.1061/(ASCE)0733-9399(1985)111:4(463).

[23] J. Brownjohn, F. Magalhães, E. Caetano, Á. Cunha, Ambient vibration re-testing and operational modal analysis of the humber bridge, Engineering Structures 32 (8) (2010) 2003 – 2018. doi:https://doi.org/10.1016/j.engstruct.2010.02.034.

[24] F. Magalhães, Á. Cunha, Explaining operational modal analysis with data from an arch bridge, Mechanical Systems and Signal Processing 25 (5) (2011) 1431 – 1450.

[25] S. Rubin, Ambient vibration survey of offshore platform, Journal of the Engineering Mechanics Division 106 (1980) 425–441.

[26] C. Devriendt, F. Magalhães, W. Weijtjens, G. D. Sitter, Á. Cunha, P. Guillaume, Structural health monitoring of offshore wind turbines using automated operational modal analysis, Structural Health Monitoring 13 (6) (2014) 644–659. doi:10.1177/1475921714556568.

[27] T. G. Carne, G. H. James, The inception of oma in the development of modal testing technology for wind turbines, Mechanical Systems and Signal Processing 24 (5) (2010) 1213 – 1226, special Issue: Operational Modal Analysis. doi:https://doi.org/10.1016/j.ymssp.2010.03.006.

[28] G. Jelicic, J. Schwochow, Y. Govers, A. Hebler, M. Böswald, Real-time assessment of flutter stability based on automated output-only modal analysis, in: ISMA 2014, 2014, pp. 3693–3706.

[29] C. R. Pickrel, P. J. White, Flight flutter testing of transport aircraft: In-flight modal analysis, 2003.

[30] L. Mevel, M. Basseville, A. Benveniste, Fast in-flight detection of flutter onset -A statistical approach, Research Report RR-4982, INRIA (2003).

[31] L. F. Ramos, R. Aguilar, P. B. Lourenço, S. Moreira, Dynamic structural health monitoring of saint torcato church, Mechanical Systems and Signal Processing 35 (1) (2013) 1 – 15. doi:https://doi.org/10.1016/j.ymssp.2012.09.007.

[32] L. Ramos, L. Marques, P. Lourenco, G. D. Roeck, A. Campos-Costa, J. Roque, Monitoring historical masonry structures with operational modal analysis: Two case studies, Mechanical Systems and Signal Processing 24 (5) (2010) 1291 – 1305, special Issue: Operational Modal Analysis. doi:https://doi.org/10.1016/j.ymssp.2010.01.011.

[33] P. Mellinger, M. Döhler, L. Mevel, Variance estimation of modal parameters from output-only and input/output subspace-based system identification, Journal of Sound and Vibration 379 (Supplement C) (2016) 1 – 27. doi:https://doi.org/10.1016/j.jsv.2016.05.037.

[34] E. Reynders, D. Degrauwe, G. D. Roeck, F. Magalhães, E. Caetano, Combined experimental-operational modal testing of footbridges, Journal of Engineering Mechanics 136 (6) (2010) 687–696. doi:10.1061/(ASCE)EM.1943-7889.0000119.

[35] C. Shih, Y. Tsuei, R. Allemang, D. Brown, Complex mode indication function and its applications to spatial domain parameter estimation, Mechanical Systems and Signal Processing 2 (4) (1988) 367 – 377. doi:https://doi.org/10.1016/0888-3270(88)90060-X.

[36] R. Brincker, L. Zhang, P. Andersen, Output-only modal analysis by frequency domain decomposition, in: P. Sas, D. Moens (Eds.), Proceedings of ISMA25, Katholieke Universiteit, Leuven, 2000, pp. 717–723.

[37] R. Brincker, C. Ventura, P. Andersen, Damping estimation by frequency domain decomposition, in: Proceedings of IMAC 19, Society for Experimental Mechanics, United States, 2001, pp. 698–703.

[38] R. Brincker, P. Andersen, N.-J. Jacobsen, Automated frequency domain decomposition for operational modal analysis, in: Conference Proceedings, Society for Experimental Mechanics, United States, 2007.

[39] P. Guillaume, P. Verboven, S. Vanlanduit, Frequency domain maximum likelihood identification of modal parameters with confidence intervals, in: Proc. 24th International Seminar on Modal Analysis (ISMA), 1998.

[40] B. Peeters, H. Van der Auweraer, P. Guillaume, J. Leuridan, The polymax frequency-domain method: A new standard for modal parameter estimation?, Shock and Vibration 11 (2004) 395–409. doi:10.1155/2004/523692.

[41] P. Guillaume, P. Verboven, B. Cauberghe, S. Vanlanduit, E. Parloo, G. D. Sitter, Frequency-domain system identification techniques for experimental and operational modal analysis, IFAC Proceedings Volumes 36 (16) (2003) 1609 – 1614, 13th IFAC Symposium on System Identification (SYSID 2003), Rotterdam, The Netherlands, 27-29 August, 2003. doi:https://doi.org/10.1016/S1474-6670(17)34990-X.

[42] D. L. Brown, R. J. Allemang, R. Zimmerman, M. Mergeay, Parameter estimation techniques for modal analysis, SAE Transactions 88 (1979) 828–846.

[43] H. Vold, J. Kundrat, G. T. Rocklin, R. Russell, A multi-input modal estimation algorithm for mini-computers, SAE Transactions 91 (1982) 815–821.

[44] M. Gevers, A personal view of the development of system identification: A 30-year journey through an exciting field, IEEE Control Systems Magazine 26 (6) (2006) 93–105. doi:10.1109/MCS.2006.252834.

[45] T. Söderström, P. Stoica (Eds.), System Identification, Prentice-Hall, Inc., Upper Saddle River, NJ, USA, 1988.

[46] L. Ljung, System Identification (2Nd Ed.): Theory for the User, Prentice Hall PTR, Upper Saddle River, NJ, USA, 1999.

[47] K.-J. Åström, B. Torsten, Numerical identification of linear dynamic systems from normal operating records, IFAC Proceedings Volumes 2 (2) (1965) 96 – 111, 2nd IFAC Symposium on the Theory of Self-Adaptive Control Systems, Teddington, UK, September 14-17, 1965. doi:https://doi.org/10.1016/S1474-6670(17)69024-4.

[48] B. A. Pridham, J. C. Wilson, Identification of base-excited structures using output-only parameter estimation, Earthquake Engineering & Structural Dynamics 33 (1) (2004) 133–155. doi:10.1002/eqe.343.

[49] F. J. Cara, J. Carpio, J. Juan, E. Alarcón, An approach to operational modal analysis using the expectation maximization algorithm, Mechanical Systems and Signal Processing 31 (2012) 109 – 129. doi:https://doi.org/10.1016/j.ymssp.2012.04.004.

[50] T. J. Matarazzo, S. N. Pakzad, Stride for structural identification using expectation maximization: Iterative output-only method for modal identification, Journal of Engineering Mechanics 142 (4) (2016) 04015109. doi:10.1061/(ASCE)EM.1943-7889.0000951.

[51] A. Benveniste, L. Mevel, Nonstationary consistency of subspace methods, IEEE Transactions on Automatic Control 52 (6) (2007) 974–984.

[52] E. Gilbert, Controllability and observability in multivariable control systems, Journal of the Society for Industrial and Applied Mathematics Series A Control 1 (2) (1963) 128–151. doi:10.1137/0301009.

[53] R. Kalman, Mathematical description of linear dynamical systems, Journal of the Society for Industrial and Applied Mathematics Series A Control 1 (2) (1963) 152–192. doi:10.1137/0301010.

[54] B. L. Ho, R. Kalman, Effective construction of linear state-variable models from input/output functions, Regelungstechnik 14 (12) (1966) 545–548.

[55] H. Akaike, Stochastic theory of minimal realization, IEEE Transactions on Automatic Control 19 (6) (1974) 667–674. doi:10.1109/TAC.1974.1100707.

[56] H. Akaike, Markovian representation of stochastic processes by canonical variables, SIAM Journal on Control 13 (1) (1975) 162–173. doi:10.1137/0313010.

[57] S. Y. Kung, A new identification and model reduction algorithm via singular value decomposition, 12th Asilomar Conference on Circuits, Systems, and Computers (1978) 705–714.

[58] A. Benveniste, J. Fuchs, Single sample modal identification of a nonstationary stochastic process, IEEE Transactions on Automatic Control 30 (1) (1985) 66–74. doi:10.1109/TAC.1985.1103787.

[59] J.-N. Juang, R. S. Pappa, An eigensystem realization algorithm for modal parameter identification and model reduction, Journal of Guidance, Control, and Dynamics 8 (1985) 620 – 627. doi:https://doi.org/10.2514/3.20031.

[60] G. James, III, T. Carne, J. Lauffer, The natural excitation technique (NExT) for modal parameter extraction from operating wind turbines, NASA STI/Recon Technical Report N 93.

[61] M. Chang, S. N. Pakzad, Observer kalman filter identification for output-only systems using interactive structural modal identification toolsuite, Journal of Bridge Engineering 19 (5) (2014) 04014002. doi:10.1061/(ASCE)BE.1943-5592.0000530.

[62] P. V. Overschee, B. D. Moor, N4sid: Subspace algorithms for the identification of combined deterministic-stochastic systems, Automatica 30 (1) (1994) 75 – 93, special issue on statistical signal processing and control. doi:https://doi.org/10.1016/0005-1098(94)90230-5.

[63] B. Peeters, G. de Roeck, Reference-based stochastic subspace identification for output-only modal analysis, Mechanical Systems and Signal Processing 13 (6) (1999) 855 – 878.

[64] E. Reynders, G. D. Roeck, Reference-based combined deterministic-stochastic subspace identification for experimental and operational modal analysis, Mechanical Systems and Signal Processing 22 (3) (2008) 617–637. doi:https://doi.org/10.1016/j.ymssp.2007.09.004.

[65] B. Peeters, G. D. Roeck, Reference based stochastic subspace identification in civil engineering, Inverse Problems in Engineering 8 (1) (2000) 47–74. doi:10.1080/174159700088027718.

[66] M. Döhler, L. Mevel, Fast multi-order computation of system matrices in subspace-based system identification, Control Engineering Practice 20 (9) (2012) 882 – 894. doi:https://doi.org/10.1016/j.conengprac.2012.05.005.

[67] E. Reynders, System identification methods for (operational) modal analysis: Review and comparison, Archives of Computational Methods in Engineering 19 (1) (2012) 51–124. doi:10.1007/s11831-012-9069-x.

[68] D. Bauer, M. Deistler, W. Scherrer, Consistency and asymptotic normality of some subspace algorithms for systems without observed inputs, Automatica 35 (7) (1999) 1243 – 1254. doi:https://doi.org/10.1016/S0005-1098(99)00031-X.

[69] M. Deistler, K. Peternell, W. Scherrer, Consistency and relative efficiency of subspace methods, IFAC Proceedings Volumes 27 (8) (1994) 461 – 466, iFAC Symposium on System Identification (SYSID'94), Copenhagen, Denmark, 4-6 July. doi:https://doi.org/10.1016/S1474-6670(17)47751-2.

[70] A. Benveniste, L. Mevel, Nonstationary consistency of subspace methods, IEEE Transactions on Automatic Control 52 (6) (2007) 974–984. doi:10.1109/TAC.2007.898970.

[71] D. Bauer, M. Jansson, Analysis of the asymptotic properties of the moesp type of subspace algorithms, Automatica 36 (4) (2000) 497 – 509. doi:https://doi.org/10.1016/S0005-1098(99)00174-0.

[72] A. Chiuso, G. Picci, The asymptotic variance of subspace estimates, Journal of Econometrics 118 (1) (2004) 257 – 291, contributions to econometrics, time series analysis, and systems identification: a Festschrift in honor of Manfred Deistler. doi:https://doi.org/10.1016/S0304-4076(03)00143-X.

[73] D. Bauer, Asymptotic properties of subspace estimators, Automatica 41 (3) (2005) 359 – 376, data-Based Modelling and System Identification. doi:https://doi.org/10.1016/j.automatica.2004.11.012.

[74] E. Reynders, R. Pintelon, G. D. Roeck, Uncertainty bounds on modal parameters obtained from stochastic subspace identification, Mechanical Systems and Signal Processing 22 (4) (2008) 948 – 969, special Issue: Crack Effects in Rotordynamics.

[75] R. Pintelon, P. Guillaume, J. Schoukens, Uncertainty calculation in (operational) modal analysis, Mechanical Systems and Signal Processing 21 (6) (2007) 2359 – 2373.

[76] M. Döhler, L. Mevel, Efficient multi-order uncertainty computation for stochastic subspace identification, Mechanical Systems and Signal Processing 38 (2) (2013) 346–366. doi:https://doi.org/10.1016/j.ymssp.2013.01.012.

[77] M. Döhler, X.-B. Lam, L. Mevel, Multi-order covariance computation for estimates in stochastic subspace identification using qr decompositions, IFAC Proceedings Volumes 47 (3) (2014) 9498 – 9503, 19th IFAC World Congress. doi:https://doi.org/10.3182/20140824-6-ZA-1003.00883.

[78] M. Döhler, F. Hille, L. Mevel, W. Rücker, Estimation of modal parameters and their uncertainty bounds from subspace-based system identification, in: M. Klocke (Ed.), IRIS Industrial Safety and Life Cycle Engineering - Technologies / Standards / Applications, VCE, 2013, pp. 91–106.

[79] M. Döhler, P. Andersen, L. Mevel, Variance computation of modal parameter estimates from upc subspace identification, in: IOMAC - 7th International Operational Modal Analysis Conference, Ingolstadt, Germany, 2017.

[80] E. Reynders, K. Maes, G. Lombaert, G. D. Roeck, Uncertainty quantification in operational modal analysis with stochastic subspace identification: Validation and applications, Mechanical Systems and Signal Processing 66-67 (2016) 13 – 30. doi:https://doi.org/10.1016/j.ymssp.2015.04.018.

[81] M. Döhler, X.-B. Lam, L. Mevel, Uncertainty quantification for modal parameters from stochastic subspace identification on multi-setup measurements, Mechanical Systems and Signal Processing 36 (2013) 562–581.

[82] Z. Fang, A. Santos, Inference on directionally differentiable functions, The Review of Economic Studies 86 (1) (2019) 377–412. doi:10.1093/restud/rdy049.

[83] K.-H. Yuan, P. M. Bentler, Two simple approximations to the distributions of quadratic forms, British Journal of Mathematical and Statistical Psychology 63 (2) (2010) 273–291. doi:10.1348/000711009X449771.

[84] H. Liu, Y. Tang, H. H. Zhang, A new chi-square approximation to the distribution of non-negative definite quadratic forms in non-central normal variables, Computational Statistics and Data Analysis 53 (4) (2009) 853 – 856. doi:https://doi.org/10.1016/j.csda.2008.11.025.

[85] R. Pappa, K. B. Elliott, A. Schenk, A consistent-mode indicator for the eigensystem realization algorithm., Journal of Guidance Control and Dynamics 16.

[86] M. Imregun, D. Ewins, Complex modes - origins and limits, Soc. Experimental Mechanics Inc, 1995, pp. 496–506.

[87] R. J. Allemang, The modal assurance criterion (MAC): Twenty years of use and abuse, Journal of Sound and Vibration 37.

[88] W. Heylen, T. Janter, Applications of the modal assurance criterion in dynamic model updating, American Society of Mechanical Engineers, Design Engineering Division (Publication) DE 18 (1989) 289–294.

[89] P. Vacher, B. Jacquier, A. Bucharles, Extensions of the mac criterion to complex modes, in: ISMA 2010 International Conference on Noise and Vibration Engineering, 2010.

[90] B. Peeters, B. Cornelis, K. Janssens, H. Van der Auweraer, Removing disturbing harmonics in operational modal analysis, in: Proceedings of the International Operational Modal Analysis Conference, 2007.

[91] F. Combet, L. Gelman, An automated methodology for performing time synchronous averaging of a gearbox signal without speed sensor, Mechanical Systems and Signal Processing 21 (6) (2007) 2590 – 2606.

[92] R. Randall, W. Smith, New cepstral techniques for operational modal analysis, in: Proceedings of the First World Congress on Condition Monitoring, 2017.

[93] R. B. Randall, A history of cepstrum analysis and its application to mechanical problems, Mechanical Systems and Signal Processing 97 (2017) 3 – 19, special Issue on Surveillance.

[94] R. Randall, M. Coats, W. Smith, Repressing the effects of variable speed harmonic orders in operational modal analysis, Mechanical Systems and Signal Processing 79 (Supplement C) (2016) 3 – 15, special Issue from ICEDyn 2015.

[95] R. Randall, J. Antoni, W. Smith, A survey of the application of the cepstrum to structural modal analysis, Mechanical Systems and Signal Processing 118 (2019) 716 – 741. doi:https://doi.org/10.1016/j.ymssp.2018.08.059.

[96] J. Bienert, P. Andersen, R. Aguirre, A harmonic peak reduction technique for operational modal analysis of rotating machinery, in: Proceedings of the International Operational Modal Analysis Conference, 2015.

[97] R. Pintelon, B. Peeters, P. Guillaume, Continuous-time operational modal analysis in the presence of harmonic disturbances-the multivariate case, Mechanical Systems and Signal Processing 24 (1) (2010) 90 – 105.

[98] C. Devriendt, P. Guillaume, The use of transmissibility measurements in output-only modal analysis, Mechanical Systems and Signal Processing 21 (7) (2007) 2689 – 2696. doi:https://doi.org/10.1016/j.ymssp.2007.02.008.

[99] W. Weijtjens, G. D. Sitter, C. Devriendt, P. Guillaume, Operational modal parameter estimation of mimo systems using transmissibility functions, Automatica 50 (2) (2014) 559 – 564. doi:https://doi.org/10.1016/j.automatica.2013.11.021.

[100] C. Devriendt, G. D. Sitter, S. Vanlanduit, P. Guillaume, Operational modal analysis in the presence of harmonic excitations by the use of transmissibility measurements, Mechanical Systems and Signal Processing 23 (3) (2009) 621 – 635. doi:https://doi.org/10.1016/j.ymssp.2008.07.009.

[101] A. Maamar, M. Abdelghani, T.-P. Le, V. Gagnol, L. Sabourin, Operational modal identification in the presence of harmonic excitation, Applied Acousticsdoi:https://doi.org/10.1016/j.apacoust.2018.02.017.

[102] M. Favaro, G. Picci, Consistency of subspace methods for signals with almost-periodic components, Automatica 48 (3) (2012) 514 – 520. doi:https://doi.org/10.1016/j.automatica.2011.08.059.

[103] M. Favaro, G. Picci, A subspace algorithm for extracting periodic components from multivariable signals in colored noise, IFAC Proceedings Volumes 45 (16) (2012) 1161 – 1166, 16th IFAC Symposium on System Identification. doi:https://doi.org/10.3182/20120711-3-BE-2027.00187.

[104] N.-J. Jacobsen, P. Andersen, R. Brincker, Using enhanced frequency domain decomposition as a robust technique to harmonic excitation in operational modal analysis, in: Proceedings of the International Operational Modal Analysis Conference (IOMAC 2007), Vol. 4, 2007.

[105] P. Andersen, R. Brincker, C. Ventura, R. Cantieni, Estimating modal parameters of civil engineering structures subject to ambient and harmonic excitation, in: EVACES - 7th International Conference of Experimental Vibration Analysis for Civil Engineering Structures, Porto, Portugal, 2007.

[106] A. Agneni, G. Coppotelli, C. Grappasonni, A method for the harmonic removal in operational modal analysis of rotating blades, Mechanical Systems and Signal Processing 27 (2012) 604 – 618. doi:https://doi.org/10.1016/j.ymssp.2011.09.013.

[107] N.-J. Jacobsen, P. Andersen, R. Brincker, Eliminating the influence of harmonic components in operational modal analysis, in: Conference Proceedings, Society for Experimental Mechanics, United States, 2007.

[108] C. R. Farrar, K. Worden, An introduction to structural health monitoring, Philosophical Transactions of the Royal Society A: Mathematical, Physical and Engineering Sciences 365 (1851) (2007) 303–315. doi:10.1098/rsta.2006.1928.

[109] A. Rytter, Vibrational based inspection of civil engineering structures, Ph.D. thesis, Aalborg University, Denmark, ph.D.-Thesis defended publicly at the University of Aalborg, April 20, 1993 PDF for print: 206 pp. (1993).

[110] M. Döhler, L. Mevel, Q. Zhang, Fault Detection, Isolation and Quantification from Gaussian Residuals with Application to Structural Damage Diagnosis, Annual Reviews in Control 42 (2016) 244–256. doi:10.1016/j.arcontrol.2016.08.002.

[111] M. Friswell, J. Mottershead, Finite Element Model Updating in Structural Dynamics, Vol. 38, 1995. doi:10.1007/978-94-015-8508-8.

[112] I. Hwang, S. Kim, Y. Kim, C. E. Seah, A survey of fault detection, isolation, and reconfiguration methods, IEEE Transactions on Control Systems Technology 18 (3) (2010) 636–653. doi:10.1109/TCST.2009.2026285.

[113] S. W. Doebling, C. R. Farrar, M. B. Prime, A summary review of vibration-based damage identification methods, Identification Methods, The Shock and Vibration Digest 30 (1998) 91–105.

[114] N. A. J. Lieven, D. J. Ewins, C. R. Farrar, S. W. Doebling, D. A. Nix, Vibration-based structural damage identification, Philosophical Transactions of the Royal Society of London. Series A: Mathematical, Physical and Engineering Sciences 359 (1778) (2001) 131–149. doi:10.1098/rsta.2000.0717.

[115] E. P. Carden, P. Fanning, Vibration based condition monitoring: A review, Structural Health Monitoring 3 (4) (2004) 355–377. doi:10.1177/1475921704047500.

[116] N. Maia, J. Silva, E. Almas, R. Sampaio, Damage detection in structures: From mode shape to frequency response function methods, Mechanical Systems and Signal Processing 17 (3) (2003) 489 – 498. doi:https://doi.org/10.1006/mssp.2002.1506.

[117] O. Salawu, Detection of structural damage through changes in frequency: a review, Engineering Structures 19 (9) (1997) 718 – 723. doi:https://doi.org/10.1016/S0141-0296(96)00149-6.

[118] J. Kullaa, Damage detection of the z24 bridge using control charts, Mechanical Systems and Signal Processing 17 (1) (2003) 163 – 170. doi:https://doi.org/10.1006/mssp.2002.1555.

[119] K. Worden, G. Manson, N. Fieller, Damage detection using outlier analysis, Journal of Sound and Vibration 229 (3) (2000) 647 – 667. doi:https://doi.org/10.1006/jsvi.1999.2514.

[120] N. Dervilis, I. Antoniadou, R. Barthorpe, E. Cross, K. Worden, Robust methods for outlier detection and regression for shm applications., International Journal of Sustainable Materials and Structural Systems 2 (1/2).

[121] M. Ulriksen, D. Tcherniak, L. Damkilde, Damage detection in an operating vestas v27 wind turbine blade by use of outlier analysis, in: IEEE Workshop on Environmental, Energy and Structural Monitoring Systems, IEEE Press, 2015. doi:10.1109/EESMS.2015.7175851.

[122] E. J. Cross, K. Worden, Q. Chen, Cointegration: a novel approach for the removal of environmental trends in structural health monitoring data, Proceedings of the Royal Society A: Mathematical, Physical and Engineering Sciences 467 (2133) (2011) 2712–2732. doi:10.1098/rspa.2011.0023.

[123] H. Shi, K. Worden, E. J. Cross, A cointegration approach for heteroscedastic data based on a time series decomposition: An application to structural health monitoring, Mechanical Systems and Signal Processing 120 (2019) 16 – 31. doi:https://doi.org/10.1016/j.ymssp.2018.09.036.

[124] D. Bernal, Kalman filter damage detection in the presence of changing process and measurement noise, Mechanical Systems and Signal Processing 39 (1) (2013) 361 – 371. doi:https://doi.org/10.1016/j.ymssp.2013.02.012.

[125] E. Reynders, G. Wursten, G. D. Roeck, Output-only structural health monitoring in changing environmental conditions by means of nonlinear system identification, Structural Health Monitoring 13 (1) (2014) 82–93. doi:10.1177/1475921713502836.

[126] E. Balmés, M. Basseville, L. Mevel, H. Nasser, F. Bourquin, F. Treysséde, Merging sensor data from multiple temperature scenarios for vibration monitoring of civil structures, Research Report PI 1824 (2006).

[127] N. Dervilis, K. Worden, E. Cross, On robust regression analysis as a means of exploring environmental and operational conditions for shm data, Journal of Sound and Vibration 347 (2015) 279 – 296. doi:https://doi.org/10.1016/j.jsv.2015.02.039.

[128] M. Basseville, M. Abdelghani, A. Benveniste, Subspace-based fault detection algorithms for vibration monitoring, Automatica 36 (1) (2000) 101 – 109.

[129] M. Döhler, L. Mevel, F. Hille, Subspace-based damage detection under changes in the ambient excitation statistics, Mechanical Systems and Signal Processing 45 (1) (2014) 207 – 224. doi:https://doi.org/10.1016/j.ymssp.2013.10.023.

[130] A.-M. Yan, J.-C. Golinval, Null subspace-based damage detection of structures using vibration measurements, Mechanical Systems and Signal Processing 20 (3) (2006) 611 – 626. doi:https://doi.org/10.1016/j.ymssp.2005.04.010.

[131] M. Döhler, F. Hille, L. Mevel, W. Rücker, Structural health monitoring with statistical methods during progressive damage test of s101 bridge, Engineering Structures 69 (2014) 183 – 193.

[132] S. Allahdadian, C. Ventura, P. Andersen, L. Mevel, M. Döhler, Investigation on the sensitivity of subspace based damage detection technique to damage and noise levels, in: IOMAC - International Operational Modal Analysis Conference, Gijón, Spain, 2015.

[133] E. Balmés, M. Basseville, L. Mevel, H. Nasser, W. Zhou, Statistical model-based damage localization: A combined subspace-based and substructuring approach, Structural Control and Health Monitoring 15 (6) (2008) 857–875.

[134] M. Döhler, L. Mevel, Subspace-based fault detection robust to changes in the noise covariances, Automatica 49 (9) (2013) 2734 – 2743. doi:https://doi.org/10.1016/j.automatica.2013.06.019.

[135] M. Döhler, F. Hille, Subspace-based damage detection on steel frame structure under changing excitation, in: IMAC - 32nd International Modal Analysis Conference, SEM, Orlando, United States, 2014.

[136] E. Viefhues, M. Döhler, F. Hille, L. Mevel, Asymptotic analysis of subspace-based data-driven residual for fault detection with uncertain reference, IFAC-PapersOnLine 51 (24) (2018) 414 – 419, 10th IFAC Symposium on Fault Detection, Supervision and Safety for Technical Processes SAFEPROCESS 2018. doi:https://doi.org/10.1016/j.ifacol.2018.09.610.

[137] S. Gres, M. Fejerskov, L. Ibsen, L. Damkilde, Experimental damping assessment of a full scale offshore mono bucket foundation, in: P. Sas, D. Moens, A. van de Walle (Eds.), Proceedings of ISMA2016, KU Leuven, Department of Mechanical Engineering, PMA, 2016, pp. 4045–4054.

[138] Structural-Vibration-Solutions-A/S, ARTeMIS Modal Pro 6.0, in: http://svibs.com, 2018.

[139] P. C. Mahalanobis, On the generalised distance in statistics, in: Proceedings National Institute of Science, India, Vol. 2, 1936, pp. 49–55.

[140] M. Döhler, Subspace-based system identification and fault detection: Algorithms for large systems and application to structural vibration analysis, Theses, Université Rennes 1 (Oct. 2011).

[141] S. Allahdadian, Robust statistical subspace-based damage assessment, Theses, University of British Columbia (July 2017).

[142] Q. Zhang, M. Basseville, Advanced numerical computation of chi-square tests for fault detection and isolation, IFAC Proceedings Volumes 36 (5) (2003) 209 – 214, 5th IFAC Symposium on Fault Detection, Supervision and Safety of Technical Processes 2003, Washington DC, 9-11 June 1997. doi:https://doi.org/10.1016/S1474-6670(17)36495-9.

[143] B. Peeters, C. Ventura, Comparative study of modal analysis techniques for bridge dynamic characteristics, Mechanical Systems and Signal Processing 17 (5) (2003) 965 – 988. doi:https://doi.org/10.1006/mssp.2002.1568.

[144] A. Teughels, G. D. Roeck, Structural damage identification of the highway bridge z24 by fe model updating, Journal of Sound and Vibration 278 (3) (2004) 589 – 610. doi:https://doi.org/10.1016/j.jsv.2003.10.041.

[145] J. Maeck, G. D. Roeck, Description of z24 benchmark, Mechanical Systems and Signal Processing 17 (1) (2003) 127 – 131. doi:https://doi.org/10.1006/mssp.2002.1548.

[146] A. Benveniste, B. Delyon, Using local tests to estimate convergence rates for identification, in: Proceedings of the 39th IEEE Conference on Decision and Control, Vol. 2, 2000, pp. 1985–1990 vol.2.

[147] G. H. Golub, V. Pereyra, The differentiation of pseudo-inverses and nonlinear least squares problems whose variables separate, SIAM Journal on Numerical Analysis 10 (2) (1973) 413–432.

[148] J. Liu, X. Liu, X. Ma, First-order perturbation analysis of singular vectors in singular value decomposition, in: 2007 IEEE/SP 14th Workshop on Statistical Signal Processing, 2007, pp. 532–536. doi:10.1109/SSP.2007.4301315.